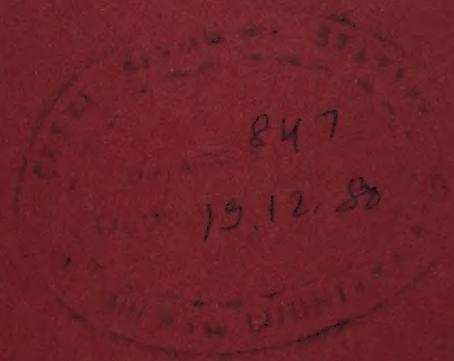


Indian J. pure appl. Phys., Vol. 18 No. 11 pp. 825-932 18/12
November 1980,
CODEN: IJOPAU ISSN: 0019-5596
18 (11) 825-932 (1980)

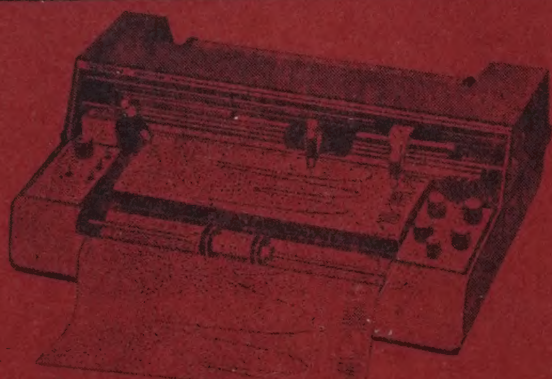


INDIAN JOURNAL OF PURE & APPLIED PHYSICS



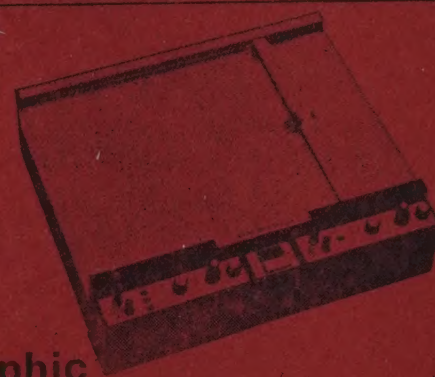
Published by
PUBLICATIONS & INFORMATION DIRECTORATE, CSIR, NEW DELHI
in association with
THE INDIAN NATIONAL SCIENCE ACADEMY, NEW DELHI

a quantum leap in recorder technology now available to the discriminating research scientist a range of reliable 'state of the art' recording instruments



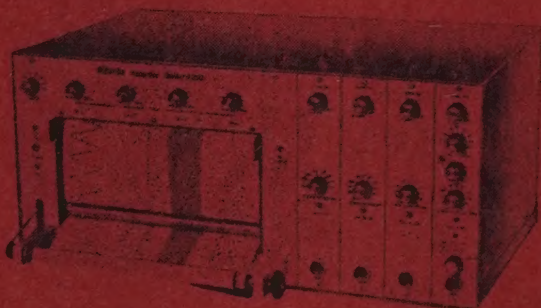
DigiScribe

Strip Chart Recorders One to Four Pens,
0.5 mV full scale and up, 0.5 sec response



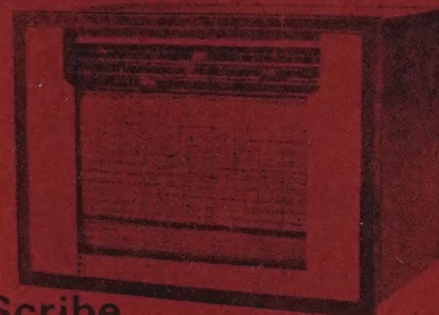
DigiGraphic

XY/t Recorders with plug-in modules to give
wide ranges of sensitivity, time base facility
and log recording.



HiScribe Oscillographic

Oscillographic Recorders DC to 80 Hz, One
to eight channels, Heat or ink writing. Plug in
modules to give wide range of sensitivities



MultiScribe

One to Three Pen and 6, 12 and 24 point
Recorders. Rack mounting with alarm
contacts, cold junction compensation, and
other features.

APPLICATIONS IN THE FIELDS OF

- METEOROLOGY • MATERIAL SCIENCES
- LIFE SCIENCES • PHYSICAL SCIENCES
- CHEMICAL AND ELECTROCHEMICAL SCIENCES
- BIOLOGICAL SCIENCES • PHYSIOLOGICAL AND
BEHAVIOURAL SCIENCES • COMPUTER SCIENCES
- ENVIRONMENTAL AND POLLUTION STUDIES
- ENERGY STUDIES • PHARMACOLOGY
- MECHANICAL/ELECTRICAL ENGINEERING
- METALLURGY/METALLURGICAL ENGINEERING
- AERODYNAMICS/AERONAUTICAL ENGINEERING
- BIO-MEDICAL ENGINEERING
- QUALITY CONTROL APPLICATIONS

MANUFACTURED BY:

DIGITAL ELECTRONICS LIMITED

A Company in collaboration with

**houston
instrument**

DIVN OF **BAUSCH & LOMB** 

Office & Factory:

Digilog House, 74/II, C, Cross Road, Marol Industrial Area, MIDC,
Andheri (East), Bombay-400 093, Phone: 577676, Gram: 'DIGILOG'

NOTICE TO AUTHORS

From January 1981

The abbreviations of journals and other serial titles in the 'References' section of papers published in the *Indian Journal of Pure & Applied Physics* (IJPAP) will be in conformity with those followed by the *Physics Abstracts* (PA) published by the INSPEC, U K. This change is being effected to ensure alignment with international usage of wide scientific following in this regard, since PA is the most widely consulted abstracting periodical by physicists all over the world and is easily accessible. Journals not covered by PA will be abbreviated according to the *Bibliographic Guide for Editors & Authors* (BGEA), 1974, published by the American Chemical Society, Washington DC. The *Chemical Abstracts* follows the abbreviations as given in BGEA.

Therefore, authors submitting papers for publication in IJPAP are requested to consult recent numbers of PA and BGEA (or the "Chemical Abstracts Service Source Index") for abbreviation of names of journals cited in the 'References' section. In the case of journals not covered by PA, the name of the country from which the journal is issued is to be included in parenthesis immediately after the abbreviated title to maintain uniformity of presentation. Also, the full stops after the abbreviated words in titles will be deleted.

Authors may please note this change in the presentation of journal title abbreviations, with effect from January 1981, and ensure that the abbreviations are made conforming to the style outlined above, before despatching the manuscripts for the editor's consideration.

The Indian Journal of Pure & Applied Physics is regularly covered by the following abstracting and current awareness services:

- | | |
|--------------------------|-----------------------|
| 1. Physics Abstracts | 4. Atom Index |
| 2. Physics Briefs | 5. Chemical Abstracts |
| 3. Solid State Abstracts | 6. Current Contents. |

Renewal Notice

Your subscription which expires with the despatch of the December 1980 issue of the journal, stands for renewal. We request you to be so good as to return the enclosed order form duly filled in early, so as to ensure continuity in despatch. Please note the revised subscription rates effective from 1 January 1981.

Sales & Distribution Officer

DATED

THE SALES & DISTRIBUTION OFFICER
PUBLICATIONS & INFORMATION DIRECTORATE (CSIR)
HILLSIDE ROAD, NEW DELHI 110 012 (INDIA)

Dear Sir,

Please renew my subscription/enrol me as subscriber to :

	Rs	£	\$
1. Journal of Scientific & Industrial Research (Monthly)	100.00	17.00	38.00
2. Indian Journal of Chemistry Sec. A (Inorganic, Physical, Theoretical and Analytical Chemistry) (Monthly)	125.00	21.00	47.00
3. Indian Journal of Chemistry, Sec. B (Organic and Medicinal Chemistry) (Monthly)	125.00	21.00	47.00
4. Indian Journal of Technology (Monthly)	90.00	15.00	34.00
5. Indian Journal of Pure & Applied Physics (Monthly)	120.00	20.00	45.00
6. Indian Journal of Experimental Biology (Monthly)	180.00	30.00	68.00
7. Indian Journal of Biochemistry & Biophysics (Bimonthly)	60.00	10.00	23.00
8. Indian Journal of Radio & Space Physics (Bimonthly)	90.00	15.00	34.00
9. Indian Journal of Marine Sciences (Quarterly)	75.00	13.00	28.00
10. Research & Industry (Quarterly)	45.00	8.00	17.00
11. Indian Journal of Textile Research (Quarterly)	45.00	8.00	17.00
12. Current Literature on Science of Science (Monthly)	50.00	6.00	15.00
13. Medicinal & Aromatic Plants Abstracts (Bimonthly)	40.00	7.00	17.00
14. Industrial News Digest (Monthly)	20.00	4.00	8.00

(Please tick off the periodicals you would like to subscribe)

for one year from January 1981 for which I/we have remitted a sum of Rs.....
£...../\$.....by Cheque/Demand Draft No.....
dated.....in favour of PUBLICATIONS & INFORMATION DIRECTORATE

COMPLETE MAILING ADDRESS

Name.....
Address.....
Country/State.....

(Signature)

- Note : 1. Subscribers at annual rates for all the periodicals are enlisted for the full volumes, i.e. for the period from January to December only.
2. The Cheque/Demand Draft may please be drawn in favour of "PUBLICATIONS & INFORMATION DIRECTORATE, NEW DELHI". Banking charges shall be borne by the subscriber. For inland outstation cheques please add Rs. 3.50. For foreign cheques please add \$ 1.00 or £ 0.45.
3. Supply will commence on receipt of subscription in advance.

Indian Journal of Pure & Applied Physics

VOLUME 18

No. 11

NOVEMBER 1980

EDITORIAL BOARD

Dr B A Dasannacharya
Bhabha Atomic Research Centre
Bombay

Prof. B M Deb
Indian Institute of Technology
Bombay

Prof. P Krishna
Banaras Hindu University
Varanasi

Prof. Krishnaji
Allahabad University
Allahabad

Prof. K V Ramanathan
Tata Institute of Fundamental Research
Bombay

Dr S Chandrasekhar
Indian National Science Academy
New Delhi/Raman Research
Institute Bangalore

Prof. A K Saha
Saha Institute of Nuclear Physics
Calcutta

Prof. N C Sil
Indian Association for
Cultivation of Science
Calcutta

Prof. R Srinivasan
Indian Institute of Science
Bangalore

Prof. K Venkata Ramiah
Osmania University
Hyderabad

Dr K L Chopra
Indian National Science Academy
New Delhi/Indian Institute of
Technology New Delhi

Shri Y R Chadha, *Ex-officio* Secretary & Chief Editor

EDITORIAL STAFF

Editors

D S Sastry & K S Rangarajan

Assistant Editors

G N Sarma, J B Dhawan & Tarun Banerjee

Published by the Publications & Information Directorate, CSIR, Hillside Road, New Delhi 110 012

Chief Editor : Y R Chadha

The Indian Journal of Pure & Applied Physics is issued monthly. The Directorate assumes no responsibility for the statements and opinions advanced by contributors. The editorial staff in its work of examining papers received for publication is assisted, in an honorary capacity, by a large number of distinguished scientists, working in various parts of India.

Communications regarding contributions for publication in the journal should be addressed to the Editor, Indian Journal of Pure & Applied Physics, Publications & Information Directorate, Hillside Road, New Delhi 110 012.

Correspondence regarding subscriptions and advertisements should be addressed to the Sales & Distribution Officer, Publications & Information Directorate, New Delhi 110 012.

Annual Subscription
Rs. 100.00 £ 16.50 \$ 42.00

Single Copy
Rs. 10.00 £ 1.80 \$ 4.50

50% Discount is admissible to research workers and students and 25 % discount to non-research individuals, on annual subscription. Payments in respect of subscriptions and advertisements may be sent by cheque, bank draft, money order or postal order marked payable *only* to Publications & Information Directorate, New Delhi 110 012. Claims for missing numbers of the journal will be allowed only if received within 3 months of the date of issue of the journal plus the time normally required for postal delivery of the journal and the claim.

CSIR SCIENTIFIC PERIODICALS

(Revised subscription rate effective from 1 Jan. 1981)

JOURNAL OF SCIENTIFIC & INDUSTRIAL RESEARCH (monthly)

With a fine record of over 35 years' service to the scientific community, this Journal has grown into India's leading general science periodical. Intended to fulfil the responsibility of helping the research workers to keep themselves abreast of current developments in various fields of science and technology, the Journal carries editorial features highlighting important scientific events in India and abroad; articles on science policy and management of science; review articles on topics of current research interest; technical reports on international and national conferences; reviews of scientific and technical publications; and notes on major advances in various fields.

Annual subscription	Rs 100.00	£ 17.00	\$ 38.00
Single copy	10.00	1.70	3.80

INDIAN JOURNAL OF CHEMISTRY (monthly)

This Journal which is running the 19th year of its publication, Consists of the following two sections.

Section A: This section is devoted to papers in Inorganic, Physical, Theoretical and Analytical Chemistry.

Annual subscription	Rs 125.00	£ 21.00	\$ 47.00
Single copy	12.50	2.10	4.70

Section B: This section is devoted to papers in Organic Chemistry including Medicinal Chemistry.

Annual subscription	Rs 125.00	£ 21.00	\$ 47.00
Single copy	12.50	2.10	4.70

INDIAN JOURNAL OF PURE & APPLIED PHYSICS (monthly)

This Journal, which is running the 19th year of its publication, is devoted to original research communications (full papers and short communications) in all conventional branches of physics (except radio and space physics).

Annual subscription	Rs 120.00	£ 20.00	\$ 45.00
Single copy	12.00	2.00	4.50

INDIAN JOURNAL OF RADIO & SPACE PHYSICS (bimonthly)

This Journal serves as a medium for the publication of original research work (full papers and communications) in various areas of radio and space physics.

Annual subscription	Rs 90.00	£ 15.00	\$ 34.00
Single copy	12.00	3.00	6.80

INDIAN JOURNAL OF TECHNOLOGY (INCLUDING ENGINEERING) (monthly)

This Journal publishes papers reporting results of original research of applied nature pertaining to unit operations, heat and mass transfer, products, processes, instruments, and appliances, etc. The Journal is of special interest to research workers in the departments of applied sciences in

universities, institutes of higher technology, commodity research laboratories, industrial cooperative research institutes, and industrial research laboratories.

Annual subscription	Rs 90.00	£ 15.00	\$ 34.00
Single copy	9.00	1.50	3.40

INDIAN JOURNAL OF EXPERIMENTAL BIOLOGY (monthly)

This Journal, devoted to the publication of research communications in the fields of experimental botany, zoology, microbiology, pharmacology, endocrinology, nutrition, etc. is the only one in India with such a wide coverage and scope.

Annual subscription	Rs 180.00	£ 30.00	\$ 68.00
Single copy	18.00	3.00	6.80

INDIAN JOURNAL OF BIOCHEMISTRY & BIOPHYSICS (bimonthly)

This Journal, published in association with the Society of Biological Chemists (India), Bangalore, is the only research Journal in India devoted exclusively to original research communications in biochemistry and biophysics.

Annual subscription	Rs 60.00	£ 10.00	\$ 23.00
Single copy	12.00	2.00	4.60

INDIAN JOURNAL OF MARINE SCIENCES (quarterly)

Commencing publication from June 1972, this Journal is devoted to research communications (full papers and short communications) pertaining to various facets of marine research, viz. biological, physical, geological and chemical oceanography.

Annual subscription	Rs 75.00	£ 13.00	\$ 28.00
Single copy	22.00	4.00	8.40

RESEARCH & INDUSTRY (quarterly)

Intended to serve as a link between science and industry, this Journal is addressed primarily to technologists, engineers, executives and others in industry and trade. It publishes informative original articles containing practical details of processes and products developed in India, which show promise of ready utilization, and technical digests on new processes, products, instruments and testing methods which are of interest to industry. Developments in Indian industry are regularly reported.

Annual subscription	Rs 45.00	£ 8.00	\$ 17.00
Single copy	13.00	2.50	5.00

INDIAN JOURNAL OF TEXTILE RESEARCH (quarterly)

Commencing publication from March 1976, this Journal is devoted to the publication of papers reporting results of fundamental and applied researches in the field of textiles.

Annual subscription	Rs 45.00	£ 8.00	\$ 17.00
Single copy	13.50	2.50	5.10

Please contact

THE SALES & DISTRIBUTION OFFICER
PUBLICATIONS & INFORMATION DIRECTORATE, CSIR
HILLSIDE ROAD, NEW DELHI 110 012

CONTENTS

Solid State Physics

- Anharmonic Coefficients of Alkali Halide Crystals ... 825
R P PANDEY & J D PANDEY

- Behaviour of Like-Dislocations Near an Interface in the Presence of
Lattice Frictional Force — There & Four Dislocations ... 829
N K GILRA

- Static & Impulse Photoconductivity in $\text{Bi}_{12}\text{GeO}_{20}$... 834
S G PRAKASH, A M MAMADOV, N N LEBEDEVA & A R MARDUXAEB

- Effect of Physical Aging on Electrical Properties of Polystyrene ... 839
RANJIT SINGH & S C DATT

- Field-dependent Electrical Conductivity of Indium Oxide Films ... 842
D K JAIN & J C GARG

- Dielectric Investigations in Magneto-Electret State of Polypropylene ... 845
S ASGHAR HUSSAIN, R K SRIVASTAVA & C S BHATNAGAR

- Electron-Plasma Model for the Electromagnetic Effect at Metallic Fracture ... 851
A MISRA & SIBDAS GHOSH

Chemical Physics

- Molecular Dynamics of Some Octahedral Hexahalide Anions ... 857
S MOHAN & K G RAVI KUMAR

- Isentropic Compressibility Behaviour of Amines in Dilute Aqueous Solutions ... 864
M V KAULGUD, (Mrs) ANJALI SHRIVASTAVA & M R AWODE

Mathematical & Theoretical Physics

- Quantum Corrections to Thermodynamic Properties of a Mixture of
Hard Sphere & Square Well Molecules ... 868
N SINGH & S K SINHA

CONTENTS (Contd.)

A Composite Fluid Sphere with Two Density Distributions in General Relativity	874
P PATRA & T ROY	
Strong Coupling Harmonic Oscillator Potential with Weakly Coupled Linear & Cubic Anharmonicities	878
JYOTI CHOUBEY & L K SHARMA	
Nuclear Physics	
Analysis of Proton-Proton Elastic Scattering at High Energies	884
FAZAL-E-ALEEM	
Dielectrics & Microwaves	
Dielectric Studies on Carboxylic Acids: Part III— Dipolar Thermodynamic Excess Functions of Acetic, Propionic & Butyric Acids in Non-Polar Solvents ...	890
R SABESAN, R VARADARAJAN & M SARGURUMOORTHY	
Spectroscopy	
Spectrochemical Determination of Eight Trace Elements in Stainless Steel ...	895
P S MURTY & (Smt) R KAIMAL	
COMMUNICATIONS	
Creep : Dislocation Acceleration	899
N K GILRA	
Electron Microscopy of TaS ₂ Single Crystals Using Weak Beam Technique ...	899
M K AGARWAL, J V PATEL & T C PATEL	
Debye Temperature of Some Solid Solution Series with the NaCl Structure ...	903
B NAGAI AH & D B SIRDESHMUKH	
A Low Noise High Gain Amplifier for Acoustic Emission	904
J SAMPATH KUMAR, S P MALLIKARJUN RAO & M SURYANARAYANA	
Accurate Measurement of Tangential Vibrations of Quartz Crystals	905
HARISH BAHADUR & R PARSHAD	

(Contd.)

CONTENTS (Contd.)

Parallel Plate Electron Multiplier Using $\text{SnO}_2\text{-Al}_2\text{O}_3$	907
P W MAHAJAN & S V BHORASKAR				
NOTES				
Heat Transmission through Jute-Fibre Packings at Low Temperature	910
S K DAS & S C CHAKRAVARTY				
Centrifugal Distortion Constants of Some Phosphorus (V) Chlorofluorides	912
R RAMASWAMI, K SABAPATHY & K VENKATESWARLU				
Viscosity Behaviour of Diphenylamine- <i>p</i> -Toluidine System	913
NARSINGH BAHADUR SINGH				
Estimation of Limiting Solid Volume of Polar Substances: An Analytical Method	915
B K SHARMA				
Green's Function Calculations on the Photoelectron Spectra of Some Small Heteroatomic π -Electron Systems	917
R GOPAL & P C MISHRA				
Temperature Variation of NQR Frequencies in 2,6-Dichlorobenzamide	922
D V RAMANAMURTI, P VENKATACHARYULU & D PREMASWARUP				
Dielectric Loss Factor in Magnetically Polarized Silicone Rubber Tubular Electrets by TSDC	923
RUDRAKANT SHRIVASTAVA, M S QURESHI, M L KHARE & C S BHATNAGAR				
Structure & Vibrational Spectra of Ethylthionformate	926
H S RANDHAWA, G S GREWAL, C L ARORA & V N SARIN				
Infrared Studies on Some Di-Substituted Pyridines	928
R K GOEL, S K GUPTA & S N SHARMA				
Infrared Absorption of 2-Amino-3-Methyl- & 6-Amino-2-Methyl-Pyridine	930
R K GOEL, S D SHARMA, K P KANSAL & S N SHARMA				

Anharmonic Coefficients of Alkali Halide Crystals

R P PANDEY & J D PANDEY

Department of Chemistry, University of Allahabad, Allahabad 211 002

Received 30 November 1979; revised received 7 March 1980

The generalized pair potential energy function of L V Woodcock [*J. chem. Soc. Faraday Trans.*, 70 II (1974), 1405] has been used to compute the anharmonic coefficients of alkali halide crystals. The effects of these co-efficients on the specific heat at constant volume and on the coefficient of thermal expansion have been discussed.

1. Introduction

The anharmonic interactions in solids play an important role in explaining the various thermodynamic properties of alkali halide crystals. The study of the thermodynamic properties of crystals is based on the free-energy and attempts have been made to evaluate the effect of anharmonic terms in the expansion of potential energy function in a power series of nuclear displacements from the equilibrium positions. Expressions for the anharmonic free-energy and specific heat of solid have been derived by a number of workers.¹⁻⁵ Recently, Woodcock⁶ has given a new pair interatomic potential function. The present report deals with the computation of the anharmonic coefficients for the principal mode of oscillations of alkali halides according to the Woodcock potential. The magnitude of the anharmonicity can be used to estimate the thermal expansion and also the specific heat at constant volume. The potential energy of a crystal is expanded in a power series of ionic displacements from their equilibrium position. In the harmonic approximation, only quadratic terms are retained, and thus the problem is solved in terms of the normal modes of vibration of the crystals. However, to understand many features of a real solid, quasi-harmonic approximation is not enough. Thus an estimation of the magnitude of the anharmonic terms is necessary. This can be done very satisfactorily by including the third and fourth order terms in the expansion of the potential energy function.

2. Theory

The potential energy per ion pair of the deformed crystal, when the lattice formed by the alkali ions is displaced with reference to the lattice of the halide ions by a small distance x ($x \ll r_0$, where r_0 is the

equilibrium interionic distance) in a particular direction, can be expressed as:

$$U = U_0 + a x^2 + C x^4 + \dots \quad \dots(1)$$

in which, terms involving odd powers of x are absent due to the centre of symmetry of lattice points. The coefficients of x^2 and x^4 determine the frequency of oscillation and the anharmonicity of the crystal, respectively. U_0 refers to the value of U at $x = 0$ and equals to,

$$U_0 = \frac{-Ae^2}{r_0} + M \phi(r_0) \quad \dots(2)$$

where, A is the Madelung constant; e the electronic charge; M the number of nearest neighbours; and $\phi(r)$ the non-Coulombic interacting terms existing between a pair of ions separated by a distance r . The potential energy $\psi(r)$ between a cation at (x', y', z') and an anion at (x'', y'', z'') from the origin, when one of them is displaced by small distance x , may be given as:

$$\psi(r) = -\frac{e^2}{r} + \phi(r) \quad \dots(3)$$

where, r is given by

$$\begin{aligned} r^2 &= (x'' - x')^2 + (y'' - y')^2 + (z'' - z')^2 \\ &= r_0'^2 + x^2 - 2Qr_0x \end{aligned} \quad \dots(4)$$

where r_0' is the distance of the anion from the origin and Q refers to the cosine of the angle between the direction of r_0' and x . $\psi(r)$ can be expressed as:

$$\psi(r) = \psi(r_0') + x \left(\frac{\partial \psi(r)}{\partial x} \right)_{x=0} + \frac{x^2}{2!} \left(\frac{\partial^2 \psi(r)}{\partial x^2} \right)_{x=0} \quad \dots(5)$$

in which $r \rightarrow r_0$ as $x \rightarrow 0$. Eq. (4) can be used to

express $\left(\frac{\partial \psi}{\partial x}\right)_{x=x_0}$ in terms of $\left(\frac{\partial \psi}{\partial r}\right)_{r=r_0}$ from which the x^4 term in Eq. (5) takes the form,

$$F x^4 = \frac{x^4}{4!} \left[3 (1 - Q^2) (5 Q^2 - 1) \left\{ \frac{\psi'}{r_0^3} - \frac{\psi''}{r_0^2} \right\} + 6 Q^2 (1 - Q^2) \frac{\psi'''}{r_0} + Q^4 \psi^{(4)} \right] \dots (6)$$

where, $F x^4$ is the coefficient of x^4 term in Eq. (5). The coefficient C of the x^4 term appearing in Eq. (1) can be calculated, since

$$C = \sum (M \bar{F}) \dots (7)$$

where \bar{F} indicates the average value of F taken over the M ions, and the summation extends over all such groups. According to Krishnan and Roy,⁷ one gets,

$$Q^2 = \frac{1}{3} \dots (8)$$

$$\text{and } Q^4 = \frac{1}{2} (1 - 3\sigma) - \frac{1}{2} (1 - 5\sigma) (l^4 + m^4 + n^4) \dots (9)$$

$$\text{where, } \sigma = \frac{x''^4}{r_0'^4} \dots (10)$$

Substituting these values of Q^2 and Q^4 in Eq. (6) and then substituting the value of \bar{F} in Eq. (7), we get

$$C = f + p (l^4 + m^4 + n^4) \dots (11)$$

$$\text{where } f = f_c + f_r \dots (12)$$

$$\text{and } p = p_c + p_r \dots (13)$$

where the subscripts c and r stand for Coulombic and non-Coulombic interactions, respectively and f_c , and f_r , p_c and p_r given by the following relations

$$f_r = \frac{1}{24} \left[\left\{ 3 - \frac{15}{2} (1 - 3\sigma) \right\} \left\{ \left(\frac{\phi'}{r_0^3} - \frac{\phi''}{r_0^2} \right) \right\} + \left\{ 2 - 3 (1 - 3\sigma) \right\} \frac{\phi'''}{r_0} + \frac{1}{2} (1 - 3\sigma) \phi^{(4)} \right] \dots (14)$$

$$p_r = \frac{1}{24} \left[\frac{15}{2} (1 - 5\sigma) \left(\frac{\phi'}{r_0^3} - \frac{\phi''}{r_0^2} \right) + 3 (1 - 5\sigma) \frac{\phi'''}{r_0} - \frac{1}{2} (1 - 5\sigma) \phi^{(4)} \right] \dots (15)$$

$$f_c = - \frac{21}{16} \frac{e^2}{r_0^5} \sum \left(M \frac{1 - 5\sigma}{\Delta^5} \right) \dots (16)$$

and

$$p_c = \frac{35 e^2}{16 r_0^5} \sum \left(M \frac{1 - 5\sigma}{\Delta^5} \right) \dots (17)$$

where $\Delta = \frac{r_0'}{r}$. The value of $\sum \left(M \frac{1 - 5\sigma}{\Delta^5} \right)$

for fcc and bcc of crystals have been used from Krishnan and Roy.⁷ For NaCl-type crystals, $\sigma = 1/3$ and for CsCl-type crystal, $\sigma = 1/9$.

In order to compute the values of C , it is necessary to use a function $\phi(r)$ which can accurately represent the repulsive interaction terms. We have taken the repulsive term of generalized pair potential of Woodcock⁶ in order to fulfil the purpose. Thus Coulombic interaction terms may be given by

$$\phi(r) = A r^{-m} \exp \left[-B (r^n - 1) \right] \dots (18)$$

where, A and B are potential parameters which have been computed by the method of Saxena and Kachhava.⁸ The values of f and p obtained by the present calculation according to Eqs. (12)-(18) are reported in Table 1 for twenty alkali halide crystals. Once the values of f and p are known it is possible to compute the values of the anharmonic coefficient C from Eq. (11) for any direction. The values of C for $\langle 100 \rangle$, $\langle 111 \rangle$ directions and the average value of \bar{C} taken over all directions can be expressed respectively as:^{7,8}

$$C \langle 100 \rangle = f + p \dots (19)$$

$$C \langle 111 \rangle = f + \frac{p}{3} \dots (20)$$

$$\bar{C} = f + \frac{3p}{5} \dots (21)$$

The values of $C \langle 100 \rangle$, $C \langle 111 \rangle$ and \bar{C} are given in Table 1.

2.1 Application of Anharmonics

The anharmonic coefficient, a fundamental parameter of crystals, has a broad application for getting a better insight of the thermodynamic properties of solids. From the computed values of the anharmonic coefficient, the effect of anharmonicity on various thermodynamic properties like, thermal expansion coefficient (α), and the specific heat at constant volume (C_v) can be calculated.

The expression for α , including the cubic and quadratic terms based on Einstein's single frequency model can be derived as shown in Eq. (22):^{3,5}

Table 1—Values of Anharmonic Coefficient for Alkali Halide Crystals in Different Directions (in kJ mole⁻¹ Å⁻⁴)

Crystal	<i>f</i>	<i>p</i>	<i>C</i> < 100 >	<i>C</i> < 111 >	<i>C̄</i>
LiF	-116.8179	360.2699	243.452	3.2781	99.3440
LiCl	-52.0943	166.5948	114.5005	3.4373	47.8626
LiBr	-48.6489	144.1968	95.5479	-0.5833	37.8692
LiI	-37.9239	117.6726	79.7487	1.3003	32.6797
NaF	-60.8897	131.8421	70.2594	16.9423	18.2156
NaCl	-64.4066	197.1206	132.714	1.3063	53.8657
NaBr	-58.7299	171.4590	112.729	-1.5769	44.1455
NaI	-40.696	122.1962	81.5002	0.0361	32.6217
KF	-94.8968	291.996	197.0992	2.4352	80.3008
KCl	-55.8596	169.6724	113.8128	0.6979	45.9438
KBr	-42.5326	129.5934	87.0608	0.6652	35.2234
KI	-34.3244	116.6877	82.3633	4.5715	35.6882
RbF	-81.3778	264.3531	182.9753	6.7399	77.2341
RbCl	-42.1817	132.4192	90.2375	1.9580	37.2698
RbBr	-35.3747	109.2917	73.917	1.0559	30.2003
RbI	-28.6903	93.4807	64.7904	2.4698	27.3981
CsF	-58.5513	193.6498	135.0985	5.9986	57.6386
CsCl	79.5787	-76.0226	3.5561	54.2378	33.9651
CsBr	75.1538	-70.9189	4.2349	51.5142	32.6025
CsI	60.7692	-56.9518	3.8174	41.7853	26.5981

$$\alpha = -\frac{C_v \psi'''}{2 r_0 [\psi'']^2} - \frac{225}{2 r_0} (b^2 K^2 T) \frac{\psi'''}{[\psi \psi'']^5} + \frac{54 C K^2 T}{2 r_0} \frac{\psi'''}{[\psi'']^4} \quad \dots(22)$$

where,

$$C_v = K \left[1 + \left(-\frac{15}{8} \frac{b^2}{a^3} \frac{3}{2} - \frac{C}{a^2} \right)^{KT} \right] \quad \dots(23)$$

In Eq. (23) *b* is a constant representing the coefficient of *x*³ in Eq. (1) which is absent in Eq. (1) because of the centre of symmetry of the lattice points in the type of crystals studied. In Eq. (22), the first term is the usual harmonic term and the last two terms represent the contribution due to the anharmonicity. On calculating the fourth order terms (as the third order term vanishes for lattice modes) of this expression, it is found that the contribution of this term to α is very small. Therefore, α , is given by Kachhawa and Saxena,⁹

$$\alpha = -\frac{C_v \psi'''}{2 r_0 [\psi'']^2} \quad \dots(24)$$

In another approach to utilize the coefficient *C* in the determination of specific heat at higher temperature for one-dimensional oscillators, Born and

Brody¹⁰ have shown that at high temperatures, the specific heat at constant volume is given by,

$$C_v = k (1 - T/\theta). \quad \dots(25)$$

where

$$\theta = \frac{8 \pi^4 m^2 v^4}{3 C k} \quad \dots(26)$$

k is the Boltzmann's constant and *m*, the reduced mass. From Eq. (26) the value of θ can be calculated from the knowledge of the infrared absorption frequency (*v*) and the coefficient *C*.

3. Results and Discussion

The computation of the anharmonic terms has been made on the basis of the most realistic potential energy function. The method of calculation of potential parameters utilizes molecular constants (Saxena and Kachhava⁸) known to a high degree of accuracy. It appears that the experimental values of anharmonic coefficients of alkali halides are not available in the literature. The magnitude of *C* has a tendency, in general, to increase with the rise in temperature and will assume a sufficiently large value at high temperature. This, in turn shows, that the contribution of fourth order term increases as we increase the temperature. The computed values

Table 2—Values of Thermal Expansion Coefficient α , and Debye Temperature θ , of Alkali Halide Crystals

Crystal	α , 10^{-5} deg^{-1}			$\theta/100$, K	
	Calc. from Eq. (24)	Exptl. from Ref. 11	Theo. from Eq. (26)	Calc. from Eq. (26)	Calc. from Ref. 7
LiF	18.35	32.90	29.06	46.94	44.0
LiCl	29.06	44.00	53.42	—	64.0
LiBr	31.80	50.00	59.88	—	72.0
LiI	37.75	59.00	68.08	—	70.0
NaF	22.62	—	—	—	70.0
NaCl	40.39	39.50	48.70	50.04	58.0
NaBr	45.09	43.00	46.25	35.50	64.0
NaI	48.22	45.10	51.14	54.98	70.0
KF	40.58	36.70	42.57	—	68.0
KCl	56.95	36.90	48.66	75.48	62.0
KBr	52.99	48.50	45.58	80.54	66.0
KI	50.27	40.00	73.18	58.03	68.0
BbF	36.62	31.67	64.16	—	68.0
RbCl	48.76	38.13	54.95	80.63	60.0
RbBr	51.45	37.43	55.34	78.97	66.0
RbI	56.63	39.20	44.51	82.46	62.0
CsF	30.14	45.50	98.4	—	64.0
CsCl	57.43	—	—	49.79	42.0
CsBr	61.06	—	53.87	54.95	44.0
CsI	65.95	—	33.98	—	44.0
Average % error	26.5	—	35.6	—	—

of thermal expansion coefficient from Eq. (24) are given in the second column of Table 2 with their experimental value.¹¹ Kumar and Kachhava¹¹ evaluated the values of α using the Born-Mayer potential. Their values are presented in the fourth column of Table 2. The average percentage deviation in the values of α from these two methods are 26.5 and 35.6 respectively. From Table 2 it is clear

that our theoretical values of thermal expansion coefficient compete well with the experimental and other theoretical values.¹¹ Using the average value, namely $C = f + 3p/5$, the values of the Debye temperature, were obtained from Eq. (26) and are presented in fifth column of Table 2. For comparison the theoretical values⁷ from Born-Mayer potential are given in the last column of Table 2. The values of θ computed for an NaCl crystal from Eq. (26), comes out to 5004 K, whereas the magnitudes of θ obtained by Eucken and Dunhol¹² and Krishnan and Roy⁷ are respectively 3000 K and 5800 K which are of the same order of magnitude. Thus inspite of the use of an over generalized pair potential model, the results on the whole are satisfactory and stands well in comparison with similar existing approximate calculation.

Acknowledgement

The authors are thankful to the University Grants Commission, New Delhi, for providing the financial assistance.

References

1. Pathak K N, *Phys. Rev.*, **139** (1965), A1569.
2. Wallace D C, *Phys. Rev.*, **139** (1965), A877.
3. Srivastava S V, Sharma M N & Madan M P, *J. Phys. Soc., Japan*, **25** (1968), 212.
4. Thakur K P, *Indian J. pure appl. Phys.*, **11** (1973), 549.
5. Pandey H C, Thakur K P & Pandey J D, *Proc. Nat. Acad. Sci., India*, **45A** (1975), 250.
6. Woodcock L V, *J. chem. Soc. Faraday Trans. II*, **70** (1974), 1405.
7. Krishnan K S & Roy S K, *Proc. R. Soc. Lond.*, **A207** (1951), 447.
8. Saxena S C & Kachhava C M, *Phil. Mag.*, **8** (1963), 1429.
9. Kachhava C M & Saxena S C, *Indian J. Phys.*, **39** (1965 b), 145.
10. Born M & Brody E, *Z. Phys.*, **6** (1921), 132.
11. Kumar V & Kachhava C M, *Proc. Indian Nat. Sci. Acad.*, **86** (1970), 170.
12. Eucken A & Dunhol W, *Z. Electrochem.*, **39** (1934), 792.

Behaviour of Like-Dislocations Near an Interface in the Presence of Lattice Frictional Force — Three & Four Dislocations

N K GILRA

Physics Department, Higher Petroleum Institute, P. O. Box 201, Tobruk, Libya

Received 22 September 1979

Behaviour of like-screw-dislocations in the presence of lattice frictional forces near an interface has been analyzed. The interface separating the materials of different elastic constants is found to repel the dislocations. It is possible for the surfaces covered by an oxide layer or some other film as well. The minimum energy criteria have been used to determine the equilibrium configuration of dislocations, which depend remarkably on the previous history of the film. Formation of these equilibrium configurations should explain the work hardening observed in the case of film coated metals. The behaviour of three and four like-screw dislocations on parallel slip planes for a particular configuration is analyzed and the analysis can be extended to more complex arrays.

1. Introduction

In previous communications^{1,2} we have analyzed the behaviour of two like-dislocations near an interface separately in the absence and in the presence of lattice frictional forces. It was shown that the like-dislocations form a stable configuration if the dislocations are repelled by the interface and the dislocations could not pass each other. In the presence of frictional forces, dislocations could pass each other and their equilibrium configuration depends on their initial position and their direction of motion. This path dependence is due to the irreversible nature of the energy loss which takes place when the dislocations move against the frictional forces. Sadananda and Marcinkowski³ have shown that the condition of a stable equilibrium for a moving dislocation under the frictional force is that the total force on the dislocation due to an applied stress and an internal stress should be less than the frictional force.

2. Theory

Here, for convenience, the notation of screw dislocations are taken to be the same as for edge dislocations. A few assumptions are made, e.g. the dislocations are constrained to remain straight in the presence of an applied stress and frictional stress. Also, they are not to cross slip due to high frictional force in the cross slip plane. Due to the movement of dislocations from one reference state to the new equilibrium state, the total change in the energy of system is given as,

$$\Delta E_T = \Delta E_I + \sum_{i=1}^n E_{\tau}^i + \sum_{i=1}^n E_f^i + \sum_{i=1}^n E_F^i \quad \dots(1)$$

where ΔE_I is the change in the total interaction energy when the dislocations move from a reference state to the equilibrium state and is given as

$$\Delta E_I = \sum_{i=1}^{n-1} \sum_{j=i+1}^n \frac{\mu b^2}{2\pi} \ln \left[\frac{(X_{i1} - X_{j1})^2 + (Y_i - Y_j)^2}{(X_{i2} - X_{j2})^2 + (Y_i - Y_j)^2} \right]^{1/2} \quad \dots(2)$$

where μ is the shear modulus of the material containing dislocation, b the Burger's vector of dislocation, x_{i1} and x_{j1} correspond to the X coordinates of dislocations in reference state and x_{i2} and x_{j2} correspond to the X coordinates in equilibrium state while Y_i and Y_j represent the Y coordinates of the dislocations i and j respectively and n is the total number of dislocations. The work done by the applied stress (τ_a) on dislocation i when it moves from reference state to equilibrium state is given by

$$E_{\tau}^i = -\tau_a b (x_{i1} - x_{i2}) \quad \dots(3)$$

The work done by the repulsive force due to the interface on the i th dislocation is given as⁴

$$E_f^i = \frac{\mu b^2 B}{2\pi} \ln \frac{x_{i1}}{x_{i2}} \quad \dots(4)$$

where

$$B = \frac{\mu^* - \mu}{\mu^* + \mu}$$

where μ^* is the shear modulus of the other material and the energy expended to overcome the frictional stress (τ_f) is given as

$$E_F^i = \left| \tau_f b (x_{i1} - x_{i2}) \right| \quad \dots(5)$$

In all these computations, lattice frictional forces are taken as constants throughout the lattice and their variation with dislocation velocity is neglected. In this analysis, all stresses are expressed in units of $10^{-4} \mu/2\pi$, while the forces are expressed in units of $10^{-4} \mu b/2\pi$, and x 's are expressed in units of Burger's vector.

The equilibrium positions are determined by taking some value for the x coordinate of dislocation 1 (x_1) and computing the x coordinates of other dislocations, so that the total change in energy of the system as given by Eq. (1) is minimized. The symmetrical orientation of dislocations are considered here, so that only two x parameters are left in Eq. (1). One is varied and the other is computed from Eq. (1) by using the computer program FUNFIT⁵ to satisfy the minimum energy change criterion.

The values of x_1 are varied from 1 (very close to the interface) to 3000 (infinite distance from the interface) in forward direction of motion of dislocation 1 or from 3000 to 1 in backward direction of motion. Two different cases are considered here. In the first case, forward direction of motion of dislocation 1 in gradual steps takes place first, and the backward direction of motion is considered afterwards. In the second case, the procedure of the first case is reversed. Different values of τ_a and τ_f have been used for computation. No stable equilibrium configurations are possible for $\tau_f < \tau_a$. Two sets of results are obtained under different stress conditions. The first stress condition is when τ_f is of the order of τ_a and the second stress condition is where $\tau_f \gg \tau_a$. Different values of B have also been used but results have been found independent of B .

After determining the equilibrium configuration of dislocations in each case for a particular stress condition, the force due to internal stresses on each dislocation has been computed by Eq. (6) and is given as

$$F_i^i = \sum_{j=1}^n \frac{\mu b^2}{2\pi} \frac{X_i - X_j}{(X_i - X_j)^2 + (Y_i - Y_j)^2} \quad \dots(6)$$

Where F_i^i is the force on i th dislocation due to the internal stresses, i.e. the force on dislocation i due to dislocation j

The cross slip force⁶ on i th dislocation is given by

$$F_c^i = \sum_{\substack{j=1 \\ j \neq i}}^n \frac{\mu b^2}{2\pi} \frac{Y_i - Y_j}{(X_i - X_j)^2 + (Y_i - Y_j)^2} \quad \dots(7)$$

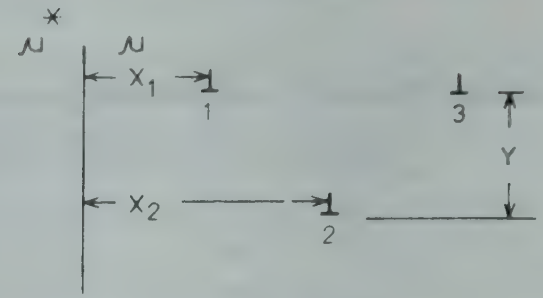


Fig. 1—Orientation of three screw-dislocations near an interface

2.1 Three Dislocations

We consider the symmetrical orientation for three dislocations as shown in Fig. 1 with $Y = 200 b$. The horizontal separation between the dislocations 1 and 2 is same as between the dislocations 2 and 3. So the position of dislocation 3 depends on the position of dislocation 2. For this orientation, the dislocations 1 and 3 will superimpose for $x_1 = x_2$. As a result, we will be left with two dislocations only, which we do not want. So the position of dislocation 2, force due to internal stress and cross slip force on dislocation 1 cannot be shown in graphs for the orientation 1. These results are presented in Table 1.

For the orientation of dislocations as shown in Fig. 1, results for the position of dislocation 2, force due to internal stress and cross slip force on dislocation 1 have been shown in Table 1 for the first case under both the stress conditions. Under the first stress condition, when x_1 is increased from 1 to 3000, x_2 decreases uniformly at a slow rate but when the cycle is repeated by decreasing x_1 , x_2 decreases at a uniform faster rate till the dislocation 1 is close to the interface. Dislocations pass each other in both the directions of motion of dislocation 1. The force due to the internal stress on dislocation 1, computed from Eq. (6) also decreases and changes sign after the dislocations have passed over each other. A similar phenomenon takes place when the dislocation 1 is brought back towards the interface. The cross slip force on dislocation 1, computed from Eq. (7) increases continuously with the increase in x_1 . The rate of increase in cross slip force is slow initially but is quite rapid once the dislocation is far from the interface. The cross slip force decreases rapidly towards the interface. Under the second stress condition, x_2 increases uniformly when x_1 is increased from 1 to 3000. When the dislocation 1 is brought back to the interface, x_2 decreases uniformly. There is a slight deviation from the uniform rate of variation in x_2 when the dislocation 1 is close to the interface in both the paths. Dislocations do not pass each other. Therefore, there is no change in the sign of force due

Table 1—Equilibrium Position of Dislocation 2 (x_2), Force Due to Internal Stress (F_I) and Cross-slip Force on Dislocation 1 (F_C) for the Various Postions of Dislocation 1 (Three Dislocations)

x_1	x_2				F_I				F_C			
	$\tau_f=2.56$	$\tau_f=12.8,$ 25.6	$\tau_f=2.56$	$\tau_f=12.8,$ 25.6	$\tau_f=2.56$	$\tau_f=12.8,$ 25.6	$\tau_f=2.56$	$\tau_f=12.8,$ 25.6	$\tau_f=2.56$	$\tau_f=12.8,$ 25.6	$\tau_f=2.56$	$\tau_f=12.8,$ 25.6
The forward direction motion of dislocation 1 takes place first												
3000	2918	2910	4400	4400	74.30	74.30	-10.50	-10.50	41.50	41.50	1.00	1.00
2500	2920	2650	4160	4140	-31.30	-57.30	-8.95	-9.06	9.24	32.00	0.71	0.73
2000	2930	2390	3920	3880	-16.00	-33.00	-7.80	-7.92	2.21	10.40	0.54	0.56
1500	2940	2130	3680	3620	-10.30	-22.00	-6.90	-7.03	0.95	4.58	0.42	0.44
1000	2950	1870	3440	3360	7.64	-16.70	-6.10	-6.32	0.52	2.51	0.33	0.36
500	2960	1610	3200	3100	6.07	-13.20	-5.50	-5.75	0.33	1.57	0.27	0.29
1	2990	1320	2990	2830	5.0	-11.20	-5.00	-5.28	0.22	1.12	0.22	0.25
The backward direction motion of dislocation 1 takes place first $\tau_a=2.1$												
3000	—	3090	2930	3090	—	-74.27	87.01	-74.27	—	41.58	44.54	41.58
2500	1430	2830	2690	2830	13.70	-37.31	-51.28	-37.31	1.69	13.43	26.28	13.43
2000	1440	2570	2450	2570	24.76	-24.39	-29.67	-24.39	5.66	5.48	8.48	5.48
1500	1450	2310	2210	2310	111.76	-17.81	-20.09	-17.81	47.06	2.87	3.67	2.87
1000	1460	2050	1970	2050	-29.15	-13.95	-15.05	-13.95	7.95	1.75	2.04	1.75
500	1470	1790	1730	1790	-15.04	-11.98	-11.98	-11.45	2.04	1.17	1.29	1.17
1	1500	1500	1520	1520	-9.89	-9.89	-9.76	-9.76	0.87	0.87	0.85	0.85

to internal stress on dislocation 1. This force goes on decreasing when x_1 is varied from 1 to 3000 and increases when x_1 is decreased from 3000 to 1. The cross slip force on dislocation 1 increases when x_1 is varied from 1 to 3000 but at a slower rate than under the first stress condition. This force decreases when the cycle is reversed.

Now the different parameters are computed as usual for the orientation of dislocations as shown in Fig. 1 for the second case under different stress conditions and are also shown in Table 1. Under the first stress condition, x_2 decreases at a uniform rate when x_1 is decreased from 3000 to 1 except when the dislocation 1 is near to the interface. Dislocations do not pass each other. When the cycle is repeated, x_2 continues to decrease at a much slower uniform rate except dislocation 1 which is close to the interface. Dislocations pass each other. There is no equilibrium configuration after x_1 has reached a value of 2500. Force due to internal stress on dislocation 1 does not change sign when x_1 is decreased from 3000 to 1 but it does when the path of dislocation 1 is retraced. Cross slip force on dislocation 1 decreases when x_1 is decreased from 3000 to 1 but it increases, attains a maximum value and then decreases

in the retraced cycle. Under the second stress condition, the results for x_2 are similar as in the first stress condition when x_1 is decreased from 3000 to 1 except when dislocation 1 is close to the interface. But there is a much faster uniform increase in x_2 when the cycle is retraced and dislocations pass each other. Force due to internal stress on dislocation 1 is similar as in the first stress condition when x_1 is decreased from 3000 to 1 but is different when the path of dislocation 1 is retraced. It changes sign only when the dislocation 1 is quite far from the interface. Cross slip force on dislocation 1 is also same as for the first stress condition when x_1 is decreased from 3000 to 1 but it increases slowly and attains a maximum value when the dislocation 1 is far from the interface in the repeated cycle.

2.2 Four Dislocations

Here we consider the symmetrical configuration of four dislocations near the interface as shown in Fig. 2 with $Y = 200 b$. The horizontal separations between dislocations 1 and 2 and between dislocations 2 and 4, are taken to be the same. Dislocations 2 and 3 have no horizontal separation. So the positions of dislocations 3 and 4 depend on the position of

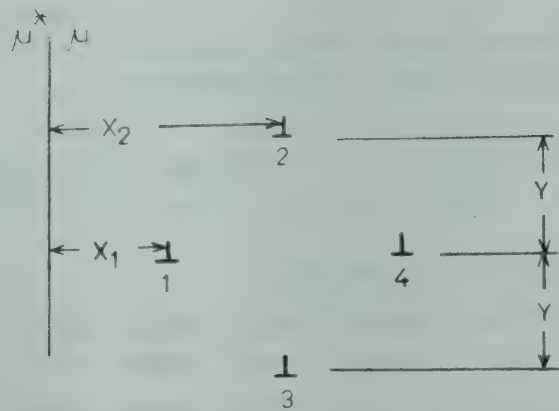


Fig. 2—Orientation of four screw-dislocations near an interface

dislocation 2. Dislocations 1 and 4 will superimpose when $x_1=x_2$. So we will be left with three dislocations only, which we do not want. The results for the position of dislocation 1 are internal stress and cross slip force on dislocation 2, force due to 1 are presented in Table 2 for both the first and second cases.

In the first case under the first stress condition, there is no equilibrium configuration after $x_1 = 2000$ and x_2 decreases uniformly when x_1 is increased from 1 to 2000. When the cycle is repeated with decreasing x_1 , x_2 again decreases but at a much faster rate. Under the second stress condition, the dislocation

form equilibrium configuration up to $x_1=2500$. But there is no equilibrium configuration after x_1 has reached 50 in the repeated cycle with decreasing x_1 . Force due to internal stress on dislocation 1 is computed and is shown in Table 2. Under the first stress condition it changes sign when x_1 is increased from 1 to 2000. In the repeated cycle with decreasing x_1 , this force also changes sign but only when the dislocation 1 is close to the interface and then decreases. Under the second stress condition results for the force due to internal stress are similar as in the first stress condition, upto $x_1 = 2000$ when x_1 is increasing from 1 to 3000. We compute this force also when $x_1=2500$ here. In the repeated cycle, this force changes its nature when dislocation 1 is quite far from the interface. Cross slip force on dislocation 2 has been computed and is shown in Table 2. Under the first stress condition this force increases, first slowly and then rapidly, attains a maximum value and decreases when x_1 is increased from 1 to 2000. This force increases, attains a maximum value and falls off rapidly first and then slowly in the repeated cycle with decreasing x_1 . Under the second stress condition, the nature of variation of this force is similar as discussed above.

Now we make the computations for the second case. Under the first stress condition, x_2 decreases

Table 2—Equilibrium Position of Dislocation 2 (x_2), Force Due to Internal Stress (F_I) and Cross-slip Force (F_C) on Dislocation 1 for the Various Positions of Dislocation 1 (Four Dislocations)

x_1	x_2				$\tau_a=2.1$ F_I				F_C			
	$\tau_g=2.56$		$\tau_f=12.8,$ 25.6		$\tau_f=2.56$		$\tau_f=12.8,$ 25.6		$\tau_f=2.56$		$\tau_f=12.8,$ 25.6	
Forward direction motion of dislocation 1 takes place first												
3000	—	—	—	—	—	—	—	—	—	—	—	—
2500	—	—	1420	1420	—	—	22.53	22.53	—	—	28.32	28.32
2000	1430	1430	1430	1170	40.01	40.01	40.01	29.37	35.96	35.96	35.96	30.63
1500	1440	1170	1440	910	11.08	59.48	11.08	38.88	116.74	51.86	116.74	35.31
1000	1450	910	1450	650	-48.22	92.98	-48.22	57.36	41.49	108.16	41.49	49.61
500	1460	650	1460	390	-25.17	-81.33	-25.17	87.68	29.16	89.00	29.16	101.78
1	1490	360	1490	6	-16.55	-56.44	-16.55	—	26.77	48.69	26.77	—
The badkward direction motion of dislocation 1 takes place first												
3000	—	3090	—	3090	—	-92.98	—	92.98	—	108.16	—	108.16
2500	1430	2830	1450	2830	22.73	-59.48	23.14	59.48	28.38	51.86	28.50	51.86
2000	1440	2570	1460	2570	40.60	-40.01	41.83	40.01	36.31	35.96	37.06	35.96
1500	1450	2310	1470	2310	123.52	-29.44	181.33	29.44	119.12	30.75	122.80	30.75
1000	1460	2050	1480	2050	-47.44	-23.14	-45.92	23.14	40.90	28.50	39.79	28.50
500	1470	1790	1490	1790	-24.93	-19.02	-24.46	19.02	29.08	27.35	28.92	27.35
1	1500	1500	1520	1520	-16.44	-16.44	-16.23	16.23	26.75	26.75	26.70	26.70

uniformly except when dislocation 1 is close to the interface. With the increase of x_1 , x_2 continues to decrease uniformly at a very slow rate and no equilibrium configuration of dislocations are possible after $x_1 = 2500$. Under the second stress condition, results for x_2 are similar as for above case except when dislocation 1 is quite close to the interface when x_1 is decreased from 3000 to 1. In the repeated cycle, a similar type of variation in x_2 takes place. Under the first stress condition, the force due to internal stress on dislocation 1 increases when x_1 is decreased from 3000. In the repeated cycle this force decreases, attains a minimum and then changes its nature. Under the second stress condition, the values of this force are the same as in the first stress condition when x_1 is decreased from 3000. In the repeated cycle, the nature of the variation of this force is similar to the nature of the force under the first stress condition. Under the first stress condition, the cross slip force on dislocation 2 decreases when the dislocation is brought from 3000 to 1 and increases in the repeated cycle. Under the second stress condition, the values for cross slip force are same as in

the first stress condition when x_1 is decreased from 3000.

3. Conclusions

From an analysis of the results we find, in no case, the dislocations pass rigidly as in the case of unlike dislocations.³ Like-dislocations also do not pass one another as super dislocation at infinite stress. This analysis can be extended to more complex arrays with unsymmetrical orientations of dislocations. The present analysis will have an important contribution in the theory of work-hardening in the thin film coated materials.

References

1. Gilra N K, *Phys. Status Solidi*, (A) 34 (1976), 79.
2. Gilra N K, *Phys. Status Solidi*, (A) 40 (1977), 685.
3. Sadananda K & Marcinkowski M J, *J. appl. Phys.*, 43 (1972), 2609.
4. Weertman J & Weertman J R, *Elementary dislocation theory*, (MacMillan, London), 1964, 172.
5. Marcinkowski M J, *Advances in materials research*, Vol. 5, (John Wiley, New York), 1971, 43.
6. Cottrell A H, *Dislocations and plastic flow in crystals*, (Clarendon Press, Oxford), 1965, 49.

Static & Impulse Photoconductivity in $\text{Bi}_{12}\text{GeO}_{20}$

S G PRAKASH*, A M MAMADOV, N N LEBEDEVA & A R MARDUXAEB

Problem Semiconductor Laboratory, Azerbaijan State University, Baku, USSR

Received 30 July 1979; revised received 17 October 1979

A study has been made on the static and dynamic photoconductivity in $\text{Bi}_{12}\text{GeO}_{20}$ crystal so as to define the conditions of maximum photosensitivity for writing optical information. The BGO mono-crystals are taken as thin plates ($d \sim 300 \mu\text{m}$) and are excited with UV laser ($\lambda = 0.33 \mu\text{m}$) and flash lamp ($\lambda = 0.44 \mu\text{m}$). The volt-ampere characteristic in the intensity region 0 to $8 \times 10^{-1} \text{ W/cm}^2$ is found linear while the lux-ampere characteristic is found sublinear ($\alpha = 0.6$). The investigation of spectral characteristic of photocurrent shows maxima at 1.3, 1.8, 2.6 and 3.15 eV. The 3.15 eV peak which corresponds to absorption edge shows 10^5 times larger photocurrent than its minimum value at 0.9 eV. With decrease in temperature the static photocurrent increases, while the impulse photocurrent decreases. This is explained as due to widening of kinetics of relaxation of photocurrent at low temperature. The impulse photocurrent is defined by temperature as well as by the pulse width. The two relaxation times—fast and slow—show opposite temperature dependence and the rest conductivity at low temperature is found to be quite significant and long persisting.

1. Introduction

Bismuth germanate, having the chemical formula $\text{Bi}_{12}\text{GeO}_{20}$ (hereafter referred to as BGO) is known as an effective photoconductor.¹ That is why it is possible to use this material for space time modulation of light in PROM² and for writing the volume hologram.³⁻⁵ The PROM system works with impulse light and hence the optimum conditions of working very much depends on kinetics of photoconductivity which involves the process of generation, recombination and capture of photocarriers in the traps. The holographic writing is accomplished by nonuniform illumination of crystal which is formed when the photoexcited charge carriers diffuse under electric field and are captured in the traps and forming thereby a space charge field, i.e. photoelectret state (PES), which modulates the refractive index, thus giving rise to electro-optic effect. To understand the physical processes involved in PROM, mechanism of hologram writing and for selecting the optimum conditions of writing, it is necessary to know about impulse and static photoconductivity and conditions of formation of PES in BGO. With this interest we studied the static and impulse photoconductivity,⁶ the analysis of which allows one to define the optimum conditions for maximum photosensitivity and PES⁷ in BGO.

2. Experimental Details

The BGO samples were taken as thin plates and the two surfaces were first plane polished ($d \approx 300 \mu$) on a grinding machine and then on one side a semi-transparent and uniform film of aluminium was deposited by vacuum evaporation technique to serve as front electrode. On the other surface, colloidal silver was painted to form the second electrode. Light impulses of different pulse widths were obtained from UV laser ($\Delta t = 10 \text{ nsec}$, $\lambda = 0.33 \mu\text{m}$), the flash lamp ($\Delta t = 2 \mu\text{sec}$, $\lambda = 0.44 \mu\text{m}$) and the mechanical modulator with a raising time of signal of 10 msec; the time constant (RC) of the measuring system was of the order of 10^{-6} sec . The photoresponse due to impulse excitation was displayed on an oscilloscope screen which could memorize the signal. The static photoconductivity was recorded with the help of electrometer-amplifier under monochromatic light excitation. The light intensity was measured with the help of EMO-2 energy meter. For temperature variation, the crystal was mounted in a cryostat in vacuum and the temperature was measured with the help of a copper-constantan thermocouple.

3. Results

3.1 Static Photoconductivity

The investigation of static volt-ampere characteristic in BGO gives rise to inconsistent results. For example, many workers^{8,9} have reported a linear

*Presently at the J K Institute of Applied Physics & Technology, University of Allahabad, Allahabad.

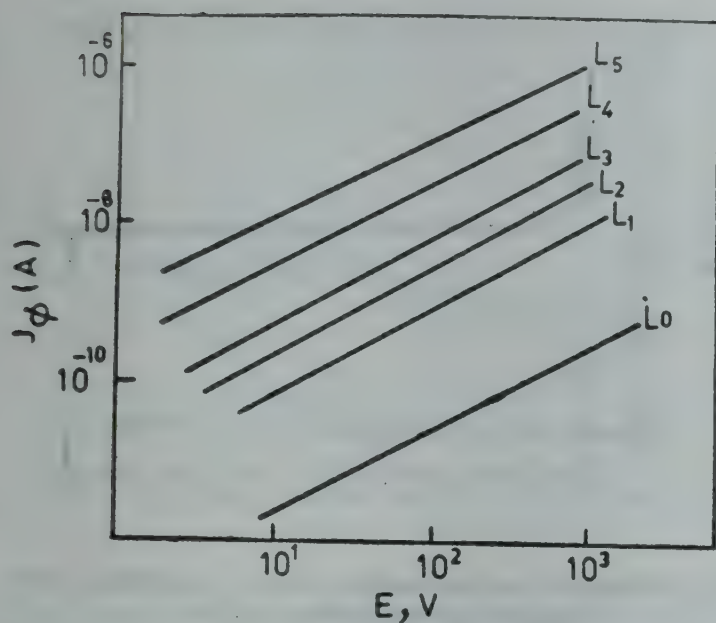


Fig. 1—Volt-ampere characteristics at different excitation light intensities (L_0 = dark, $L_1 = 4 \times 10^{-4}$, $L_2 = 3 \times 10^{-3}$, $L_3 = 1 \times 10^{-2}$, $L_4 = 3 \times 10^{-1}$, $L_5 = 8 \times 10^{-1} \text{ W/cm}^2$)

have measured the LAC in BGO using exciting light of $\lambda = 0.4 \mu\text{m}$ in the intensity range 4×10^{-4} to 0.8 W/cm^2 . The intensity of the light was varied with the help of neutral filters. The plot of LAC on double logarithmic scale is shown in Fig. 2. From the characteristics, the coefficient ($\alpha = \log J_\phi / \log L$) is equal to 0.6, i.e. LAC is sublinear. According to Lushkarov,¹⁵ the LAC may represent the characteristics of recombination process. The linear LAC ($\alpha = 1$) would mean that with change in excitation intensity, the recombination process is not changing for electron photoconductors which otherwise means that the lifetime of photoelectrons throughout the range of change in their concentration (n) remains constant. This may be true under the condition when the equilibrium (dark) concentration of filled recombination hole centres (P_r) is large enough ($P_r \gg n$) so that illumination of crystal does not make any noticeable change in lifetime [$\tau \propto \{1/(P_r + n)\}$]. The sublinear nature of LAC means the violation of conditions that give rise to static lifetime dependence of photoelectrons under varied light intensity.

The investigation of absorption spectral characteristic in BGO in the photo energy interval 2.1–3.6 eV is used to explore its energy levels.^{6,16,17} The measurement of photoconductivity by Bikovekey¹⁴ in the energy interval 0.75–2.6 eV shows the centres of photoconductivity at 0.75, 1.3 and 2.3 eV. In Fig. 3

characteristic up to 10^3 V/cm field, whereas in other studies^{10–13} the volt-ampere characteristic is partly linear, partly square and shows sharp increase in current. Besides, many workers^{12–14} observed negative resistance characteristic and oscillating current as well. We measured the volt-ampere characteristic of dark current and photocurrent in the field interval 1 to 10^3 V/cm for different light intensities and the results are presented in Fig. 1. It is apparent that for given conditions, the volt-ampere characteristic is linear.

The Lux-ampere characteristics (LAC) in BGO were studied earlier by Gudaev⁸ using non-injective electrodes and he observed a linear dependence. We

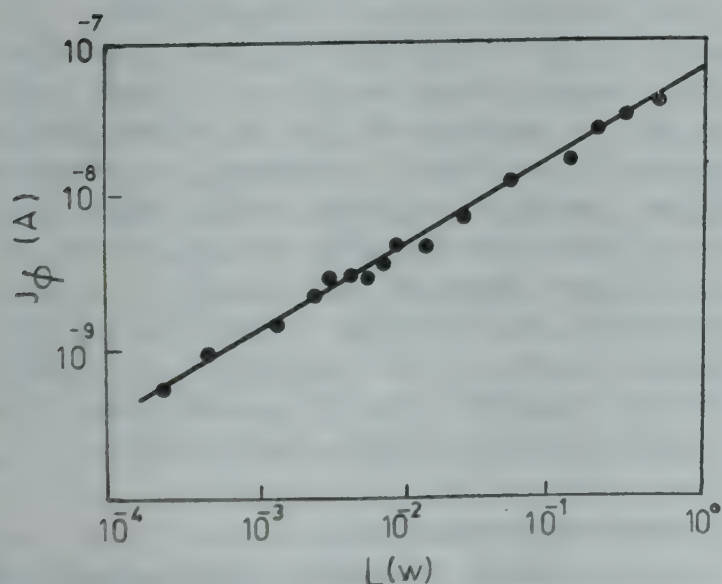


Fig. 2—Lux-ampere characteristics at fixed applied voltage and $\lambda = 0.4 \mu\text{m}$

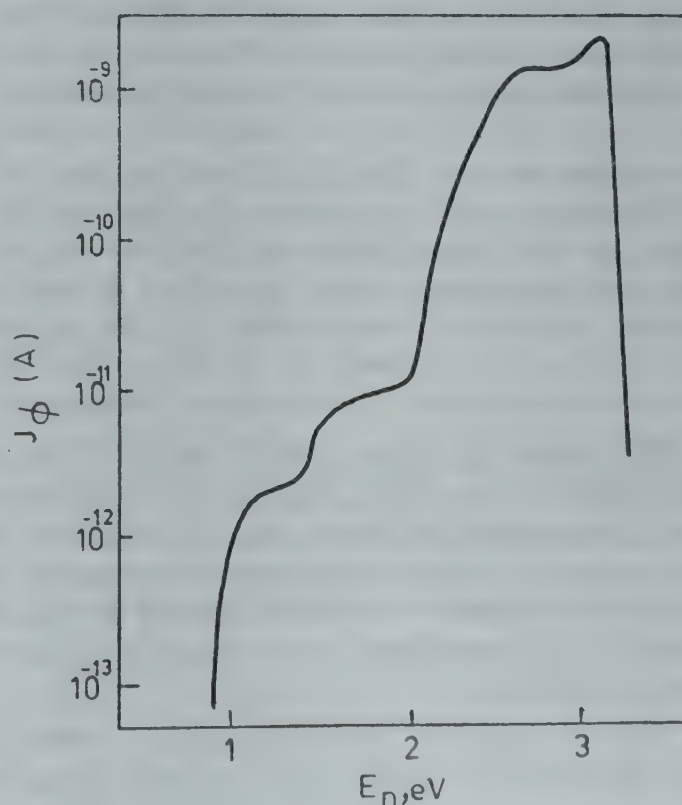


Fig. 3—Spectral characteristics of photocurrent under normalized exciting light intensity

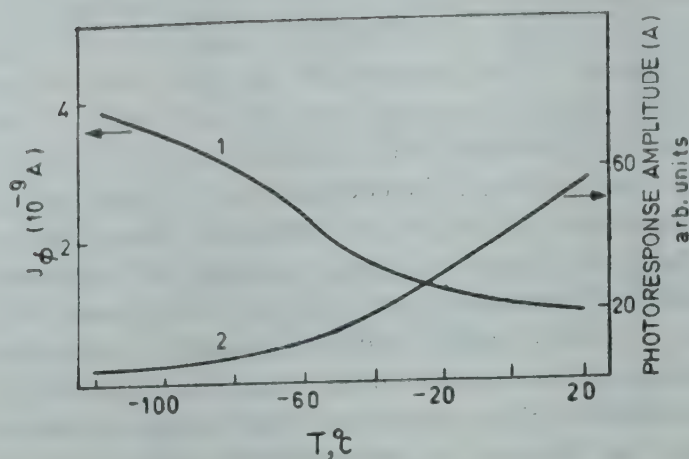


Fig. 4—Temperature dependence of static (curve 1) and impulse (curve 2) photocurrent

we have shown the spectral characteristic of photocurrent under normalized exciting light intensity in the energy interval 0.9–3.3 eV. The maximum photocurrent at 3.15 eV, is 10^5 times larger than its value at 0.9 eV, i.e. the growth of photocurrent in this range is about 5 orders. The longwave side decay of photocurrent shows maxima at 1.3, 1.8 and 2.6 eV which are not well defined. In agreement with the measurements of absorption coefficient by Hau *et al.*,¹⁸ the level placed 2.6 eV below the conduction band and filled with electrons presents the Ge ion vacancy, the density being of the order of 10^{19} per cm.³ The information about level at 1.3 eV is obtained by photoluminescence measurements of Lauer *et al.*¹⁹ This level represents the centre of radiative recombination, only in the cases when it is not filled with the electrons. During photoluminescence study of BGO this level could not be recorded in our measurements. The 1.8 eV level was observed by Bikovskay *et al.*¹⁴ as maxima of photoconductivity in spectral dependence study, but the authors have not commented about its role. A similar spectral dependence characteristic in the region 0.9–3.3 eV is also observed for $\text{Bi}_{12}\text{SiO}_{20}$ (Ref. 20) which is closely similar in properties to BGO.

The temperature dependence of photocurrent in BGO, as far as we know, is not so far investigated. Our measurement of temperature dependence of photocurrent J_ϕ during constant illumination of crystal with light ($\lambda = 0.4 \mu\text{m}$) is given in Fig. 4, curve (1). It is seen that with decrease in temperature J_ϕ increases.

The observation of photoconductivity in BGO at low temperature (-133°C) with long time relaxation is known as rest conductivity (R-C). The R-C is observed in many highly photosensitive semiconductors,²¹ which gets stored in the sample during

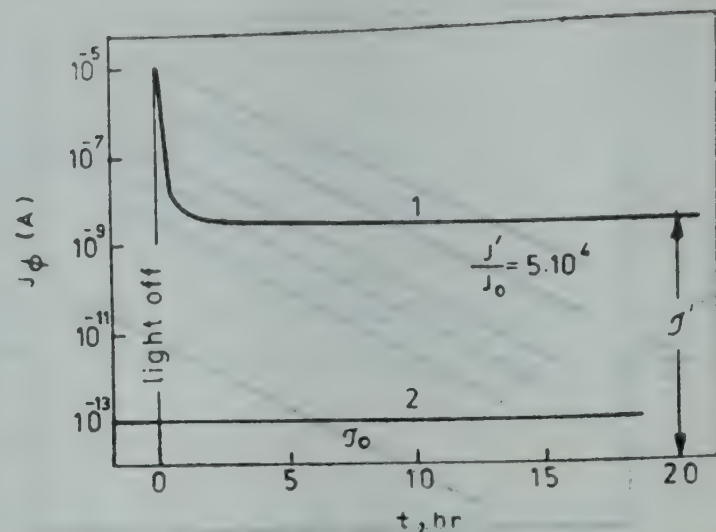


Fig. 5—Decay of rest conductivity (curve 1) and static dark current (curve 2) at $T = -133^\circ\text{C}$

illumination for a long time (up to 10^7 sec). For R-C characteristic we introduce a parameter σ'/σ_0 where σ_0 is dark conductivity at any temperature T , and σ' the dark conductivity at temperature T , under the condition when sample is first illuminated and then the measurements are made after an interval Δt after putting off the light. As an illustration of rest conductivity in BGO, Fig. 5, curve (1) shows the kinetics of relaxation of photocurrent (J') after putting off the light at $T = -133^\circ\text{C}$; the curve (2) shows the static dark current (J_0). To find out J_0 at $T = -133^\circ\text{C}$, the crystal is heated above the room temperature (up to 67°C) and then cooled to -133°C in dark. From Fig. 5, even after 20 hr of putting off the light, the parameter of R-C is equal to $J'/J_0 = 5 \times 10^4$. Thus at the low temperature, the storage of charges in BGO during conductivity measurement is quite significant. For most of the cases R-C must be present in crystals having collective potential barriers related to different kinds of inhomogeneities. The electric field at barriers causes the space distribution of light-excited charge carriers. As a result, when the light is switched off, for the nonequilibrium electrons to recombine, it is necessary to overcome the space barrier having holes. At low temperature, there is little probability of this process to occur and it causes large relaxation time anomaly. At a higher temperature, the probability of penetration through barrier increases and R-C characteristic $\rightarrow 1$. In BGO at room temperature, the R-C characteristic when measured even after 10 min, equals to unity.

3.2 Impulse Photoconductivity

The magnitude of impulse photoconductivity is estimated by the amplitude of photoresponse (A) during pulse excitation of the sample. Temperature

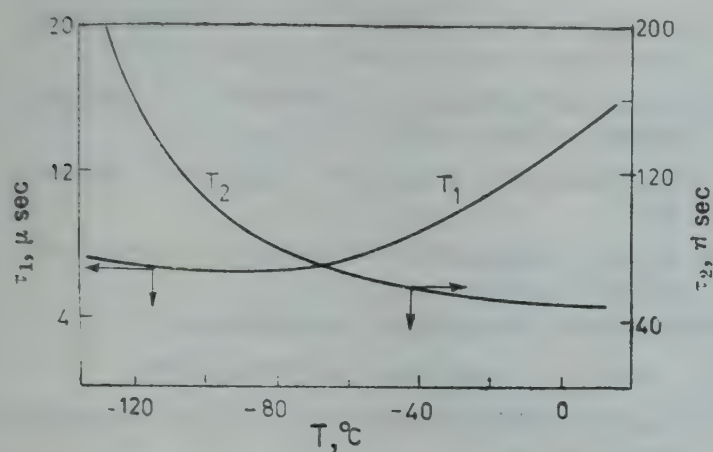
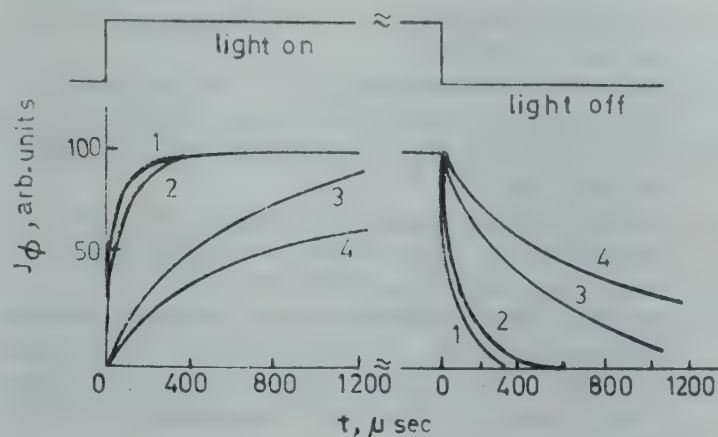


Fig. 6—Variation of relaxation times with temperature

dependence of impulse photoconductivity during illumination with $\lambda = 0.44 \mu\text{m}$ and pulse width (Δt) $2 \mu\text{sec}$ is given in Fig. 4, curve (2). It is seen that in contrast with static photoconductivity, with decrease in temperature, A decreases. To explain the different characteristics of static and impulse photoconductivity, we investigated the kinetics of photocurrent in the temperature interval -133°C to 27°C during excitation with light of different pulse widths.

During excitation of crystal with impulse light with $\lambda = 0.44 \mu\text{m}$ and $\Delta t = 2 \mu\text{sec}$, the kinetics shows two different relaxation times, fast ($-\tau_1$) and slow ($-\tau_2$). The temperature dependence of these times is different; with decreasing temperature, τ_2 decreases while τ_1 increases (Fig. 6). The time dependence of photocurrent on sufficiently long impulse ($\Delta t = 1 \text{ min}$) at different temperatures, is given Fig. 7. It is seen that at low temperature, the photocurrent shows long time decay and at higher temperature, the kinetics narrows down. For short intervals of illumination (pulse width $\Delta t = 2 \mu\text{sec}$) the degree of photocurrent is governed by its kinetics. At low temperature since the photo-current achieves its saturation value rather slowly, within the time of photo-impulse ($\Delta t = 2 \mu\text{sec}$), the photo-current achieves a little fraction of its stable value. With increased temperature, the kinetics narrows down, and within the same interval ($\Delta t = 2 \mu\text{sec}$), the photocurrent achieved a greater fraction of its stable value. Thus with increasing temperature the amplitude of photocurrent increases, i.e. impulse photoconductivity increases and at a given temperature it will be determined by the duration of illumination. For given external conditions, the optimum regime of writing is determined by photosensitivity as well as by the degree of realization of photo-electret state in the crystal. The investigation of PES by Zainally *et al.*,⁷ showed that for getting maximum photo-electret charge, the temperature of polarization (otherwise temperature of

Fig. 7—Time dependence of photocurrent on sufficiently long excitation impulse ($\Delta t = 1 \text{ min}$) at different temperatures [curve: 1, 30°C ; 2, -20°C ; 3, -70°C ; and 4, -120°C]

writing) must lie near 0°C . The decrease of photo-electret charge at $T < 0^\circ\text{C}$ and rise of static photoconductivity at $T < 0^\circ\text{C}$ is explained in Ref. 7 assuming two possibilities: (a) the decrease of trap concentration due to their transition as recombination centres because of shift of Fermi level towards edge of conduction band and (b) presence of barriers in the traps, i.e. in order to get trapped, electrons need certain threshold energy. The measurements of kinetics of photoconductivity may be used to make a selection out of them. From Fig. 7, with decreasing temperature the kinetics slows down; that obviously means some change in kinetics of recombination. The increased role of centre of recombination with low capture cross-section of electrons would correspond to higher lifetime for electrons, i.e. higher photosensitivity. The second hypothesis would mean decrease of photo-electret charge irrespective of kinetics.

The complex measurement of static and impulse photoconductivity and photo-electret state in BGO, allows us to define the conditions of maximum sensitivity for writing optical information in devices utilizing BGO.

References

1. Ablova M S, Andreev A A, Crekhov U M, Gundirev A A, Pevtsov A B, Toepakov V A & Shadeav N I, *J. tech. Phys. (Letters Section)*, **3** (1977), 537.
2. Netorov M P, Prakalev A S & Khomenko A V, in *Proc. Space Modulation of Light L.*, (1977), 42.
3. Huiguard J P & Micheron F, *Appl. Phys. Lett.*, **29** (1976), 591.
4. Micheron F, *Opt. Commun.*, **15** (1976), 216.
5. Peltier M & Micheron F, *J. appl. Phys.*, **48** (1977), 3683.
6. Zakharov E S, Petukhov P A & Skorokov V M, *Izv. Vyzov Fizika*, **5** (1978), 132.
7. Zainally A K, Lebedeva N N, Mamedov A M, Mardukhaev A R & Prakash S G, *Indian J. pure appl. Phys.*, **17** (1979), 661.

8. Gudaev O A, Kctsov A G & Malinovsky V, *Avtometriia*, 1 (1978), 92.
9. Guenok E P & Kudzeen A U, *J. Ukrain Phys.*, 21 (1976), 866.
10. Hayakawa E, Joshisato J & Mikoshiba N, *J. appl. Phys.*, 44 (1973), 2897.
11. Zakharov E S, Akinphiev P P, Petukhov P A & Skorukov V M, *Izv. Vyzov Physika*, 4 (1978), 121.
12. Lenzo P V, *Appl. Phys.*, 43 (1972), 1107.
13. Avramenko V P, Kleamenko L P, Kydzean A U & Sokolyansky G K, *Fiz. tverd. Tela*, 19 (1977), 1201.
14. Bikovskiy U A, Zuev V V, Kharukun A P, Skorukov V M & Imirev I V, *Fiz. Tekh. Polyprobodn.*, 12 (1978), 2004.
15. Lashkarev V E, Lubienko A V & Shenkman M K, *Dokl. Akad. Nauk, SSSR*, 161 (1963), 1310.
16. Aldrich R E, Hou S L & Horvill M L, *J. appl. Phys.*, 42 (1971), 493.
17. Douglas G G & Zitter R N, *J. appl. Phys.*, 39 (1968), 2133.
18. Hau S L, Lauer R B & Aldrich R E, *J. appl. Phys.*, 44 (1973), 2652.
19. Lauer R B, *J. appl. Phys.*, 42 (1971), 2147.
20. Lauer R B, *J. appl. Phys.*, 45 (1974), 1794.
21. Shenkman M K & Shik A Ya, *Fiz. Tekh. Polyprobodn.*, 10 (1976), 210.

Effect of Physical Aging on Electrical Properties of Polystyrene

RANJIT SINGH & S C DATT

Department of Postgraduate Studies & Research in Physics, University of Jabalpur, Jabalpur 482 001

Received 27 October 1979; revised received 14 April 1980

A study of the effect of physical aging on the electrical properties of polystyrene has been carried out. From measurements of the dc-conduction current, and of the thermally stimulated current of aged and non-aged 75 μm bilaterally metallized samples of polystyrene, it has been shown that physical aging considerably affects the electrical properties of this polymer. This effect, which has been considered to be caused by continuous vitrification of a glassy polymer, is considered to enhance the lifetime of a polymer electret.

1. Introduction

There are various reports¹⁻⁶ available in the literature, indicating the definite effect of physical aging on mechanical and electrical properties of polymers. From careful investigations on polyvinyl chloride, van Turnhout *et al.*⁵ have arrived at the conclusion that aging should always be taken into consideration for specifying the low frequency electrical properties of polymers. These authors have also indicated that aging may considerably lengthen the service time of polymer electrets.

In continuation of our previous reports on the electret properties of polystyrene,^{7,8} the present investigation has been undertaken to study the effect of physical aging on the electrical properties of this polymer.

2. Experimental Details

The polystyrene (Styron 685) used for the present study was obtained from Dow Chemical Co. The polymer was dissolved in purified benzene and the solution was filtered. Thin films of polystyrene of appropriate thickness were obtained by floating the cleaned, optically plain glass plate on mercury and then pouring the solution on it. After the solvent evaporated, the film was gently lifted off the glass plate. After mounting between two metal rings of same inner diameter (36 mm), the films were annealed in air at 70°C for 8 hr, and were subjected to room-temperature outgassing at 10^{-4} torr for 24 hr.

Circular samples of polystyrene, 75 μm thick and 45 mm in diameter, were used for the present study. Both the surfaces of the sample were metallized with an evaporated silver layer over a centred circular area of 36 mm diameter.

The thermal polarization as well as the other electrical measurements were carried out by sandwiching the sample between two polished aluminium electrodes of the same diameter as that of the silver layer evaporated onto the sample, so that small insulating edges were provided for. These edges were wide enough to avoid arcing between the electrodes. The electrode assembly was encased in a grounded metal box which served as an adequate shield from electrical pick-up. One of the two metal electrodes was fixed while the other was movable, exerting a slight pressure on the sample. These metal electrodes were efficiently insulated from the metal box with teflon and were connected by coaxial cables to the external circuit.

For maintaining the sample at a desired temperature and for heating it at a linear heating rate the electrode assembly was kept in an oven fitted with a Cole-Parmer temperature programmer. Thermal polarization as well as dc-conductivity measurements were carried out by connecting dc power supply in series with the sample and a vibrating condenser electrometer type EA 811.

The conductivity measurements were made as a function of time at various temperatures ranging from 50 to 110°C with a field of 50 kV/cm. To eliminate the possible contribution of the polarization currents, the samples were first polarized at 120°C for 90 min and then were quenched to the desired measuring temperature under the application of the polarizing field. After allowing 15 min for thermal equilibrium the currents were measured as a function of time t . During the time for thermal equilibrium and aging, the field was kept constant.

To study the thermally stimulated current in short-circuit condition, the bilaterally metallized

samples were quenched from 120 to 100°C, 90 and 70°C. After being aged at 100, 90 and 70°C for various periods of time, the samples were polarized at these temperatures with a polarizing field of 50 kV/cm. The time of polarization in each case was adjusted to be 2 hr. During polarization, the polarizing voltage was applied to the lower electrode with the upper electrode connected to the electrometer. Thermally stimulated currents in shorted sample were measured with the lower electrode connected to the ground. The electrets were depolarized at a linear heating rate of 1°C/min.

3. Results and Discussion

The results of some of the dc-conductivity experiments are given in Fig. 1, which shows the variation of currents with the time t , elapsed after quenching, at different temperatures. These currents are considered to be purely the conduction currents (I_c). The contribution of the time-dependent polarization currents (I_p), has been eliminated by first polarizing the samples at a temperature well above the glass-rubber transition temperature (T_g), and then quenching them to the desired temperature under the application of the polarizing voltage. Inspection of Fig. 1 shows that at temperatures below T_g the conduction current continuously decreases with time t , whereas above T_g , it remains constant. In general, I_c follows the relation, $I_c \propto t^{-n}$, where t is the time and n is a decreasing function of temperature lying between zero and unity. It becomes zero at temperatures

above T_g and thus I_c remains constant at such temperatures. The values of n at temperatures 50, 60, 70 and 90°C, which are below T_g have been found to be 0.7, 0.6, 0.4 and 0.15, respectively.

These results are consistent with the free-volume model.^{3,4} When after being quenched to the temperature below T_g , the polymer is kept at this temperature, neither the transport mobility (μ_t) of molecular segments nor the free-volume reach their equilibrium values. Since they depend on each other, an equilibrium state is attained only after a long time. The free-volume is necessary not only for the segmental motion of chain segments, but also for charge carrier transport processes to occur. The obvious consequence of this fact is that the mobility of chain segments and also that of charge carriers, which have to move from one trapping site to the other to give rise to the conduction current, is decreased due to the decrease in free-volume which takes place during aging at temperatures below T_g . It has been reported that unsaturation sites along main chains act like traps in the bulk.⁹ In addition to this, alteration of bond lengths and chain folds also act like traps in polymers.⁹ Thus, the motion of chain segments may lead to a change in the trap distribution and density in polymers. The redistribution of traps in energy and change in their density are expected to modify the mobility of charge carriers which is reported to be trap-modulated in polymers.¹⁰ As has been suggested by Perlman,¹¹ the charge release requires the motion of atoms and also that of main chains, and hence the decrease in mobility of chain segments is considered to lower the mobility of charge carriers. Thus, the decrease in mobilities of charge carriers and chain segments during aging at temperatures below T_g causes the decrease in conduction current with aging at such temperatures. However, the polymer attains thermodynamic equilibrium at temperatures above T_g , and therefore the conduction current remains constant at such temperatures.

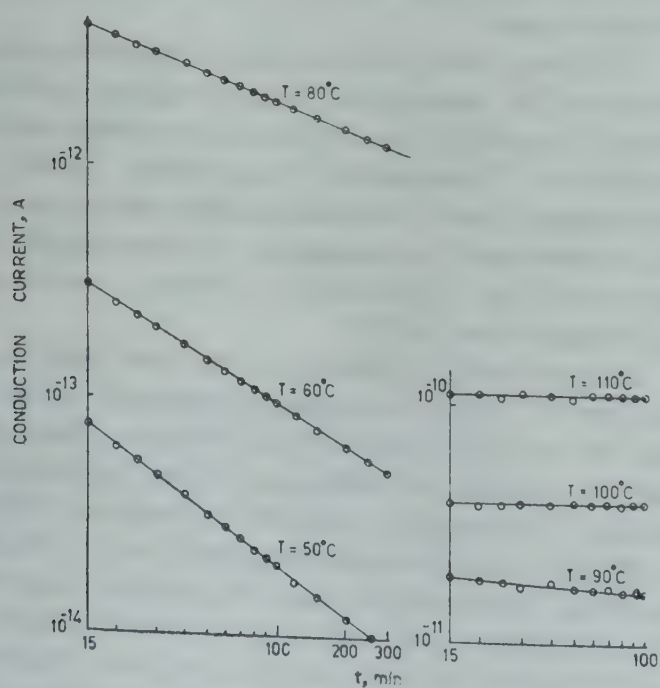


Fig. 1—Variation of conduction current with time t , elapsed after quenching the polystyrene electrets from the polarizing temperature of 120°C to the measuring temperature T

Short-circuit thermally stimulated current spectra, obtained from samples which were polarized at 70, 90 and 100°C after being aged for different periods of time at these temperatures, are shown in Fig. 2. It is noted that the depolarization current, obtained from electrets polarized at 70°C, is considerably reduced by aging. However, such effect of aging is sufficiently minimized in the case of electrets polarized at 90°C and is present only slightly in the case of electrets polarized at 100°C. This behaviour is again in agreement with the free-volume theory, according to which aging increases relaxation times at temperatures below T_g . At such temperatures, the relaxation times increase with aging time because μ_t con-

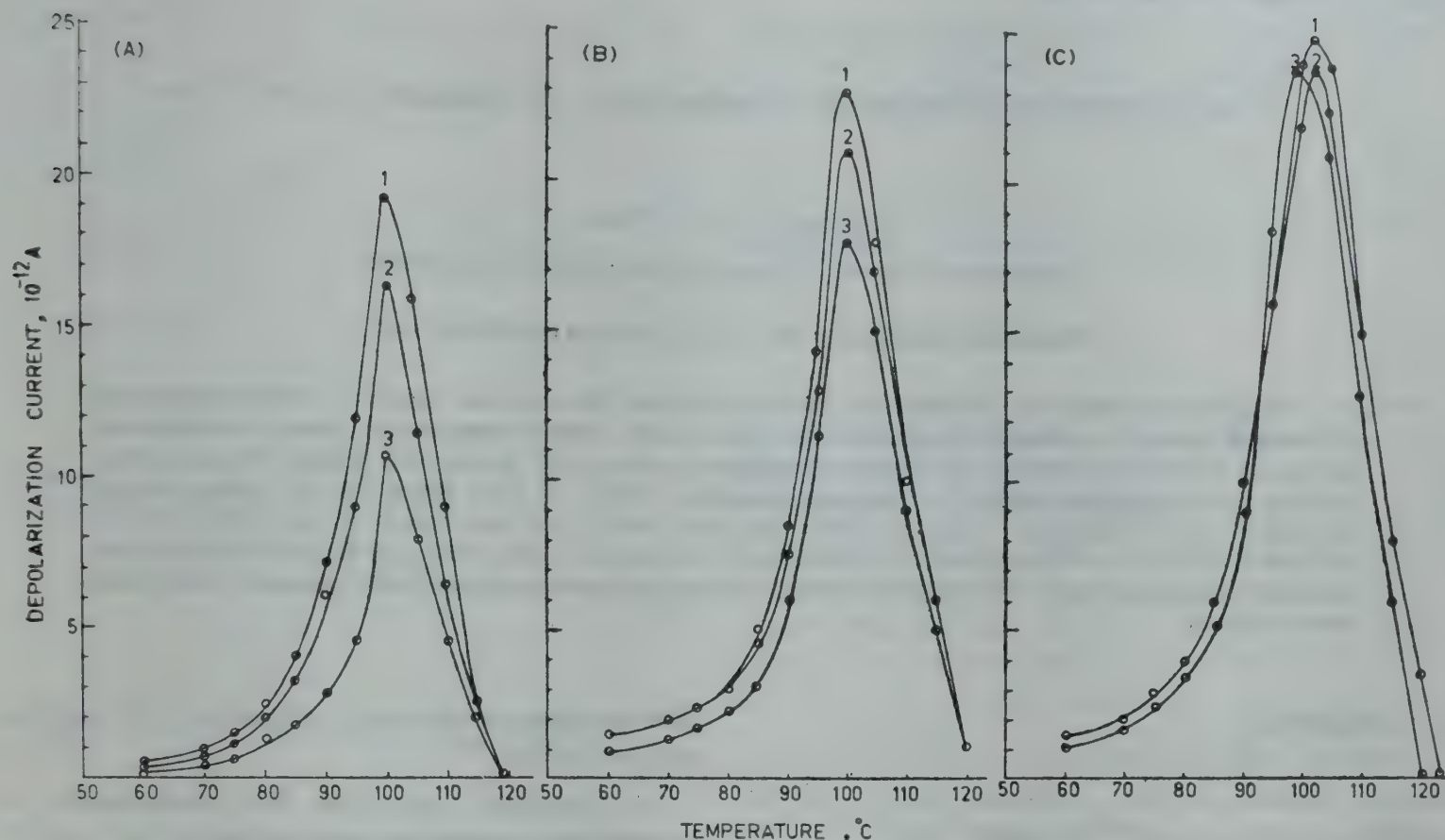


Fig. 2—Short-circuit thermally stimulated current spectra from polystyrene electrets polarized with a field of 50 kV/cm, after quenching and aged at (A) 70°C; (B) 90°C and (C) 100°C. [Aging time (in hr) : Curve 1, 0; Curve 2, 1 and Curve 3, 72].

tinuously decreases. Due to the increase in relaxation times with aging, the polarization produced in the sample becomes smaller the longer the sample has been aged.

From the present investigation, it has been concluded that physical aging is a phenomenon that causes considerable changes in the electrical properties of the polymers, and for the complete characterization of these properties it should be given proper consideration.

Acknowledgement

The authors are thankful to the University Grants Commission, New Delhi, for sanctioning a

research project under which this work has been carried out.

References

1. Struik L C E, *Ann. New York Acad. Sci.*, **279** (1976), 78.
2. Struik L C E, *Polymer Engng. Sci.*, **17** (1977), 165.
3. Kovacs A J, *Fortschr. Hochpolym. Forsch.*, **3** (1964), 394.
4. Ferry J D, *Viscoelastic properties of polymers* (Wiley, New York), 2nd Edn, 1970, 326.
5. Van Turnhout J, Klaase P T H A, Ong P H & Struik L C E, *J. Electrostatics*, **3** (1977), 171.
6. Sharp E J & Garn L E, *Appl. Phys. Lett.*, **29** (1976), 480.
7. Singh R & Datt S C, *J. Electrostatics*, **6** (1979), 297.
8. Singh R & Datt S C, *Thin Solid Films*, **70** (1980), 235.
9. Creswell R A, Gribbon B I, Kabayama M A & Perlman M M, *Telesls*, **211** (1971), 21.
10. Sessler G M & West J E, *J. appl. Phys.*, **47** (1976), 3480.
11. Perlman M M, *J. electrochem. Soc.*, **119** (1972), 892.

Field-dependent Electrical Conductivity of Indium Oxide Films

D K JAIN & J C GARG

Department of Physics, University of Rajasthan, Jaipur 302 004

Received 13 September 1979; revised received 14 December 1979

The current-voltage characteristics of Al-In₂O₃-Al thin film sandwich system in the thickness range 2000-6000 Å of In₂O₃ at different temperatures have been studied. From thermoelectric power measurements, the nature of current carriers in In₂O₃ films has been found to be *n*-type. In low field region, the conduction is ohmic while in high field region, the results are interpreted in terms of Rose theory of space-charge-limited currents in defect insulators. The trap density per unit energy has been found to be of the order of 10¹⁸ cm⁻³ eV⁻¹ and it decreases slightly with increase of temperature. The position of Fermi level lies 0.65 eV below the conduction band. The dielectric constant of the films decreases slightly as the thickness varies from 6000 to 2000 Å.

1. Introduction

Indium oxide (In₂O₃) is an *n*-type semi-conductor¹ because of the non-stoichiometry of the compound with an In/O ratio larger than 2/3. The electrical and optical properties of this compound have been the subject of a number of investigations. Electrical properties of In₂O₃ were studied by Rupprecht,² Weiher,³ Muller⁴ and DeWit.⁵⁻⁷ Weiher,³ from the electrical conductivity measurements on In₂O₃ single crystals, reported that donor ionization energy decreases with impurity concentration with an activation energy of 1.55 eV. Most of the investigations were carried out to study the temperature dependence of electrical conductivity, mobility, etc. In the present paper, the effect of high field on the electrical conductivity of In₂O₃ thin films sandwiched between aluminium electrodes, has been studied and the possible nature of defects discussed.

2. Experimental Procedure

In₂O₃ films were prepared by vacuum deposition of bulk material (Koch Light, 99.99% pure) from molybdenum boat through suitable masks, on the metallic electrode film of aluminium (lower electrode) which was formerly deposited on a Corning 7059 glass plate. On the system Al-In₂O₃, another electrode of the same metal (upper electrode) was deposited so as to form Al-In₂O₃-Al sandwich system. The vacuum chamber was maintained at a pressure of about 5 × 10⁻⁵ torr during deposition. The technique of measuring film thickness was the same as described earlier.⁸ The varying electric field was applied to the sample by an electronically regulated dc power supply (range 0-30V). The techniques to measure electric capacity and current at

different temperatures and voltages were the same as reported earlier.^{9,10}

The electrical set-up for the measurement of thermoelectric power is shown in Fig. 1.

3. Results and Discussion

Fig. 2 represents the log *I* versus 10³/*T* curves for films of different thicknesses (6000, 3000 and 2000 Å) at low voltage (0.1 V). The values of activation energy (*E_a*) were then determined from the slope of the Arrhenius plot and *E_a* is plotted against thickness (*d*) in the inset of Fig. 2. It may be noted that *E_a* increases slightly with decrease in *d*. The values are in good agreement with those obtained by Sasaki and Hijikatu.¹¹ The observed variation of *E_a* with *d* appears to be due to the dissociation of In₂O₃ at the time of deposition, leading to films of different island sizes and having varying amounts of the dissociated species and grain boundaries.

Plots between log *I* and log *V* for different thicknesses (2000, 3000 and 6000 Å) of In₂O₃ films sandwiched between aluminium electrodes at different

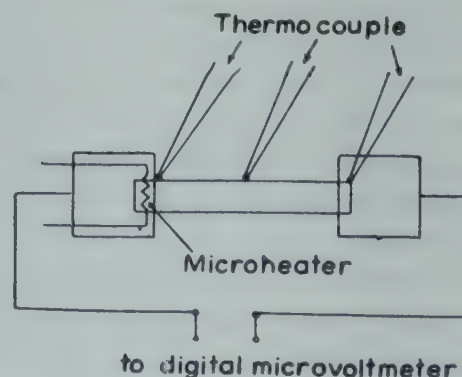


Fig. 1—Circuit diagram for measuring thermoelectric power

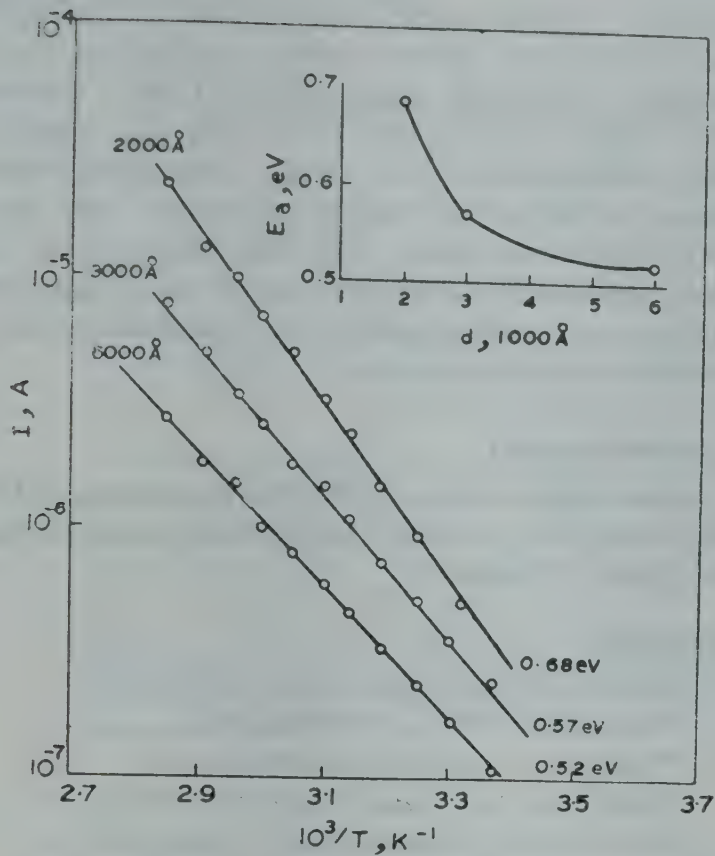


Fig. 2—Log I versus $10^3/T$ for In_2O_3 films of different thicknesses

temperatures show that at low voltages, I increases linearly with V , obeying Ohm's law. At high voltages, there is a non-ohmic variation of I .

The ohmic behaviour at low voltages can be explained by the fact that there is negligible injection of carriers from the electrode in the In_2O_3 film and the initial current is governed by the intrinsic free carriers in the material.

At high voltages, the non-ohmic behaviour can be explained on the model of space charge-limited (SCL) currents in defect insulators. Mott and Gurney¹² proposed that in insulators at high fields SCL currents are formed, and they arrived at the following relation

$$I = \frac{9}{8} \frac{A \epsilon \mu V^2}{d^3} \quad \dots (1)$$

where ϵ is the dielectric constant, μ the mobility, V the voltage applied, d the distance between the contacts and A the area of cross-section of the sample. As the plots are obtained at characteristic current densities $J \propto V^n$ where $n > 2$, the observed results are in contradiction with the theoretical approach.

To give a suitable explanation in such cases, Rose¹³ introduced a uniform density of traps which reduces the number of injected carriers whose distribution is located in the band gap having a density per unit energy given by

$$N_t = d n_t / d E \quad \dots (2)$$

where n_t is the density of traps. With this distribution, the I - V relationship can be written as

$$I = \frac{9}{8} \mu N_0 e A \frac{V}{d} \exp(tV) \quad \dots (3)$$

where N_0 is the number of carriers removed by thermal agitation, e the electronic charge, and

$$t = \frac{\epsilon}{4 \pi e N_t d^2 k_B T} \quad \dots (4)$$

k_B being the Boltzmann's constant. Eq. (4) suggests that a plot of $\log(I/V)$ versus V should be a straight line.

Plots between the experimental values of $\log(I/V)$ versus V show that in high field region the curves are linear. The slope t of the straight lines give the value of N_t at different temperatures. The linear portion of the straight line on extending gives the intercept K_0 on the vertical axis. This intercept gives the value of N_0 with the help of the relation,

$$N_0 = \frac{8}{9} \frac{d}{\mu e A} K_0 \quad \dots (5)$$

The value of N_0 can be related to the density of states of the lower conduction band as

$$N_0 = N_c \exp \left[- \frac{(E_c - E_F)}{k_B T} \right] \quad \dots (6)$$

$$\text{where } N_c = 2 \left(\frac{2 \pi m_e^* k_B T}{h^2} \right)^{3/2}$$

m_e^* is the effective mass of carriers. It is possible to calculate the position of Fermi level E_F below the conduction band.

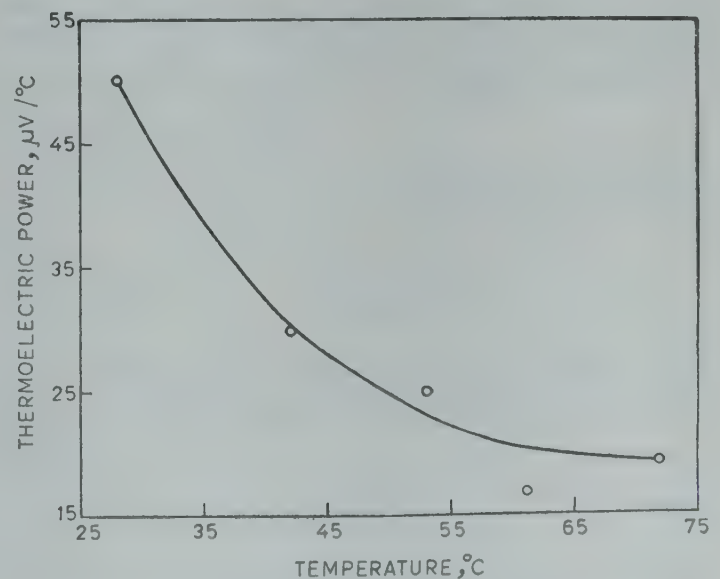


Fig. 3—Variation of thermoelectric power with temperature for 3000 Å thick film of In_2O_3

Table 1—Values of d , ϵ , T , N_t , N_0 and $(E_c - E_F)$

d Å	ϵ	T K	$N_t \times 10^{-18}$ $\text{cm}^{-3} \text{eV}^{-1}$	$N_0 \times 10^{-6}$ cm^{-3}	$E_c - E_F$ eV
6000	68.8	297	0.919	3.77	0.65
		313	0.783	1.01	0.66
		323	0.715	1.84	0.67
3000	67.8	297	2.17	3.47	0.65
		313	1.88	11.3	0.63
		323	1.47	20.7	0.66
2000	67.4	301	2.37	6.17	0.65
		313	1.76	9.75	0.66
		323	1.81	37.0	0.66

In these calculations, the following values of μ and m_e^* are used,⁴

$$\mu = 10 \text{ cm}^2/\text{V-sec}, m_e^* = 0.3 m_e$$

The values of dielectric constant obtained from capacity measurements are given in Table 1. The values are in good agreement with those obtained by Goswami and Goswami¹⁴ in In_2O_3 films. The calculated values of N_t , N_0 and $E_c - E_F$ are also included in Table 1. It is evident that the trap density per unit energy is of the order of $10^{18} \text{ cm}^{-3} \text{eV}^{-1}$ and the position of Fermi level lies 0.65 eV below the conduction band. The value of N_t decreases slightly with increasing temperature.

Fig. 3 shows the variation of thermoelectric power of a linear film of thickness 3000 Å as a function of temperature. It suggests that the sample has n -type behaviour in the temperature range

studied. It may be due to the presence of defects involving either oxygen vacancy or indium interstitials. In both the cases, the In/O ratio exceeds 2/3. Both types of defects can explain the conduction phenomenon to some extent. The slight dissociation of In_2O_3 at the time of deposition may also lead to the above effect. The films may consist of In_2O_3 mixed with varying amounts of the dissociated species, e.g. In-O, leading to the formation of non-stoichiometric composition.

Acknowledgement

One of the authors (DKJ) is grateful to CSIR, New Delhi, for providing financial assistance during the course of this work.

References

1. Arvin M J, *Phys. Chem. Solids*, **23** (1962), 1681.
2. Rupprecht G, *Z. Phys.*, **139** (1954), 504.
3. Weiher R L, *J. appl. Phys.*, **33** (1962), 2834.
4. Muller H K, *Phys. Status Solidi B*, **27** (1968), 723.
5. DeWit J H W, *J. Solid St. Chem.*, **8** (1973), 142.
6. DeWit J H W, *J. Solid St. Chem.*, **13** (1975), 192.
7. DeWit J H W, *J. Phys. Chem. Solids*, **38** (1977), 819.
8. Jain D K & Garg J C, *Indian J. pure appl. Phys.*, **17** (1979), 642.
9. Jain D K & Garg J C, *Proc. Indian Natl. Sci. Acad., Part A*, **44** (1978), 281.
10. Jain D K & Garg J C, *Indian J. pure appl. Phys.*, **17** (1979), 10.
11. Sasaki T & Hijikatu K, *Nippon Diagaku Bunrigakubu Shizenkagaku Kenkusho Kenkyu Kiyo*, **10** (1975), 1.
12. Mott N F & Gurney R W, *Electronic processes in ionic crystals* (Dover Publishing Co., New York), 1948.
13. Rose A, *Phys. Rev.*, **97** (1955), 1538.
14. Goswami A & Goswami A P, *Pramana*, **8** (1977), 335.

Dielectric Investigations in Magneto-Electret State of Polypropylene

S ASGHAR HUSSAIN, R K SRIVASTAVA & C S BHATNAGAR

Department of Physics, M A College of Technology, Bhopal-7

Received 25 October 1979; revised received 20 December 1979

Dielectric behaviour of polypropylene has been investigated in its magneto-electret (ME) state. ME samples have been prepared at forming temperatures (T_f) from 22½ (RT) to 135°C and forming magnetic fields (H_f) ranging from 0.8 to 17.5 kOe. In general, an increase in the dielectric constant (ϵ) has been observed on almost all the samples, which recovers to some extent with time. The variation in ϵ has been explained on the basis of positive isocharge observed in the samples. The theory of M M Perlman and J L Meunier [*J. appl. Phys.*, 36 (1965), 420] on charge decay of carnauba wax electret has been extended to the case of ME for the absolute determination of ϵ from the surface charge study. The calculated theoretical value comes out to be 2.231 which agrees well with the experimental value 1.87, thereby supporting the idea of volume polarization in polypropylene MEs.

1. Introduction

Dielectric behaviour of magneto-electrets (MES) prepared from various substances has been studied by different workers¹⁻⁶ (both at audio and radio frequencies), to understand the mechanism of formation of MEs. At audio frequency, polyvinylchloride (PVC) (Ref. 1) and polyvinylidene fluoride (PVF₂) (Ref. 2) MEs have been reported to show decrease in the value of dielectric constant (ϵ), while perspex^{3,4} MEs show an increase in ϵ for the samples formed below the softening temperature and a decrease above the softening temperature. At radio frequency, PVC (Ref. 5) and perspex⁶ show, in general, a decrease in ϵ while PVF₂ (Ref. 2) shows a mixed character of increase and decrease in ϵ , below and above the softening temperature of the sample.

Besides the various commercial applications, polypropylene (PP), has a potential for applications in making synthetic fibre and in optical polaroids, as suggested by the authors⁷ earlier. Therefore, it was thought proper to investigate its various properties using the ME effect.⁸ The earlier work on optical anisotropy in polypropylene ME has been quite encouraging. Hence, in the present study, the dielectric behaviour of polypropylene magneto-electret has been investigated at a fixed audio frequency of 1 kHz, since PP is a non-polar substance and its dielectric behaviour does not depend on frequency. A very insignificant change in ϵ has been observed in the frequency range 0-16 kHz.

2. Method of Calculation of ϵ

An attempt is made, for the first time, to calculate the absolute value of ϵ in the case of MEs using

the study of surface charge. In view of the lack of a proper phenomenological explanation for the ME state in dielectric, the basic formula for the calculation of absolute value of ϵ as derived by Perlman and Meunier⁹ in case of carnauba wax thermo-electret is used here. According to Perlman, the absolute value of ϵ is given by

$$\epsilon = 1 + \frac{\pi(0)}{\epsilon_0} \quad \dots(1)$$

where $\pi(0)$ is the specific polarization function, i.e. polarization per unit field at time $t = 0$ and ϵ_0 is permittivity of free space. The value of $\pi(0)$ in Eq. (1) can be obtained from the relation

$$\pi(0) = -\epsilon_0 + \frac{C \cdot d \cdot v(0)}{A \cdot V} \quad \dots(2)$$

where C is capacitance of sample, d the thickness, $v(0)$ the potential across the sample, A the area of the sample surface and V is the voltage applied for the formation of sample.

In case of MEs since we do not use any voltage during its formation, Eq. (2) is modified accordingly as

$$\pi(0) = -\epsilon_0 + \frac{C \cdot v(0)}{A \cdot (V/d)}$$

where (V/d) is the intensity of the electric field, which can be replaced in our case by E_{eq} , and therefore

$$\pi(0) = -\epsilon_0 + \frac{C \cdot v(0)}{A \cdot E_{eq}} \quad \dots(3)$$

where E_{eq} is the equivalent electric field which will produce the same effect as produced by the magnetic field.^{10,11}

In Eq. (3), the term $C.v(0)$ can be replaced by the net charge Q on the sample, and therefore,

$$\pi(0) = -\epsilon_0 + \frac{Q}{A} \cdot \frac{1}{E_{eq}}$$

or

$$\pi(0) = -\epsilon_0 + \frac{\sigma}{E_{eq}} \quad \dots(4)$$

where σ is the net surface charge density of the sample.

3. Experimental Details

Discs of 4 cm diameter, cut out from 1.5 mm thick sheet of polypropylene (procured from M/s Unipol Plastics Ltd, Ahmedabad) were cleaned with benzene and kept shorted in metallized paper (to remove frictional charges) and were stored in a desiccator. These discs were used for ME preparation and study of their dielectric behaviour. With the disc as dielectric, the capacity of parallel plate condenser was measured at 1 kHz both before and after ME preparation, using Marconi Universal Bridge (TF 2700). MEs were then prepared by the usual method as described earlier⁷ at forming temperatures (T_f) 22 (RT), 80, 100, 120, 130 and 135°C using forming magnetic fields (H_f) of strength 0.8, 3.75, 6.5, 9.75, 12.5, 15.5, 17.5 kOe. The total duration of application of magnetic field was 2½ hr, with 2 hr at a particular T_f and ½ hr during cooling of the sample to room temperature (RT). Blank samples were also prepared at each T_f , with similar heat treatment but without the application of magnetic field, and were studied similarly for their dielectric behaviour.

The surface charge on the disc ME sample was measured on both the surfaces, as described earlier.⁷ The measurement of surface charge and capacitance for each sample was continued for a period of 30 days to see if there was any variation in their values with time, because it attains an almost constant value after 20 days of routine measurement.

4. Results

4.1 Charge Characteristics

The surface charge behaviour of all the ME samples can be categorized into three distinct types. Representation of the different types of charge decay curve is given in Figs. 1 (a), (b) and (c).

In the first type of charge decay behaviour [Fig. 1 (a)], observed for T_f values of 22°C (RT), 80 and 130°C (below 9.75 kOe), one surface shows positive initial charge and the other surface negative one. Reversal of charge takes place on the surface which was initially negatively charged, giving rise to positive charge on both the surfaces. Reversal time increases with increase in T_f (3 days for samples prepared at

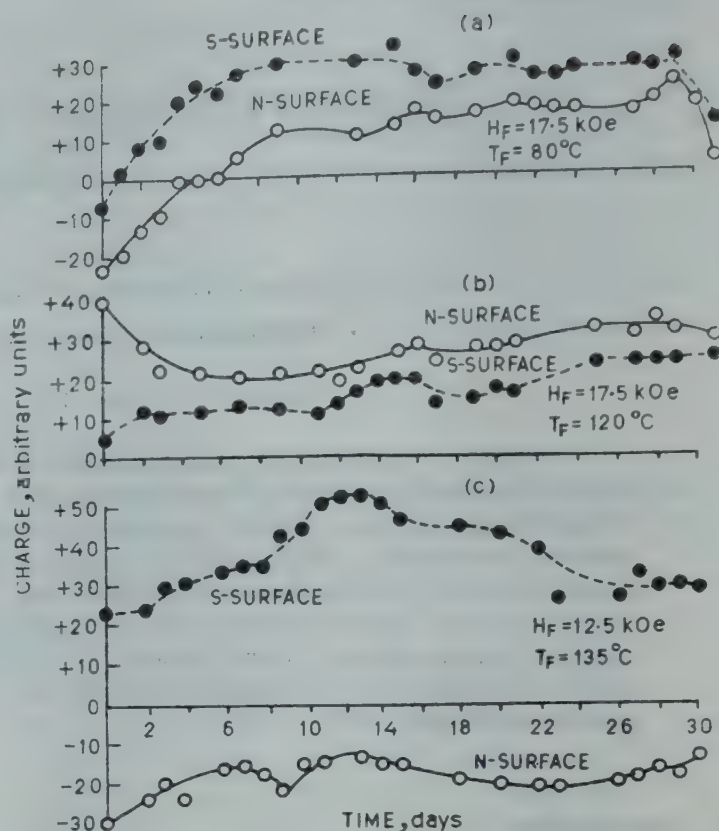


Fig. 1—Charge decay curves for polypropylene magneto-electrets prepared at different H_f and T_f

$T_f=22$ and 8-16 days for those at 80 and 130°C). The charge on the surface stabilizes in 4-8 days for samples with $T_f=22$ and 80°C while it takes 20-24 days for those having higher T_f , i.e. 130°C.

In the second type, [Fig. 1 (b)], observed for samples prepared at $T_f=100, 120$ and 130°C (above 6.5 kOe), the charges on both the surfaces of the sample are positive initially (except for samples prepared at 130°C; 15.5 kOe) and no reversal of charge is observed on any of the surfaces of the sample within 30 days. The charges stabilize in about 18 days.

In the third type [Fig. 1 (c)], observed for samples prepared at $T_f=135^\circ\text{C}$ (except for fields at 15.5 and 17.5 kOe), the charges on the two surfaces are opposite in nature and there is no reversal of charge on any of the surfaces for 30 days and the charges stabilize in about 24 days.

It can be concluded from the above charge characteristics that the final charge, i.e. the charge after its decay, on almost all the samples (except for samples prepared at 135°C, 12.5 kOe) is positive on both the surfaces.

4.2 Dielectric Behaviour

Fig. 2(a) shows the percentage change in ϵ with H_f for three forming temperatures, viz. 100, 120 and 135°C, while Fig. 2 (b) shows the corresponding variations for isocharge (charge of the same nature on both the surfaces of the sample). Fig. 2 shows an

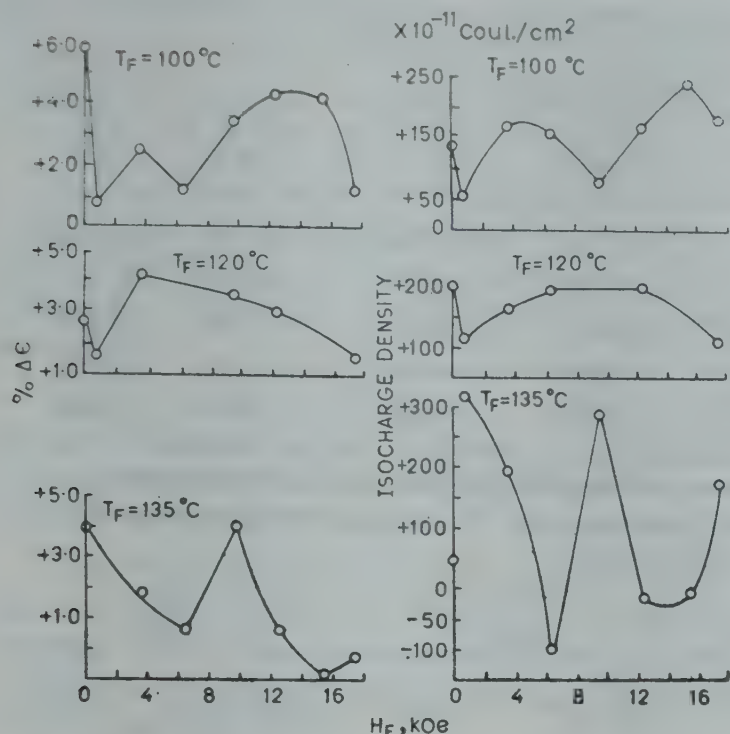


Fig. 2—(a) Percentage change in ϵ with H_f at T_f values 100, 120 and 135°C (b) Variation of isocharge density with H_f at values of T_f 100, 120 and 135°C

increase in the value of ϵ after the formation of MEs leaving cases of T_f and H_f being 135°C; 15.5 kOe and 135°C; 17.5 kOe respectively, where a decrease in ϵ value has been observed.

Fig. 3 (a) presents percentage change in ϵ with respect to various T_f at four H_f (3.75, 6.5, 9.75 and 15.5 kOe) and Fig. 3 (b) shows the corresponding variations of isocharge density. In all the cases, initial increase in $\Delta\epsilon$ has been observed which decreases, thus forming a peak. However, the position of peak is different for different fields. From Fig. 4 the variation of the maximum value of $\Delta\epsilon$ with forming temperature and forming field can be seen.

Fig. 5 represents the variation of capacitance with time for the blank sample (120°C) as well as for the sample prepared at 120°C 17.5 kOe though all the samples show a similar nature of variation after an initial increase in capacitance values which decreases and then stabilizes to a value more than its original value C_i .

Variation of percentage change in ϵ with H_f and T_f are shown in Table 1. After 30 days, a recovery is observed in the changed value of ϵ for all the samples prepared in the range of T_f from RT to 120°C, it being maximum (1.36%) for sample prepared at 100°C, 3.75 kOe. For samples prepared at temperatures 130 and 135°C with different H_f , further increase in the value of ϵ is observed, whereas for samples prepared at 130°C, 17.5 kOe and blank sample at 135°C a recovery in the value of ϵ is obtained.

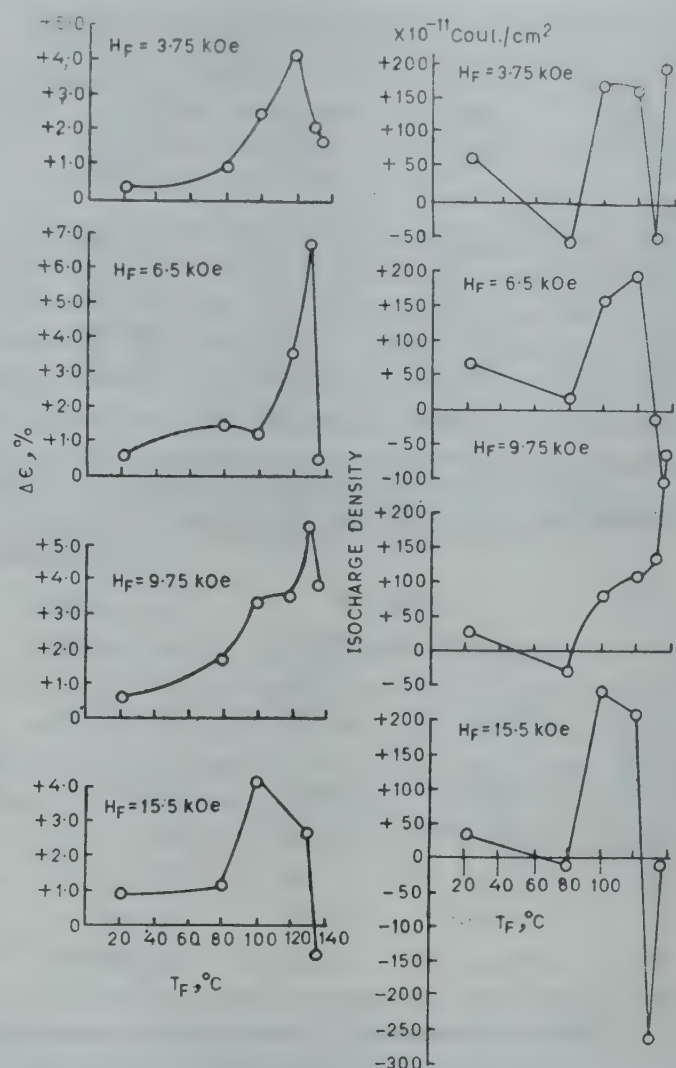


Fig. 3—(a) Percentage change in ϵ with T_f at values of H_f 3.75, 6.5, 9.75 and 15.5 kOe; (b) Variation of isocharge density with T_f at values of H_f 3.75, 6.5, 9.75 and 15.5 kOe

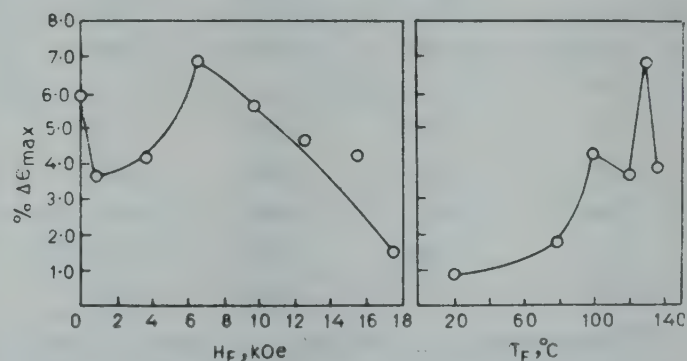


Fig. 4—Variation of maximum change in ϵ (a) with H_f and (b) with T_f

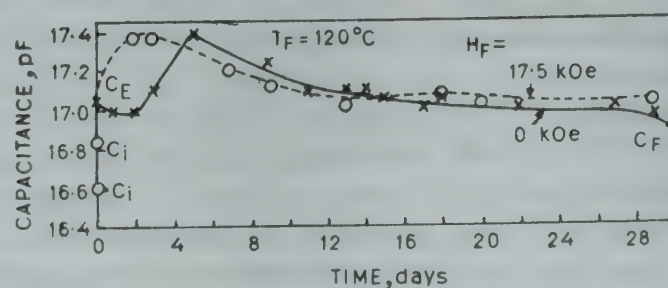


Fig. 5—Variation of capacitance with time for a blank sample (120°C) and for a sample prepared at 17.5 kOe; 120°C [C_i , C_E and C_F represent the capacity of a parallel plate capacitor with the sample disc before electret formation, just after electret formation and after 30 days, respectively.]

Table 1—Percentage Change in ϵ with H_f and T_f for Polypropylene MEs

$T_f, ^\circ\text{C}$	% Change in ϵ for H_f values (in kOe) of							
	0.0	0.8	3.75	6.5	9.75	12.5	15.5	17.5
22	—	+0.890	+0.296	+0.593	+0.595	+0.598	+0.901	0.00
(RT)								
80	+0.595	+1.470	+0.893	+1.506	+1.780	+0.890	+1.197	+1.490
100	+5.860	+0.872	+2.510	+1.183	+3.380	+4.270	+4.216	+1.176
120	+2.710	+1.490	+4.190	+3.590	+3.647	+3.067	+0.294	+1.488
130	+4.250	+3.630	+2.083	+6.833	+5.607	+4.630	+2.690	+1.490
135	+3.910	+2.380	+1.786	+0.606	+3.940	+0.560	-0.904	-0.281

 Table 2—Theoretical Values of ϵ at Different T_f and σ Values for Polypropylene MEs [H_f , forming magnetic field in kOe; E_{eq} , equivalent electric field in V/cm; T_f , forming temperature in $^\circ\text{C}$; and σ , net density (in coul/cm²) of surface charge magnitude only]

$T_f, ^\circ\text{C}$	H_f kOe: 0.8		6.5		9.75		12.5	
	E_{eq} , V/cm: 6900		4210		5260		5330	
	σ	ϵ	σ	ϵ	σ	ϵ	σ	ϵ
22	8.99×10^{-10}	1.472	3.01×10^{-10}	0.807	9.52×10^{-10}	2.045	8.02×10^{-10}	1.700
(RT)								
80	2.25×10^{-9}	3.684	1.25×10^{-10}	0.335	6.5×10^{-10}	1.396	1.95×10^{-9}	4.134
100	1.10×10^{-9}	1.801	4.01×10^{-10}	1.076	1.45×10^{-9}	3.113	2.70×10^{-9}	5.724
120	7.52×10^{-10}	1.231	1.40×10^{-9}	3.757	1.15×10^{-9}	2.470	1.35×10^{-9}	2.862
130	1.05×10^{-9}	1.719	7.02×10^{-10}	1.884	1.2×10^{-9}	2.578	6.52×10^{-10}	1.382
135	6.85×10^{-10}	1.122	5.01×10^{-11}	0.134	2.15×10^{-9}	4.618	1.20×10^{-9}	2.544

 Table 3—Experimental Values of ϵ at Different H_f and T_f [C_E is the Capacitance Value after magneto-electret formation and C_0 is air capacitance $C_0=9.1$ pF unless otherwise stated. Values of C_0 and C_E are in pF]

$T_f, ^\circ\text{C}$	H_f , in kOe: 0.8		6.5		9.5		12.5	
	E_{eq} , in V/cm: 6900		4210		5260		5330	
	C_E	ϵ	C_E	ϵ	C_E	ϵ	C_E	ϵ
22	17.0	1.868	16.95	1.862	16.9	1.857	16.8	1.846
(RT)								
80	17.25	1.895	16.85	1.851	17.15	1.884	17.0	1.868
100	17.35	1.906	17.1	1.879	16.8	1.846	17.1	1.879
120	17.0	1.868	17.3	1.901	17.05	1.873	16.8	1.846
130	17.10	1.879	17.2	1.890	16.95	1.862	16.95	1.862
135	17.2	1.890	16.6	1.824	17.15	1.884	17.95*	1.869*

*Those values of C_E and ϵ refer to a value of $C_0=9.6$ pF.

The theoretical values of ϵ as calculated from Eq. (1) are shown in Table 2. These values are calculated using the approximate values of equivalent electric fields¹¹ for H_f as evaluated by Qureshi and Bhatnagar.¹⁰ The theoretical value of ϵ comes out to be 2.231 ± 0.682 which agrees well with the average experimental value given in Table 3. However, a calculation for the evaluation of theoretical value of ϵ using Eqs. (1) and (4) is detailed below for a sample prepared at 130°C , 6.5 kOe:

$$\sigma = 7.02 \times 10^{-10} \text{ coul/cm}^2$$

$$E_{eq} = 4210 \text{ V/cm}$$

$$\epsilon_0 = 8.85 \times 10^{-14} \text{ F/cm}$$

Substituting these values in Eq. (4) one obtains

$$\pi(0) = 7.8245 \times 10^{-14}$$

and hence from Eq. (1)

$$\epsilon = 1 + \frac{7.8245 \times 10^{-14}}{8.85 \times 10^{-14}} = 1.884$$

5. Discussion

5.1 Explanation for Charge Decay Curves

Charge decay curves can be explained on the basis of the two-charge theory propounded by Khare and Bhatnagar.¹² According to this theory, the charge on the ME is mainly due to two types of charges called 'iso' and 'idio'. Isocharge is a charge of same

sign on both surfaces (+ve or -ve depending upon the material) which is more at lower temperatures while idio charge is more at higher temperature and is +ve on one surface and -ve on the other.

At lower temperature ($\sim 80^\circ\text{C}$), the total surface charge is due to the isocharge and shortlived idio charge. The idio charge decays giving rise to reversal of charge in 10-16 days leaving +ve charge on both the surfaces.

At 100, 120 and 130°C (above 6.5 kOe), the idio charge component is less and there is a dominance of isocharge which slowly decays with time; hence there is no reversal of charge.

At 135°C (except for 15.5 kOe) there is no reversal of charge though the surfaces have opposite charges. This is because of the contribution of long-decaying idio charge at higher temperature, according to the two-charge theory.

The existence of idio charge at lower temperature may be due to trapping of ionic charge in the defects of the crystallites¹³ giving rise to space charge separation resulting in idio charge.¹⁴

The decrease of idio charge for $T_f = 100, 120, 130^\circ\text{C}$ may be due to lesser trapping of charge as a result of increased mobility of ions at higher temperatures. The increase in isocharge may be due to transfer of charges between the metal and the polymer surface, because of the thermal energy as explained in an earlier communication.⁷

The increase in the duration in decay of idio charge at 135°C may be due to the loosely bound charges provided by the small scale heterogeneities and impurities in the structure of plastics.¹⁵ These ionic, low-molecular weight impurities dissociate at higher temperature and provide charge carriers. The presence of magnetic field is responsible to create impurity band, which acts as a trap site for the liberated charges.¹⁶ Thus during cooling, in the presence of magnetic field, the charges get trapped and frozen, giving rise to persistent polarization resulting in idio charge.

5.2 Explanation for Dielectric Behaviour

The increase in capacitance and hence in ϵ is due to the iso +ve charge which is significant in the temperature range $100-120^\circ\text{C}$ (for some cases at 130°C also). The decrease in ϵ at 135°C (at H_f 15.5 and 17.5 kOe) is due to the predominant idiocharge and -ve iso charge.⁵ This is according to the earlier findings,⁷ i.e. the idio charge decays with time, the value of ϵ increases and subsequently stabilizes after a little fall.

The variations of percentage change in ϵ value with H_f and temperature are found to be in accordance with the variations of iso charge^{14,17} (Figs. 2 and 3). However, the small discrepancies may be due to the presence of idio charges.

It can be seen from Tables 2 and 3 that the theoretical and experimental values of ϵ agree well and also to the value (2.1-2.3) reported in literature.¹⁸ Therefore, the ideas of (i) volume polarization in the dielectric (ii) the phenomenological theory of Wiseman and Feaster,¹⁹ based on the two-charge theory of Gross,²⁰ as assumed by Perlmann and Meunier in the derivations of Eqs. (1) and (4) can well be applied in the case of MEs also.

6. Conclusion

It is concluded from the above study that in general there is an increase in the dielectric constant of polypropylene after its magneto-electret formation and is due to increase in +ve iso charge on the samples. However, a decrease of idio charge also contributes to the increase in the value of dielectric constant.

Acknowledgement

The authors are grateful to Principal Dr B L Mehrotra for providing the necessary facilities. Further, they are thankful to Shri M S Qureshi for stimulating discussions. One of the authors (S A H) is thankful to the University Grants Commission, New Delhi, for awarding a teacher fellowship and also to the Government of Madhya Pradesh for permitting him to avail of the fellowship.

References

1. Deshpande G K & Khare M L, *Indian J. pure appl. Phys.*, 15 (1977), 692.
2. Quamara J K, Khare M L & Bhatnagar C S, *Indian J. pure appl. Phys.*, 18 (1980), 24.
3. Qureshi M S & Bhatnagar C S, *Indian J. pure appl. Phys.*, 10 (1972), 220.
4. Qureshi M S & Bhatnagar C S, *Indian J. pure appl. Phys.*, 13 (1975), 797.
5. Quamara J K, Khare M L & Bhatnagar C S, *Indian J. pure appl. Phys.*, 15 (1977), 617.
6. Quamara J K, *Studies on optical properties of magneto-electrets of transparent plastics*, Ph D thesis, Bhopal University, Bhopal, 1977.
7. Husain S A & Bhatnagar C S, *Indian J. pure appl. Phys.*, 18 (1980), 167.
8. Bhatnagar C S, *Indian J. pure appl. Phys.*, 2 (1964), 331.
9. Perlman M M & Meunier J L, *J. appl. Phys.*, 36 (1965), 420.
10. Qureshi M S & Bhatnagar C S, *Indian J. pure appl. Phys.*, 17 (1979), 575.

11. Srivastava R K, *Studies on isothermal charge decay TSDC & comparative study of electric and magnetic field in tubular magnetoelectrets of silicone rubber (silastic) and perspex*, Ph D thesis, Bhopal University, Bhopal, 1979, (Submitted).
12. Khare M L & Bhatnagar C S, *Indian J. pure appl. Phys.*, **7** (1969), 160.
13. Takamatsu T & Fukada Eiichi, *Rep. Prog. Polymer Phys., Japan*, **XV** (1972), 393.
14. Bhatnagar C S, Khare M L & Qureshi M S, *A Review on Magnetoelectret*, Extended Abstracts Workshop on Electric Charges in Dielectrics, Oct. 1978, Japan, 172.
15. Ritche P D, *Physics of Plastics*, (D Van Nostrand Princeton, New Jersey), 1965.
16. Hasegawa H & Nakamura M, *J. phys. Soc. Japan*, **26** (1969), 1362.
17. Qureshi M S, Bhatnagar C S, *Indian J. pure appl. Phys.*, **10** (1972), 220.
18. Clark F M, *Insulating material for design and engineering practice* (John Wiley, New York), 1962, 654.
19. Wiseman G & Feaster G, *J. chem. Phys.*, **26** (1957), 521.
20. Gross B, *Phys. Rev.*, **66** (1944), 26.

Electron-Plasma Model for the Electromagnetic Effect at Metallic Fracture

A MISRA & SIBDAS GHOSH

Department of Mechanical Engineering, Birla Institute of Technology, Mesra, Ranchi 835 215

Received 3 March 1980

A new physical model for the fracture-induced electromagnetic effect in metals is presented. The model attributes the observed effect to the emission of photons from the interaction of the solid-state plasma of conduction electrons and phonons of maximum frequency in the metal undergoing fracture, and predicts a parabolic variation of the fracture-induced peak potential with the angular Debye frequency of the metal.

1. Introduction

Discovery of stress-induced transient magnetic (TM) and electromagnetic (TEM) effects in metals and alloys, and first physical models for explaining them, have earlier been reported.¹⁻⁶ The fact that the fracture stress-induced TM effect¹⁻³ is a breakthrough can well be realized by the conclusion⁷ that both theoretical and experimental research works of the past, have prohibited the possibility of creation of a magnetic field by stress alone. It would not be out of place to mention here that first, this TM effect^{1,2} was challenged by Nuti *et al.*⁸ arguing that the general equation of reluctance variation $\dot{R} \sim [(\mu) \text{ metal} - (\mu) \text{ air}] v$, does not require the existence of gross TM field of 10^3 gauss as claimed by Misra.^{1,2} All the more, they attributed the small signal, observed by them during their experiments with the help of a Hall probe⁸ at the instant of tensile fracture, simply to the movement of fractured pieces in the earth's magnetic field. On the other hand, a theoretical model was put forward by Misra⁴ justifying the validity of the existence of a high TM field of the order of 10^3 gauss [Refs. 1, 2] on the ground that as the effect is apparently a breakthrough, it cannot be tackled by conventional theoretical approaches.³ Finally, the same research group of Erber and coworkers, after thorough experiments, confirmed the existence of the high TM field as claimed by Misra^{1,2} attributing it to a possible physical phenomenon connected with the rupture process and crack propagation.⁹

It was further pointed out in an earlier paper² that these two effects—TM and TEM are complementary aspects of one fundamental phenomenon and that the stress-induced TEM effect appears to be a universal one³ in the sense that this should be

expected in non-metals as well. This latter proposition³ has recently got a strong support from the work of Vorob'ev¹⁰ who has observed that electromagnetic radiation occurs when cracks are formed in dielectrics. Based on this expected universal characteristics, an interesting bio-physical application of electromagnetic effect to head injury was presented by Misra.^{3,11}

We now convincingly feel that these TM and TEM, characteristics of almost all materials during stressing up to fracture under tension, can be pictured in one single fundamental range with two extreme limits: at one end, the material which shows predominance of TM effect and the other which shows the predominance of transient electrical effects. And, this generalized characteristic can definitely be explained by one single unified theory but that is possible only when sufficient experimental data and various theoretical approaches are obtained and analyzed carefully. With this aim in view, the present paper describes a new theoretical approach to explain the observed electromagnetic effect at metallic fracture,² attributing it to the emission of photons from the interaction of the solid-state plasma of conduction electrons and phonons of maximum frequency in the metal undergoing fracture. Quantitative results are obtained by assuming the independent particle model of solid-state plasma and then applying the known laws of classical electrodynamics. This approach is one step ahead of the previous one^{3,5} and predicts a new aspect of the fundamental phenomenon, namely, the parabolic variation of the induced peak voltage with the angular Debye frequency of the metal. Our recent experimental results show the practicability of this new approach.

2. The New Model

The characteristic frequency ω_p of plasma oscillations involving conduction electrons in a metal is given by,¹²

$$\omega_p = \left(\frac{ne^2}{\epsilon_0 \epsilon_l m} \right)^{1/2} \quad \dots(1)$$

where e and m are electronic charge and mass respectively; n is the conduction electron density in the metal and ϵ_l , its dielectric constant. Due to the high value of conduction electron density in a metal, the plasma frequency ω_p is normally very high. The energy necessary for exciting plasma oscillations in a metal is, therefore, much higher than the energy of the lattice vibrations or phonons in metals. This forbids the emission of radiation by plasma oscillations in a metal under normal conditions. However, the conditions are drastically altered in a metal at the transition stages of elastic-plastic deformations (EPD) under tension, like yield, Luders' strain, crack-propagation and fracture, such that radiation by plasma oscillations seems permissible.

The effect of crystal imperfections on the electrons has not yet been correctly established but it is certain that the effect is localized on the imperfection planes, and all the electrons are not affected.¹³ It is further supported from Landauer's work¹⁴ that the space charge which produces the potential, is composed of electrons which move in a potential of the same form. On the expanded side of the dislocation this potential is attractive, and some of the electrons are localized on bound states near the dislocation line. And, in an inhomogeneously strained metal, the highest occupied states in different regions have different energies. Further, the main part of the energy of a dislocation in a crystal is spread through the medium and stored as the potential energy of elastic strain.¹³ Moreover, on either side of the dislocation the crystal lattice is essentially perfect, but in the immediate vicinity of the dislocation the lattice is severely distorted.¹⁵ A non-uniform distribution of the more energetic electrons may affect the normal conduction electron density in regions centred on straight lines drawn between contiguous ions. The electron density is higher or lower depending upon the prevailing circumstances.¹⁶

Based on the above considerations we visualize the physical picture of the stress-induced TEM effect in metals as follows: During the non-uniform distribution of dislocations which occur at the transition stages of elastic-plastic deformation, mobile dislocations arrange themselves into some configuration that is mechanically stable, i.e. it cannot be changed into another one of lower energy without passing

through the intermediate configuration of higher energy.¹⁷ As a non-conservative dislocation (NCD) moves through a crystal, it moves between alternate positions of high and of low energy due to the presence of positive ions arranged at lattice points. It may happen that an NCD which rests for a time in a potential trough, can reduce its energy by a process which rarely or never happens to a moving dislocation.

When a metal is highly deformed, its dislocation density usually rises. Since the effect of crystal imperfections on the electrons, as pointed out above is localized, it appears that only the quasi-free electrons (QFE) in the immediate vicinity of the dislocation will be excited to a higher energy state due to the dissipation of dislocation energy while other electrons will normally be not excited. Therefore, the behaviour of these excited QFE will definitely be different from that of the rest of the conduction electrons in the metal.

No information is available in literature on the number of the QFE surrounding the dislocation. Hence let us analyze the behaviour of the QFE; these are itinerant and move from region of one atom to another, but not with regard to the potential fields of the atomic nuclei.¹⁵ When an NCD moves, the equilibrium potential surrounding this dislocation changes. In order to compensate this variation of potential therefore, the number of QFE in the immediate vicinity of the dislocation (since the effect is localized) must be of the order of the affected atoms, may be slightly higher or lower. Hence, to a first approximation, let us assume that the order remains the same.

Therefore, during each transition stage of EPD when a non-conservative dislocation is self-trapped in a potential trough, the QFEs associated with this dislocation, may be regarded as trapped or brought to rest relative to the positive ions; in other words, these QFEs may be regarded as decelerated relative to the remaining conduction electrons. Hence, during the transition stages of EPD the equilibrium distribution of the electrons may be perturbed, and non-equilibrium states arise. It is the distribution of the electrons (from energy point of view) in the metals that changes and not the number of electrons. Obviously, the behaviour of this excited trapped QFE cloud associated with the NCD will be different from that of the remaining conduction electron cloud.

It is, therefore, possible that this excited trapped QFE cloud, at the transition stages of EPD may attain an electron density suitable enough to permit plasma oscillations within the system. Moreover,

plasma oscillations are known to occur in the frequency range of 10^{14} Hz or lower, requiring according to Eq. (1), an electron density of 10^{24} electrons/m³, as in the case of a semiconductor. This frequency range is in the neighbourhood of the angular Debye frequency ω_D of the metals. An isolation of 10^{24} electrons/m³ (from energy point of view) associated with the NCD makes an insignificant change in the normal conduction electron density of 10^{29} /m³ within the rest of the metal. Further, the dislocation density for well-annealed crystals is usually of the order of 10^8 to 10^{10} /m² and rises to about 10^{14} to 10^{16} /m² for highly deformed crystals.¹⁸ A simple calculation will show¹⁵ for the simple case of a cubic crystal structure (1 atom per unit cell) having a dislocation density of 10^{14} /m³ along $\langle 100 \rangle$ directions, that approximately 10^{24} atoms/m³ will be associated with the dislocation lines. Therefore, as discussed above, when an NCD moves, due to the localized energy perturbation effects, the surrounding 10^{24} QFE/m³ are excited and form a plasma which has a characteristic entirely different from the rest of the conduction electron plasma. Moreover, it is the individual NCD surrounding, which produces an associated electron plasma, and gives plasma oscillations. This isolation of the space-charge is a condition which is characteristic of the NCD at the transition stages of EPD and does not occur in other cases of external influences, like melting, where the metal plasma frequency remains unaffected and hence does not permit any plasma oscillations. And also, it can be shown very easily as indicated below that the dislocation energy in a highly deformed metal is high enough to excite 10^{24} conduction electrons/m³ to a frequency of 10^{14} rad/sec. Therefore, from energy considerations also, radiation from the isolated electron cloud configuration is permissible.

It may, therefore, be assumed that the transition stages of EPD including fracture, synchronize with the transverse oscillations of the QFE plasma associated with the NCD in the metal. This maximum phonon frequency ω_m must be in the neighbourhood of the angular Debye frequency of the metal so that for resonance of plasma and phonons one may take

$$\omega_p = \omega_m = \omega_D \quad \dots (2)$$

It is also endorsed from the fact that the energy per unit length of dislocation is approximately Gb^2 ,² where G is the shear modulus and b , the Burger's vector in the deformed metal; if the dislocation density ρ is of the order of 10^{14} m⁻² the total dislocation energy per cubic metre $Gb^2 \rho$ will excite 10^{24} conduction electrons/m³ such that the quanta of plasma

oscillations will have a frequency ω_p of the order of 10^{14} rad/sec ($Gb^2 \rho / n = \hbar \omega_p$) for the normal value of b as 1 \AA . This frequency is in the range of angular Debye frequency for most metals.

Now, during the transition stages of EPD when the electron plasma associated with the NCD is set into resonance oscillations by maximum frequency phonons, an electromagnetic pulse is generated. The generation of electromagnetic radiation by transverse plasma oscillations at the characteristic frequency ω_p can be treated by classical methods according to the independent particle model of solid-state plasma, treating it as a collection of non-interacting vibrating particles with random phases.

According to the classical electrodynamics, an accelerated charge e emits electromagnetic radiation, the electric and magnetic field vectors of the radiation for non-relativistic charge velocities are given by,¹⁹

$$\mathbf{E} = \frac{e}{4\pi \epsilon_0 C^2 r^3} [\mathbf{r} \times (\mathbf{r} \times \dot{\mathbf{u}})]$$

$$\mathbf{H} = \frac{e}{4\pi Cr^2} [\dot{\mathbf{u}} \times \mathbf{r}] \quad \dots (3)$$

where \mathbf{r} is the retarded radius vector, \mathbf{u} the acceleration of the charge and C , the velocity of light in vacuum, the vectors \mathbf{r} , \mathbf{E} and \mathbf{H} being mutually orthogonal to each other.

During resonance oscillations of electron-plasma in a metal at the transition stages of EPD the electromagnetic pulse will be emitted by the vibrating electrons in a direction perpendicular to its tensile axis, as shown in the inset of Fig. 1.

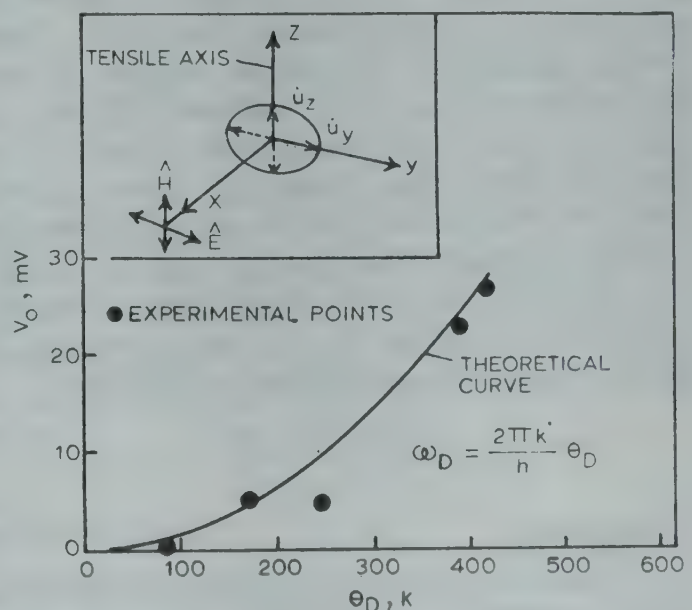


Fig. 1—Variation of fracture-induced peak potentials (V_0) with angular Debye frequency (ω_D) of the metal. Inset shows the vector-configuration for the electromagnetic radiation

For an electron vibrating with frequency p , the acceleration is given by

$$\ddot{u} = -\omega_p^2 y \quad \dots(4)$$

where $y = y_0 \exp [i(\omega_p t + \alpha)]$, y_0 being the amplitude and α an arbitrary phase constant, damping being neglected.

If N be the effective number of vibrating electrons, then the amplitude of the resultant electric field at some point x_0 is \sqrt{N} times that due to a single electron, under random phase approximation, and hence it may be given by

$$E = \left(\frac{1}{4\pi\epsilon_0} \right) \left(\frac{y_0 e}{x_0 c^2} \right) 2 \sqrt{N} \omega_p^2 \quad \dots(5)$$

where the factor 2 is introduced to take into account the two transverse modes of vibration of the electrons.

If x_0 is sufficiently large, the electromagnetic waves may be treated as plane for distances $x \gg x_0$, and the electric field of the radiation be represented by

$$E = E_0 \exp \left[i \left(\omega_p t - \frac{2\pi x}{\lambda_p} \right) \right] \quad \dots(6)$$

where λ_p is the wavelength of the radiation of angular frequency ω_p in free space.

The potential difference caused by the electromagnetic radiation may be calculated by the relation, $V = -\int E dx$. The peak value of the potential difference V_0 is given by

$$V_0 = \epsilon_0 \frac{\lambda_p}{2\pi} \quad \dots(7)$$

The effective dipoles are obviously those which lie near the metallic surface so that the radiation emerges from the surface without absorption. Hence N in Eq. (5), may be taken as the number of conduction electrons associated with the NCD within a sphere of radius δ , near the surface, where δ is the skin depth of the metal under the above imposed conditions. Further, in order to satisfy the condition for plane wave approximation, x_0 in Eq. (5) is taken to be 100δ [Ref. 20]. Substituting these parameters in equations preceding Eq. (7), the expression for V_0 , just outside the metallic surface is given by

$$V_0 = \frac{1}{4\pi\epsilon_0} \left(\frac{\epsilon_L m \delta}{7500} \right)^{1/2} \left(\frac{y_0}{c} \right) \omega_D^2 \quad \dots(8)$$

3. Discussion

(i) In many cases the experimental results show that there is a critical stress τ_0 at which dislocations can escape freely from a potential trough and the velocity of dislocations $V(\tau)$ under stress $\tau > \tau_0$ increases as τ increases. The critical stress τ_0 is roughly equal

to the critical resolved shear stress τ_c , below which no dislocation motion occurs.¹⁴ For most metals τ_c is close to the yield stress.²¹ The physical model proposed here, attributes the stress-induced TEM effect to mobile dislocation mechanism; hence below the yield stress, according to this model, no electromagnetic radiation should be emitted. Further, since the conditions imposed for the generation of electromagnetic radiation in the present model are applicable at the transition stages only, electromagnetic radiation should be generated only at these stages. These facts are clearly borne out by the experimental observations.⁵

(ii) In Eq. (8) y_0 is the amplitude of the stress-induced electron oscillations, according to Eq. (4). Obviously, this will depend upon the magnitude of stress and be maximum at the instant of fracture. This fact is in conformity with the experimental results.⁵

The energy (W), radiated by each vibrating electron of frequency ω_p during a complete vibration is given by²²

$$W = \left(\frac{1}{4\pi\epsilon_0} - \frac{16\pi^4 e^2}{3 C^2} \right) \left(\frac{\omega_p}{2\pi} \right) y_0^2 \quad \dots(9)$$

and for the present case $\omega_p = \omega_D$.

The energy of an accelerated electron is generally of the order of electron volts. Hence if Eq. (9) is equated to the order of electron volts ($\hbar \omega_D$ also comes to the order of 10^{-19} J), a value of y_0 of the order of 10^{-6} m is obtained. Therefore, the maximum amplitude of electron oscillation at the instant of fracture may be taken as 10^{-6} m; values of y_0 at the transition stages other than fracture, will obviously be smaller.

(iii) As discussed earlier, the electron-plasma configuration around the NCD at the transition stages of EPD attains an effective conduction electron density of the order of $10^{24}/\text{m}^3$ which is in the range of that for a semiconductor. Moreover, plastic deformations are known to decrease the electrical conductivity of the metal,¹⁴ hence one may take for quantitative assessment $\delta \sim 10^{-6}$ m and $\epsilon_L \sim 10$ as in the case of semiconductors.²³ Substituting the known values of the Debye temperature²⁴ and other parameters in Eq. (8), a parabolic variation of V_0 with ω_D is obtained (Fig. 1).

(iv) Since the mechanical behaviour of Pb is very similar to that of organic viscoelastic materials such as polymers and resins, Eq. (8) may require some modifications in case of these types of materials.

(v) The peak value of the magnetic field intensity H_0 as calculated from this model with the help of Eq. (3) comes to be 0.16 Oe which is too small to be

observed experimentally in nonmagnetic metals and this is in conformity with the experimental results.²

(vi) One aspect of the phenomenon which still requires some explanation is that of radiation frequency.

As mentioned earlier, the physical model proposed above, attributes the stress-induced TEM effect to the emission of photons due to electron-phonon-resonance interactions in the independent particle model of solid-state plasma in a metal. The model imagines that the electron-plasma of density 10^{24} electrons/m³ associated with the NCD, within a sphere of radius δ near the metallic surface, generates the plasma oscillations at the angular Debye frequency ω_D , the quantum of the plasma oscillations being $\hbar \omega_D$. But this sphere also contains the rest of the conduction electrons of density $(10^{29}-10^{24})$, i.e. approximately 10^{29} electrons/m³. It is possible that some of the plasmons generated by these 10^{24} electrons/m³ at the transition stages of EPD, are absorbed by the rest of the conduction electrons of density 10^{29} electrons/m³ within the sphere. Under such a critical interaction, this excitation of the conduction electrons results in a spontaneous emission of photons, because only the ground state of the conduction electrons will be stable in the absence of any external radiation field. Hence this becomes the mechanism of spontaneous transition between two quantum states of rest of the conduction electrons and they, in other words, act as an energy carrier.

An exact quantitative assessment of the photon frequency, at this stage, would be complicated since the absorption and emission processes in electron plasma are not so simple. However, a quantitative assessment of the upper limit of the emission frequency may be obtained as follows. Under the most ideal upper limit let us assume that all the quanta of plasmons generated by 10^{24} electrons/m³ are absorbed by the rest $(10^{29}-10^{24})$ conduction electrons/m³ under the spontaneous transition between two quantum states. Then the maximum frequency of the photons thus emitted would be lower than ω_D by the ratio of 10^{24} to $(10^{29}-10^{24})$, i.e. approximately 10^{-5} . Since ω_D for most metals is of the order of 10^{14} rad/sec the emitted photon frequency in the stress-induced, electromagnetic effect at the transition stages of elastic-plastic deformation cannot exceed 10^9 rad/sec. This is, indeed, in conformity with the experimental results;⁵ most ductile metals have been found to emit radiation at a frequency 10^7 Hz at the instant of fracture and in rare cases of brittle metals, the frequency was observed to be of the order of 10^9 Hz but never more than that in any case.

4. Experiment

Experiments were conducted, exactly as described in an earlier paper,² on 0.18% carbon steel, aluminium (4.5% Si, 0.5% Fe, 95% Al), zinc (99.67% pure) cadmium (99.63% pure) and lead (99.43% pure) with specimen dimensions 9 mm diameter and 160 mm long, machine-turned gradually to a diameter of 6 mm in the central zone to ensure fracture in the centre. All specimens were prepared from the same hot-rolled stock. A Hewlett Packard storage oscilloscope was employed for induced voltage measurements. The experimental values of V_0 , thus obtained, have been plotted with encircled points in Fig. 1 which show a close agreement with theoretically predicted values for steel, aluminium and cadmium specimens, a 50% scattering for zinc specimens while that for lead specimens, the scattering is enormous. The close agreement in case of steel, aluminium and cadmium specimens should not be given a high significance as the theoretical assessment of V_0 involves some approximations; but one fact is certain that Eq. (8) predicts a parabolic variation of V_0 with ω_D irrespective of the values of other parameters and our experimental results show the validity of this approach. The exact quantitative assessment for V_0 for various metals with the help of Eq. (8) would be possible only when other parameters such as ϵ_l , γ_0 , etc. are accurately determined.

5. Conclusion

Apparently, the postulation of the existence of a trapped electron cloud with an electron density 10^{-6} (that of the bulk) associated with each dislocation, seems to be a hypothesis but it deserves a careful attention from both future experimental and theoretical aspects due to the strange characteristics of the observed effects. The next step would be to study these new effects, in analogy with the present model, in terms of electron-magnon-resonance interactions, since experimentally, a high value of H_0 has been observed in steel specimens.^{1,3,9} Probably a superimposed electron-phonon and electron-magnon-resonance interactions model would give a new direction in developing the single unified theory for these effects.

Acknowledgement

Research correspondence with Prof. T Erber, Illinois Institute of Technology, Chicago, USA is gratefully acknowledged. This research project has been sponsored by the science and Engineering Research Council, Government of India.

References

1. Misra A, *Indian J. pure appl. Phys.*, **11** (1973), 419-421.
2. Misra A, *Nature, Lond.*, **254** (1975), 133-134.
3. Misra A, *Discovery of stress-induced magnetic and electromagnetic effects in metals*, D Sc dissertation, Ranchi University, Ranchi, 1976.
4. Misra A, *Physics Lett.*, **62A** (1977), 234-236.
5. Misra A, *Appl. Phys.*, **16** (1978), 195-199.
6. Misra A & Jha S K, *The new stress-induced magnetic and electromagnetic effects in metals*, Paper presented to the 66th Indian Science Congress, 1979.
7. Cullity B D, *Introduction to magnetic materials* (Addison Wesley, New York), 1972, 268.
8. Nuti J, Erber T & Guralnick S A, *Physics Lett.*, **57A** (1976), 357-358.
9. Nuti J, *Magnetic effects associated with the rupture of steel bars under tensile stress*, M S thesis, Illinois Institute of Technology, Chicago, USA, 1977.
10. Vorob'ev A A, *Defektoskopiya*, **13** (1977), 128-129.
11. Misra A, *Stress-induced electromagnetic effect—a new biophysical approach to head injury*, under Publication.
12. Cracknell A P & Wong K C, *The Fermi surface* (Clarendon Press, Oxford), 1973, 411.
13. Ziman J M, *Electrons and phonons*, (Clarendon Press, Oxford), 1972, 235-245, 229.
14. Nobarro F R N, *Theory of crystal dislocation*, (Clarendon Press, Oxford), 1967, 381, 632-633 & 619.
15. Barrett C R, Nix W D & Tetelman A S, *The principles of engineering materials* (Prentice-Hall, New Jersey), 1973, 79-83.
16. Hurd C M, *Electrons in metals* (John Wiley, New York), 1975, 13-15.
17. Cottrell A H, *Dislocations and plastic flow in crystals* (Clarendon Press, Oxford), 1953, 100.
18. Mc Clintock F A & Argon A S, *Mechanical behaviour of materials* (Addison Wesley, New York), 1966, 106.
19. Shohet J C, *The plasma state* (Academic Press, New York), 1971, 293.
20. Jenkins F A & White H E, *Fundamentals of optics* (McGraw-Hill, New York), 1950, 188.
21. Kubo R & Nagamiya T, *Solid state physics* (McGraw-Hill, New York), 1968, 788.
22. Rajam J B, *Atomic physics* (C S Chand, New Delhi), 1966, 428.
23. Platzman P M & Wolff P A, *Waves and interactions in solid state plasmas* (Academic Press, New York), 1973, 4, 133.
24. Seitz F, *The modern theory of solids* (McGraw-Hill, New York), 1940, 110.

Molecular Dynamics of Some Octahedral Hexahalide Anions

S MOHAN*

Department of Physics, Presidency College, Madras 600 005

&

K G RAVI KUMAR

Madras Christian College, Tambaram 600 059

Received 30 November 1979

The general quadratic valence force field has been applied to some octahedral hexahalide anions using molecular kinetic constants and Wilson's *FG* matrix method. The compliance constants, vibrational mean amplitudes, shrinkage constants, Coriolis coupling constants and rotational distortion constants are reported here for these ions for the first time. The ionic character of the bonds are briefly discussed. It is also shown that kinetic constants method leads to acceptable sets of characteristic constants for these ions.

1. Introduction

The attention of chemists and molecular spectroscopists has been drawn to the concept of kinetic constants recently.¹⁻⁵ Molecular kinetic constants are the vibrational inertial coefficients involved in Wilson's expression⁶ for the kinetic energy relating to molecular vibrations, given by, $2T = \dot{\mathbf{S}}\mathbf{G}^{-1}\dot{\mathbf{S}}$ when $\mathbf{G}^{-1} \equiv \mathbf{K}$. The kinetic constants of molecules and ions appear to be of significance in the study of molecular dynamics. They have been evaluated and utilized advantageously in different cases¹⁻⁵ to obtain acceptable sets of molecular constants in polyatomic molecules in a simple manner.

With the advent of laser Raman spectroscopy and the advancement in infrared techniques, a considerable amount of experimental data on the vibrational spectra of molecules and ions are appearing in literature. The current data can be considered now to be more reliable than the previous data. If these data are analysed properly with the help of group theoretical considerations, valuable informations can be obtained regarding the nature and structure of molecules and ions.

Very recently Reisfeld⁷ has investigated the infrared and Raman spectra of the solid compounds of the type A_3MF_6 , where M represents the group III A trivalent metal ions (Al, Ga, In and Tl). The spectra have been interpreted on the basis of octahedral symmetry. The vibrational spectrum of $PtCl_6^{2-}$ anion has been studied by Good⁸ in different environments and interpreted assuming O_h point group.

The purpose of the present paper is (a) to obtain all the seven independent potential constants for all the ions under study using the general quadratic valence force field and molecular kinetic constants, (b) to evaluate the other molecular constants, viz. Compliance constants, vibrational mean amplitudes and shrinkage constants at 298.16 K, Coriolis coupling constants and rotational distortion constants for these ions and (c) to discuss the relative strengths of the various chemical bonds and influence of the oxidation state and cation on the molecular constants. At present, these data are incomplete or unavailable.

2. Theoretical Considerations

The octahedral molecules or ions of the type XY_6 belonging to the O_h point group are characterized by six fundamental frequencies distributed among various species as

$$1A_{1g} + 1E_g + 2F_{1u} + 1F_{2g} + 1F_{2u}$$

The frequencies $\nu_1(A_{1g})$, $\nu_2(E_g)$, and $\nu_3(F_{2g})$ are Raman active, and $\nu_4(F_{1u})$ and $\nu_5(F_{1u})$ are infrared active and $\nu_6(F_{2u})$ is inactive in both.

The symmetry coordinates and *F* and *K* matrices used in the present investigation are taken from our earlier paper.⁵

The method of kinetic constants for solving the secular equation has been found to give quite agreeable results in different molecular types as mentioned earlier.¹⁻⁵ The determination of symmetry force constants involved in the secular equation from the n_i vibrational frequencies alone has remained a mathematically unsolved problem so far. Therefore, any genuine attempt to evaluate all the symmetry

* Present address: Faculty of Science, Peraringar Anna University of Technology, MIT Campus, Madras 600 044

force constants associated with a problem of order $n > 1$ should involve the incorporation of at least $n_i (n_i - 1)/2$ additional data other than the n_i frequencies.

The method of kinetic constants seeks to relate the off-diagonal elements to the diagonal elements of the F matrix through the relation

$$F_{ij}/F_{jj} = K_{ij} K_{jj} \quad (i < j; i, j = 1, 2)$$

The compliance constants are also calculated by Decius⁹ method.

Utilizing Cyvin's equation¹⁰ $\Sigma = L\Delta L'$, the symmetrized mean square amplitudes and hence the valence mean square amplitude quantities for both the bonded and the non-bonded distances are evaluated at 298.16 K using the present set of force constants. On the basis of these values, the mean amplitudes of vibration and shrinkage constants for these ions are calculated.

The Coriolis vibration-rotation constants ζ^α ($\alpha = x, y, z$) in this type of ions arise from the couplings $F_g \times F_{2g}$, $F_{2g} \times F_{2g}$, $F_{2u} \times F_{2u}$, $F_{1u} \times F_{2u}$, and $F_{1u} \times F_{1u}$. The Coriolis matrix elements C_{ij}^α ($\alpha = x, y, z$) are obtained according to the vector method of Meal and Polo.¹¹ The ζ^α matrices are related to the C^α matrices by a relation of this form:

$$\zeta^\alpha = L^{-1} C^\alpha (L')^{-1}$$

where L is the normal coordinate transformation matrix. The couplings of $E_g \times F_{2g}$, $F_{2g} \times F_{2g}$, and $F_{2u} \times F_{2u}$ are trivial as they involve one-dimensional species only. The Coriolis coupling constants for these types are:

- (i) $F_g \times F_{2g} : \zeta_{23} = -1$
- (ii) $F_{2g} \times F_{2g} : \zeta_{33} = -1/2$
- (iii) $F_{2u} \times F_{2u} : \zeta_{66} = -1/2$

Cyvin *et al.*¹² have reformulated the theory of centrifugal distortion by introducing certain new elements $t_{\alpha\beta\gamma\delta}$ instead of partial derivatives of inertia tensor components $J_{\alpha\beta\gamma\delta}$ of Kivelson and Wilson.¹³ The quantities $t_{\alpha\beta\gamma\delta}$ are easily obtained using Cyvin's method. Hence the distortion parameter is given by

$$\tau_{\alpha\beta\gamma\delta} = -(1/2) (4d^2 m_y)^{-4} t_{\alpha\beta\gamma\delta}$$

Thus, the expressions relating to the centrifugal distortion constants are:

$$\begin{aligned} D_J &= -(1/16) \hbar^4 (3\tau_{xxxx} + \tau_{xxyy} + 2\tau_{xyxy}) \\ D_K &= -(7/16) \hbar^4 (\tau_{xxxx} - \tau_{xxyy} - 2\tau_{xyxy}) \\ D_{JK} &= -(6/7) D_K \\ R_6 &= -(1/14) D_K \\ R_5 &= \delta_J = 0 \end{aligned}$$

3. Results and Discussion

The fundamental vibrational frequencies used in the present investigation are given in Table 1. The evaluated kinetic constants of octahedral hexahalide anions are also presented in Table 1. The stretch-stretch interaction kinetic constant K_{dd} is zero for this type of ions. The angle-angle interaction kinetic constants $k_{\alpha\alpha}$ and $k'_{\alpha\alpha}$ are negative in all these ions. For a given Y atom, the interaction kinetic constant $k'_{\alpha\alpha}$ is unchanged as it depends only on the mass of the Y atom. Further, for a given Y atom, the kinetic constants k_d and k_α increase in value while the interaction kinetic constants k'_{dd} , $k_{d\alpha}$ and $|k_{\alpha\alpha}|$ decrease with the increase in the mass of the central atom.

The general valence force field has seven independent potential constants. All the potential constants evaluated in the present work are listed in Table 2. The following observations are made from Table 2. As expected, the angle-angle interaction force constant $f'_{\alpha\alpha}$ is negative for all the ions studied here. The force constants are a convenient measure of the strength of a chemical bond and it is interesting to study the variation of the force constants between the hexafluorides and hexachlorides. It may also be noted that the strength of the chemical bonds in ReCl_6^{2-} and ReBr_6^{2-} ions is in the order $\text{Re}-\text{Cl} > \text{Re}-\text{Br}$.

Further, it may be seen that decrease of electronegativity of halogen atom decreases the value of stretching force constant. In case of Group III A hexafluoride ions (AlF_6^{2-} , GaF_6^{2-} , InF_6^{2-} and TlF_6^{2-}), the stretching force constant f_d decreases with increase of mass of the central atom. Thus it is apparent that relative strength of the chemical bond is in the sequence $\text{Al}-\text{F} > \text{Ga}-\text{F} > \text{In}-\text{F} > \text{Tl}-\text{F}$. Similar observations may also be made with respect to Group V B hexachloride ions (SbCl_6^{2-} and BiCl_6^{2-}), i.e. $\text{Sb}-\text{Cl}$ bond strength is greater than $\text{Bi}-\text{Cl}$ bond strength, as expected.

The stretching force constant f_d and the bond-bond interaction force constant f_{dd} decrease with increase in the cation size in the case of PtCl_6^{2-} anion. From this it may be concluded that $\text{Pt}-\text{Cl}$ bond is relatively strong in the presence of K cation than in the presence of Rb and Cs cations. The other force constants in PtCl_6^{2-} anion do not show any marked variation. Further, it may also be noticed that, in general, $f'_{dd} > f_{dd}$ in case of complexes of transition elements while in case of hexafluorides of Group III A elements and TaCl_6^{2-} , the trend is reversed. These observations clearly indicate that the ionic character of the bond is an important factor in determining the force constants.

Table I—Values of Vibrational Frequencies and Kinetic Constants of Octahedral Hexahalide Anions

Ion	Vibrational frequencies in cm ⁻¹						Kinetic constants in 10 ⁻²⁶ kg					
	$\nu_1 (A_{1g})$	$\nu_2 (E_g)$	$\nu_3 (F_{2g})$	$\nu_4 (F_{1g})$	$\nu_5 (F_{1g})$	$\nu_6 (F_{2g})$	k_d	k'_{dd}	k_α	$-k_{\alpha\alpha}$	$-k'_{\alpha\alpha}$	k_{dd}
³⁻ AlF ₆ ⁻	541	395	322	568	387	228	2.7294	0.4251	0.7732	0.1063	0.1972	0.2126
³⁻ GaF ₆ ⁻	535	358	281	481	298	199	2.8273	0.3277	0.8221	0.0819	0.1972	0.0164
³⁻ ⁹⁸ MoF ₆ ⁻	742	652	263	741	317	117	2.8636	0.2910	0.8403	0.0727	0.1972	0.1455
³⁻ INF ₆ ⁻	497	362	229	447	226	162	2.8927	0.2618	0.8549	0.0655	0.1972	0.1309
³⁻ TlF ₆ ⁻	478	340	209	412	202	148	2.9666	0.1878	0.8918	0.0470	0.1972	0.0939
⁻ NbCl ₆ ⁻	368	288	183	333	162	129	5.1369	0.6707	1.4795	0.1677	0.3629	0.3354
⁻ SbCl ₆ ⁻	333	291	174	350	180	128	5.1921	0.6139	1.5074	0.1535	0.3629	0.3070
⁻ TaCl ₆ ⁻	378	298	180	330	158	127	5.2860	0.5195	1.5545	0.1299	0.3629	0.2598
²⁻ ReCl ₆ ⁻	346	275	172	313	159	112	5.2951	0.5118	1.5588	0.1279	0.3629	0.2559
²⁻ K ₂ PtCl ₆ ⁻	350	320	173	341	186	121	5.3051	0.5016	1.5638	0.1254	0.3629	0.2508
²⁻ Rb ₂ PtCl ₆ ⁻	342	316	172	347	185	122	5.3051	0.5016	1.5638	0.1254	0.3629	0.2508
²⁻ Cs ₂ PtCl ₆ ⁻	337	312	173	332	186	122	5.3051	0.5016	1.5638	0.1254	0.3629	0.2508
⁻ BiCl ₆ ⁻	251	202	134	171	120	95	5.3209	0.4848	1.5719	0.1212	0.3629	0.2424
²⁻ ReBr ₆ ⁻	213	174	118	217	104	74	11.5411	1.5661	3.310	0.3915	0.8190	0.7831

Table 2—Values of Potential Constants and Compliance Constants of Octahedral Hexahalide Ions

Ion	Potential constants in 10 ² N m ⁻¹						Compliance constants in 10 ⁻² m/N							
	<i>f_d</i>	<i>f_{dd}</i>	<i>f'_{dd}</i>	<i>f_α</i>	<i>f_{αα}</i>	- <i>f_{αα}</i>	<i>f_{dα}</i>	<i>n_d</i>	- <i>n_{dd}</i>	- <i>n'_{dd}</i>	<i>n_α</i>	- <i>n_{αα}</i>	- <i>n'_{αα}</i>	- <i>n_{dα}</i>
AlF ₆ ³⁻	2.1422	0.2549	0.1128	0.2419	0.0119	0.0725	0.1130	0.5751	0.0446	0.0916	2.5959	-0.0078	0.8617	0.1949
GaF ₆ ³⁻	1.9747	0.2949	0.0496	0.2372	0.0356	0.0552	0.0900	0.5839	0.0642	0.0151	2.8289	0.2793	1.1315	0.1064
⁹² MoF ₆ ³⁻	4.8485	0.2340	0.3777	0.1563	0.0348	0.0483	0.0519	0.2135	0.0080	0.0193	5.2790	1.2696	1.2917	0.0336
InF ₆ ³⁻	1.8136	0.2163	0.0858	0.1211	0.0055	0.0367	0.0237	0.5850	0.0534	0.0100	4.7517	0.1781	1.7037	0.0739
TlF ₆ ³⁻	1.6675	0.2106	0.0476	0.3019	0.0064	0.2277	0.0136	0.6347	0.0636	-0.0108	3.7663	0.2934	0.2745	0.0488
NbCl ₆ ⁻	1.7399	0.1802	0.3292	0.1223	-0.0033	0.0431	0.0312	0.6184	0.0278	0.1488	4.7684	-0.2011	1.4495	0.1648
SbCl ₆ ⁻	1.8005	0.0900	0.1240	0.2310	-0.0014	0.1559	0.0265	0.5768	0.0226	0.0487	3.8187	-0.4047	0.4008	0.1146
TaCl ₆ ⁻	1.9351	0.1857	0.0266	0.1245	-0.0001	0.0417	0.0230	0.5478	0.0345	0.0702	4.5651	-0.0287	1.4982	0.0861
ReCl ₆ ²⁻	1.6898	0.1514	0.1710	0.1126	0.0049	0.0381	0.0230	0.6219	0.0394	0.0589	5.1086	0.4015	1.6407	0.0927
K ₂ PtCl ₆ ²⁻	2.0379	0.0690	0.2097	0.1345	0.0103	0.0385	0.0308	0.5077	0.0130	0.0595	4.3910	0.2730	1.6219	0.0749
Rb ₂ PtCl ₆ ²⁻	2.0323	0.0588	0.1423	0.1341	0.0097	0.0381	0.0305	-0.5051	0.0119	0.0427	4.3932	0.2545	1.6407	0.0723
Cs ₂ PtCl ₆ ²⁻	1.9265	0.0557	0.1903	0.1833	-0.0141	0.0385	0.0308	-0.5366	0.0119	0.0617	3.4581	-0.1956	1.6219	0.0790
BiCl ₆ ⁻	0.7346	0.0762	0.2584	0.0711	0.0007	0.0231	0.0124	1.6327	0.0699	0.5829	8.0628	0.0095	2.7033	0.2778
ReBr ₆ ²⁻	1.4695	0.1170	0.1722	0.1051	0.0005	0.0405	0.0301	0.7370	0.0394	0.1054	5.5891	0.0585	1.5447	0.1928

Table 3—Values of Valence Mean Square Amplitudes, Mean Amplitudes and Shrinkage Effect at 298·16 K

Mean square amplitudes in 10^{-3} \AA^2

Ion	$\sigma_d(X-Y)$	Mean square amplitudes in 10^{-3} \AA^2				Mean amplitudes in 10^{-2} \AA				Shrinkage constants	
		$-\sigma_{dd}$	σ_α	$-\sigma_{\alpha\alpha}$	$-\sigma_{d\alpha}$	$\sigma_p(Y-Y \text{ short})$ $\sigma_q(Y-X-Y)$	$I(X...Y)$	$I(Y...Y)$ short	$I(Y...Y)$ long	δ_p	δ_q
AlF_6^{3-}	3·4633	0·1882 0·8122	12·9645	-0·4854 4·4285	1·2498	7·2577 3·6778	5·8850	8·5192	6·0645	0·3862	0·4827
GaF_6^{3-}	3·2437	0·2697 0·2372	13·1411	1·0905 5·3440	0·6185	8·30765 5·5388	5·6954	9·1146	7·4423	0·2344/d	0·7797/d
$^{92}\text{MoF}_6^{3-}$	1·5980	0·0365 0·1892	23·3696	5·0894 6·0053	0·2612	12·7239 2·4390	3·9975	11·2800	4·9387	0·0240	0·9541
InF_6^{3-}	3·1688	0·2367 0·1600	21·1668	0·6196 0·7035	0·4136	12·6883 5·6977	5·6292	11·2642	7·5483	0·3782	0·6784
TlF_6^{3-}	3·3439	0·2660 0·0154	24·3010	1·1434 9·1106	0·2627	14·7031 6·6261	5·7827	12·1256	8·1401	0·3377	0·7288
NbCl_6^-	3·1376	0·1564 0·6690	20·6570	-0·9687 6·3415	0·8174	11·6149 3·5993	5·6014	10·7773	5·9994	0·5138	0·6251
SbCl_6^-	2·8506	0·0933 0·3056	21·7416	-0·5947 6·9753	0·5783	12·4715 4·4788	5·3391	11·1676	6·6924	0·4614	0·5978
TaCl_6^-	2·6960	0·1430 0·3605	19·6850	-0·1916 6·5430	0·4260	11·5436 3·9498	5·1923	10·7441	6·2847	0·4640	0·6672
ReCl_6^{2-}	3·0014	0·1631 1·3448	21·9144	0·7553 7·1286	0·4509	12·8937 3·3131	5·4785	11·3550	5·7560	0·3363	0·6239
$\text{K}_2\text{PtCl}_6^{2-}$	2·5253	0·0537 0·3110	18·9558	1·0557 7·5110	0·3744	11·2007 3·8067	5·0252	10·5833	6·1699	0·2636	0·5109
$\text{Rb}_2\text{PtCl}_6^{2-}$	2·5139	0·0491 0·2404	18·9652	0·9787 7·1286	0·3636	11·2202 4·0660	5·0139	10·5926	6·3765	0·2721	0·5102
$\text{Cs}_2\text{PtCl}_6^{2-}$	2·6450	0·0491 0·3199	18·8537	0·9957 7·0512	0·3914	11·2400 4·0104	5·1430	10·6019	6·3328	0·2619	0·5044
BiCl_6^-	7·1584	0·2876 2·4617	34·0492	-0·0247 11·4998	1·2061	21·5032 4·4707	8·4607	14·6640	6·6863	0·5301	0·8948
ReBr_6^{2-}	3·2703	0·1622 0·5041	23·4660	0·3125 6·5215	0·8639	13·1134 4·5243	5·7187	11·4514	6·7263	0·4475	0·6778

Table 4—Values of Coriolis Coupling Constants and Rotational Distortion Constants

Ion	Coriolis coupling constants				Distortion constants (kHz)			
	ζ_{44}	ζ_{55}	ζ_{45}	ζ_{46}	$-\zeta_{56}$	D_J	$-D_K$	D_{JK}
AlF_6^{3-}	0.5848	—0.0848	0.6712	0.4557	0.7365	168.1978	105.3856	90.3305
GaF_6^{3-}	0.3554	0.1446	0.7426	0.5677	0.6540	Data not available		
$^{92}\text{MoF}_6^{3-}$	0.2923	0.2077	0.7488	0.5949	0.6294	126.3466	381.4637	326.9689
InF_6^{3-}	0.2485	0.2515	0.7500	0.6130	0.6118	142.9006	214.3401	183.7201
TlF_6^{3-}	0.1564	0.3436	0.7441	0.6495	0.5729	121.0026	198.8952	170.4816
NbCl_6^-	0.4295	0.0705	0.7282	0.5341	0.6817	16.2556	22.6785	19.4387
SbCl_6^-	0.3665	0.1336	0.7409	0.5628	0.6582	11.6492	17.1661	14.7138
TaCl_6^-	0.2787	0.2213	0.7495	0.6005	0.6240	39.0386	61.6044	52.8038
ReCl_6^-	0.2722	0.2278	0.7497	0.6032	0.6214	8.9563	21.3304	18.2832
$\text{K}_2\text{PtCl}_6^{2-}$	0.2640	0.2360	0.7499	0.6066	0.6181	12.9414	22.9787	19.6960
$\text{Rb}_2\text{PtCl}_6^{2-}$	0.2640	0.2360	0.7499	0.6066	0.6181	16.1707	28.0213	24.0183
$\text{Cs}_2\text{PtCl}_6^{2-}$	0.2640	0.2360	0.7499	0.6066	0.6181	16.5270	32.4943	14.2163
BiCl_6^-	0.2508	0.2493	0.7500	0.6121	0.6127	18.5657	22.3676	19.1722
ReBr_6^{2-}	0.4578	0.0422	0.7207	0.5207	0.6920	2.2855	2.5388	2.1761
								0.1813

The compliance constants for the ions under consideration are also given in Table 2. These constants are invariant to the choice of coordinates defining the force field and they may be used as a measure of the bond strengths and interactions instead of force constants as pointed out by Decius⁹ and Jones.¹⁴ From Table 2, it may be seen that the compliance constants exhibit trends opposite to that of the force constants.

The valence mean square amplitudes and the vibrational mean amplitudes for both the bonded and the non-bonded distances along with the shrinkage constants at 298.16 K are reported in Table 3. It may be seen from these tables that the values of $I(Y \dots Y)$ short is greater than that of $I(Y \dots Y)$ long, which in turn is greater than the bonded $X-Y$ distance in all the ions studied here. In a similar manner, δ_q is found to be greater than δ_p in all these ions. These results may be useful in the interpretation of electron diffraction data of these ions.

The first order Coriolis coupling constants ζ_{44} , ζ_{55} , ζ_{45} and the second order constants ζ_{46} and ζ_{56} of these ions are presented in Table 4. The zeta values may be seen to obey the following sum rules.¹⁵

$$\zeta_{44} + \zeta_{55} = 1/2$$

$$\zeta_{44} \zeta_{55} - \zeta_{45}^2 = -1/2$$

$$\zeta_{46}^2 + \zeta_{56}^2 = 3/4$$

The second order constant ζ_{56} is negative in all the ions where as ζ_{55} is negative in AlF_6^{3-} ion only.

The rotational distortion constants of octahedral hexahalide anions are also reported in Table 4 and they are in the expected range. It is interesting to note that the rotational distortion constants for this type of ions are independent of the mass of the X atom and are dependent only on the mass of the Y atom, the internuclear distance and the three vibrational frequencies of the species A_{1g} , E_g and F_{2g} .

References

1. Mohan S, *Bull. Soc. Chim. Belg.*, **86** (1977), 531.
2. Mohan S, *Acta Phys. Polon.*, **A52** (1977), 747.
3. Mohan S, *Proc. Indian Acad. Sci.*, **A86** (1977), 299.
4. Mohan S, *Acta Ciencia Indica*, **4** (1978), 173.
5. Thirugnanasambandam P & Mohan S, *Bull. Soc. Chim. Belg.*, **84** (1975), 987.
6. Wilson E B (Jr), Decius J C & Cross P C, *Molecular Vibrations*, (McGraw-Hill, New York), 1955.
7. Reisfeld M J, *Spectrochim. Acta*, **29A** (1973), 1923.
8. Good M L, *Spectrochim. Acta*, **28A** (1972), 1529.
9. Decius J C, *J. Chem. Phys.*, **38** (1963), 241.
10. Cyvin S J, *Molecular vibrations and mean square amplitudes*, (Elsevier, Amsterdam), 1968.
11. Meal J H & Polo S R, *J. chem. Phys.*, **24** (1956), 1119, 1126.
12. Cyvin S J, Cyvin B N & Hoger G, *Z. Naturf.*, **23 a** (1968), 1694.
13. Kivelson D & Wilson (Jr) E B, *J. chem. Phys.*, **20** (1953), 1575; **21** (1953), 1229.
14. Jones L H, *Inorganic vibrational spectroscopy*, Vol. I, (Marcel Dekker, New York), 1971.
15. Mc Dowell R S, *J. chem. Phys.*, **41** (1964), 2557; **34** (1965), 419.

Isentropic Compressibility Behaviour of Amines in Dilute Aqueous Solutions

M V KAULGUD,* (Mrs) ANJALI SHRIVASTAVA† & M R AWODE

Department of Chemistry, Nagpur University, Nagpur 440 010

Received 5 February 1979; accepted 16 June 1980

Limiting apparent molal adiabatic compressibilities have been determined for the following amines at 5, 15 and 25°C: ammonia, MeNH₂, Et-NH₂, *n*-PrNH₂, *n*-BuNH₂, *t*-BuNH₂, Me₂NH and Me₃N. Sound velocities were measured differentially using a phase comparison interferometer and the densities using a differential buoyancy balance. Corrections to ϕ_k^0 arising out of hydrolysis have been applied. The results for amines have been compared with those for alcohols in water. It has been found that in comparison to —OH, the —NH₂ group causes a disruptive effect on the water structure.

1. Introduction

It is popularly believed that alcohols, amines, ethers, ketones and esters in dilute aqueous solutions behave as soluble hydrocarbons and it has been said that the functional group provides only a minor contribution to the measured thermodynamic properties.^{1,2} But chemical intuition tells that —OH group and —NH₂ group would behave differently especially in a hydrogen bonded solvent like water and will have different and appreciable contributions to the measured properties. Several systematic studies of bulk and molecular properties of dilute aqueous solutions of monofunctional solutes such as alcohols, amines and ethers are available, but they are directed to explain the nature of interaction between water and apolar moieties.^{1,2} In an earlier communication³ from this laboratory, values of the limiting apparent molal compressibilities (ϕ_{ks}^0) of amines in aqueous solution were reported. As these ϕ_{ks}^0 values were obtained from extrapolations from higher concentrations (> 0.5 M) at which the measurements were carried out, they cannot be relied upon as representing true limiting compressibilities in view of the fact that at higher concentrations there is large degree of solute-solute interaction. It was, therefore, thought necessary to determine ϕ_{ks}^0 more reliably by carrying out measurements in a very dilute aqueous solution. In such a dilute range, the amines studied undergo hydrolysis to the extent of 30 to 40%. Barring the work of Cabani *et al.*⁴ on the evaluation of true limiting partial molal volumes no attention seems to have been paid to the hydrolysis correction. In a

recent communication⁵ from this laboratory, a method for obtaining true ϕ_{ks}^0 after accounting for hydrolysis has been proposed. The present work deals with presentation of true ϕ_{ks}^0 values (corrected hydrolysis) for amines at different temperatures and their interpretation.

2. Experimental Details

The method adopted for purification of amines has been described earlier.⁵ Sound velocity *U* in aqueous solution of amines was measured by a phase comparison interferometer.⁶ Details regarding the method of measurement have also been described earlier.^{7,8}

2.1 Method of Hydrolysis Correction

First the adiabatic compressibilities (β) of amine solutions were determined from measured velocities using the relation $\beta = 1/U^2 d$ where *d* is the density. Compressibilities thus calculated were used to calculate the apparent molal adiabatic compressibility (ϕ_{ks}) using the relation

$$\phi_{ks} = \frac{1000(\beta - \beta^0)}{c} + \phi_v \beta^0 \quad \dots (1)$$

where β and ϕ_v are compressibility and apparent molal volume respectively of *c* molar solution, and β^0 the compressibility of the solvent. Hydrolysis correction was then applied by assuming the hydrolysis to be taking place from a hypothetical species..... B·H₂O as :



where B stands for the amine molecule.

By setting up a suitable equation for the observed partial compressibility in terms of those of the

* To whom all correspondence is to be addressed

† Present address: Chemistry Department, Allahabad University, Allahabad

components of Eq. (2), the concentration of which can be known from the degree of hydrolysis⁵ (α) one gets

$$\frac{\phi_{ks}^*}{(1-\alpha)} = \phi_{ks}^0 (\text{B} \cdot \text{H}_2\text{O}) + (1-\alpha) c S_{ks} \quad \dots(3)$$

where $\phi_{ks}^* = \phi_{ks}^{\text{obs}} - \alpha \phi_{ks}^0 (\text{BH}^+\text{OH}^-)$

This equation gives asymptotic curves and hence it is difficult to evaluate $\phi_{ks}^0 (\text{B} \cdot \text{H}_2\text{O})$ reliably by plotting the LHS of Eq. (3) versus $(1-\alpha) c$. However, Eq. (3) can be easily linearized. After multiplying both sides by $(1-\alpha) c$ one gets

$$\phi_{ks}^* c = (1-\alpha) c \phi_{ks}^0 (\text{B} \cdot \text{H}_2\text{O}) + (1-\alpha)^2 c^2 S_{ks} \quad \dots(4)$$

$$= (1-\alpha) c \left[\phi_{ks}^0 (\text{B} \cdot \text{H}_2\text{O}) + (1-\alpha) c S_{ks} \right] \quad \dots(5)$$

If $(1-\alpha) c S_{ks}$ is small, plots of $\phi_{ks}^* c$ against $(1-\alpha) c$ would be linear with $\phi_{ks}^0 (\text{B} \cdot \text{H}_2\text{O})$ as slopes. To illustrate the method, plots of $n\text{-BuNH}_2$ and $n\text{-PrNH}_2$ at 5, 15, and 25°C are shown in Figs. 1 and 2. It is seen from Figs. 1 and 2 that only at 25°C the plots are linear throughout the concentration range. This is true in case of amines. However, at 15 and 5°C, a marked deviation from linearity is observed (Figs. 1 and 2) after a certain concentration. This feature is observed in all amines studied except for ammonia

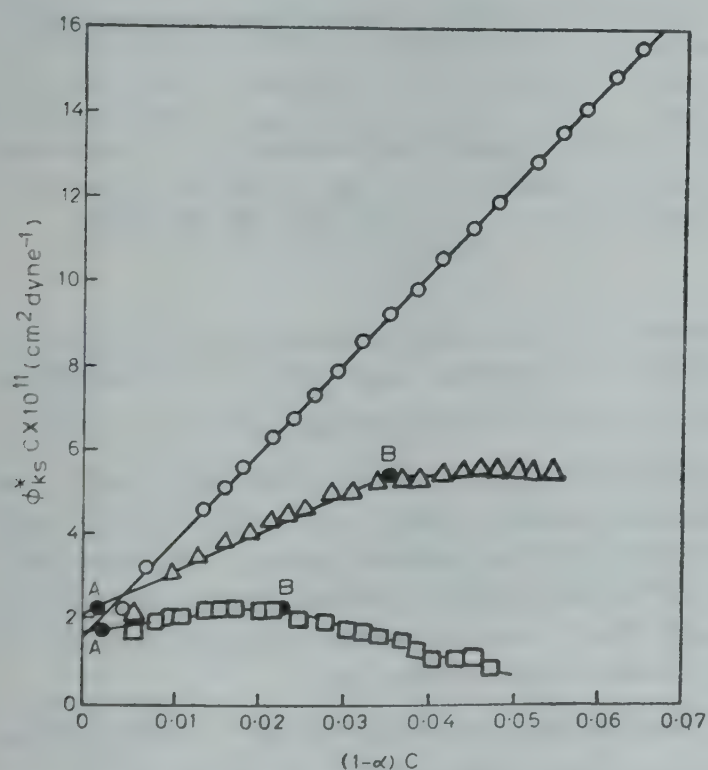


Fig. 1—Plot of $\phi_{ks}^* c$ against $(1-\alpha) c$ for $n\text{-PrNH}_2$ in water at 25°C (—○—○—), 15°C (—△—△—) and 5°C (—□—□—)

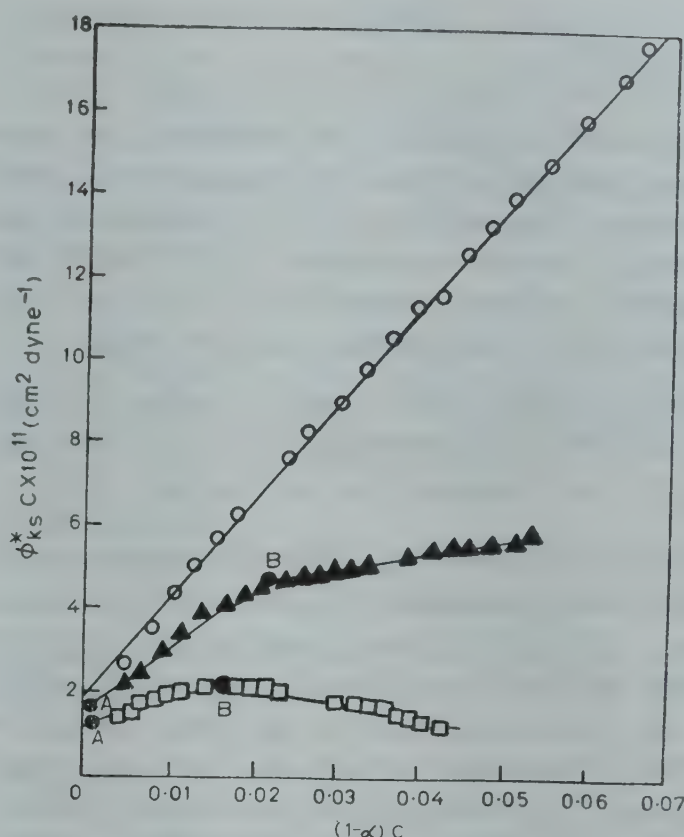


Fig. 2—Plot of $\phi_{ks}^* c$ against $(1-\alpha) c$ for $n\text{-BuNH}_2$ in water at 25°C (—○—○—), 15°C (—▲—▲—) and 5°C (—□—□—)

and methylamine. The deviation from linearity, in general, is more pronounced at low temperatures and for higher amines. The quantity in the square bracket in Eq. (5) can be looked upon as the actual ϕ_{ks} of the amine at a particular concentration c , the second term $(1-\alpha)cS_{ks}$, then representing the effect of solute-solute interaction. Deviation from linearity in the plots of $\phi_{ks}^* c$ versus $(1-\alpha) c$ can be due to the effect of solute-solute interaction on $\phi_{ks}^0 (\text{B} \cdot \text{H}_2\text{O})$. The fact that at 25°C all amines show linear plots but deviation occurs more at lower temperature and for higher amines is consistent with the above observation, since decrease in temperature and increase in the size of the molecules generally enhance solute-solute interactions. From Eq. (5) it is thus clear that in the plots of $\phi_{ks}^* c$ versus $(1-\alpha) c$, unless the term $(1-\alpha)cS_{ks}$ is almost negligible, one cannot obtain the true limiting slope $\phi_{ks}^0 (\text{B} \cdot \text{H}_2\text{O})$ very reliably. Therefore, where a change in linearity occurs indicating the onset of solute-solute interaction, the $\phi_{ks}^0 (\text{B} \cdot \text{H}_2\text{O})$ values have been obtained from the linear portion AB (Figs. 1 and 2) found in the lower concentration region. This procedure has been followed in this work and ensured that the values of the $\phi_{ks}^0 (\text{B})$ were always obtained from the true linear form of Eq. (5) in which the contribution of the nonlinear

term and hence solute-solute interaction was small or negligible.

We may mention here that the estimated limits of error in $\phi_{ks}^* c$ in this concentration range (around 0.01 moles/l) is of the order of $\pm 0.1 \times 10^{-11} \text{ cm}^2 \text{ dyne}^{-1}$ (almost equal to the dimension of the symbols at lowest concentration, Figs. 1 and 2) and it gives a standard deviation of $\pm 1 \times 10^{-10} \text{ cm}^5 \text{ dyne}^{-1} \text{ mole}^{-1}$ in $\phi_{ks}^0 (\text{B} \cdot \text{H}_2\text{O})$ which is quite reliable in the above limits of error. Finally, the limiting apparent molal compressibility of the molecule. $\phi_{ks}^0 (\text{B})$ was obtained by subtracting $\phi_k^0 (\text{H}_2\text{O})$

from the values of $\phi_{ks}^0 (\text{B} \cdot \text{H}_2\text{O})$. Inspection of Figs. 1 and 2 shows that the plots of $\phi_{ks}^* c$ versus $(1-\alpha) c$ do not pass through the origin as predicted by Eq. (4). This is accounted for by the presence of a finite term as intercept on the RHS of Eq. (4) having a magnitude of the order of $1 \text{ cm}^2 \text{ dyne}^{-1}$ obtained by a more rigorous derivation of Eq. (4) (Ref. 5). However, the presence of the intercept does not affect the slope and hence the values of $\phi_{ks}^0 (\text{B})$.

3. Results and Discussion

The results of ϕ_{ks}^0 of amines (Table 1) show that

- (i) ϕ_{ks}^0 are positive at 15 and 25°C and negative at 5°C (excepting for EtNH_2 and Me_2NH)

and (ii) $\frac{d\phi_{ks}^0}{dT}$ are positive.

The ϕ_{ks}^0 values of amines at 25°C (Table 1) show that as the hydrophobic chain lengthens or becomes large the values of ϕ_{ks}^0 increase. This trend is similar to that for alcohols⁸ at 45°C. At 5 and 15°C, ϕ_{ks}^0 values do not show any regular trend as in case of the alcohols⁸ in the range 35° to 45°C. It can be said that amines in aqueous solutions in the range 5-25°C give rise to similar structural situations as those of aqueous alcohol solutions in the range 35 to 45°C.

The temperature dependence of ϕ_{ks}^0 is shown in Fig. 3. It is seen that $d\phi_{ks}^0/dT$ at lower temperatures is positive for all amines, a behaviour similar to that of alcohols.⁸ At higher temperatures only higher amines retain the positive slope whereas $d\phi_{ks}^0/dT$ for lower amines is small and becomes negative in case of MeNH_2 . This shows that when the

Table 1—Values of ϕ_{ks}^0 ($10^{-10} \text{ cm}^5 \text{ dyne}^{-1} \text{ mole}^{-1}$) of Amines Studied in Aqueous Solution at Different Temperatures

Base	At 5°C	At 15°C	At 25°C
NH_3	-0.19	4.1	4.22
MeNH_2	-3.15	11.1	7.72
EtNH_2	5.12	11.8	13.32
$n\text{-PrNH}_2$	-5.55	1.6	13.4
$n\text{-BuNH}_2$	-1.85	6.2	15.42
$t\text{-BuNH}_2$	-2.00	6.8	12.92
Me_2NH	2.75	20.8	21.06
Me_3N	-5.52	9.6	15.52

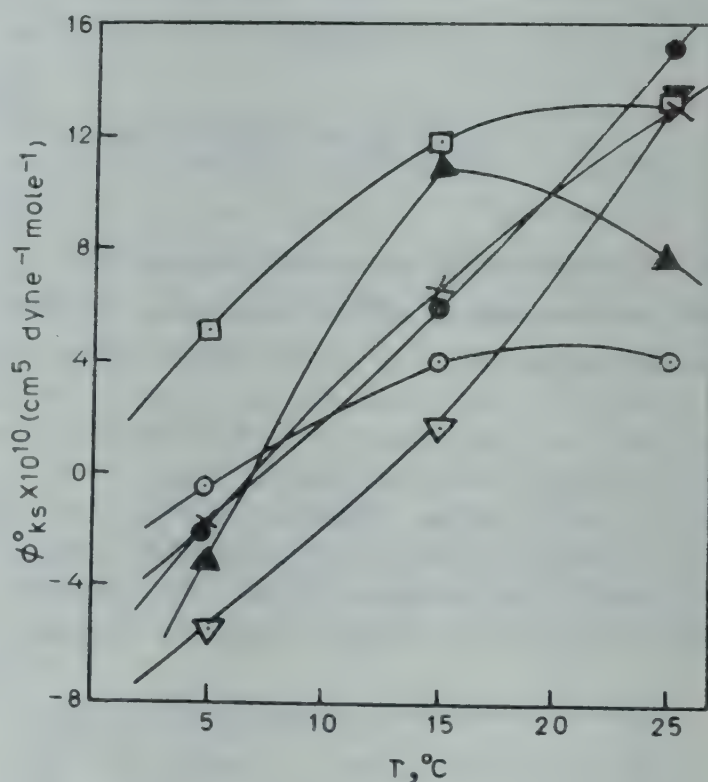


Fig. 3—Plot of ϕ_{ks}^0 against temperature ($t^\circ\text{C}$) for ammonia (\circ), MeNH_2 (\blacktriangle), EtNH_2 (\square), $n\text{-PrNH}_2$ (∇), $n\text{-BuNH}_2$ (\bullet) and $t\text{-BuNH}_2$ (\times)

hydrophobic chain is large, amines tend to behave as alcohols, i.e. structure stabilizers. The results of $d\phi_{ks}^0/dT$ in case of lower amines must then be interpreted as showing the structure disturbing effect of NH_2 group acting against the structure-stabilizing influence of the hydrophobic groups. This behaviour of $-\text{NH}_2$ group contrasts sharply with that of $-\text{OH}$ group, which does not seem to oppose the effect of the attached hydrophobic chain.

Kaulgud⁹ has shown that $\partial\phi_{ks}^0/\partial T$ at 4°C is related to $\partial/\partial P/(\Delta\theta)_{st} (\partial/\partial p) (\Delta\theta)_{st}$, where $\Delta\theta_{st}$ is the structural contribution to the change in the temperature of maximum density ($\Delta\theta$) of water in presence of solute.

Table 2—Temperature Coefficients of ϕ_{ks}^0 at 5°C for Amines Studied (revised values) and Alcohols (Ref. 9)

Solute	$\left(\frac{\partial}{\partial T} \phi_{ks}^0\right)$ $\times 10^{10}$ $\text{cm}^5 \text{dyne}^{-1}$ $\text{mole}^{-1} \text{deg}^{-1}$	$\left(\frac{\partial}{\partial T} \beta_2^0 V_2^0\right)$ $\times 10^{10}$ $\text{cm}^5 \text{dyne}^{-1}$ $\text{mole}^{-1} \text{deg}^{-1}$	$\frac{\partial (\Delta \theta_{str})}{\partial P}$
MeNH ₂	1.425	—	—
EtNH ₂	0.67	—	—
<i>n</i> -PrNH ₂	0.715	0.56	0.155
<i>n</i> -BuNH ₂	0.805	0.60	0.205
<i>t</i> -BuNH ₂	0.985	—	—
Me ₂ NH	1.805	—	—
Me ₃ N	1.52	—	—
MeOH	0.29	0.31	-0.02
EtOH	0.614	0.41	0.204
<i>n</i> -PrOH	1.027	0.42	0.607
<i>n</i> -BuOH	1.469	0.46	1.01
<i>t</i> -BuOH	1.123	0.85	0.27

This represents the magnitude of structure-strengthening ability. The $\frac{\partial}{\partial T} \phi_{ks}^0$ values reported in this work are at variance with those reported earlier.⁹ Values reported in the present work are some more reliable as a modified procedure⁵ for the evaluation of ϕ_{ks}^0 has been applied. The values of $\frac{\partial \phi_{ks}^0}{\partial T}$ of amines ϕ are less than those of the corresponding alcohols (Table 2). The values of $(\partial/\partial P) (\Delta \theta_{str})$ are thus smaller than those for alcohols. This indicates that the amines do not stabilize water structure to the same extent as alcohols do. The

hydrophobic part of both series of solutes will behave in the same manner and hence this difference must be arising due to the opposite nature of interaction of —OH group and —NH₂ group. Since the former is known to be a structure stabilizer it follows as a consequence that —NH₂ group must be acting as structure disrupter.

Summarizing, it can be said that the trends of the true apparent molal compressibilities of amines in aqueous solution and their temperature coefficients when compared with those of alcohols point out that amines behave as structure breakers.

Acknowledgement

Two of the authors (AS) and (MRA) are thankful to the University Grants Commission, New Delhi, for the grant of junior research fellowship and faculty improvement programme fellowship respectively.

References

1. Franks F, *Water: A comprehensive treatise*. Vol. 4 Chapter I (Plenum Press, New York), 1974.
2. Franks F, *Water: A comprehensive treatise*, Vol. 2 Chapters 1, 3 & 5 (Plenum Press, New York), 1974.
3. Kaulgud MV & Patil K J, *J. phys. Chem.*, **80** (1976), 138.
4. Cabani S, Conti G & Lepori L, *J. phys. Chem.* **76** (1972), 1338.
5. Kaulgud M V, Awode M R & Shrivastava A, *Indian J. Chem.*, **19A** (1980), 295.
6. Lall A, (now, A. Shrivastava), Ph.D. thesis Nagpur University, Nagpur, 1978.
7. Kaulgud M V, Pandya G H & Rao K S M, *Indian J. pure appl. Phys.*, **16** (1968), 459.
8. Kaulgud M V & Rao K S M, *J. chem. Soc., Faraday Trans.*, **175** (1979), 2237.
9. Kaulgud M V, *J. chem. Soc. Faraday Trans.*, **175** (1979), 2246.

Quantum Corrections to Thermodynamic Properties of a Mixture of Hard Sphere & Square Well Molecules

N SINGH* & S K SINHA

Department of Physics, L S College, Bihar University, Muzaffarpur 842 001

Received 3 May 1979

Using the 'modified' Wigner-Kirkwood method, the general expressions are given for the thermodynamic properties of a fluid mixture. The theory is applied to evaluate the quantum corrections to the equation of state, excess Helmholtz free-energy and isothermal compressibility of a mixture of hard sphere and square well molecules.

1. Introduction

In an earlier paper,¹ we had developed the theory for single component fluids, using the 'modified' Wigner-Kirkwood (WK) method.² The basic physical concept associated with this theory is that for a dense fluid, the repulsive forces dominate the fluid structure and the attractive forces and the quantum effects in the semiclassical limit play a minor role.

Many authors¹⁻⁶ have discussed the problem concerning the evaluation of the structural and thermodynamic properties of dense fluids with hard core potentials. But almost all these attempts have been confined to single-component fluids. Recently, we⁷ have evaluated the quantum corrections to the virial coefficients of a binary mixture of hard sphere and square well molecules.

In this paper, we have developed a simple theory for the thermodynamic properties of a fluid mixture in the semiclassical limit. The derivation, which generalizes the theory developed in the earlier paper,¹ gives expressions for the equation of state, excess Helmholtz free-energy and isothermal compressibility in simple forms. The theory is applied to a mixture of hard sphere and square well molecules.

2. Theory of a Fluid Mixture

We consider a mixture containing N_1 molecules of hard sphere type and N_2 molecules of square well type. Both types of molecules have the same diameter. We take $N = N_1 + N_2$ molecules, each of mass m and in thermal equilibrium in a container of volume V at temperature T . Like single-component fluid, the thermodynamic properties of

quantum fluid mixtures can be obtained from the canonical partition function defined by⁸

$$Q_N = \frac{1}{N_1! N_2! \lambda^{3N}} \int \cdots \int W_N(1, 2, \dots, N) \prod_{i=1}^N d\vec{r}_i \quad \dots(1)$$

where $\lambda = [2\pi\hbar^2\beta/m]^{1/2}$, $\beta = (kT)^{-1}$ and W_N is the Slater sum defined as

$$W_N(1, 2, \dots, N) = \lambda^{3N} \langle 1, 2, \dots, N | e^{-\beta \hat{H}_N} | 1, 2, \dots, N \rangle \quad \dots(2)$$

Here the Hamiltonian \hat{H}_N can be written as

$$\hat{H}_N = -\frac{\hbar^2}{2m} \sum_{i=1}^N \nabla_i^2 + \sum_{i < j} u_{\alpha\beta}(i, j) \quad \dots(3)$$

where $u_{\alpha\beta}(i, j)$ is the pair potential energy between particle i of type α and particle j of type β . If we write the pair potential in the form

$$u_{\alpha\beta}(i, j) = u_{\alpha\beta}^{hs}(i, j) + u_{\alpha\beta}^p(i, j) \quad \dots(4)$$

where $u_{\alpha\beta}^{hs}(i, j)$ is the hard sphere (reference) potential and $u_{\alpha\beta}^p(i, j)$ is the perturbation, then the canonical partition function can be written as^{1,4}

$$Q^N = \frac{1}{N_1! N_2! \lambda^{3N}} \int \cdots \int \prod_{i < j} [1 + f_{\alpha\beta}(i, j)] \prod_{i < j < k} [1 + f_{\alpha\beta\lambda}^{III}(i, j, k)] \times \prod_{i=1}^N d\vec{r}_i \quad \dots(5)$$

where

$$f_{\alpha\beta}(i, j) = f_{\alpha\beta}^c(i, j) + [1 + f_{\alpha\beta}^c(i, j)] f_{\alpha\beta}^{II}(i, j) \quad \dots(6)$$

* Permanent address : Department of Physics, R S College Muzaffarpur 842 001

$$f_{\alpha\beta}^{II}(i, j) = f_{hs}^{II}(i, j) + \left[1 + f_{hs}^{II}(i, j) \right] f_{\alpha\beta}^{II,P}(i, j) \quad \dots(7)$$

$$f_{\alpha\beta\gamma}^{III}(i, j, k) = f_{hs}^{III}(i, j, k) + \left[1 + f_{hs}^{III}(i, j, k) \right] f_{\alpha\beta\gamma}^{III,P}(i, j, k) \quad \dots(8)$$

and

$$f_{\alpha\beta}^c(i, j) = \exp \left[-\beta u_{\alpha\beta}(i, j) \right] - 1 \quad \dots(9)$$

where $f_{hs}^l(1, 2, \dots, l)$ is the l -particle 'modified' Mayer function for a hard sphere system; $f_{\alpha\beta}^{II,P}(i, j)$ and $f_{\alpha\beta\gamma}^{III,P}(i, j, k)$ are the two- and three-particle 'modified' Mayer functions respectively due to perturbation potential and are given by

$$f_{\alpha\beta}^{II,P}(i, j) = \frac{\lambda^2 \beta}{2\pi} \left[\frac{\partial^2 u_{\alpha\beta}^p(i, j)}{\partial r_{ij}^2} - \frac{11}{12} \beta \left(\frac{\partial^2 u_{\alpha\beta}^p(i, j)}{\partial r_{ij}} \right)^2 \right] \quad \dots(10)$$

and

$$f_{\alpha\beta\gamma}^{III,P}(i, j, k) = -\frac{\lambda^2 \beta^2}{24\pi} \left[\nabla_i u_{\alpha\beta}^p(i, j) \cdot \nabla_i u_{\beta\gamma}^p(i, j) + \nabla_j u_{\alpha\beta}^p(i, j) \cdot \nabla_j u_{\beta\gamma}^p(j, k) + \nabla_k u_{\alpha\beta}^p(i, k) \cdot \nabla_k u_{\alpha\beta}^p(j, k) \right] \quad \dots(11)$$

The chemical potential μ of a quantum fluid mixture can be obtained by the relation⁹

$$\beta \mu(\beta, \rho) = -\ln [Q_{N+1}/Q_N] \quad \dots(12)$$

Substituting Eq. (5) in Eq. (12), we get

$$\beta \mu = \beta \mu_{id} + \ln a \quad \dots(13)$$

where

$$\beta \mu_{id} = -\ln [V \lambda^{-3}/N] + [x_1 \ln x_1 + x_2 \ln x_2] \quad \dots(14)$$

is the chemical potential for an ideal gas at temperature T and density ρ (where $\rho = N/V$), $x_\alpha = N_\alpha/N = \rho_\alpha/\rho$, a is the activity of the fluid mixture relative to that of the ideal gas at the same temperature T and density ρ . Thus

$$a^{-1} = \frac{\int \prod_{j=1}^{N+1} d\bar{r}_j \prod_{i<j}^{N+1} \left[1 + f_{\alpha\beta}(i, j) \right]}{V \int \prod_{i=1}^N d\bar{r}_i \prod_{i<j}^N \left[1 + f_{\alpha\beta}(i, j) \right]}$$

$$\times \frac{\prod_{i<j<k}^{N+1} \left[1 + f_{\alpha\beta\gamma}^{III}(i, j, k) \right]}{\prod_{i<j<k}^N \left[1 + f_{\alpha\beta\gamma}^{III}(i, j, k) \right]} \quad \dots(15)$$

As in a previous paper,¹⁰ it can be shown that

$$Va^{-1} = \int d\bar{r}_{N+1} \prod_{i=1}^N \left[1 + f_{\alpha\beta}(i, N+1) \right] \prod_{j<i}^N \left[1 + f_{\alpha\beta\gamma}^{III}(i, j, N+1) \right] \quad \dots(16)$$

Eq. (16) shows that $N = N_1 + N_2$ particles are fixed in a most likely configuration and $(N+1)$ the particle of either type wanders throughout the entire system.

Eq.(16) is used to obtain expressions for thermodynamic properties. The details of the method for writing expressions for the equation of state and excess Helmholtz free-energy are given by Singh and Sinha.¹⁰ In this paper, we give the final results. Thus the equation of state of a fluid mixture in the semiclassical limit is given by

$$\frac{\beta P}{\rho} = \frac{\beta P_{hs}^c}{\rho} - \frac{1}{2} \rho \sum_{\alpha} x_{\alpha} x_{\beta} \int_d^{\tau} d\bar{r} \bar{f}_{\alpha\beta}(r) - \frac{1}{3} \rho^2 \sum_{\alpha} x_{\alpha} x_{\beta} x_{\gamma} \int_d^{\tau} \int_d^{\tau} d\bar{r}_{12} d\bar{r}_{13} \left[1 + f_{\alpha\beta}(1, 2) \right] \left[1 + f_{\beta\gamma}(1, 3) \right] f_{\alpha\beta\gamma}^{III}(1, 2, 3) + \dots \quad \dots(17)$$

where P_{hs}^c is the pressure of classical hard sphere fluid given by Andrews.¹¹ The excess Helmholtz free-energy is

$$\frac{\beta \Delta F}{N} = \frac{\beta \Delta F_{hs}^c}{N} - \frac{1}{2} \rho \sum_{\alpha} x_{\alpha} x_{\beta} \int_d^{\tau} d\bar{r} \bar{f}_{\alpha\beta}(r) - \frac{1}{6} \rho^2 \sum_{\alpha} x_{\alpha} x_{\beta} x_{\gamma} \int_d^{\tau} \int_d^{\tau} d\bar{r}_{12} d\bar{r}_{13} \left[1 + f_{\alpha\beta}(1, 2) \right] \left[1 + f_{\beta\gamma}(1, 3) \right] f_{\alpha\beta\gamma}^{III}(1, 2, 3) + \dots \quad \dots(18)$$

where ΔF_{hs}^c is the excess Helmholtz free-energy of classical hard sphere fluid given by Singh and Sinha.¹⁰

Using Eq. (17), the isothermal compressibility of a fluid mixture in the semiclassical limit is given by

$$\begin{aligned} \frac{\beta K^{-1}}{\rho} = & \frac{\beta K_{hs}^{c-1}}{\rho} - \rho \sum_{\alpha, \beta} x_{\alpha} x_{\beta} \int_d^{\tau} d\bar{r} f_{\alpha\beta}(r) \\ & - \rho^2 \sum_{\alpha, \beta, \gamma} x_{\alpha} x_{\beta} x_{\gamma} \int_d^{\tau} \int_d^{\tau} d\bar{r}_{12} d\bar{r}_{13} \\ & \left[1 + f_{\alpha\beta}(1, 2) \right] \\ & \left[1 + f_{\beta\gamma}(1, 3) \right] f_{\alpha\beta\gamma}^{III}(1, 2, 3) \\ & + \dots \end{aligned} \quad \dots(19)$$

where $K = \rho^{-1} \left(\frac{\partial \rho}{\partial P} \right)_T$ is known as isothermal compressibility and K_{hs}^c is K of classical hard sphere fluid and is given by

$$\begin{aligned} \left(\frac{\beta K_{hs}^{c-1}}{\rho} \right) = & \frac{1.1359}{1-0.7405Z} + \frac{8.5317}{1-0.5340Z} \\ & - \frac{15.977}{1-Z} \\ & + 7.4466 \frac{[1 + 0.6959Z]}{[1 - 1.5340Z + 0.5340Z^2]} \\ & + 7.9513 \frac{[Z^2 - 0.6962Z^3]}{[1 - 1.5340Z + 0.5340Z^2]^2} \end{aligned} \quad \dots(20)$$

where $Z = \rho d^3 / \sqrt{2}$

Eqs. (17)-(19) give simple expressions for the equation of state, excess Helmholtz free-energy and isothermal compressibility of binary mixtures in the semiclassical limit.

3. Thermodynamic Properties of a mixture of Hard Sphere and Square Well Molecules

We shall now apply the theory developed in the previous section to a mixture of hard sphere and square well molecules. Both types of molecules have the same diameter. If the molecules of the actual mixture differ in size, then the reference system would be a mixture of hard spheres. However, we are not considering this in the present case. In addition, the interaction between unlike molecules is assumed to be given by the hard sphere interaction.

Then

$$\begin{aligned} u_{\alpha\beta}(r) = & \infty & r < d \\ = & -\epsilon_{\alpha\beta} & d < r < \eta d \\ = & 0 & r > \eta d \end{aligned} \quad \dots(21)$$

where d is the diameter of hard sphere, $\eta = 1.50$, $\epsilon_{11} = \epsilon_{12} = 0$ and $\epsilon_{22} = \epsilon$. For this mixture, Eqs. (17)-(19) reduce to

$$\begin{aligned} \frac{\beta P}{\rho} = & \frac{\beta P^c}{\rho} - \frac{1}{2} \rho \left[I_1 + x_2^2 I_2 \right] \\ & - \frac{1}{3} \rho^2 \left[J_1 + 2 x_1 x_2^2 J_2 + x_2^3 J_3 \right] + \dots \end{aligned} \quad \dots(22)$$

$$\begin{aligned} \frac{\beta \Delta F}{N} = & \frac{\beta \Delta F^c}{N} - \frac{1}{2} \rho \left[I_1 + x_2^2 I_2 \right] \\ & - \frac{1}{6} \rho^2 \left[J_1 + 2 x_1 x_2^2 J_2 + x_2^3 J_3 \right] + \dots \end{aligned} \quad \dots(23)$$

and

$$\begin{aligned} \frac{\beta K^{-1}}{\rho} = & \frac{\beta K_{hs}^{c-1}}{\rho} - \rho \left[I_1 + x_2^2 I_2 \right] \\ & - \rho^2 \left[J_1 + 2 x_1 x_2^2 J_2 + x_2^3 J_3 \right] + \dots \end{aligned} \quad \dots(24)$$

where

$$I_1 = \int_d^{\tau} d\bar{r} f_{hs}^{II}(r) \quad \dots(25)$$

$$I_2 = \int_d^{\tau} f_{22}^c(r) f_{hs}^{II}(r) d\bar{r} + \left(\frac{\lambda^2}{2\pi} \right) \int_d^{\tau} d\bar{r}$$

$$\begin{aligned} \exp \left\{ -\beta u_{22}^p(r) \right\} \times & \left[\beta \frac{\partial^2 u_{32}^p(r)}{\partial r^2} \right. \\ & \left. - \frac{11}{12} \beta^2 \left(\frac{\partial u_{22}^p(r)}{\partial r} \right)^2 \right] \left[1 + f_{hs}^{II}(r) \right] \end{aligned} \quad \dots(26)$$

$$J_1 = \int_d^{\tau} \int_d^{\tau} d\bar{r}_{12} d\bar{r}_{13} f_{hs}^{III}(1, 2, 3) \quad \dots(27)$$

$$J_2 = \int_d^{\tau} \int_d^{\tau} d\bar{r}_{12} d\bar{r}_{13} f_{hs}^{III}(1, 2, 3) f_{22}^c(1, 3) \dots(28)$$

$$J_3 = \int_d^{\tau} \int_d^{\tau} d\bar{r}_{12} d\bar{r}_{13} f_{hs}^{III}(1, 2, 3) f_{22}^c(1, 2) f_{22}^c(1, 3)$$

$$- \frac{\lambda^2 \beta^2}{24 \pi} \int_a^r \int_a^r d\bar{r}_{12} d\bar{r}_{13} \exp \left\{ - \rho \left[u_{22}^p(1, 2) + u_{22}^p(1, 3) \right] \right\} \times \left[\nabla_1 u_{22}^p(1, 2) \nabla_1 u_{22}^p(1, 3) \right] \quad \dots(29)$$

where P^c , ΔF^c and K^c are respectively the pressure, excess free-energy and compressibility of a classical fluid mixture of hard sphere and square well molecules. They are respectively given by

$$\frac{\beta P^c}{\rho} = \frac{\beta P_{hs}^c}{\rho} - \frac{2 \pi}{3} (\rho d^3) x_2^2 (e^{\beta \epsilon} - 1) (\eta^3 - 1) \quad \dots(30)$$

$$\frac{\beta \Delta F^c}{N} = \frac{\beta \Delta F_{hs}^c}{N} - \frac{2 \pi}{3} (\rho d^3) x_2^2 (e^{\beta \epsilon} - 1) (\eta^3 - 1) \quad \dots(31)$$

$$\frac{\beta K^{c-1}}{\rho} = \frac{\beta K_{hs}^{c-1}}{\rho} - \frac{4 \pi}{3} (\rho d^3) x_2^2 (e^{\beta \epsilon} - 1) (\eta^3 - 1) \quad \dots(32)$$

Eqs. (25)-(29) have been evaluated in the previous papers.^{1,5} Hence the final results for a semiclassical mixture of hard sphere and sphere well molecules may be obtained. Thus the equation of state is given by

$$\frac{\beta P}{\rho} = \frac{\beta P^c}{\rho} + P_I (\lambda/d) + P_{II} (\lambda/d)^2 + \dots \quad \dots(33)$$

where

$$P_I = (\rho d^3) A \quad \dots(34)$$

$$P_{II} = (\rho d^3) B + (\rho d^3)^2 C \quad \dots(35)$$

The excess Helmholtz energy is

$$\frac{\beta \Delta F}{N} = \frac{\beta \Delta F^c}{N} + F_I (\lambda/d) + F_{II} (\lambda/d)^2 + \dots \quad \dots(36)$$

where

$$F_I = (\rho d^3) A \quad \dots(37)$$

$$F_{II} = (\rho d^3) B + \frac{1}{2} (\rho d^3)^2 C \quad \dots(38)$$

The isothermal compressibility is given by

$$\frac{\beta K^{-1}}{\rho} = \frac{\beta K^{c-1}}{\rho} + K_I (\lambda/d) + K_{II} (\lambda/d)^2 + \dots(39)$$

where

$$K_I = 2 (\rho d^3) A \quad \dots(40)$$

$$K_{II} = 2 (\rho d^3)^2 B + 3 (\rho d^3)^2 C \quad \dots(41)$$

In Eqs. (40) and (41).

$$A = \frac{\pi}{\sqrt{2}} \left[1 + x_2^2 (e^{\beta \epsilon} - 1) \operatorname{erf}(\xi) \right] \quad \dots(42)$$

$$B = \frac{2}{3} \left\{ 1 + x_2^2 \left[(e^{\beta \epsilon} - 1) \left(1 - \frac{3}{4} e^{-\xi^2} \right) - \frac{(\ln 2 - \frac{1}{4})}{12} \eta e^{\beta \epsilon} (\beta \epsilon)^2 \right] \right\} \quad \dots(43)$$

and

$$C = \frac{3 \cdot 2175 \pi^2}{18} \left[1 + 2 x_1 x_2^2 (e^{\beta \epsilon} - 1) + x_2^3 (e^{\beta \epsilon} - 1)^2 \right] \quad \dots(44)$$

$$\text{with } \xi = \frac{(2 \pi)^{1/2}}{(\lambda/d)} (\eta - 1)$$

In terms of reduced quantities, $T^* = (\beta \epsilon)^{-1}$ and $\pi^* = h/d \sqrt{m \epsilon}$, and Eqs. (33), (36) and (39) respectively reduce respectively to

$$\frac{\beta P}{\rho} = \frac{\beta P^c}{\rho} + P_I^* \pi^* + P_{II}^* \pi^{*2} + \dots \quad \dots(45)$$

where

$$P_I^* = (\rho d^3) A^* \quad \dots(46)$$

$$P_{II}^* = (\rho d^3) B^* + (\rho d^3)^2 C^* \quad \dots(47)$$

$$\frac{\beta \Delta F}{N} = \frac{\beta F^c}{N} + F_I^* \pi^* + F_{II}^* \pi^{*2} + \dots \quad \dots(48)$$

where

$$F_I^* = (\rho d^3) A^* \quad \dots(49)$$

$$F_{II}^* = (\rho d^3) B^* + \frac{1}{2} (\rho d^3)^2 C^* \quad \dots(50)$$

and

$$\frac{\beta K^{-1}}{\rho} = \frac{\beta K^{c-1}}{\rho} + K_I^* \pi^* + K_{II}^* \pi^{*2} + \dots \quad \dots(51)$$

where

$$K_I^* = 2 (\rho d^3) A^* \quad \dots(52)$$

$$K_{II}^* = 2 (\rho d^3) B^* + 3 (\rho d^3)^2 C^* \quad \dots(53)$$

In Eqs. (52) and (53)

$$A^* = \frac{\sqrt{\pi}}{2} (1/T^*)^{1/2} \left[1 + x_2^2 (e^{1/T^*} - 1) \operatorname{erf}(\xi^*) \right] \quad \dots(54)$$

$$B^* = \frac{1}{3 \pi} (1/T^*) \left\{ 1 + x_2^2 \left[(e^{1/T^*} - 1) \left(1 - \frac{3}{4} e^{-\xi^{*2}} \right) - \frac{(\ln 2 - \frac{1}{4})}{12} \eta (1/T^*)^2 e^{1/T^*} \right] \right\} \quad \dots(55)$$

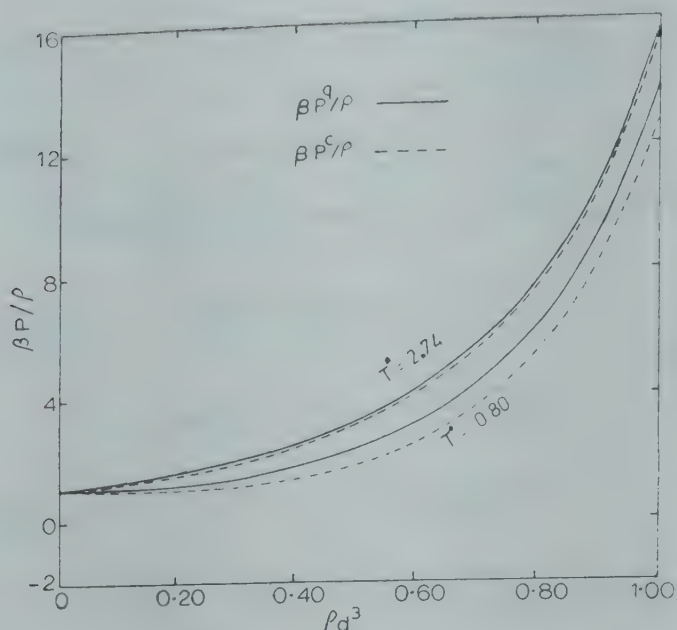


Fig. 1—Equation of state ($\beta P/\rho$) of a mixture of hard sphere and square well molecules with $\eta = 1.50$, $x_2 = 0.50$ for $\pi^* = 0.593$ at $T^* = 0.80$ and 2.74 .

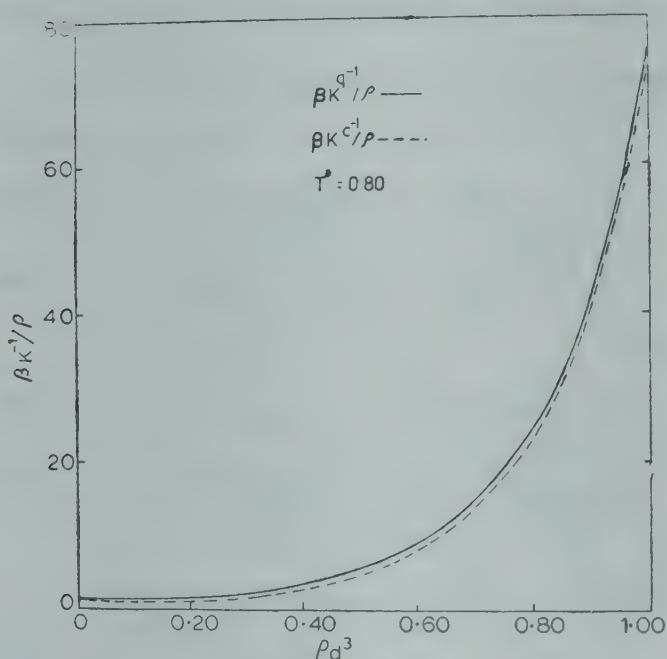


Fig. 2—Compressibility ($\beta K^{-1}/\rho$) of hard sphere and square well molecules with $\eta = 1.50$, $x_2 = 0.50$ for $\pi^* = 0.593$ at $T^* = 0.80$

and

$$C^* = \frac{3.2175 \pi}{36} (1/T^*) \left[1 + 2 x_1 x_2^2 (e^{1/T^*} - 1) + x_2^3 (e^{1/T^*} - 1)^2 \right] \quad \dots (56)$$

where $\xi^* = T^{*1/2}/\pi^* (\eta - 1)$. For a pure fluid of square well molecules, $x_1 = x_2 = 1$, and for a pure hard sphere fluid, $x_1 = x_2 = 0$.

The coefficients P_I^* , P_{II}^* , F_I^* , F_{II}^* and K_I^* , K_{II}^* are functions of density ρd^3 and temperature T^* and depend on the values of η , x_1 and x_2 .

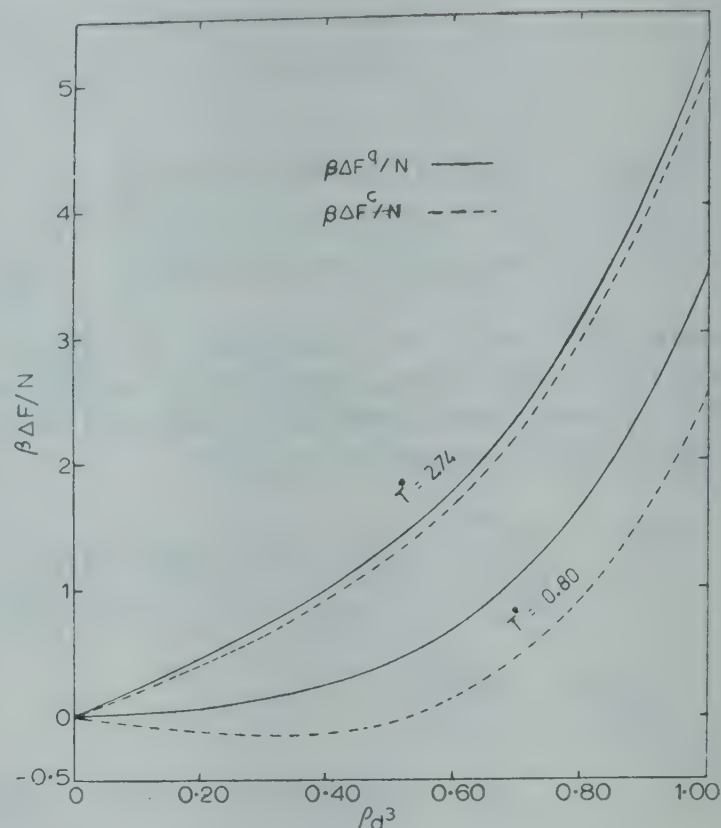


Fig. 3—Excess Helmholtz free-energy ($\beta \Delta F/N$) of hard sphere and square well molecules with $\eta = 1.50$ for $\pi^* = 0.593$, $x_2 = 0.50$ at $T^* = 0.80$ and 2.74

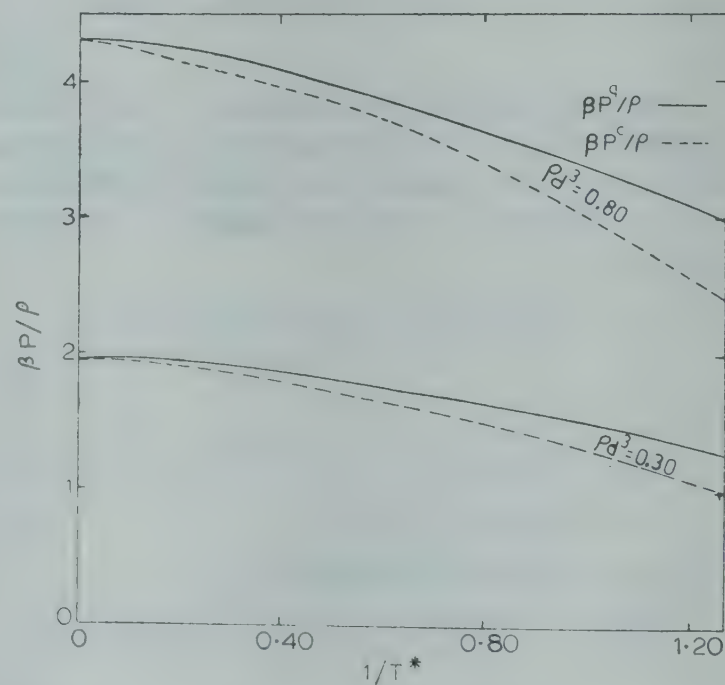


Fig. 4—Equation of state ($\beta P/\rho$) of a mixture of hard sphere and square well molecules with $\eta = 1.50$, $x_2 = 0.50$ against $1/T^*$ for $\pi^* = 0.593$ at $\rho d^3 = 0.30$ and 0.80

The thermodynamic properties are calculated for a fluid mixture of hard sphere and square well molecules with $x_2 = 0.50$ and $\eta = 1.50$. The values of $\beta P/\rho$ and $\beta \Delta F/N$ for the mixture for $\pi^* = 0.593$ at $T^* = 0.80$ and 2.74 are reported in Figs. 1 and 2 respectively. In Fig. 3, the values of $\beta K^{-1}/\rho$ for the

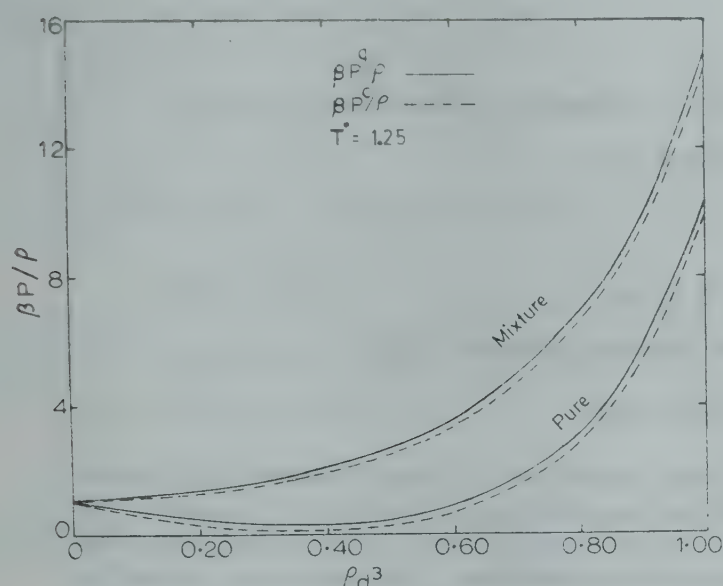


Fig. 5—Equation of state ($\beta P/\rho$) for a mixture of hard sphere and square well molecules with $\eta = 1.50$ and $x_2 = 0.50$ and 1.00 for $\pi^* = 0.593$ at $T^* = 1.25$

mixture are reported for $\pi^* = 0.593$ at $T^* = 0.80$; the corresponding classical values are shown in Fig. 3 for comparison. In Fig. 4, the values of $\beta P/\rho$ are plotted against $1/T^*$ at the densities $\rho d^3 = 0.30$ and

0.80 . From Figs. 1-4, we see that the quantum effect increases with the increase of density and decrease of temperature.

The values of $\beta P/\rho$ for the mixture with $x_2 = 0.50$ and the pure square well fluid with $x_2 = 1$ are shown in Fig. 5 for $\pi^* = 0.593$ at $T^* = 1.25$; the corresponding classical values are also reported in Fig. 5 for comparison. It is evident from Fig. 5 that the quantum effect increases with the value of x_2 .

References

1. Singh N & Sinha S K, *J. chem. Phys.*, 70 (1979), 552.
2. Singh B P & Sinha S K, *J. chem. Phys.*, 68 (1978), 562.
3. Gibson W G, *Phys. Rev. A*, 5 (1972), 862.
4. Singh N & Sinha S K, *J. chem. Phys.*, 69 (1978), 2709.
5. Sinha A K & Sinha S K, *J. chem. Phys.*, 70 (1979), 3502.
6. Singh B P & Sinha S K, *Phys. Rev. A*, 18 (1978), 2701.
7. Singh N & Sinha S K, *J. chem. Phys.*, 71 (1979), 3099.
8. Hill T L, *Statistical mechanics* (McGraw - Hill, New York), 1956.
9. Hirschfelder J O, Curtiss C F & Bird R B, *Molecular theory of gases and liquids* (Wiley, New York), 1954.
10. Singh B P & Sinha S K, *J. chem. Phys.*, 67 (1977), 3645; 69 (1978), 2927.
11. Andrew F C, *J. chem. Phys.*, 62 (1975), 272; 64 (1976), 1941, 1948.

A Composite Fluid Sphere with Two Density Distributions in General Relativity

P PATRA* & T ROY

Department of Physics, Jadavpur University, Calcutta 700 032

Received 21 December 1979

Field equations are exactly solved for a composite fluid sphere with two density distributions, in which the central core ($0 \leq r \leq a$) is a fluid of constant density and the envelope ($a \leq r \leq r_0$) is formed of the Tolman's Fluid No. IV. The Tolman's solution No. IV, which is valid for $M/r_0 < 1/3$, is continued to the region $1/3 \leq M/r_0 < 1/2$ and may be important in studying dense massive stars. The restrictions imposed by the relations of central pressure to the central density limit the upper value of M/r_0 . The expression for M/r_0 is found out in terms of ρ_c , r_0^2 and a/r_0 .

1. Introduction

Oppenheimer and Volkoff,¹ in their pioneering work on massive neutron cores, solved numerically the Einstein's field equations using the equation of state of a degenerated Fermi gas and they compared their result with several exact solutions discovered by Tolman.² They found that Tolman's fluid sphere No. IV represents fairly heavy spheres of degenerated Fermi gas. But for Tolman's fluid sphere No. IV, $r_0 > 3M$, where M is the mass and r_0 the radius of the sphere and when $r_0 = 3M$, both the central density ρ_c and the central pressure p_c diverge to infinite value although it satisfies the condition $p_c \leq \rho_c/3$. For $r_0 < 3M$, the pressure is negative in the central region of the sphere upto a certain value of r depending on the value of M/r_0 .

As the range $2M < r_0 \leq 3M$, is very important for dense massive stars, we study the composite sphere consisting of a central core of constant density surrounded by a concentric spherical shell of fluid, in which the mass is distributed obeying Tolman's solution No. IV. Such a composite sphere overcomes the difficulty mentioned and it has been possible to include the region $r_0/3 \leq M < r_0/2$, the upper limit being restricted to $3r_0/8$ by the condition, $p_c \leq \rho_c$.

We have found interior solution for such a composite sphere, which is free from singularity under the specified conditions, and also the relation showing interdependence of M/r_0 , $\rho_c r_0^2$ and a/r_0 .

2. Field Equations

For a static spherically symmetric system, an appropriate line element is

*Permanent Address: David Hare Training College
Calcutta 700 019

$$ds^2 = e^{\nu(r)} dt^2 - e^{\lambda(r)} dr^2 - r^2 (d\theta^2 + \sin^2 \theta d\phi^2).$$

It then follows that the Einstein's field equations reduce to³

$$8\pi \rho(r) = e^{-\lambda} \left(\frac{\lambda'}{r} - \frac{1}{r^2} \right) + \frac{1}{r^2} \quad \dots(1)$$

$$8\pi p(r) = e^{-\lambda} \left(\frac{\nu'}{r} + \frac{1}{r^2} \right) - \frac{1}{r^2} \quad \dots(2)$$

$$\frac{dp}{dr} = - \frac{p + \rho}{2} \cdot \nu' \quad \dots(3)$$

where a prime denotes differentiation with respect to r .

3. The Outer Region ($a \leq r \leq r_0$) — Tolman's Fluid No. IV

3.1 Solutions of Field Equations

Tolman's solution No. IV for the interior of a fluid sphere is²

$$e^{\lambda} = \frac{1 + 2r^2/A^2}{(1 - r^2/R^2)(1 + r^2/A^2)} \quad \dots(4)$$

$$e^{\nu} = B^2 (1 + r^2/A^2) \quad \dots(5)$$

$$8\pi \rho = \frac{1}{A^2} \frac{1 + 3A^2/R^2 + 3r^2/R^2}{1 + 2r^2/A^2} + \frac{2}{A^2} \frac{1 - r^2/R^2}{(1 + 2r^2/A^2)^2} \quad \dots(6)$$

$$8\pi p = \frac{1}{A^2} \frac{1 - A^2/R^2 - 3r^2/R^2}{1 + 2r^2/A^2} \quad \dots(7)$$

3.2 Fixing the Constants

The exterior metric is necessarily the Schwarzschild metric for empty space,

$$ds^2 = (1 - 2M/r) dt^2 - (1 - 2M/r)^{-1} dr^2 - r^2 (d\theta^2 + \sin^2 \theta d\phi^2)$$

where M is the total mass of the composite sphere.

- (i) Continuity of e^ν across the boundary ($r = r_0$) implies

$$B^2 (1 + r_0^2/A^2) = 1 - 2M/r_0 \quad \dots(8)$$

- (ii) Continuity of $e^{\lambda+\nu}$ across the boundary implies

$$B^2 \frac{1 + 2r_0^2/A^2}{1 - r_0^2/R^2} = 1 \quad \dots(9)$$

- (iii) Since the pressure is zero at the boundary, from Eq. (7), we have

$$R^2 - A^2 = 3r_0^2 \quad \dots(10)$$

From Eqs. (8), (9) and (10), we have

$$A^2 = \frac{r_0^2}{M_0} (1 - 3M_0) \quad \dots(11)$$

$$B^2 = A^2/R^2 = 1 - 3M_0 \quad \dots(12)$$

$$R^2 = r_0^2/M_0 \quad \dots(13)$$

where $M_0 = M/r_0$.

Writing in terms of M_0 and r/r_0 , we find the solution in the region $a \leq r \leq r_0$ as

$$e^\lambda = \frac{1 - 3M_0 + 2M_0 r^2/r_0^2}{(1 - M_0 r^2/r_0^2) (1 - 3M_0 + M_0 r^2/r_0^2)} \quad \dots(14)$$

$$e^\nu = 1 - 3M_0 + M_0 r^2/r_0^2 \quad \dots(15)$$

$$8\pi \rho r_0^2 = M_0 \frac{1 + 3(1 - 3M_0 + M_0 r^2/r_0^2)}{1 - 3M_0 + 2M_0 r^2/r_0^2} + 2M_0 \frac{(1 - 3M_0)(1 - M_0 r^2/r_0^2)}{(1 - 3M_0 + 2M_0 r^2/r_0^2)^2} \quad \dots(16)$$

$$8\pi p r_0^2 = 3M_0^2 \frac{1 - r^2/r_0^2}{1 - 3M_0 + 2M_0 r^2/r_0^2} \quad \dots(17)$$

3.3 Conditions for Physical Relevance

- (i) In order that e^λ and e^ν be non-zero positive and finite quantities, we must have

$$\{1 - 3M_0 + M_0 r^2/r_0^2\} > 0,$$

$$\text{i.e., } r^2/r_0^2 > 3 - (1/M_0) \quad \dots(18)$$

If the origin ($r = 0$) be included, then the condition to be satisfied is

$$M_0 < 1/3, \text{ i.e. } r_0 > 3M,$$

showing that Tolman's solution No. IV for a complete sphere is not valid in the region $2M < r_0 \leq 3M$

Since $a \leq r \leq r_0$, we have

$$3 - 1/M_0 < a^2 \quad \dots(19)$$

where $a_0 = a/r_0$.

Thus on introducing a central core, it becomes possible to continue Tolman's solution IV to the region $2M < r_0 \leq 3M$.

- (ii) Eq. (17) shows that the pressure is positive every where in the region $a_0 \leq r/r_0 \leq 1$ under the specified condition in Eq. (18).

- (iii) Since $r^2/r_0^2 \leq 1$, from Eq. (16), we have

$$8\pi \rho r_0^2 \geq \frac{M_0}{1 - 3M_0 + 2M_0 r^2/r_0^2} \times [3(1 - 3M_0 + M_0 r^2/r_0^2) + 3(1 - 2M_0)]$$

and under the specified condition in Eq. (18), we have

$$8\pi \rho r_0^2 > 0 \text{ in the region } a_0 \leq r/r_0 \leq 1.$$

4. Central Core ($0 \leq r \leq a$) of Constant Density (ρ_c)

4.1 Solutions of Field Equations

From Schwarzschild's interior solution for a fluid sphere of constant density ρ_c , we have³

$$e^{-\lambda} = 1 - r^2/R_1^2, \quad \dots(20)$$

$$e^{\nu/2} = A_1 - B_1 (1 - r^2/R_1^2)^{1/2} \quad \dots(21)$$

$$8\pi p = \frac{1}{R_1^2} \left[\frac{3B_1 (1 - r^2/R_1^2)^{1/2} - A_1}{A_1 - B_1 (1 - r^2/R_1^2)^{1/2}} \right] \quad \dots(22)$$

where

$$\frac{1}{R_1^2} = \frac{8\pi \rho_c}{3} \quad \dots(23)$$

4.2 Fixing the Constants

- (i) Continuity of $e^{-\lambda}$ across the surface at $r = a$ implies

$$\frac{(1 - M_0 a^2/r_0^2)(1 - 3M_0 + M_0 a^2/r_0^2)}{1 - 3M_0 + 2M_0 a^2/r_0^2} = 1 - a^2/R_1^2$$

and on writing R_0 for R_1/r_0 , we have

$$\frac{1}{R_0^2} = \frac{M_0 (2 - 3M_0 + M_0 a_0^2)}{1 - 3M_0 + 2M_0 a_0^2} \quad \dots(24)$$

Since $3/R_0^2 = 8\pi \rho_c r_0^2$, Eq. (24) gives the central density, ρ_c in terms of M_0 and a_0 .

- (ii) Continuity of e^ν at $r = a$ implies

$$A_1 - B_1 (1 - a_0^2/R_0^2)^{1/2} = (1 - 3M_0 + M_0 a_0^2)^{1/2} \quad \dots(25)$$

- (iii) Equating pressure on both sides of the surface

$r = a$, we have

$$\frac{1}{R_0^2} \left[\frac{2A_1}{A_1 - B_1 (1 - a_0^2/R_0^2)^{1/2}} - 3 \right] = \frac{3M_0^2 (1 - a_0^2)}{1 - 3M_0 + 2M_0 a_0^2} \quad \dots(26)$$

From Eqs. (24), (25) and (26), we get

$$A_1 = \frac{3(1-M_0)(1-3M_0+M_0a_0^2)^{1/2}}{2-3M_0+M_0a_0^2} \quad \dots(27)$$

and

$$B_1 = \frac{(1-M_0a_0^2)^{1/2}(1-3M_0+2M_0a_0^2)^{1/2}}{2-3M_0+M_0a_0^2} \quad \dots(28)$$

Thus the constants A_1 , B_1 and R_1^2 are fixed in terms of a_0 and M_0 .

4.3 Conditions for Physical Relevance

The central pressure p_c should satisfy either of the two conditions, viz. (i) $p_c \leq \rho_c$ and (ii) $p_c \leq \rho_c/3$ for physical solutions.

(i) For $p_c \leq \rho_c$, we must have, from Eq. (22),

$$3B_1 \leq 2A_1 \quad \dots(29)$$

and making use of Eqs. (27) and (28), we have

$$(1-M_0a_0^2)^{1/2}(1-3M_0+2M_0a_0^2)^{1/2} \leq 2(1-M_0)(1-3M_0+M_0a_0^2)^{1/2} \quad \dots(30)$$

from which we observe that

$$\text{when } M_0 \geq 1/3, a_0^2 \geq 1/3 \quad \dots(31)$$

$$\text{and when } a_0^2 \leq 1, M_0 \leq 3/8 \quad \dots(32)$$

(ii) For $p_c \leq \rho_c/3$, we must have

$$2B_1 \leq A_1 \quad \dots(33)$$

and similarly we observe that

$$a_0^2 \geq 3/2, \text{ when } M_0 \geq 1/3.$$

Hence for $M_0 \geq 1/3$, the condition $p_c \leq \rho_c/3$ is not satisfied.

(iii) The pressure at $r = a$ is necessarily positive.

For this, we must have from Eq. (22)

$$A_1 < 3B_1(1-a_0^2/R_0^2)^{1/2} \quad \dots(34)$$

Since for $p_c \leq \rho_c$, $B_1 \leq 2A_1/3$,

Eq. (34) gives

$$a_0^2 \leq 3R_0^2/4 \quad \dots(35)$$

or,

$$8\pi\rho_c r_0^2 < 9/(4a_0^2) \quad \dots(36)$$

which with Eqs. (31) and (32) limits the central density.

Values of ρ_c computed from Eq. (24) and p_c/ρ_c computed from Eqs. (22), (27), (28) for given values of a_0 and for $M_0 \geq 1/3$ are reported in Table 1.

Table 1—Values of ρ_c and p_c/ρ_c for Different Values of a_0

a_0^2	M_0	$8\pi\rho_c r_0^2$	p_c/ρ_c	Limiting values of M_0
0.4000	0.3333	4.2486	0.9510	
	0.3350	4.3146	0.9958	≥ 0.3350
	0.3360	4.3528	1.0257	
0.6000	0.3333	2.9994	0.8137	
	0.3400	3.1123	0.9282	≥ 0.3430
	0.3430	3.1648	0.9904	
	0.3450	3.2003	1.0366	
0.9000	0.3333	2.1660	0.6330	
	0.3400	2.2157	0.6889	
	0.3500	2.2901	0.7918	
	0.3600	2.3651	0.9238	≥ 0.3645
	0.3625	2.3843	0.9623	
	0.3640	2.3957	0.9873	
	0.3645	2.3995	0.9952	
	0.3650	2.4032	1.0038	

5. Mass of the Composite Sphere

Eq. (24) can be expressed as a quadratic in M_0 as

$$\frac{1}{2} \left(3 - a_0^2 \right) M_0^2 - \left\{ \frac{1}{2} \left(3 - 2a_0^2 \right) / R_0^2 + 1 \right\} M_0 - \frac{1}{2} / R_0^2 = 0 \quad \dots(37)$$

which gives

$$M_0 = \left[\frac{1}{2} \left(3 - 2a_0^2 \right) / R_0^2 + 1 \pm \left\{ \frac{1}{2} \left(3 - 2a_0^2 \right) / R_0^2 + 1 \right\}^2 - \left(3 - a_0^2 \right) / R_0^2 \right]^{1/2} / \left(3 - a_0^2 \right)$$

Now,

$$\begin{aligned} & \left\{ \frac{1}{2} \left(3 - 2a_0^2 \right) / R_0^2 + 1 \right\}^2 - \left(3 - a_0^2 \right) / R_0^2 \\ &= \left\{ \frac{1}{2} \left(3 - 2a_0^2 \right) / R_0^2 \right\}^2 + \left(1 - a_0^2 \right) / R_0^2 \\ &> \left\{ \frac{1}{2} \left(3 - 2a_0^2 \right) / R_0^2 \right\}^2 \end{aligned}$$

(i) Considering + ve sign in the expression for M_0 , we have

$$M_0 > \frac{\left(3 - 2a_0^2 \right) / R_0^2 + 1}{3 - a_0^2}$$

and since $a_0^2 \leq 1$,

$$M_0 > 1/(3 - a_0^2),$$

which is just the reverse of the condition in Eq. (19)

(ii) Considering -ve sign, we have

$$M_0 < 1/(3 - a_0^2),$$

which is the condition in Eq. (19) for physical solution,

Hence -ve sign conforms to physical solution.

Thus we have the dimensionless expression for the mass of the composite sphere as

$$M_0 = \left[1 + \frac{1}{2} (3 - 2a_0^2) \right] / R_0^2 - \left[\left\{ 1 + \frac{1}{2} (3 - 2a_0^2) \right\} / R_0^2 \right]^2 - (3 - a_0^2) / R_0^2 \Bigg]^{1/2} / (3 - a_0^2) \quad \dots(38)$$

or,

$$M_0 = \left[1 + m_0 (3 - 2a_0^2) / a_0^3 - \left[\left\{ 1 + m_0 (3 - 2a_0^2) / a_0^3 \right\} / a_0^3 \right]^2 - 2m_0 (3 - a_0^2) / a_0^3 \right]^{1/2} / (3 - a_0^2) \quad \dots(39)$$

where m is the mass of the central core and

$$m_0 = m/r_0 = \frac{1}{2} a_0^3 / R_0^2 \quad \dots(40)$$

(i) When

$$a_0 \geq 0, M_0 \leq \frac{1}{3} \left[1 + \frac{3}{2R_0^2} - \left\{ 1 + \left(\frac{3}{2R_0^2} \right) \right\}^{1/2} \right]$$

and

$$M_0 \leq 1/3, \text{ if } 3/R_0^2 = 8\pi \rho_c r_0^2 \geq 1.$$

(ii) When $a_0 \leq 1$, $M_0 \leq 1/2R_0^2$, i.e. $M_0 \geq m_0$.

6. Discussion

(i) The solution is free from singularity throughout the configuration under the specified conditions.

(ii) When $a = 0$, the solution stands for Tolman's fluid sphere No. IV, and when $a = r_0$, it stands for Schwarzschild's fluid sphere of constant density

(iii) From the Eqs. (16) and (24), the density ρ_a of the outer region at $r = a$ can be written as

$$8\pi \rho_a r_0^2 = \frac{M_0}{1 - 3M_0 + 2M_0 a_0^2} \times$$

$$\left[1 + 3 (1 - 3M_0 + M_0 a_0^2) + \frac{2 (1 - 3M_0) (1 - M_0 a_0^2)}{1 - 3M_0 + 2M_0 a_0^2} \right]$$

$$< \frac{M}{1 - 3M_0 + 2M_0 a_0^2} \left[1 + 3 (1 - 3M_0 + M_0 a_0^2) + 2 \right]$$

$$\therefore 8\pi \rho_c r_0^2 < 3/R_0^2$$

$$\text{, i.e. } \rho_a < \rho_c$$

Thus the density of the outer region at $r=a$ is less than the density of the core.

(iv) When M/r_0 and a/r_0 are given, the expression (24) gives the density of the central core. We observe from Table 1 and also from the conditions in Eqs. (31) and (36) that for large large values of $8\pi \rho_c r_0^2$, a_0 and also the limiting values of M_0 get smaller and both tend to the value $1/3$, when $8\pi \rho_c r_0^2$ tends to the value 5. With this model, we can construct models for massive stars with a dense central core and having a concentric envelope of some lower density.

Acknowledgement

One of the authors (P P) wishes to thank the Education Department, Government of West Bengal and the University Grant Commission, New Delhi, for financial support and help.

References

1. Oppenheimer J R & Volkoff G M, *Phys. Rev.*, **55** (1939), 374.
2. Tolman R C, *Phys. Rev.*, **55** (1939), 364.
3. Tolman R C, *Relativity thermodynamics and Cosmology*, (Oxford University Press, Oxford), 1950, 244-247.

Strong Coupling Harmonic Oscillator Potential with Weakly Coupled Linear & Cubic Anharmonicities

JYOTI CHOUBEY & L K SHARMA

Department of Applied Physics, Government Engineering College, Jabalpur 482 011

Received 29 December 1979

Large coupling expansions for eigen energies and Regge trajectories of the harmonic oscillator potential coupled weakly with linear and cubic anharmonicities, have been derived. It has been observed that rise of Regge trajectories is almost rapid for the polynomial interaction.

1. Introduction

Recently there has been a considerable revival of interest in the analytic properties of scattering amplitudes in the frame of quantum mechanics and potential theory. This interest is largely due to the fact that in potential theory many problems are solvable either exactly or else approximately by well-defined perturbation methods, whereas more ambitious fully relativistic theories often lead to unsurmountable difficulties. Moreover, the potential theory has served as an invaluable prototype of almost any kind of model theory in all branches of molecular, atomic, nuclear and elementary particle physics. Particularly in elementary particle physics the study of potential-like interactions has contributed substantially to a deeper understanding of the analytic behaviour of scattering amplitude, in general. For instance, both Regge-pole and Mandelstam theories emerged from and found their most rigorous justification in the potential theory.

Large coupling solutions to various problems arising in particle physics have, of late, attracted considerable interest, particularly in view of the desire to understand strong interaction of purely field-theoretic formulations. However, attempts in this direction were severely handicapped due to the fact that the relevant coupling parameter is larger by a factor of about 1000 compared to the fine structure constant of quantum electrodynamics. Non-relativistic wave equation for large coupling constants of the potential have been studied by several authors. Cheng *et al.*¹ discussed the approximate behaviour of Regge trajectories for the Yukawa potential. Iafrate and Mendelsohn^{2,3} and Zauderer⁴ investigated the large coupling energy values for the Yukawa potential. Other cases for which large coupling

solutions have been derived are the Gauss potential⁵ and its generalized form.⁶ Müller and Vahedi⁷ obtained complete large coupling expansions of energy eigen values and Regge trajectories for the generalized Yukawa potential. They have shown that for this potential for the large coupling expansion of the Regge trajectories, the zero-energy intercept may rise above 1. In physical theory, this may be taken to imply an upper limit for the possible value of the coupling constant. It is interesting, therefore, to study large coupling solution of more realistic models. Raghuwanshi and Sharma^{8,9} derived large coupling expansions for the eigen energies for the superposition of Kratzer and a general potential; and of inverse square and Yukawa potentials. Choubey and Sharma¹³ have formulated a large coupling constant perturbation technique for obtaining the solution of a double exponential potential, and have further suggested the possibility of using this procedure to solve certain singular potentials. Recently Bose¹¹ and Müller *et al.*¹² have presented most complete solutions of the Schrödinger equation for logarithmic and power potentials respectively. The method of solution adopted by these authors is very general and parallels the methods of solution of more complicated standard differential equations such as the Mathieu equation — as a comparison with the relevant literature (Dingle and Müller¹³, Aly *et al.*¹⁴) reveals. These authors have obtained high energy asymptotic expansions for the discrete eigen functions together with the corresponding asymptotic expansion for the eigen values. They have investigated the physical implication of the asymptotic expansions of the energy eigen values and Regge trajectories and have also discussed the relevance of the above investigation in particle spectroscopy.

In Sec. 2, we have derived the expansions for eigen energy and Regge trajectories for the superposition of harmonic oscillator potential with weakly coupled linear and cubic anharmonicities. The behaviour of the Regge trajectories for the potentials $(r^2 + r)$, $(r^2 + r^3)$ and polynomial interaction $(r^2 + r + r^3)$ for different values of quantum number n have also been shown in Fig. 1. In Sec. 3, uniformly convergent-expansions for the solutions have been derived and their relevance for the scattering problem of the potential considered in this paper, has been discussed. In Sec. 4, we make some concluding remarks.

2. Calculation of Eigen Energies and Regge Trajectories

We consider the radial Schrödinger equation

$$\left[\frac{d^2}{dr^2} + \frac{2\mu k^2}{\hbar^2} - \frac{l(l+1)}{r^2} - \frac{2\mu}{\hbar^2} V(r) \right] \psi = 0 \quad \dots(1)$$

with the following potential

$$V(r) = g_1 r + g_2 r^2 + g_3 r^3$$

where $g_2 > 0$ and g_1 and g_3 are both < 1 . Here as usual $\mu = m_1 m_2 / (m_1 + m_2)$ is the reduced mass of the two particles and r is their separation. Our first aim is to derive the Regge trajectory expansion.

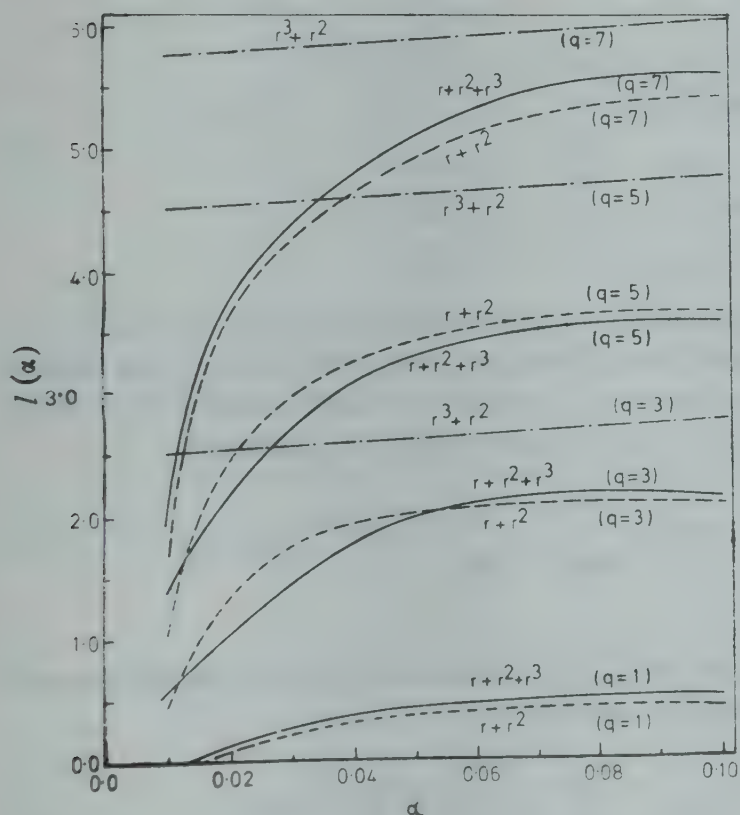


Fig. 1—Regge trajectories for the strong coupling harmonic oscillator potential with weakly coupled linear cubic anharmonicities for different values of q ($q = 2n + 1$)

On substituting Eq. (2) in Eq. (1) and on rearrangement of terms, one gets

$$\frac{d^2 \psi}{dr^2} + \left[\alpha - \frac{\gamma}{r^2} - \beta r - \delta r^2 - \eta r^3 \right] \psi = 0 \quad \dots(3)$$

where we have set

$$\alpha = \frac{2\mu k^2}{\hbar^2}, \beta = \frac{2\mu g_1}{\hbar^2}, \delta = \frac{2\mu g_2}{\hbar^2}, \eta = \frac{2\mu g_3}{\hbar^2} \quad \text{and } \gamma = l(l+1) = L^2 - 1/4 \quad \dots(4)$$

on further setting

$$r = e^z \text{ and } \psi = e^{z/2} \phi \quad (-\infty < z < \infty) \quad \dots(5)$$

yields

$$\frac{d^2 \phi}{dz^2} + \left[-L^2 + v(z) \right] \phi = 0 \quad \dots(6)$$

$$\text{where } v(z) = \alpha e^{2z} - \beta e^{3z} - \delta e^{4z} - \eta e^{5z} \quad \dots(7)$$

We now determine the value of z say z_0 for which $v(z)$ becomes maximal. In the neighbourhood of this maximum, $[v(z) - L^2]$ may become positive there by making the solutions oscillatory as needed for the existence of eigen values. Hence setting

$$\left(\frac{dv}{dz} \right)_{z=z_0} = 0 \text{ and solving for } z_0, \text{ one gets}$$

$$z_0 = \log \left[\frac{\alpha}{2\delta} - \left\{ 3\beta \left(\frac{\alpha}{2\delta} \right)^{1/2} + 5\eta \left(\frac{\alpha}{2\delta} \right)^{3/2} \right\} \frac{1}{4\delta} \right]^{1/2} \quad \dots(8)$$

Expanding $v(z)$ in the vicinity of the maximum at z_0 gives

$$v(z) = v(z_0) + \sum_{i=2}^{\infty} \frac{(z-z_0)^i}{i!} v^{(i)}(z_0) \quad \dots(9)$$

where $i = 0, 1, 2, \dots$

$$v^{(i)}(z_0) = 2^i \alpha e^{2z_0} - 3^i \beta e^{3z_0} - 4^i \delta e^{4z_0} - 5^i \eta e^{5z_0} \quad \dots(10)$$

For $i = 0$, this expression is positive, for $i = 1$, it is zero and for $i > 1$ it is negative [as required for a maximum of $v(z)$ at $z = z_0$ for $k^2 > 0$].

Putting $h = \{-2v^2(z_0)\}^{1/4}$

$$\text{i.e. } h^4 = \frac{4\alpha^2}{\delta} - 18\beta \left(\frac{\alpha}{2\delta} \right)^{3/2} - 10\eta \left(\frac{\alpha}{2\delta} \right)^{5/2} \quad \dots(11)$$

and

$$h^2 = \frac{2\alpha}{\sqrt{\delta}} \left[1 - \frac{9\beta\delta}{4\alpha^2} \left(\frac{\alpha}{2\delta} \right)^{3/2} - \frac{5\eta\delta}{4\alpha^2} \left(\frac{\alpha}{2\delta} \right)^{5/2} \right] \quad \dots(11a)$$

Now changing the independent variable in Eq. (6) to $\omega = h(z - z_0)$... (12)

gives

$$\frac{d^2 \phi}{d\omega^2} + \left[\frac{-L^2 + v(z_0)}{h^2} - \frac{\omega^2}{4} \right] \phi = \sum_{i=3}^{\infty} \left[\frac{v^{(i)}(z_0)}{2v^{(2)}(z_0)} \right] \frac{\omega^i}{i! h^{i-2}} \phi \quad \dots (13)$$

where

$$\frac{v^{(i)}(z_0)}{v^{(2)}(z_0)} = \frac{2^i \alpha e^{2z_0} - 3^i \beta e^{3z_0} - 4^i \delta e^{4z_0} - 5^i \eta e^{5z_0}}{2^2 \alpha e^{2z_0} - 3^2 \beta e^{3z_0} - 4^2 \delta e^{4z_0} - 5^2 \eta e^{5z_0}} \quad \dots (14)$$

In particular for $i = 3, 4$

$$\frac{v^{(3)}(z_0)}{v^{(2)}(z_0)} = 6 - \frac{3\beta}{4\alpha} \left(\frac{\alpha}{2\delta} \right)^{1/2} + \frac{15\eta}{4\alpha} \left(\frac{\alpha}{2\delta} \right)^{3/2} \quad \dots (15)$$

and

$$\frac{v^{(4)}(z_0)}{v^{(2)}(z_0)} = 28 - \frac{27\beta}{4\alpha} \left(\frac{\alpha}{2\delta} \right)^{1/2} + \frac{165\eta}{4\alpha} \left(\frac{\alpha}{2\delta} \right)^{3/2} \quad \dots (16)$$

For large value of h , the right hand side of Eq. (13) can to a first approximation be neglected. The corresponding behaviour of the eigen values $1/h^2 [-L^2 + v(z_0)]$ can then be determined by comparing the equation with the equation of parabolic cylinder functions. The solutions are square-integrable only if

$$1/h^2 [-L^2 + v(z_0)] = 1/2 q$$

where q is an odd integer, i.e. $q = (2n+1)$, $n = 0, 1, 2, \dots$

$$\text{and setting } \frac{1}{h^2} [-L^2 + v(z_0)] = \frac{1}{2} q + \frac{\Delta}{h} \quad \dots (17)$$

for obtaining the complete solution of Eq. (13).

Now the value of Δ in Eq. (17) remains to be determined. Substituting Eq. (14) into Eq. (13) one gets

$$D_q \phi = \frac{2\Delta}{h} \phi - \sum_{i=3}^{\infty} \left\{ \frac{v^{(i)}(z_0)}{v^{(2)}(z_0)} \right\} \frac{\omega^i}{i! h^{i-2}} \phi \quad \dots (18)$$

where

$$D_q = -2 \frac{d^2}{d\omega^2} - q + \frac{1}{2} \omega^2 \quad \dots (19)$$

To solve Eq. (18), the perturbation procedure formulated by Müller *et al*¹² is adopted. One gets to first approximation $\phi = \phi^{(0)}$ which is simply a parabolic cylinder function $D_{(q-1)/2}(\omega)$, i.e.

$$\phi^{(0)} = \phi_0 = D_{(q-1)/2}(\omega), \quad D_q \phi_0 = 0 \quad \dots (20)$$

where $D_{(q-1)/2}(\omega) = 2^{(q-3)/4} \exp(-\omega^2/4)$

$$\psi \left(\frac{3-q}{4}, \frac{3}{2}, \frac{\omega^2}{4} \right),$$

ψ being a confluent hypergeometric function. The function ϕ_q is well known to obey the recurrence formula

$$\omega \phi_q = (q, q+2) \phi_{q+2} + (q, q-2) \phi_{q-2} \quad \dots (21)$$

where $(q, q+2) = 1$, $(q, q-2) = 1/2 (q-1) \dots$ (22) for higher powers one has

$$\omega^i \phi_q = \sum_{j=2i}^{-2i} S_i(q, j) \phi_{q+j} \quad \dots (23)$$

and a recurrence relation can be written down for the coefficients S_i . The first approximation $\phi = \phi^{(0)}$ then leaves uncompensated terms amounting to

$$\begin{aligned} R_q^{(0)} &= \left[\frac{2\Delta}{h} - \sum_{i=3}^{\infty} \left\{ \frac{v^{(i)}(z_0)}{v^{(2)}(z_0)} \right\} \frac{\omega^i}{i! h^{i-2}} \right] \phi_q(\omega) \\ &= \frac{2\Delta}{h} \phi_q - \sum_{i=3}^{\infty} \frac{1}{h^{i-2}} \sum_{j=2i}^{-2i} \tilde{S}_i(q, j) \phi_{q+j}(\omega) \end{aligned} \quad \dots (24)$$

where

$$\tilde{S}_i(q, j) = \frac{v^{(i)}(z_0)}{v^{(2)}(z_0)} \frac{1}{i!} S_i(q, j) \quad \dots (25)$$

Rewriting Eq. (24) in the form

$$R_q^{(0)} = \sum_{i=3}^{\infty} \frac{1}{h^{i-2}} \sum_{j=2i}^{-2i} [q, q+j]_i \phi_{q+j}(\omega) \quad \dots (26)$$

where $[q, q]_3 = 2\Delta - \tilde{S}_3(q, 0)$

and for $j \neq 0$

$$[q, q+j]_3 = -\tilde{S}_3(q, j)$$

and for $i > 3$, $-2i \leq j \leq 2i$,

$$[q, q+j]_i = -\tilde{S}_i(q, j)$$

Since $D_{q+j} = D_{q-j}$, $D_q \phi_{q+j} = j \phi_{q+j}$, a term $\mu \phi_{q+j}$ in $R_q^{(0)}$ can be removed by adding to $\phi^{(0)}$ the contribution $\mu \phi_{q+j}/j$ except, of course, when $j = 0$. Thus the next order contribution of ϕ becomes

$$\phi^{(1)} = \sum_{i=3}^{\infty} \frac{1}{h^{i-2}} \sum_{\substack{j \neq 0 \\ j=2i}}^{-2i} \frac{[q, q+j]_i}{j} \phi_{q+j}(\omega) \quad \dots (28)$$

In its turn, this contribution leaves uncompensated terms amounting to

$$R_q^{(1)} = \sum_{i=3}^{\infty} \frac{1}{h^{i-2}} \sum_{\substack{j \neq 0 \\ j=2i}}^{-2i} \frac{[q, q+j]_i}{j} R_{q+j}^{(0)} \quad \dots (29)$$

and yields then the next contribution of ϕ :

$$\phi^{(2)} = \sum_{i=3}^{\infty} \frac{1}{h^{i-2}} \sum_{\substack{j \neq 0 \\ j=2i}}^{-2i} \frac{[q, q+j]_i}{j} \sum_{i=3}^{\infty} \frac{1}{h^{i-2}} \times \sum_{\substack{j=2i \\ j+j' \neq 0}}^{-2i} \frac{[q+j, q+j+j']_{i'}}{j+j'} \phi_{q+j+j'} \quad \dots(30)$$

Proceeding in this way, one obtains the solution

$$\phi = \phi^{(0)} + \phi^{(1)} + \phi^{(2)} + \dots,$$

which is an asymptotic expansion in descending powers of h valid for

$$z - z_0 = 0 \quad (1/h) \quad \dots(31)$$

that is around $z = z_0$. However, the sum of contributions $\phi^{(0)} + \phi^{(1)} + \phi^{(2)} + \dots$ is a solution only if the terms in $R^{(0)}_q, R^{(1)}_q, \dots$ (left uncompensated so far) are set equal to zero. Thus

$$0 = \sum_{i=3}^{\infty} \frac{1}{h^{i-2}} [q, q]_i + \sum_{i=3}^{\infty} \frac{1}{h^{i-3}} \sum_{\substack{j=2i \\ j \neq 0}}^{-2i} \frac{[q, q+j]_i}{j} \times \sum_{i'=3}^{\infty} \frac{1}{h^{i'-2}} [q+j, q]_{i'} + \dots$$

or

$$0 = \frac{1}{h} [q, q]_3 + \frac{1}{h^2} \left\{ [q, q]_4 + \sum_{\substack{j=6 \\ j \neq 0}}^{-6} \frac{[q, q+j]_3}{j} [q+j, q]_3 \right\} + 0 \left(\frac{1}{h^3} \right) \dots(32)$$

This is the equation from which Δ and hence the eigen values are determined. Using Eq. (27), one gets the following expression for

$$2 h \Delta = \left[\tilde{S}_4(q, 0) - \frac{1}{6} \tilde{S}_3(q, 6) \tilde{S}_3(q+6, -6) + \frac{1}{6} \tilde{S}_3(q, -6) \tilde{S}_3(q-6, +6) - \frac{1}{2} \tilde{S}_3(q, +2) \tilde{S}_3(q+2, -2) - \frac{1}{2} \tilde{S}_3(q, -2) \tilde{S}_3(q-2, 2) + 0 \left(\frac{1}{h^2} \right) \right] \dots(33)$$

Thus

$$2 h \Delta = \frac{(q^2+1)}{2^4} \left[28 - \frac{27\beta}{4\alpha} \left(\frac{\alpha}{2\delta} \right)^{1/2} + \frac{165\eta}{4\alpha} \right]$$

$$\left(\frac{\alpha}{2\delta} \right)^{3/2} \left] - \frac{(15q^2+7)}{2^4 \cdot 3^2} \left[6 - \frac{3\beta}{4\alpha} \left(\frac{\alpha}{2\delta} \right)^{1/2} + \frac{15\eta}{4\alpha} \left(\frac{\alpha}{2\delta} \right) \right] + 0 \left(\frac{1}{h^2} \right) \quad \dots(34)$$

Utilizing Eqs. (4), (14) and (17), yield

$$\left(l + \frac{1}{2} \right)^2 = \frac{\alpha^2}{4\delta} - \beta \left(\frac{\alpha}{2\delta} \right)^{3/2} - \eta \left(\frac{\alpha}{2\delta} \right)^{5/2} - \frac{1}{2} q h^2 + q^2 - \frac{\beta}{8\alpha} \left(\frac{\alpha}{2\delta} \right)^{1/2} \times \left\{ \frac{33q^2+1}{2^4} \right\} - \frac{\eta}{8\alpha} \left(\frac{\alpha}{2\delta} \right)^{3/2} \times \left\{ \frac{25-139q^2}{2^4} \right\} + 0 \left(\frac{1}{h^2} \right) \quad \dots(35)$$

Setting $\beta = \eta = 0$ in the expression of Eq. (35) gives the following Regge trajectory expansion for the harmonic oscillator potential, i.e. for $v(r) = g_2 r^2$

$$\left(l + \frac{1}{2} \right)^2 = \frac{h^4}{2^4} - \frac{1}{2} q h^2 + q^2 + 0 \left(\frac{1}{h^2} \right) \quad \dots(36)$$

The expression (36) is in exact agreement with the result obtained by Müller *et al.*¹² by putting $\lambda = 2$ in his equation (33 a).

3. Uniformly Convergent Solutions and the Scattering Problem

For the extension of our analysis it is useful and desirable to have yet another type of solution. For this reason, we now derive an expansion which is uniformly convergent for finite values of h .

We start with Eq. (6)

$$\frac{d^2 \phi}{dz^2} - L^2 \phi = (\eta e^{5z} + \delta e^{4z} + \beta e^{3z} - \alpha e^{2z}) \phi \quad \dots(37)$$

$$\text{Setting } \phi = e^{\pm Lz} f(z) \quad \dots(38)$$

We find that f satisfies the following equation

$$\frac{d^2 f}{dz^2} \pm 2L \frac{df}{dz} = \alpha e^{2z} \left[\frac{\eta}{\alpha} e^{3z} + \frac{\delta}{\alpha} e^{2z} + \frac{\beta}{\alpha} e^z - 1 \right] f \quad \dots(39)$$

From now on, we consider only the + part of the L.H.S. of Eq. (39). The solution of the -ve part of equation then follows by changing the sign of L . We solve Eq. (39) by iteration. Thus, if f_L is the solution of

$$\frac{d^2 f_L}{dz^2} + 2L \frac{df_L}{dz} = 0$$

we have $f_L = \text{constant}$ or $f_L \propto e^{-2Lz}$

We take the first of these alternatives, because the second form leads to $\phi e^{-Lz} f$. Ignoring an overall

constant, we take $f_L = 1$, and set

$$f = 1 + \sum_{i=1}^{\infty} \alpha^i f_i \quad \dots(40)$$

where f_i is the solution of

$$\frac{d^2 f_i}{dz^2} + L \frac{df_i}{dz} = e^{2z} \left[\frac{\eta}{\alpha} e^{3z} + \frac{\delta}{\alpha} e^{2z} + \frac{\beta}{\alpha} e^z - 1 \right] f_{i-1} \quad \dots(41)$$

Solving for f_i we set $f_i = e^{2z} G_1(z)$ and then

$$G_1(z) = e^{2z} H_1 - \frac{1}{4(L+1)} \quad \dots(42)$$

Solving the resulting equation for H_1 we find

$$H_1 = \frac{(\beta/\alpha) e^{-x} + (\delta/\alpha) + (\eta/\alpha) e^x}{(8L+16)} \quad \dots(43)$$

$$\text{and } f_1 = \left[\frac{(\beta/\alpha) e^{3z} + (\delta/\alpha) e^{4z} + (\eta/\alpha) e^{5z}}{(8L+16)} - \frac{e^{2z}}{4(L+1)} \right] \quad \dots(44)$$

Proceeding in this way we obtain the solution

$$f = 1 + \left[\frac{\beta e^{3z} + \delta e^{4z} + \eta e^{5z}}{(8L+16)} - \frac{\alpha e^{2z}}{4(L+1)} \right] \left[\frac{\beta^2 e^{6z} + \delta^2 e^{8z} + \eta^2 e^{10z}}{64(L+4)(2L+4)} + \frac{\alpha^2 e^{4z}}{32(L+1)(L+2)} - \frac{\alpha \beta e^{5z} + \alpha \delta e^{6z} + \alpha \eta e^{7z}}{6(L+6)} \left\{ \frac{1}{4(L+1)} + \frac{1}{4(2L+4)} \right\} \right] + 0(\beta^3, \eta^3, \delta^3) \quad \dots(45)$$

As pointed out earlier, a second solution is obtained by reversing the sign of L , or by replacing l by $(-l-1)$. The solution $\phi = e^{Lz} f(z)$ is obviously the so called regular solution.

We now sum the terms containing leading powers of z , i.e. terms in $\alpha, \alpha^2, \alpha^3, \dots$ or terms in $\beta, \beta^2, \beta^3, \dots$, summing the terms in $\alpha, \alpha^2, \alpha^3, \dots$ we obtain:

$$f \rightarrow f^{(\alpha)} = L(!) J_L(\alpha^{1/2} e^z) \left| \left(\frac{1}{2} \alpha^{1/2} e^z \right)^L \right| \quad \dots(46)$$

and summing the terms in $\beta, \beta^2, \beta^3, \dots$ we obtain

$$f \rightarrow f^{(\beta)} = \left(\frac{L}{2} \right)! I_{L/2} \left(\pm \frac{\beta^{1/2} e^{3z/2} + \delta^{1/2} e^{2z} + \eta^{1/2} e^{5z/2}}{2} \right) \left[\pm 1/2 \{ \beta^{1/2} e^{3z/2} + \delta^{1/2} e^{2z} + \eta^{1/2} e^{5z/2} \} \right]^{1/2} \quad \dots(47)$$

where J and I are Bessel functions of real and imaginary argument respectively. In each case, an overall multiplicative constant has been ignored. The expression (46) is independent of the potential and so tells us simply that in this case the solution can be expressed as a Bessel function. The expression (47) on the other hand, gives us the behaviour of

the wave function for $z \rightarrow \infty$ and so for $r \rightarrow \infty$. The function I_n has the following asymptotic behaviour

$$I_n(x) = \frac{e^x}{(2\pi x)^{1/2}} \left[1 + O\left(\frac{1}{x}\right) \right]$$

Considering only the dominant term of this expansion and the leading terms summed by Eq. (47), we have (inserting a constant N)

$$\psi(r) \simeq$$

$$\frac{N \left(\frac{L}{2} \right)! \exp \left(\pm \frac{\beta^{1/2} (r^{3/2}) + \delta^{1/2} r^2 + \eta^{1/2} (r^{5/2})}{2} \right)}{\left(\pm \frac{\beta^{1/2} + \delta^{1/2} + \eta^{1/2}}{4} \right) \left[\pi \left\{ \beta^{1/2} r^{1/2} + \delta^{1/2} r + \eta^{1/2} r^{3/2} \right\} \right]^{1/2}} \quad \dots(48)$$

The expression with the minus sign gives the asymptotic behaviour of the bound state wave function. This expression is independent of the energy parameter and thus indicates that the set of discrete states is complete, i.e. there are no scattering solutions. However, if the potential is cut off at some finite distance R_0 , the asymptotic behaviour of ψ is no longer given by Eq. (48) and scattering becomes possible. In fact, requiring the wave function to be continuous at R_0 , the S -matrix is

$$S = e^{-ikR_0} \frac{d\psi_R(R_0)/dr + ik\psi_R(R_0)}{d\psi_R(R_0)/dr - ik\psi_R(R_0)} \quad \dots(49)$$

where $\alpha = k^2$ and the subscript R indicates that the solution used is the regular solution discussed above. The Jost function $f_+(k) = f_-(e^{-i\pi k})$ is given by

$$f_+(k) = e^{ikR_0} \left(\frac{d\psi_R(R_0)}{dr} - ik\psi_S(R_0) \right) \quad \dots(50)$$

By reducing Eq. (48) for harmonic oscillator potential we get

$$\psi(r) \simeq \frac{N \left(\frac{L}{2} \right)! \exp \left(\pm \frac{\delta^{1/2} r^2}{2} \right)}{\left(\pm \frac{\delta^{1/2}}{4} \right)^{L/2} \left(\pi \delta^{1/2} \right)^{1/2} \cdot r^{1/2}} \quad \dots(51)$$

This expression agrees with the result obtained by Muller *et al.*¹² for harmonic oscillator potential ($\lambda = 2$).

4. Conclusion

In the foregoing, we have investigated the radial Schrödinger equation for the superposition of a strong coupling harmonic oscillator potential with weakly coupled linear and cubic anharmonicities. In particular, expansions for Regge trajectories for the following combinations have been investigated: (i) $r^2 + r$, (ii) $r^2 + r^3$ and (iii) $r^2 + r + r^3$, and their behaviour have been depicted graphically in Fig. 1.

It is observed from Fig. 1 that rise in Regge trajectories is more rapid for the polynomial interaction ($r^2 + r + r^3$) than for the case of ($r^2 + r$) interaction. The interaction ($r^2 + r^3$), however, gives only a gradual rise for these trajectories.

On comparing the Regge trajectory curves for ($r^2 + r$) and ($r^2 + r^3$) interactions, it is seen that with increase in anharmonicity, the rise becomes gradual.

Acknowledgement

The authors are grateful to Prof. H J W Müller-Kirsten for many useful suggestions. One of them (JC) is thankful to the University Grants Commission, New Delhi, for the award of a fellowship.

References

1. Cheng H & Wu T T, *Regge poles for large coupling constants II*, DESY Preprint 11/31 (unpublished), 1971.
2. Iafate G J & Mendelsohn L B, *Phys. Rev.*, **182** (1969), 244.
3. Iafate G J & Mendelsohn L B, *Phys. Rev.*, **2A** (1970), 561.
4. Zauderer E, *J. math. Phys.*, **13** (1972), 42.
5. Müller H J W, *J. math. Phys.*, **11** (1970), 355.
6. Sharma L K, Choubey J & Müller H J W, *J. Math. Phys.*, **21** (6), (1980), 1533.
7. Müller H J W & Faridi N Vahedi, *J. math. Phys.*, **14** (1973), 1291.
8. Raghuwanshi S S & Sharma L K, *Indian J. Phys.*, **52B** (1978a) 410.
9. Raghuwanshi S S & Sharma L K, *Indian J. Phys.*, **52B** (1978b) 19.
10. Choubey J & Sharma L K, *Pramana*, **9** (1977), 303.
11. Bose S K & Müller H J W, *Solutions of the wave equation for the logarithmic potential with application to particle spectroscopy*, Preprint, Kaiseralautern University, 1978.
12. Müller H J W, Hite C E & Bose S K, *Explicit solutions of the wave equation for arbitrary power potentials with applications to charmonium spectroscopy*, Preprint, Kaiseralautern University, 1978.
13. Dingle R B & Müller H J W, *J. reine. angew. Math.*, **211** (1962), 11.
14. Aly H H, Müller H J W & Faridi, N Vahedi, *J. Math. Phys.*, **16** (1975), 961.

Analysis of Proton-Proton Elastic Scattering at High Energies

FAZAL-E-ALEEM

Department of Physics, Punjab University, New Campus, Lahore, Pakistan

Received 10 December 1979; revised received 3 May 1980

The angular distribution, total cross-section and dip structure in high energy pp elastic scattering between $23 \leq \sqrt{s} \leq 62$, including the most recent differential cross-section measurements at $\sqrt{s} = 19.4$ and 27.4 GeV with $-t$ extending up to 14 (GeV/c)², have been explained with dipole pomeron model.

1. Literature Survey on pp-Elastic Scattering

The proton-proton elastic scattering at high energy is known to be one of the best measured but most-elusive problems in high energy physics. The measurements of differential and total cross-sections have been made¹⁻⁷ up to $\sqrt{s}=62$ GeV and for $-t$ extending up to nearly 14 (GeV/c)². Figs. 1 to 6 show the differential cross-section measurement at $\sqrt{s} = 19.4, 23, 27.4, 44.9, 53$ and 62 GeV while Fig. 7 shows the total cross-section measurements in the high energy region up to $\sqrt{s} = 62$ GeV. Figs. 1-7 exhibit the following important characteristics of the data.

1. A pronounced dip moving inwards with increasing energy. The differential cross-section at the dip rises with energy.
2. A bump at $-t \approx 1.8$ (GeV/c)² approximately six orders of magnitude below the optical point. The differential cross-section at the bump also rises with energy.
3. A smooth fall off beyond the bump which continues without showing any indication of the second diffraction minimum in $d\sigma/dt$ up to $-t \approx 14$ (GeV/c)². The value of $d\sigma/dt$ at $-t \approx 14$ (GeV/c)² is approximately 10 orders of magnitude below the optical point.
4. A rising total cross-section.

The conventional Regge models^{8,9} when applied to pp elastic scattering do not lead to a structure in differential cross-section $d\sigma/dt$. The qualitative description of pp elastic scattering at high energies is given by Chou and Yang¹⁰ and Durand and Lipes,¹¹ but their models do not involve any energy dependence. Buras and Deus¹² as well as Henzi and Valin¹³ have tried to explain the pp differential cross-section data by using the idea of geometrical scaling but the agreement in the vicinity of the dip is not good. Gotsman and Maor¹⁴ have tried to improve the geometrical model for pp elastic scat-

tering by parameterizing the data with a more complicated form but still fail to explain the dip structure quantitatively. Ng and Sukhatme¹⁵ and Pajares and Schiff¹⁶ have explained one or more characteristics of high energy elastic pp scattering by employing Gribov's reggeon calculus^{17,19}. Saleem *et al.*²⁰ and Kamran and Saleem²¹ have explained many features of high energy pp elastic scattering on dual absorptive model with peripheral pomeron. Phillips and Barger²² have made an empirical study of pp elastic scattering in terms of two experimental amplitudes plus interference. Araki *et al.*²³ have tried to give an explanation with a model based upon van der waals equation of state. It has been claimed that with this model, which strongly suggests the existence of a kind of a phase transition in the pp elastic scattering, the second dip is absent even up to $-t \approx 10$ (GeV/c)². However, over the entire range, the agreement between theory and experiment is only qualitative. Moreover, beyond $\sqrt{s} = 72$ GeV, it predicts a structure in angular distribution which is quite different from the structure at presently available energies. Attempt by Shiohara and Yano²⁴ to improve the model based on VDW type equation has not succeeded. Saleem and Fazal-e-Aleem²⁵ have modified this model and explained the differential cross-section results in the domain $0 \leq -t \leq 9$ (GeV/c)². In this paper, we will show that the aforementioned characteristics of pp elastic scattering can be explained on dipole pomeron model by using energy-dependent parameters.

2. General Characteristics of the Helicity Amplitudes

We will first consider some of the general characteristics of the helicity amplitudes for this reaction. The pp \rightarrow pp scattering is $\frac{1}{2} + \frac{1}{2} \rightarrow \frac{1}{2} + \frac{1}{2}$ process. The total number of helicity amplitudes is sixteen. If the principles of conservation of

parity, time reversal and charge conjugation are made use of, then the number of independent helicity amplitudes reduces to five. The s -channel helicity amplitudes are given by :

$$\begin{aligned}
 \phi_1 &= \langle ++ | ++ \rangle = \langle -- | -- \rangle \\
 \phi_2 &= \langle -- | ++ \rangle = \langle ++ | -- \rangle \\
 \phi_3 &= \langle +- | +- \rangle = \langle -+ | -+ \rangle \\
 \phi_4 &= \langle +- | -+ \rangle = \langle -+ | +- \rangle \\
 \phi_5 &= \langle ++ | +- \rangle = \langle -- | -+ \rangle \\
 &= \langle -- | +- \rangle = \langle ++ | -+ \rangle \\
 &= \langle -+ | -- \rangle = \langle ++ | -- \rangle \\
 &= \langle -+ | ++ \rangle = \langle +- | -- \rangle
 \end{aligned}
 \left. \begin{array}{l} \text{helicity non-flip} \\ \text{double flip} \\ \text{single flip} \end{array} \right\}$$

The signs denote the helicities of the respective protons. In the s -channel, ϕ_1 , ϕ_2 and ϕ_3 correspond to non-helicity flip, ϕ_5 corresponds to single helicity flip and ϕ_4 to double helicity flip. It is useful to introduce the following linear combinations which correspond asymptotically to the exchange of definite quantum numbers in the t -channel:

$$N_0 \approx 1/2 (\phi_1 + \phi_3)$$

$$N_1 \approx \phi_5$$

$$N_2 \approx 1/2 (\phi_4 - \phi_2)$$

$$U_1 \approx 1/2 (\phi_1 - \phi_3)$$

$$U_2 \approx 1/2 (\phi_4 - \phi_2)$$

The subscripts of N and U gives the amount of t -channel helicity flip Δ which is given by

$$\Delta = |\lambda_1 - \lambda_3| + |\lambda_2 - \lambda_4|$$

Exchange of the Pomeron p , ω , f , ρ or A trajectories (natural parity exchange) can contribute to N_0 , N_1 and N_2 whereas U_1 corresponds to A -like exchange and U_2 to π and B exchange.

If the spin considerations are completely ignored, there would be only one helicity amplitude, T say, to represent the scattering process.

3. Dipole Pomeron Model

This is a model in which the pomeron is considered a dipole trajectory in the t -plane generated by coalescing to two single-pole trajectories for all t , such that the dipole amplitude can be obtained from the single-pole amplitude by differentiating with respect to $\alpha(t)$. The relevance of the double pomeron pole to diffraction phenomena has been emphasized by several authors.^{1,26-30} Jenkovszky and Wall³⁰

have tried to explain pp elastic scattering at high energy for $0 \leq -t < 4$ (GeV/c).² We reproduce their technique with some modification.

Neglecting spin, the scattering amplitude in this model can be written as

$$\begin{aligned}
 T(s, t) &= d/d\alpha [\exp(-i\pi\alpha/2) (s/s_0)^\alpha G(\alpha)] \\
 &= \exp(-i\pi\alpha/2) (s/s_0)^\alpha G'(\alpha) [1 + \phi(\alpha) \ln s/s_0 - i\pi/2 \phi(\alpha)] \dots(1)
 \end{aligned}$$

where $\alpha = \alpha(t)$ is the pomeron trajectory, s_0 is the scaling factor, $\phi(\alpha) = G(\alpha)/G'(\alpha)$ and the factor $1/\sin(\pi\alpha/2)$ has been absorbed in $G(\alpha)$. In Ref. 30, $\sin(\pi\alpha/2)$ has been taken as approximately constant. This is, however, not valid because $\alpha(t)$ varies from 1 to -1 as $-t$ goes from zero to 8 (GeV/c)². From the structure of Eq. (1), we note that the first term gives the contribution from the simple pole, $G'(\alpha) \sin(\pi\alpha/2)$ being the residue at this pole. The function $G'(\alpha)$ is assumed to fall exponentially. If we take the pomeron trajectory as linear, $\alpha(t) = \alpha_0 + \alpha' t$, we may write

$$G'(z) = A \exp[b\{\alpha(t) - \alpha_0\}] = A \exp(b\alpha' t) \dots(2)$$

where A and b are free parameters to be fixed from experiment. The function $G(\alpha)$ is obtained by integrating the above equation:

$$G(\alpha) = A/b \exp(b\alpha' t) + \gamma \dots(3)$$

where γ is a constant. From Eqs. (2) and (3), we get

$$\phi(\alpha) = \frac{G(\alpha)}{G'(\alpha)} = \frac{1}{b} + \frac{\gamma}{A \exp(-b\alpha' t)}$$

The parameter γ can be determined from the condition

$$\phi[\alpha(t=0)] = \lambda$$

By using the norm

$$\frac{d\sigma}{dt} = \frac{s_0^2}{s^2} |T(s, t)|^2$$

We get the following form for the differential cross-section:

$$\begin{aligned}
 \frac{d\sigma}{dt} &= \left(\frac{s}{s_0}\right)^{2\alpha-2} G'(\alpha) \left[\left\{ 1 + \phi(\alpha) \ln(s/s_0) \right\}^2 + \frac{\pi^2}{4} \phi^2(\alpha) \right] \\
 &= A^2 \exp \left[2\alpha' \left\{ b + \ln(s/s_0) \right\} t \right] \\
 &\quad \left[\left(1 + \left\{ \frac{1}{b} + \left(\lambda - \frac{1}{b} \right) \exp(-b\alpha' t) \right\} \ln s/s_0 \right)^2 + \frac{\pi^2}{4} \left\{ \frac{1}{b} + \left(\lambda - \frac{1}{b} \right) \exp(-b\alpha' t) \right\}^2 \right] \text{mb} \\
 &\quad \text{(GeV/c)}^2
 \end{aligned}$$

4. Results and Discussion

In Ref. 30, the values of α , α' , b_0 and λ have been taken as 1.0, $0.25 \text{ (GeV/c)}^{-2}$, 12.0 and 0.7 respectively. They, however, do not give results consistent with experiment. This can be easily seen as follows.

For large and small values of $-t$, the behaviour of $d\sigma/dt$ is determined by $\exp(2\alpha't \ln s/s_0)$ and $\exp[2\alpha'(b + \ln s/s_0)t]$ respectively. If we take $s_0 = 1 \text{ GeV}^2$ and substitute the values of b and α' , these expressions reduce to $\exp(0.5 t \ln s)$ and $\exp[0.5(12 + \ln s)t]$. For $\sqrt{s} = 53 \text{ GeV}$, they yield $\exp(3.97 t)$ and $\exp(9.97 t)$ respectively. This is not consistent with experiment which gives $\exp(1.8 t)$ and $\exp(10.2 t)$ as approximate behaviour for the differential cross-section for large and small values of $-t$. Moreover, this formula predicts a dip at $-t = 0.92 \text{ (GeV/c)}^2$ which is in disagreement with experiment.

For $\sqrt{s} = 30.8$ to 62 GeV , a good fit with experiment is obtained by the following choice of parameters:³¹

$$\alpha_0 = 1, \alpha' = 0.21 \text{ (GeV/c)}^{-2}$$

$A = -8\sqrt{\text{mb}} \text{ (GeV/c)}^{-1}$; $s_0 = 50 \text{ GeV}^2$ and $\lambda = 0.04895$. However, the energy dependence is not correct at $\sqrt{s} = 19.4$ and 27.4 GeV where the measurements have been performed very recently. The differential cross-sections at these values of \sqrt{s} as calculated from this model, therefore, do not agree with experiment. It is interesting to note that this model predicts energy dependence of dip which moves slowly towards $t = 0$ as the energy increases. But the rate of movement of the position of the dip is not in agreement with the experimental data. Moreover, the differential cross-section at the dip is different from the experimental values. The same is true for the bump.

It has recently been asserted³² that a single (spin-averaged, non-flip) amplitude should be sufficient to explain the experimental data for pp elastic scattering at high energies and flip amplitudes cannot contribute significantly because large flip amplitudes usually give large polarization effects which are not present in this reaction. This argument is not convincing because if a single exchange trajectory dominates, then on the conventional Regge pole models the polarization would be zero irrespective of the magnitude of the flip amplitudes.

At high energy, the pomeron dominates the behaviour of the scattering process. Since, in the t -channel, U_1 and U_2 correspond to unnatural parity exchange, only three amplitudes N_0 , N_1 and N_2

would contribute to the differential cross-section. Neglecting the N_2 amplitude for simplicity and proceeding as shown above, the scattering amplitudes N_0 and N_1 in the dipole pomeron model can be written as:

$$N_0 = \exp(-i\pi\alpha/2) (s/s_0)^\alpha G'(\alpha) [1 + \phi(\alpha) \ln s/s_0 - i\pi/2 \phi(\alpha)]$$

and

$$N_1 = \sqrt{-t} \exp(-i\pi\alpha/2) (s/s_0)^\alpha G'(\alpha) [1 + \phi(\alpha) \ln s/s_0 - i\pi/2 \phi(\alpha)]$$

To take care of the dimensions, N_1 has to be divided by a mass factor. The differential cross-section is then given by

$$\frac{d\sigma}{dt} = \left(\frac{s_0}{s}\right)^2 (|N_0|^2 + |N_1|^2)$$

We find that a very good fit with experiment is obtained by using the energy-dependent parameters whose values are shown in Table 1. Figs. 1 to 6 show $d\sigma/dt$ plotted against $-t$ for $\sqrt{s} = 19.4, 23, 27.4, 44.9, 53$ and 62 GeV . The curves which represent the calculated values of $d\sigma/dt$ obtained from this model show that the agreement with experiment is good for $0 \leq -t < 14 \text{ (GeV/c)}^2$. This model predicts energy dependence of dip which moves slowly towards $t = 0$ as the energy increases. But the rate of movement of the position of the dip is not in agreement with experiment. It would be interesting to note that the van der Walls type model, the dual absorptive and the simple Regge pole model with phenomenological residue functions also predict movement of the dip position towards $t = 0$ with an increase in energy but the movement of the dip in the case of the last two models is not in accordance with experiment.

The experiment shows that from $\sqrt{s} = 19.4 \text{ GeV}$ upwards, the dip becomes shallower as energy in-

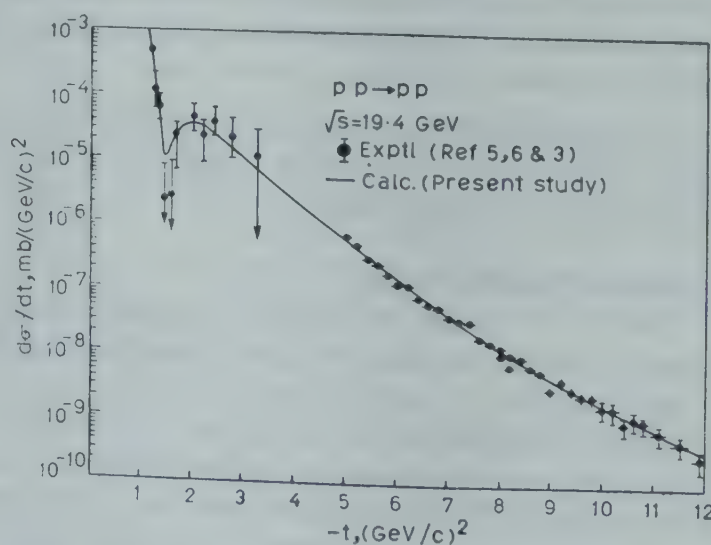


Fig. 1—Variation of $d\sigma/dt$ with $-t$ [$1 < -t \lesssim 14 \text{ (GeV/c)}^2$]

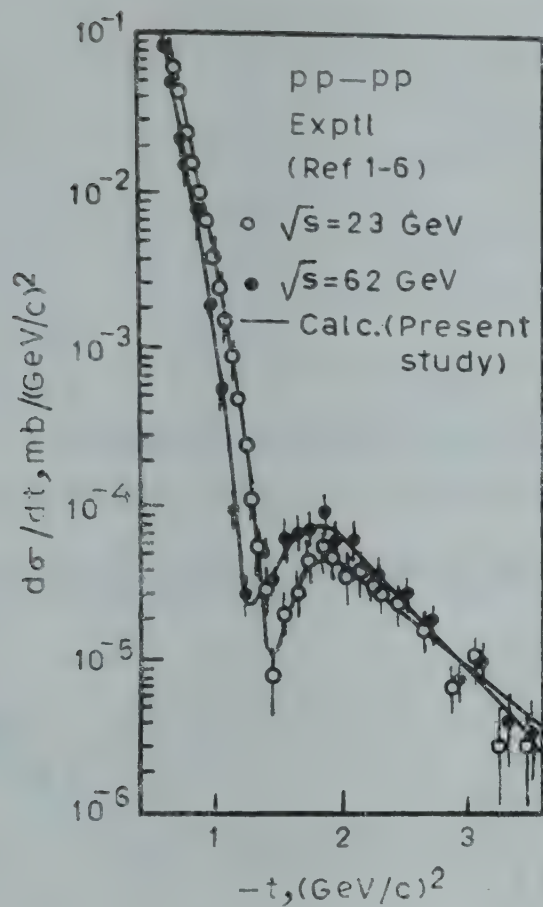


Fig. 2—Variation of $d\sigma/dt$ with $-t$ [$0.5 < -t \lesssim 3.5$ (GeV/c)²]

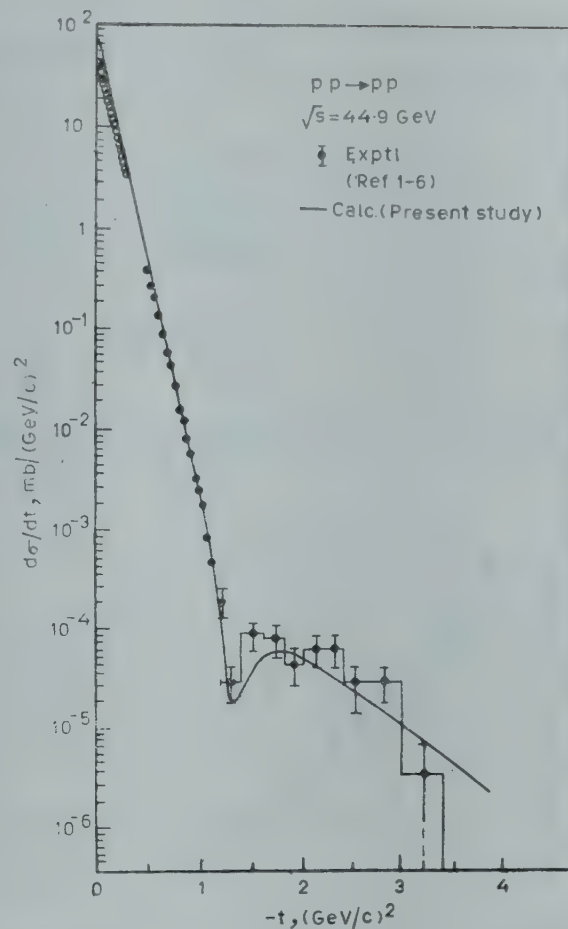


Fig. 4—Variation of $d\sigma/dt$ with $-t$ [$0 < -t \lesssim 3.5$ (GeV/c)²]

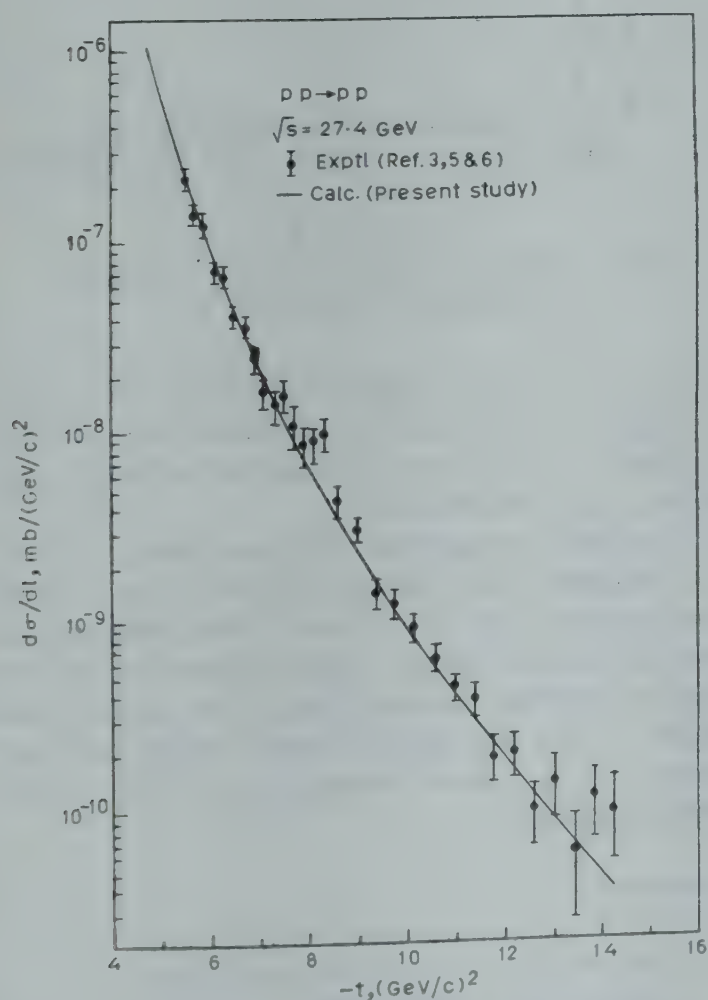


Fig. 3—Variation of $d\sigma/dt$ with $-t$ [$5.5 < -t \lesssim 14$ (GeV/c)²]

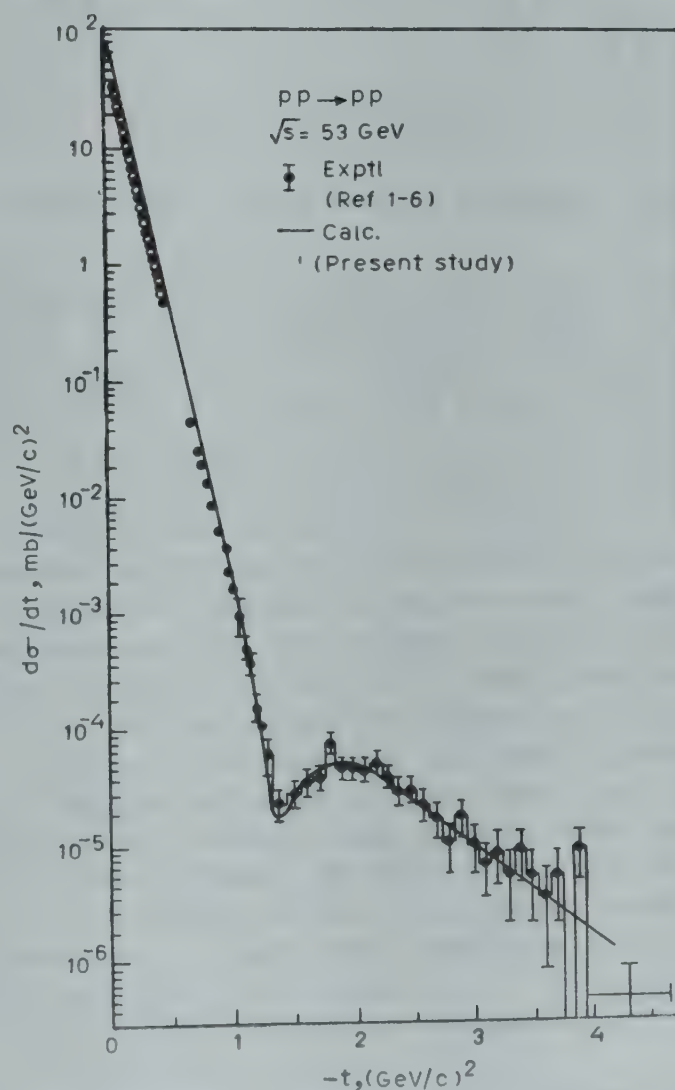


Fig. 5—Variation of $d\sigma/dt$ with $-t$ [$0 < -t \lesssim 3.5$ (GeV/c)²]

Table 1—Values of Energy-dependent Parameters ($s_0 = 10 \text{ GeV}^2$)

\sqrt{s}	b_0	λ_0	A_0^2	α'	b_1	λ_1	A_1^2
19.4	19.00	0.06162	54	0.21	-1.68	-0.5952	2.39×10^{-7}
23	21.56	0.04542	56	0.19	-0.178	-0.5618	2.45×10^{-7}
27.4	22.47	0.04344	57	0.182	-1.98	-0.5051	2.49×10^{-7}
44.9	23.66	0.04108	60	0.17	-1.48	-0.6757	2.7×10^{-6}
53	24.36	0.03992	62	0.165	-1.214	-0.8237	2.11×10^{-6}
62	26	0.03727	63	0.16	-0.952	-1.05	2.06×10^{-6}

The parameters b_0, λ_0, A_0 are associated with the amplitude N_0 while b_1, λ_1, A_1 are associated with the amplitude N_1 .

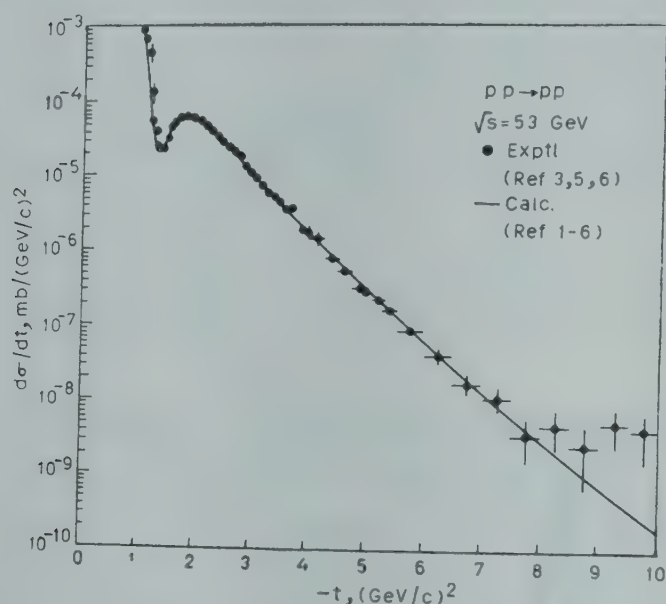


Fig. 6—Variation of $d\sigma/dt$ with $-t$ [$1 < -t \lesssim 14 \text{ (GeV/c)}^2$]

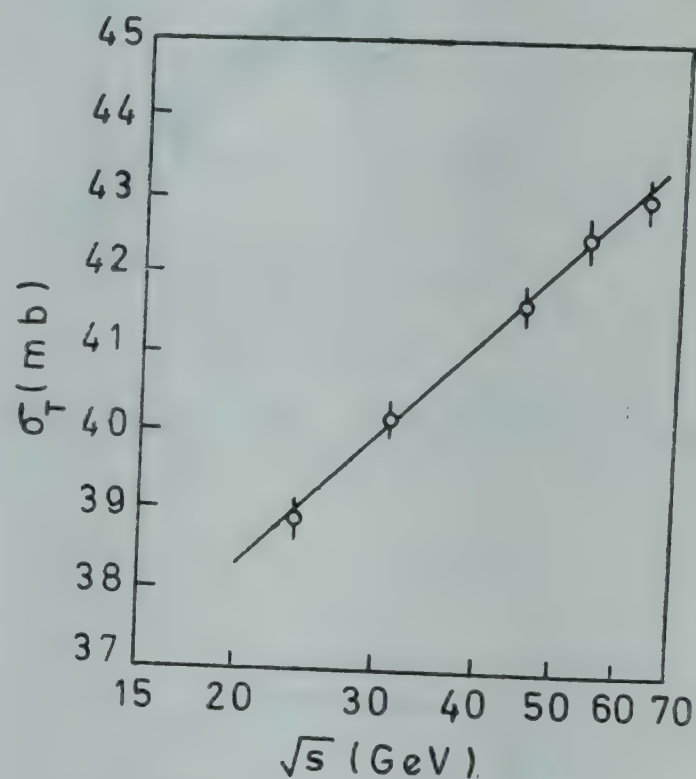


Fig. 7—Comparison of the calculated σ_T with the experimental values (Ref. 7)

creases. This result is exactly the same as calculated by using the dipole pomeron model. It would be interesting to compare the results regarding dip with those derived from other models. The van der Waals type model in which only the imaginary part of the scattering amplitude is taken into consideration predicts that in contradiction with experiment, the depth of the dip should increase with an increase in energy. Moreover, at high energies, the calculated $d\sigma/dt$ at the dip is smaller than the corresponding experimental value. This difference should be compensated by contribution from the real part of the scattering amplitude. However, it appears that at least up to the presently accessible energies, the major contribution to the differential cross-section at the dip comes from the imaginary part of the scattering amplitude, the real part making an insignificant contribution. In the case of the eikonal model or the model suggested by Shiohara and Yano, the imaginary part of the amplitude has a zero in the dip region and the non-vanishing real part gives the depth of the dip. In these models, it

is only if the real part happens to be energy dependent, and that too in a particular way, that the variation of the differential cross-section with energy at the dip can be explained.

The total cross-section results are shown in Fig. 7. The agreement between the calculated values and the experimental results is very good. It is interesting to note that without violating the Froissart bound, the Regge pole models cannot explain the rising cross-sections. This rise in σ_T at high energies, however, emerges as a natural consequence of the dipole pomeron model.

References

1. Kwak N et al., *Physics Lett.*, **58B** (1975), 233.
2. De Kerret H et al., *Physics Lett.*, **62B** (1976), 363.
3. De Kerret H et al., *Physics Lett.*, **68B** (1977), 374.
4. Akerlof C W et al., *Phys. Rev.*, **41D** (1976), 2864.

5. Hartmann J L *et al.*, *Phys. Rev. Lett.*, 39 (1977), 975.
6. Conetti S *et al.*, *Phys. Rev. Lett.*, 41 (1978), 924.
7. CERN:Rome-Stony Brooke Collaboration, *Physics Lett.*, 62B (1976), 460 and Preprint, July 1978, European Organization for Nuclear Research.
8. Rarita W, Riddell (Jr) R J, Chiu C B & Phillips R J N, *Phys. Rev.*, 165 (1968), 1615.
9. Austin D M, Greiman W H & Rarita W, *Phys. Rev.*, D2 (1970), 2613.
10. Chou T T & Yang C N, *Phys. Rev. Lett.*, 20 (1968), 1213.
11. Durand III L & Lipes R, *Phys. Rev. Lett.*, 20 (1968), 637.
12. Buras A J & Dies de Deus J, *Nucl. Phys.*, B71 (1974), 481.
13. Henzi R & Valin P, *Physics Lett.*, 488 (1973), 119.
14. Gotsman, E & Maor U, *Lett. Nuovo Cim.*, 13 (1975), 113.
15. Ng J N & Sukhatme U P, *Nucl. Phys.*, B55 (1973), 253.
16. Pajares C & Schiff D, *Lett. Nuovo Cim.*, 8 (1973), 237.
17. Gribov V N & Migdal A A, *Zh. Eksp Teor. Fiz.*, 55 (1968), 1948. (English Translation in *Soviet Phys. JETP*, 38 (1969), 679.
18. Gribov V M & Migdal A A, *Yadernaya Fizika*, 8 (1968), 1002, 1213. (English Translation in *Soviet J. Nucl. Phys.* 8, 583, (1969) 703.
19. Baker M, *Proc. 8th Rencontre de Moriond on Reggeon Theory on Differential Scattering, Meribel* (1973), pp 125-56.
20. Saleem M, Rafique M, Mir K L, Mirza J S & Tirmazi S H, *Aust. J. Phys.*, 28 (1975), 365.
21. Kamran M & Saleem M, *Aust. J. Phys.*, 30 (1977), 355.
22. Phillips R J N & Barger V, *Physics Lett.* 46B (1973), 412.
23. Araki J, Shiohara M & Yano T, *Prog. theor. Phys.*, 58 (1977), 1649.
24. Shiohara M & Yano T, in *The Memories of Nihama Technical College (Japan)*, 14 (1978), 20.
25. Saleem M & Fazal-e-Aleem, *Prog. theor. Phys.*, 61 (1979), 516.
26. Burgi A I, *Lett. Nuovo Cim.*, 6 (1973), 577.
27. Jenkovszki L L, *Rising total cross-sections and multipole pomeron phenomenology*, Preprint for Institute Theoretical Physics (ITP)- 74-102E, Kiev (1974).
28. Phillips R J N, *A Dipole Pomeron Ansatz* : Rutherford Laboratory Preprint RL-74-034, Chilton (1974).
29. Joshi G C, *Lett. Nuovo Cim.*, 10 (1974), 815.
30. Jenkovszky L L & Wall A N, *Czech. J. Phys.*, B26 (1976), 447.
31. Saleem M, Fazal-e-Aleem & Kamran M, *Aust. J. Phys.*, (1979), in Press.
32. Sukatme U P, *Phys. Rev. Lett.*, 38 (1977), 124.

Dielectric Studies on Carboxylic Acids: Part III—Dipolar Thermodynamic Excess Functions of Acetic, Propionic & Butyric Acids in Non-Polar Solvents

R SABESAN & R VARADARAJAN

Department of Physics, National College, Tiruchirapalli 623 001
&

M SARGURUMOORTHY

Department of Physics, Periyar EVR College, Tiruchirapalli 623 020

Received 10 October 1979

The dipolar excess heat of mixing for systems of acetic, propionic and butyric acids plus non-polar solvents has been studied by measuring dielectric polarization. The information obtained is more direct regarding the nature of solute-solvent interaction than that obtained by the calorimetric methods. The demultimerization of α -multimers with parallel dipole orientations and the non-stoichiometric solute-solvent interactions contribute to the excess thermodynamic functions.

1. Introduction

In our earlier investigations,^{1,2} the variation of the Kirkwood correlation factor R_p measured from the dielectric polarization studies for acetic acid in different solvents was found to be a function of the composition. It has been found that due to the predominance of the *cis* configuration and the coplanarity of the C—CH₃ bond with the carbonyl bond, the β -multimers with an anti-parallel orientation of the dipoles are predominant. At low concentrations of acetic acid in inert solvents, only the cyclic dimers are favoured since the bond angle deviation from the ideal value is minimum. However, at high concentrations of acetic acid, α -multimers with open dimer or polymer could also coexist in high proportions with β -multimers.

The non-ideal behaviour³⁻⁶ of the so-called non-polar solvents was also brought out by our measurements of R_p and it was shown that solvents benzene and carbon tetrachloride interact with the O—H proton of the acid more than with the aliphatic hydrocarbons.

Among the diverse experimental techniques employed to study the intermolecular interactions, measurement of thermodynamic excess functions⁷⁻¹⁰ provides the most useful information regarding the cohesive energy of the system. The calorimetric and vapour pressure measurements could give only the total excess heat of mixing which is composed of such components as dipolar, dispersion and short-range forces. The decomposition of these forces

would provide useful information. The homomorph concept¹¹⁻¹⁴ of separating the dipolar and dispersion forces does not always give consistent values. Hence direct methods of finding the dipole-dipole and dipole-induced-dipole interactions have been attempted.^{15,16} However, the essential requirement of the measurement of several parameters like the variation of the dielectric constant, the refractive index and the specific volume with temperature for both the solute and the solution rendered these methods less attractive.

In the present investigation, we have calculated the dipolar internal energy through the Onsager reaction field factor employing the method of Haskell¹⁷ by measuring the molar dielectric polarization of the liquids and liquid mixtures and calculated the thermodynamic excess functions. No attempt seems to have been made for the direct measurement of the dipolar contribution to the thermodynamic excess functions on systems of carboxylic acids with inert solvents, which could give valuable and direct information regarding solute-solvent interaction.

2. Materials and Methods

Dielectric measurements were carried out using a Toshniwal RL09 dipolemeter with the cell temperature maintained at $35 \pm 0.1^\circ\text{C}$. The methods employed for the purification of the chemicals used and for the measurement of dipole moment were the same as described earlier.¹⁸

3. Theory

Assuming a spherical cavity of radius a in which the dipolar molecule i is placed, it is possible to calculate the reaction field parameter r_i as:

$$r_i = \frac{2\epsilon + 1}{2\epsilon + n_i^2} \frac{n_i^2 + 2}{3} = \left[1 - \frac{2(\epsilon - 1)\alpha_i}{(2\epsilon + 1)a_i^3} \right]^{-1} \quad \dots(1)$$

where n_i and α_i are the refractive index and polarizability of molecule i and ϵ is the dielectric constant of the solution. Writing from the Onsager theory¹⁹ the value of molar polarization of a binary mixture of volume fractions v_1 and v_2

$$v_1 P_1^* + v_2 P_2^* = \frac{(\epsilon - 1)(2\epsilon + 1)}{9\epsilon} \quad \dots(2)$$

where the molar polarization

$$P_i^* = \frac{4\pi N}{3\phi_i} \left[r_i \alpha_i + \frac{(r_i \mu_i)^2}{3k_B T} \right] \quad \dots(3)$$

where μ_i is the intrinsic dipole moment of i , k_B the Boltzmann's constant, N the Avogadro number, ϕ_i the molar volume of i , and T the absolute temperature.

Considering the partition functions corresponding to the dipole-dipole and dipole-induced-dipole interaction effects, the interaction energies of the dipoles in the field could be factorized out and hence the dipolar excess Helmholtz energy F_P^E , which is almost equal to the Gibbs free-energy for matter in condensed phase, is determined from the equation

$$F_P^E = \frac{3(P_2 - P_1)N}{3 + 2 \left\{ \frac{P_1 X_1 \phi_1 + P_2 X_2 \phi_2}{\phi} \right\}} \times \left[\frac{X_1 X_2 \phi_1 r_2 \mu_2^2}{\phi a_2^3 (2P_2 + 3)} \right] \quad \dots(4)$$

where $P_i = \frac{9\epsilon}{2\epsilon + 1} P_i^*$; $\phi = \sum X_i \phi_i$

X_1 and X_2 are the mole fractions of the solvent and the solute.

Since the molar polarization is a temperature-dependent quantity, its derivative with respect to temperature will give the dipolar excess entropy of mixing due to dipolar interactions,

$$S_P^E = - \frac{3 X_2 \mu_2^2 r_2 N}{a_2^3} \left[\frac{P'_2}{(2P_2 + 3)^2} - \frac{\Sigma'}{(2\Sigma + 3)^2} \right] \quad \dots(5)$$

where $P'_i = - \frac{2\pi N}{k_B \phi_i} \left(\frac{r_i \mu_i}{T} \right)^2$

$$\Sigma' = P'_2 \frac{X_2 \phi_2}{\phi} \text{ and } \Sigma = \frac{P_1 X_1 \phi_1 + P_2 X_2 \phi_2}{\phi}$$

4. Results and Discussion

The measured values of ϵ and ϕ at different concentrations of three different solutes in carbon tetrachloride and calculated values of F_P^E and TS_P^E are given in Table 1. Similar measurements were made for twelve other systems and the calculated values of F_P^E and TS_P^E plotted against the mole fractions of the solutes (Fig. 1).

The behaviour of the dipolar thermodynamic excess functions of carboxylic acids diluted with inert solvents is related directly to the nature of associations of the solute in the solvent at the given concentrations. The progressive addition of non-polar solvents to the solute yields positive values of excess heat of mixing (H_P^E) in the entire concentration range indicating that demultimerization takes place by rupture of hydrogen bonds.²⁰⁻²² However, the progressive lowering of the Kirkwood correlation factor² shows that the β -multimers are not broken, but only the α -multimers with parallel dipole orientations are demultimerized.

Fig. 1 shows that the dipolar heat of mixing is larger in hexane and cyclohexane than in carbon tetrachloride and benzene systems with the solute. The increasing order of excess heat of mixing H_P^E could be given as benzene < carbon tetrachloride < dioxane < cyclohexane < hexane. If all the solvents are equally inert, one would expect the contribution to Onsager's long-range interactions to be the same and hence equal values of H_P^E , contrary to what is observed here. The result could be explained only if one assumes that besides bond breaking another endothermic process also takes place, lowering H_P^E in systems like benzene and carbon tetrachloride through a solute-solvent interaction. It was reported by us earlier² from the observed R_p values of carboxylic acids in these systems that such non-specific interactions as $R-O-H \dots \Pi$ ^{23,24} and $R-O-H \dots Cl-CCl_3$ ²⁵⁻²⁸ do take place. The increasing order of interaction is given as hexane < cyclohexane < carbon tetrachloride < benzene.² Hence it may be concluded that the lower values of H_P^E in benzene and carbon tetrachloride could be ascribed to the existence of non-stoichiometric solvent-solute interactions. However, the near linear increase of $H_P^E/X_1 \cdot X_2$ with increasing dilution of the acids shows that the demultimerization of the α -multimers is the predominant process outweighing the solute-solvent interactions in all these systems including that with dioxane as solvent. It is suggested that a direct study of dipolar thermodynamic excess functions in polar mixtures could give useful information on dipole-dipole interactions and solvent effects.

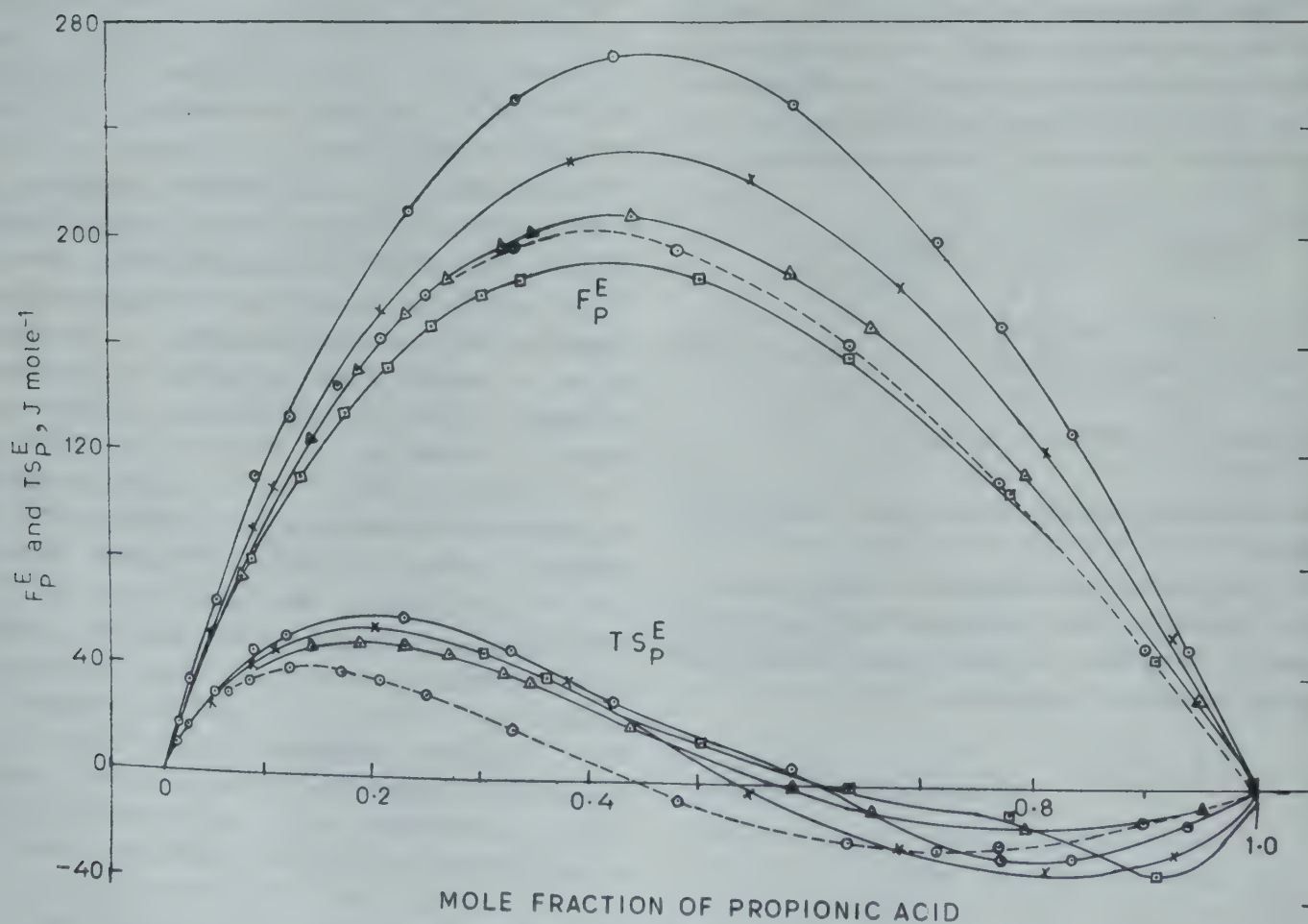
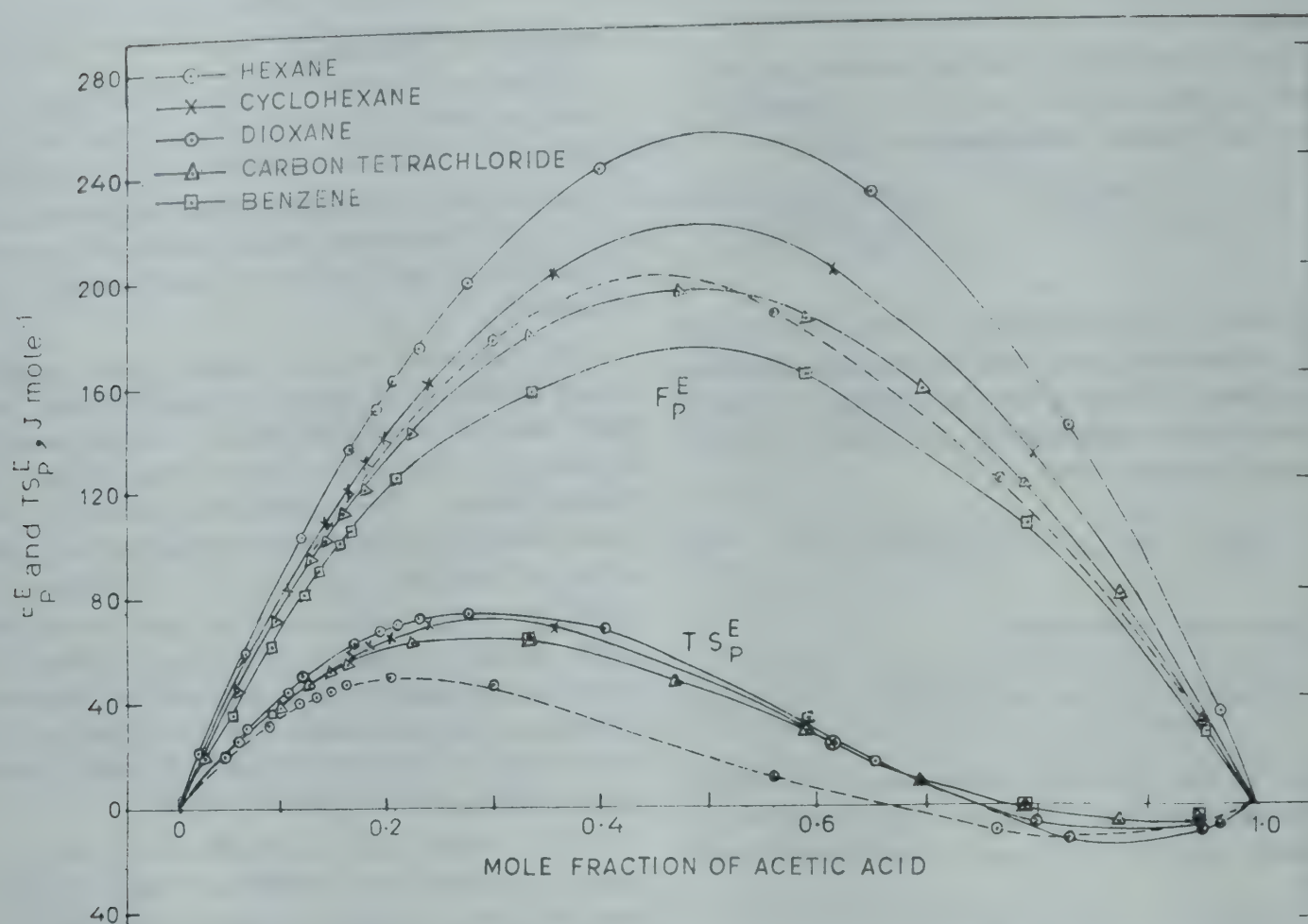


Fig. 1—Calculated values of F_P^E and $T S_P^E$ versus mole fraction of solute (X_2) in non-polar solvents [Solute : acetic and propionic acids]

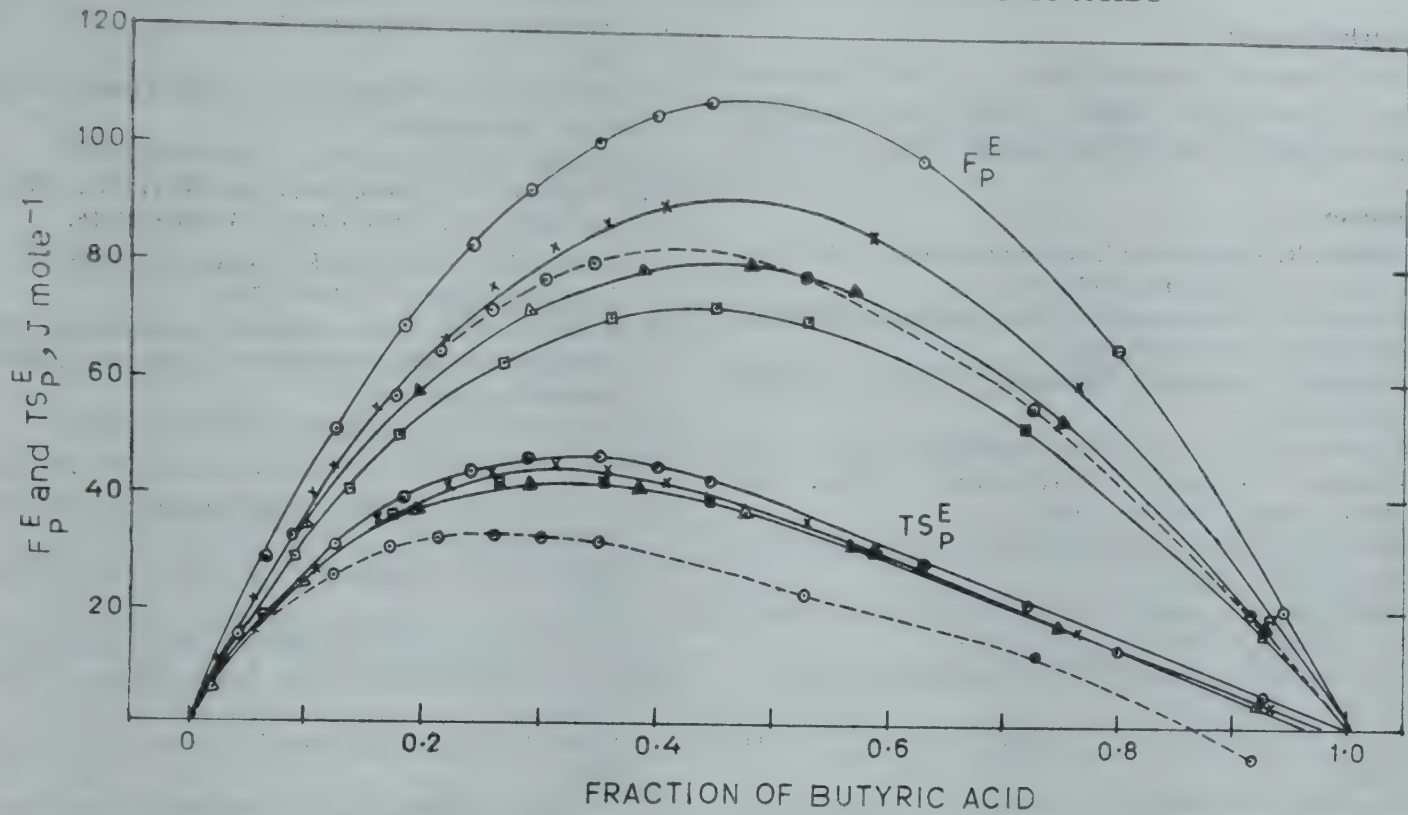


Fig. 1 (contd)—Values of F_P^E and TS_E^P versus fraction of solute in non-polar solvent
[Solute : butyric acid; Legend same as in portion of Figure in p-892]

Table 1—Values of ϵ , ϕ , F_P^E and TS_E^P at Different Concentrations of Solutes in Carbon Tetrachloride

X_2	ϵ	ϕ	F_P^E J mole ⁻¹	TS_E^P J mole ⁻¹	X_2	ϵ	ϕ	F_P^E J mole ⁻¹	TS_E^P J mole ⁻¹
Acetic acid					Propionic acid				
0.022	2.216	96.99	17.14	10.99	0.142	2.255	94.70	124.57	46.84
0.054	2.224	96.65	42.79	25.30	0.185	2.286	93.76	149.62	49.13
0.094	2.263	95.49	70.41	39.23	0.230	2.302	92.86	170.46	48.16
0.129	2.276	94.56	91.80	48.63	0.270	2.338	92.00	184.57	44.81
0.143	2.296	93.82	100.29	51.74	0.322	2.348	90.94	197.38	38.85
0.160	2.311	93.11	109.53	54.91	0.346	2.354	90.32	201.58	35.53
0.179	2.318	92.27	119.39	57.96	0.437	2.437	88.56	206.90	20.33
0.223	2.366	90.49	139.38	62.41	0.585	2.577	85.31	186.96	-2.34
0.337	2.411	84.96	176.62	63.07	0.657	3.629	83.33	167.01	-9.18
0.472	2.614	79.75	191.73	46.45	0.792	2.822	80.14	113.20	-15.33
0.588	2.858	75.11	181.53	27.81	0.948	3.128	76.64	31.26	-7.29
0.695	3.212	70.85	155.01	10.32	Butyric acid				
0.789	3.690	66.81	118.91	-0.91	0.021	2.213	98.11	8.19	5.88
0.874	4.340	63.26	76.79	-5.83	0.051	2.218	97.46	19.38	14.59
0.952	5.245	60.03	31.41	-4.72	0.099	2.255	97.42	34.46	24.59
Propionic acid					0.196	2.281	96.83	58.03	37.17
0.010	2.208	97.50	11.31	6.07	0.288	2.322	96.72	72.12	41.52
0.019	2.213	97.24	21.37	11.19	0.387	2.354	96.10	79.53	40.88
0.038	2.218	96.91	40.55	20.26	0.478	2.426	95.70	80.27	36.80
0.078	2.224	96.08	77.15	34.77	0.571	2.458	95.09	75.61	30.92
0.094	2.244	95.75	90.16	38.80	0.751	2.603	94.14	53.59	17.06
					0.928	2.770	93.44	17.78	4.25

Acknowledgement

The financial support given by the University Grants Commission, New Delhi, is gratefully acknowledged by two of the authors (RV and MS).

References

1. Sabesan R, Varadarajan R & Sargurumoorthy M, *Indian J. pure appl. Phys.*, **15** (1977), 538.
2. Sabesan R, Varadarajan R & Sargurumoorthy M, *Acta Chim. hung.*, **102** (1979), 165.
3. Campbell C, Brink G & Glasser L, *J. phys. Chem.*, **79** (1975), 660.
4. Fletcher A N, *J. phys. Chem.*, **73** (1969), 2217.
5. Mullens J, Hanssens L & Huyskens P, *Glasn. hem. Drust., Beogr.*, **79** (1971), 539.
6. Bordewijk P, Kunst M & Rip A, *Ber. Bunsenges. Phys. chem.*, **80** (1976), 839.
7. Lakhanpal M L, Kapoor K K, Gurcharanlal & Mandal H G, *Indian J. Chem.*, **11** (1973), 471.
8. Lakhanpal M L, Mandal M G & Gurcharanlal, *Indian J. Chem.*, **13** (1975), 673.
9. Nigam R K & Mahl B S, *Indian J. Chem.*, **9** (1971), 1250.
10. Nigam R K & Mahl B S, *J. chem. Soc. Faraday Trans.*, **1** (1972), 1508.
11. Bondi A & Simkin D J, *J. chem. Phys.*, **25** (1956), 1073.
12. Bondi A & Simkin D J, *A. I. ch. E. Jl.*, **3** (1957), 473.
13. Anderson R & Prausnitz J M, *A. I. ch. E. Jl.*, **7** (1961), 96.
14. Meyer E F & Wagner R E, *J. phys. Chem.*, **70** (1966), 3162; **75** (1971), 642.
15. Barker J A, *Proc. R. Soc., A*, **219** (1953), 367.
16. Amaya K, *Bull. chem. Soc. Japan*, **34** (1961), 1349.
17. Haskell R W, *J. phys. Chem.*, **73** (1969), 2916.
18. Sabesan R, Varadarajan R & Sargurumoorthy M, *Indian J. pure appl. Phys.*, **17** (1979), 229.
19. Bottcher C J F, Theory of electric polarization, revised by OC Van Belle P, Bordewijk & A Rip, Vol 1, (Elsevier, Amsterdam) 1973.
20. Flory P J, *J. Am. chem. Soc.*, **87** (1965), 1833.
21. Flory P J & Abbe A, *J. Am. chem. Soc.*, **87** (1965), 1838.
22. Rowlinson J S, *Liquids and liquid mixtures* (Butterworths London), 1959.
23. Hwa S C P & Ziegler W T, *J. phys. Chem.*, **70** (1966), 2572.
24. Singh S & Rao C N R, *J. phys. Chem.*, **71** (1967), 1074.
25. Fletcher A N & Heller C A, *J. phys. Chem.*, **71** (1967), 3742.
26. Fletcher A N, *J. phys. Chem.*, **73** (1969) 2217; **74** (1970), 216.
27. Wolf H & Hoppel H E, *Ber. Bunsenges Phys., Chem.*, **72** (1968), 710, 1173.
28. Tucker E E, Farnham S B & Christian S D, *J. phys. Chem.*, **73** (1969), 3820.

Spectrochemical Determination of Trace Elements in Stainless Steel

P S MURTY & (Smt) R KAIMAL

Spectroscopy Division, Bhabha Atomic Research Centre, Bombay 400 085

Received 20 November 1979; revised received 19 June 1980

A method for the spectrochemical determination of Al, Pb, Sn, V, Nb, Cu, Co and Ti at trace levels in stainless steel is reported. One hundred milligrammes of the stainless steel sample (in the form of turnings, filings, etc.) were dissolved in aqua regia. The solution is evaporated to dryness and then ignited over Bunsen flame to get a dark brown powder. The powder thus obtained was ground thoroughly with specpure conducting graphite powder in the ratio 1:1 by weight and then with 2% NaF. Fifteen milligrammes of this mixture were taken in the cavity of a graphite electrode and excited in a dc arc at 10 As. The spectra of the sample and synthetic standards were recorded on a JACO 3'4 on plane grating spectrograph, using 1200 grooves/mm grating in the first order. The elements Al, Pb, Sn and V are estimated in the concentration range 50-500ppm and Nb, Cu, Co and Ti in the range 250-2500 ppm, by choosing suitable lines for intensity measurement. Iron was used as the internal standard element.

1. Introduction

Stainless steels of varying specifications are in increasing demand in the construction of nuclear power reactors and are also important from the metallurgical point of view. Elements such as Al, V, Nb, etc. present at residual levels are as much important as the major alloying constituents, Cr and Ni, in the preparation of stainless steels to different specifications. Consequently, it is necessary to determine rapidly these residual elements in stainless steel in order to decide upon its suitability for any specific purpose. Methods employing photoelectric spectrometers and point-to-plane technique are commonly used for the rapid analysis of all kinds of steels. However, these methods are suitable only for the estimation of C, S, P and alloying constituents such as Cr, Ni, etc. because chemically pre-analyzed standards are not available for the determination of Al, Pb, Sn, V, Nb, Cu, Co and Ti at trace levels in any type of steel. Therefore, it is necessary to employ synthetic standards for the analysis of the above elements. In our laboratory we have developed a spectrographic method for the analysis of Al, Pb, etc. in stainless steel employing synthetic standards and dc arc excitation. Several methods¹⁻¹⁴ are found in literature, which deal with the determination of one or the other of the eight elements determined by our present method. Vassilaros and Mckaveney⁹ used a rotating disk spectrographic technique for the estimation of residual amounts of Al, Ca, V and Ti in steel and Ni-base alloys. They

employed a separation procedure to remove the matrix iron or nickel, prior to spectrographic analysis.

2. Experimental Details

2.1 Preparation of Standards

Initially a matrix mixture was prepared by simulating the average composition of stainless steel. For this purpose, specpure oxides of Fe, Cr, Ni and Mn (obtained from M/s Johnson and Matthey Chemicals Ltd.) were mixed in such a proportion that the mixture contained 70% of Fe, 19% of Cr, 10% of Ni and 1% of Mn by weight as metals. The matrix mixture was ground thoroughly so that it was homogeneous. Using this matrix mixture, a set of standards containing eight trace elements, Al, Pb, etc. was prepared. Details of steps involved in the preparation of standards are given in Tables 1 and 2. Out of the eight elements added to the matrix, Al, Pb, Sn, and V form one group with individual concentration ranging from 50 to 500 ppm. The remaining four elements, Nb, Cu, Co and Ti form another group with individual concentration ranging from 250 to 2500 ppm. All the standards were initially ground with specpure conducting graphite powder (200 mesh) in the ratio 1:1 and finally with 2% NaF.

2.2 Preparation of Sample

One hundred milligrammes of the stainless steel sample, in the form of turnings, were dissolved in a

Table 1—Details of Preparation of Matrix and Trace Element Mixtures

(i) Preparation of matrix mixture (M)				
Total weight of the matrix mixture = 7.107 g [equivalent to 5 g wt of (Fe+Cr+Ni+Mn) as metals]				
Element	Wt as metal (g)	Added as	Gravimetric factor	Wt of compound added (g)
Fe	3.500	Fe ₂ O ₃	1.4296	5.004
Cr	0.950	Cr ₂ O ₃	1.4614	1.388
Ni	0.500	NiO	1.2724	0.636
Mn	0.050	MnO ₂	1.5828	0.079
Total wt (g) = 5.000				= 7.107
(ii) Preparation of trace element mixture (A)				
Element	Wt as metal (mg)	Added as	Gravimetric factor	Wt of compound added (mg)
Al	10	Al ₂ O ₃	1.89	18.9
Pb	10	PbO	1.08	10.8
Sn	10	SnO ₂	1.27	12.7
V	10	V ₂ O ₅	1.79	17.9
Total wt (mg) = 40				= 60.3
(iii) Preparation of trace element mixture (B)				
Element	Wt as metal (mg)	Added as	Gravimetric factor	Wt of compound added (mg)
Nb	10	Nb ₂ O ₅	1.43	14.3
Cu	10	CuO	1.25	12.5
Co	10	CoO ₂	1.41	14.1
Ti	10	TiO ₂	1.67	16.7
Total wt (mg) = 40				= 57.6

minimum quantity (3 ml approx) of aqua regia and evaporated to dryness over a sand bath. The dried residue was heated directly over Bunsen flame to get a dark brown powder, which was collected and ground thoroughly in an agate mortar. The powder thus obtained was first mixed with specpure conducting graphite powder (200 mesh) in the ratio 1:1 by weight and then with 2% NaF. From this final mixture two 15 mg portions were weighed out and filled in the cup of two 6.35 mm diam., ultrahigh purity graphite electrodes.

2.3 Procedure

Standards, prepared as outlined in Sec. 2.1, were also loaded in ultrahigh purity graphite electrodes (6.35 mm diam.). The spectra of sample and standards were photographed by employing a Jarrell Ash 3.4-m plane grating spectrograph under the experimental conditions given in Table 3. A standard

Table 2—Details of Preparation of standards S₀–S₄
Standard S₀ (Containing 1000 ppm of Al, Pb, Sn, V;
5000 ppm of Nb, Cu, Co, Ti)

$$\frac{1}{10} \left[\text{Wt of trace element mixture, A} \right] + \frac{1}{2} \left[\text{Wt of trace element mixture B} \right] + \text{Balance Wt of matrix mixture M to get a total Wt of 1000 mg.}$$

That is,

$$6.03 \text{ mg of mixture A} + 28.80 \text{ mg of mixture B} + 965.17 \text{ mg of mixture M.}$$

Standard S₁ (Containing 500 ppm of Al, Pb, Sn, V;
2500 ppm of Nb, Cu, Co, Ti)

$$1000 \text{ mg of } S_0 + 1000 \text{ mg of M} = 2000 \text{ mg of } S_1$$

Standard S₂ (Containing 200 ppm of Al, Pb, Sn, V;
1000 ppm of Nb, Cu, Co, Ti)

$$500 \text{ mg of } S_1 + 750 \text{ mg of M} = 1250 \text{ mg of } S_2$$

Standard S₃ (Containing 100 ppm of Al, Pb, Sn, V;
500 ppm of Nb, Cu, Co, Ti)

$$200 \text{ mg of } S_1 + 800 \text{ mg of M} = 1000 \text{ mg of } S_3$$

Standard S₄ (Containing 50 ppm of Al, Pb, Sn, V;
250 ppm of Nb, Cu, Co, Ti)

$$250 \text{ mg of } S_2 + 750 \text{ mg of M} = 1000 \text{ mg of } S_4$$

Note : More than 1 g of S₀ can be prepared and kept for further use.

procedure was followed in processing the Ilford N-30 emulsion on which the spectra were recorded. The calibration of the emulsion was done by the rotating seven-step sector method. The optical densities of analytical lines listed in Table 4 were measured on a Hilger non-recording microphotometer. The densities were converted to intensities on a Respektra calculating board which facilitates the plotting of the emulsion calibration curve in the corrected form by incorporating the Kaiser's constant (K).

3. Discussion

In the point-to-plane technique routinely used in the analysis of stainless steel by employing quantometers, excitation is done either by pulsed arcs or by the so-called controlled waveform source. Both these sources are suitable if the samples are in block form. These sources are known to contribute low spectral background and offer high precision. In the present case, as pointed out in Sec 1, synthetic standards in powder form had to be prepared by simulating the composition of stainless steel and incorporating the eight trace elements. The above sources cannot be used for the excitation of samples in the powder form. Therefore, the dc arc was chosen as the source of excitation in the present case. However, the matrix spectrum resulting from dc arc excitation was very complex in the wavelength region of interest and also had high

Table 3—Experimental Conditions

Spectrograph	: Jarrell-Ash 3'4 m Ebert plane grating spectrograph
Grating; wavelength range	: 1200 grooves per mm; 2375-order; blaze
	: 3625 Å; I order; 3300 Å
Reciprocal linear dispersion	: 2.5 Å/mm in I order
External optical system	: A cylindrical lens was used to focus the image on to the slit.
Filter	: A neutral density filter with transmissions 100 and 10% was placed in front of the slit.
Analytical gap	: 4 mm
Slit width	: 10 μ
Electrode assembly	
Upper electrode (cathode)	: 3.18 mm dia ultra high purity graphite printed electrode
Lower electrode (anode)	: 6.35 mm dia ultra high purity graphite electrode with a cup to contain 15 mg of sample or standard.
Excitation source	: Jarrell-Ash custom vari source;
Excitation current	: 10 Adc.
Exposure time	: 20 sec
Emulsion	: Ilford N-30 ordinary photographic plates

background. Therefore, the Jarrell-Ash 3'4-m plane grating spectrograph with a grating having 1200 grooves/mm was used in the present work, since it provided adequate dispersion and resolution in the first order. In order to improve upon the line-to-background ratio by decreasing the background, sodium fluoride at 2% concentration was added to both standards and samples.

The analytical lines used for plotting the working curves shown in Fig. 1 are given in col. 2 of Table 4. Two lines of Fe were used as internal standard lines (col. 3, Table 4). The working curves are linear in the concentration range listed for each element in

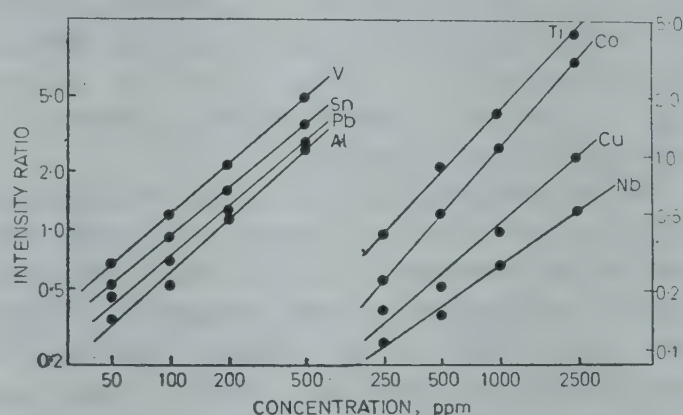


Fig. 1—Working curves for Al, Pb, Sn & V, and Nb, Cu, Co and Ti in stainless steel (Table 4 may be referred to for analytical lines)

Table 4—Analytical Data

Element	Analytical line* Å	Internal standard line* Å	Concentration range (ppm)	Coefficient of variation %	Interfering lines* Å
Al	2575.100	Fe 2868.871	50—500	18.2	{ Nb 2574.843; Co 2574.862; Fe 2574.890; Fe 2575.344
Pb	2614.178	—do—	50—500	14.9	{ Nb 2613.931; Mn 2614.037 Co 2614.128; Ta 2614.173; Nb 2614.310; Co 2614.361
Cu	2824.369	—do—	250—2500	15.5	{ Mo 2824.172; W 2824.296; Co 2824.364; V 2824.441; Cr 2824.537
Nb	2950.878	—do—	250—2500	24.5	{ Cr 2950.687; W 2950.690; Fe 2950.930; Fe 2951.098
Ti	3168.521	Fe 3178.546	250—2500	22.2	Nb 3168.598; Mo 3168.726
Sn	3175.019	—do—	50—500	14.6	{ Ti 3174.800; Co 3174.905; Fe 3174.960; Fe 3175.035; Mo 3175.049; Fe 3175.080;
V	3185.396	—do—	50—500	15.7	{ W 3185.202; Fe 3185.316; Si 3185.280
Co	3395.375	—do—	250—2500	15.9	{ Fe 3395.329; Mo 3395.360; Cu 3395.476; W 3395.478; V 3395.524

* Wavelength data taken from *Tables of Spectrum Lines* by A N Zaidel, V K Prokofev & S M Raikii (Pergamon Press, New York), 1961.

Table 5—Results of a sample Analyzed by Spectrographic and Chemical Methods

Element	Value, %	
	Spectrographic method	Chemical method
Cu	> 0.25 (0.28)	0.30
Nb	0.035	< 0.05
Ti	< 0.025	< 0.05
V	0.036	< 0.05
Co	0.17	0.18

col. 4. The possible interfering lines are given in col. 6. The intensities of the interfering lines of various elements are low and, therefore, do not affect the analytical lines unless those elements are present at high concentration.

The precision of the method was evaluated by calculating the coefficient of variation of the intensity ratios for each standard. The standards composing the eight residual elements were exposed on different plates. Ten values of the intensity ratios for each standard measured from the different plates were made use of in calculating the coefficient of variation. The mean coefficient of variation for each element in the concentration range 50-500 ppm or 250-2500 ppm as the case may be, is listed in col. 5 of Table 4. The precision is within $\pm 20\%$ for all elements except for Nb and Ti.

The accuracy of the method was tested by analyzing a sample using the present method as well as a chemical method. The results are shown in Table 5.

The values listed in the second column of Table 5 are obtained by the present method. The chemical analysis results are given in col. 3. In the case of the chemical method, the detection limit for Nb, Ti and V is 0.05% and hence these are reported as < 0.05% in the sample. The value given in brackets for Cu (col. 2) is the extrapolated value. The sample contained < 0.005% each of Al, Pb and Sn which could not be determined by the chemical method.

Acknowledgement

The authors sincerely thank Dr N A Narasimham, Head, Spectroscopy Division, for his keen interest during the course of this work.

References

1. Kolbovski Yu Ya & Krizhanovskaya M K, *Flz. Sb. L'vov. Gos. Univ.* 4 (1958), 402.
2. Neuilly M, *Mem. Sci. Rev. Met.* 56 (1959), 484.
3. Ishida M, *Bunseki Kagaku*, 9 (1960), 209.
4. deLaffolie H, *Arch. Eisenhüttenwes.*, 32 (1961), 145.
5. Kudelya E S & Plotnitskii V M, *Zavod. Lab.*, 28 (1962), 558.
6. Ellenberg J Y, *Anal. Chem.*, 34 (1962), 230.
7. Morita K, Veda S & Kato Y, *Nagoya Kogyo Gijutsu Shikensho Hokoku.*, 13 (1964), 342.
8. Bodya E & Ftorek M, *Zavod. Lab.* 32 (1966), 1473
9. Vassilaros G L & Mckaveney J P, *Talanta*, 13 (1966), 15.
10. Kawashima I & Miyazaki T, *Bunko Kank.*, 14 (1966), 186.
11. Jeffery W C, *Mod. Cast*, 49 (1966), 85.
12. Hines C R & Hurwitz J K, *Appl. Spectrosc.*, 21 (1967), 277.
13. Kristina P, Pavel G. Venetta N & Antoanetta D, *Z. Anal. Chem.*, 255 (1971), 113.
14. Cerjan-Stefanovic S, Turina S & Marjanovic V, *Croat. Chem. Acta*, 43 (1971), 83.

Communications

Creep : Dislocation Acceleration

N K GILRA

Physics Department, Higher Petroleum Institute
P. O. Box 201 Tobruk, Libya

Received 22 September 1979

Using the dislocation kinetics and phenomenological point of view, it has been shown that the instantaneous mean dislocation acceleration is directly proportional to dislocation velocity and is inversely proportional to the mean dislocation density

Recently Mejia and Mendoza¹ studied the creep behaviour using the phenomenological view point² as well as dislocation kinetics³ and found a relation between density of mobile dislocations (ρ) and the instantaneous mean dislocation velocity (v) as follows:

$$v = \frac{K}{\rho} + k \quad \dots(1)$$

where K and k are constants.

From Eq. (1), we get

$$\dot{v} = - \frac{K}{\rho^2} \dot{\rho} \quad \dots(2)$$

From kinetics of dislocation creation and annihilation,³ we have

$$\dot{\rho} = a_1 v \rho + a_2 \rho^2 \quad \dots(3)$$

where a_1 and a_2 are constants. From Eqs. (2) and (3), one gets

$$\begin{aligned} \dot{v} &= - \frac{K}{\rho^2} \left[a_1 v \rho + a_2 \rho^2 \right] \\ &= - K_1 \frac{v}{\rho} + K_2 \end{aligned} \quad \dots(4)$$

where K_1 and K_2 are now constants.

From Eq. (4), we see that the instantaneous mean dislocation acceleration (\dot{v}) is directly proportional to the dislocation velocity and is inversely proportional to the mean density. That means with more dislocations, the motion of a dislocation is hampered whereas with more momentum, due to more velocity, it surpasses the obstacles and its motion is not hampered during creep.

References

1. Mejia M & Mendoza A, *Scripta Met.*, **11** (1977), 411.
2. Mejia M, Gomez Ramirez R & Martinez M A, *Scripta Met.*, **10** (1976), 589.
3. Barrett C R, Nix W D & Sherby O D, *Trans. ASM*, **59** (1966), 3.

Electron Microscopy of TaS₂ Single Crystals Using Weak Beam Technique

M K AGARWAL, J V PATEL* & T C PATEL

Department of Physics, Sardar Patel University,
Vallabh Vidyanagar 388 120

Received 26 March 1980

The weak beam technique of DJH Cockayne, ILF Ray and M J Whelan [*Phil. Mag.*, **20** (1969), 1265] for imaging dislocations in the electron microscope has been applied to observe dislocations in TaS₂. Partial dislocations at alternate extended and contracted nodes have been observed. An estimate of the stacking fault energy has been made from the dissociated dislocation configurations.

Recently, there has been considerable interest in the chalcogenide layer compounds such as TaS₂, NbS₂ and related crystals. These highly anisotropic layered materials possess a wide range of electrical and optical properties including semiconducting, metallic and superconducting behaviour. The structure and physical properties of these materials have been reviewed by Wilson and Yoffe.¹ The 1T polytype of TaS₂ is a unique substance since it undergoes two phase transitions as its temperature is varied. The work reported in this paper is a TEM study of 1T-TaS₂.

It has been shown by Cockayne *et al.*² that the structure of lattice defects can be significantly improved if the dark field electron micrographs are taken in weak diffracted beams. This effect is possible because the weak beam intensity can be considerably increased only very close to the defect where sufficiently large local tilts of the crystal take place to bring the weak beam near to the Bragg position. In this case, dislocations appear as very narrow bright lines against a low intensity background.

* Permanent address : Department of Physics,
Shree Jayendrapuri Arts & Science College,
Broach 392 002

Since the weak beam method of electron microscopy increases the resolution of the defect structure, all our TEM studies of TaS₂ have been made using this technique. The improvement resulting from the weak beam pictures can be immediately seen from the corresponding bright field pictures of the same regions.

Crystal structure—1T-TaS₂ belongs to the hexagonal system; it has the cadmium iodide structure which can be described by the symbol $avb\ avb\ avb$. The Latin letters represent sulphur, whilst the Greek letters represent tantalum. The close packed layers of tantalum atoms are sandwiched between two close packed sulphur layers, they occupy the octahedral interstices. The binding between tantalum and sulphur is profusely stronger than van der Waals binding between the two sulphur layers. The lattice parameters are:

$$a = 3.426 \text{ \AA} \text{ and } c = 5.927 \text{ \AA}.$$

Specimen preparation—1T tantalum disulphide was prepared by the direct reaction between the two elements.³ Cleavage flakes sufficiently thin to transmit electrons, i.e. $\approx 700 \text{ \AA}$, were prepared by repeated cleavage using an adhesive tape.

Micrographs were taken on a Phillips EM 400 electron microscope operating at 120 kV. This microscope has a built-in facility for taking the weak beam pictures. For this purpose, first of all a strong two-beam dark field condition is set up for $(\bar{h}\ \bar{k}\ \bar{l})$ using beam tilt settings X and Y , and focusing and adjustments are carried out in this range. The weak beam condition for the systematic $(\bar{h}\ \bar{k}\ \bar{l})$ reflection can be achieved immediately by setting the opposite deflection fields settings $-X$, $-Y$.

The advantage of using the weak beam method of electron microscopy for analysing dislocation system is illustrated in Figs. 1(a) and 1(b). Fig. 1(a)

shows an electron micrograph of a TaS₂ crystal taken in the $\bar{2}1\bar{0}$ diffracted beam with the crystal oriented close to the exact Bragg reflection condition. The dislocation images are very wide and it is difficult to resolve the dislocation structure at points marked as \times . Fig. 1(b) shows the corresponding weak beam image taken in the $\bar{2}\ 1\bar{0}$ diffracted beam.

It is seen that the resolution of the dislocation detail is greatly improved and in particular, the structure is resolved at the points \times . Some details which are not evident in the strong beam image [Fig. 1(a)] are also revealed in the weak beam image [Figs. 1(b), 2(b)] at points A and B. Moreover, the formation of nodes marked by points $\times \times$ is clearly observed in the weak beam picture [Fig. 1(b)] whereas no such information is available at a glance from bright field pictures [Figs. 1(a), 2(a)]. In Fig. 2(b), the dislocation marked with BB is clearly seen as dissociated while the same is not true in the corresponding bright field picture.

Another example of the improvement of resolution of the picture when taken in a weak beam is revealed in Figs. 3(a) and 3(b), which are the bright field and weak beam pictures respectively. In Fig. 3(a), the pattern shown in the hexagon ABCDEF is not clearly seen. As a matter of fact it is difficult to interpret the pattern. The weak beam picture clearly reveals that the pattern is formed from extended nodes.

The net-work in Fig. 4(a) is exactly similar to the net-work pattern shown in Fig. 4(b), where we are tempted to say that the pattern is due to two families of dislocations lying in separate planes and this interaction is only an electron optical effect. But the weak beam picture of Fig. 4(b) shows how false one's interpretation can be. The same sets of

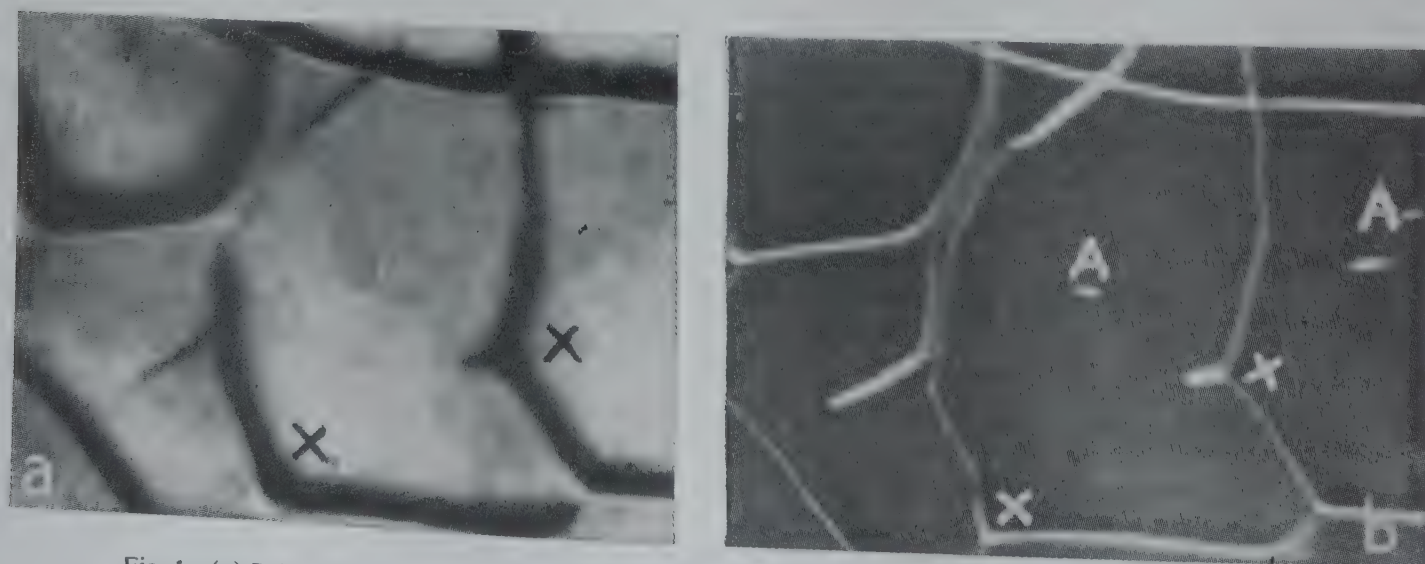


Fig. 1—(a) Bright field picture showing nodes, (b) Corresponding weak beam picture ($\times 135000$)

COMMUNICATIONS

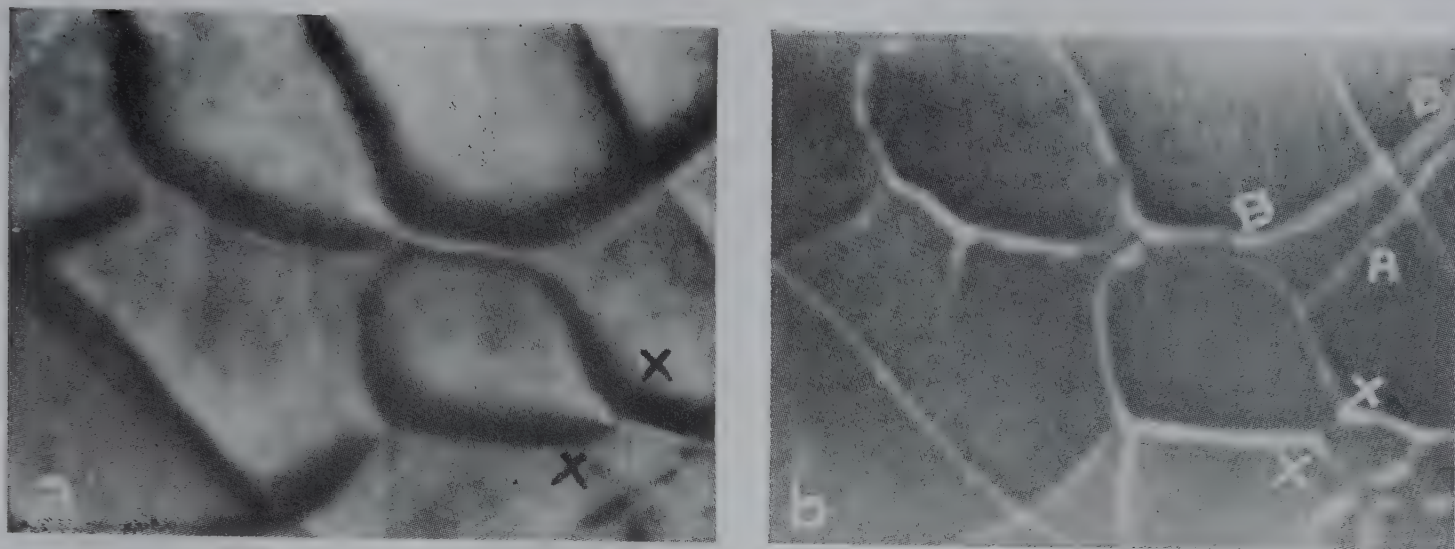


Fig. 2—(a) Bright field picture of dislocations in TaS_2 , (b) Corresponding weak beam picture ($\times 135000$)

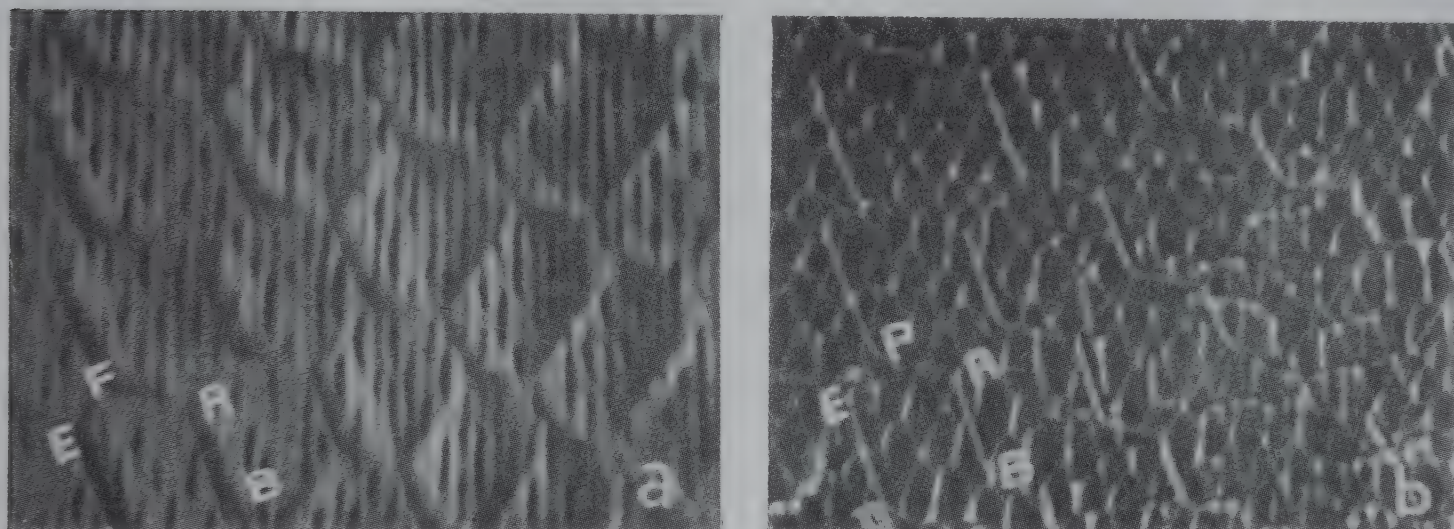


Fig. 3—(a) Bright field picture showing net-work pattern of the extended nodes, (b) Corresponding weak beam picture ($\times 105000$)

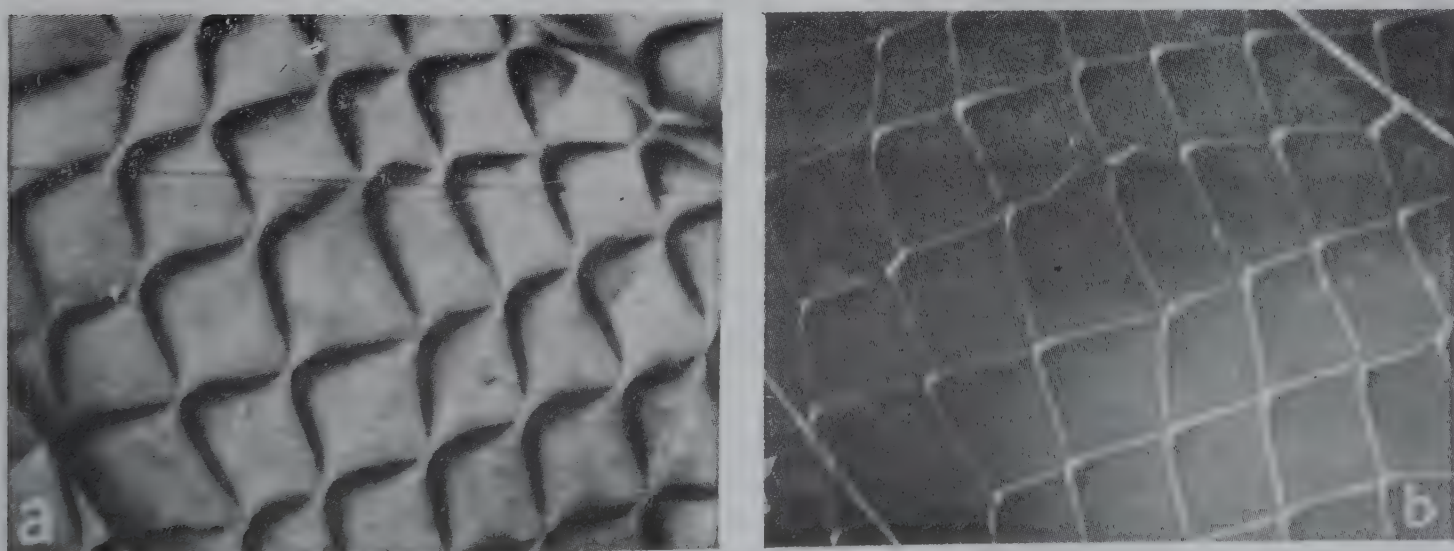


Fig. 4—(a) Bright field picture of a net-work pattern, (b) Corresponding weak beam picture ($\times 81000$)

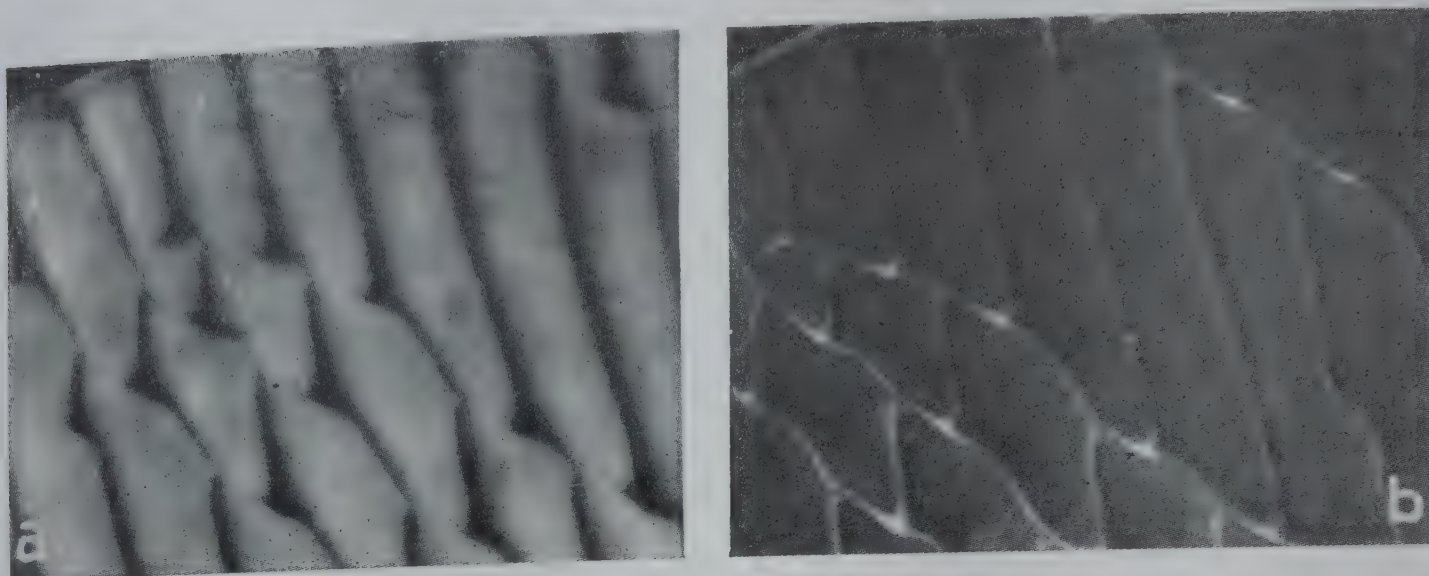


Fig. 5—(a) Bright field picture of the network pattern showing extrinsic and intrinsic nodes, (b) Corresponding weak beam picture ($\times 135000$)

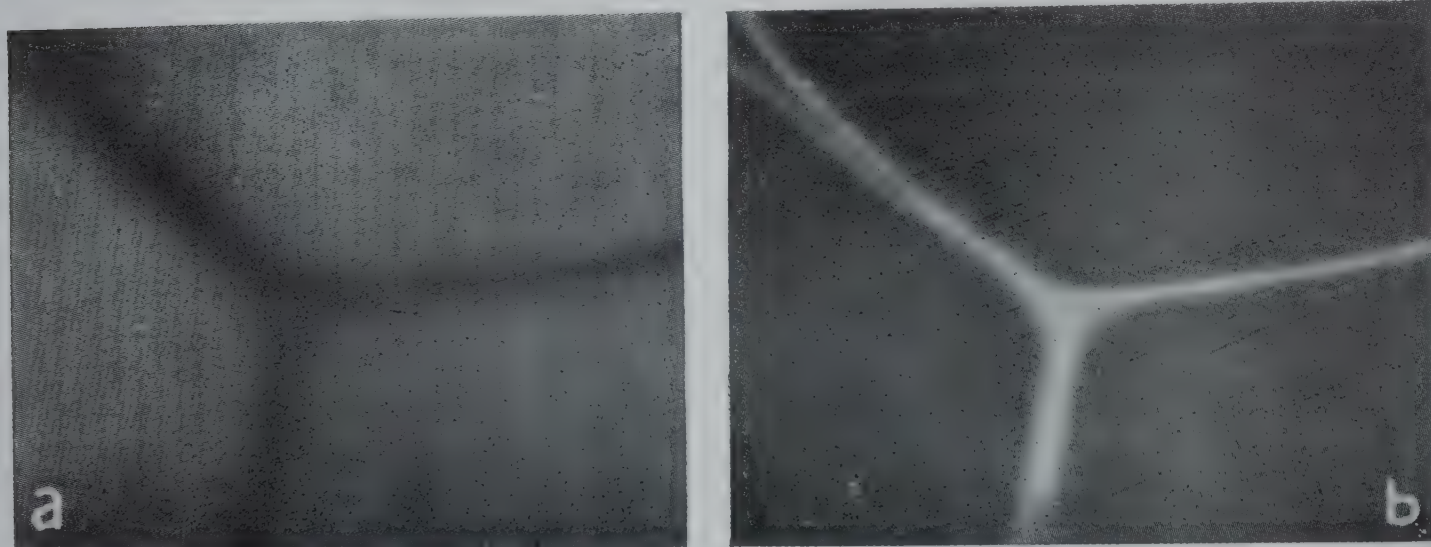


Fig. 6—(a) Bright field picture of an isolated node, (b) Corresponding weak beam picture ($\times 174000$)

dislocations do interact with each other and form the familiar node pattern seen earlier.

Weak beam images of dislocation networks showing extrinsic and intrinsic nodes [Fig. 5(a)] were also taken. Fig. 5(b) shows such a pattern taken in $(\bar{2}10)$ diffracted beam. The geometry of the nodes is clearly revealed in the weak beam picture.

One can estimate the stacking fault energy γ from the radius of curvature R of an extended node by using the relation $\gamma = \mu b^2/2R$ where, b is the Burger's vector ($b = a/\sqrt{3}$) and μ the shear modulus. Since μ for TaS_2 is not known, only the ratio γ/μ which is proportional to stacking fault energy alone can be estimated.

For an accurate estimation, it is advisable to use only those nodes which are relatively free from interaction with the other dislocations. Regions showing isolated nodes were, therefore, selected and

the bright field picture and the weak beam picture of an isolated node is shown in Figs. 6(a) and 6(b) respectively. The boundaries of the partials forming the nodes are clearly seen in Fig. 6(b).

Value of γ/μ estimated from the radii of curvature of the nodes comes out to be 20.181×10^{-12} cm.

The authors are thankful to Prof. A R Patel for valuable discussions and keen interest in the work. One of them (JVP) is indebted to the University Grants Commission, New Delhi, for the award of a teacher fellowship and, in particular, to the Principal and Management of Shri Jayendrapuri Arts and Science College, Broach, for the grant of study leave.

References

1. Wilson J A & Yoffe A D, *Adv. Phys.*, 18 (1969).
2. Cockayne D J H, Ray I L F & Whelan M J, *Phil. Mag.*, 20 (1969), 1265.
3. Agarwal M K, Patel J V & Patel H B, *Bull. Mater. Sci.*, 1 (1979), 107.

Debye Temperature of Some Solid Solution Series with the NaCl Structure

B NAGAI AH & D B SIRDESHMUKH

Physics Department, Kakatiya University,
Warangal 506 009

Received 3 May 1980

The Debye temperatures (θ_E) of crystals in the solid solution series KCl-KBr, AgCl-AgBr and MgO-FeO have been evaluated from elastic properties. The Debye temperatures of the solid solutions are also calculated from the equation $\theta_C^n = x \theta_1^n + (1-x) \theta_2^n$, where θ_1 and θ_2 are the Debye temperatures of the end members and x and $(1-x)$ the composition of the solid solution, n being given values -3 , 2 and -1 . The best agreement of θ_C with θ_E is obtained when $n = -1$.

There are several reports on the Debye characteristic temperatures of crystals with the sodium chloride structure.¹⁻⁴ The data on the Debye temperatures of solid solutions with this structure are, however, meagre. The elastic constants of mixed crystals of three systems have been reported in recent years. These are the KCl-KBr system,⁵ the AgCl-AgBr system⁶ and the MgO-FeO system.⁷ The Debye temperatures of crystals in these systems have been evaluated and their dependance on the composition is examined.

There are several methods of evaluation of Debye temperature from the elastic constants. Some of these methods have been discussed in an earlier communication.⁴ Since the elastic properties of the MgO-FeO system have been measured on polycrystalline samples, Anderson's⁸ method of calculating Debye temperatures from elastic properties of polycrystalline aggregates have been chosen for the evaluation of Debye temperatures for all the three systems. For the KCl-KBr system and the AgCl-AgBr system, these values are obtained using the Voigt-Reuss-Hill approximation. The results (θ_E) are given in Table 1. The values of the bulk modulus (B in units of 10^{11} dynes cm^{-2}) and the shear modulus (G in units of 10^{11} dynes cm^{-2}) are also given in Table 1. The values of θ_E for KCl, KBr, AgCl, AgBr and MgO agree with earlier estimates;¹ the value for FeO is being reported for the first time.

It is customary to expect the Debye temperatures of a solid solution series to follow the Kopp-Neumann, relation given below:

$$\theta_C^{-3} = x \theta_1^{-3} + (1-x) \theta_2^{-3} \quad \dots(1)$$

Here, θ_C , θ_1 and θ_2 are the Debye temperatures of the solid solution and the two end members and x

and $(1-x)$ are the concentrations. The values calculated from this equation are given in Table 1. It is found that these values (θ_C) differ slightly from the values obtained from the elastic constants (θ_E) in the case of the systems KCl-KBr and AgCl-AgBr but the differences are rather large in the case of the system MgO-FeO as indicated by the estimated standard deviation (esd) of $(\theta_E - \theta_C)$.

The Kopp-Neumann relation results from the Debye- T^3 law and the assumption of additivity of specific heats. It is known that the Debye- T^3 law holds at extremely low temperatures and hence Debye temperatures calculated from room temperature elastic properties could deviate from Eq. (1). At somewhat elevated temperatures, the specific heat is given by the equation:⁹

$$C_V = 3NK \left(1 - \frac{\theta^2}{T^2} + \dots \right) \quad \dots(2)$$

Table 1 Debye Temperatures of Crystals in the Three Systems Studied

x	B	G	θ_E, K	θ_E, K		
				Eq. (1)	Eq. (3)	Eq. (6)
KCl _x -KBr _(1-x) System						
0.0	1.54	0.78	169.8	—	—	—
0.2	1.59	0.81	178.6	177.2	183.5	179.2
0.41	1.64	0.84	189.9	186.7	197.0	190.4
0.61	1.69	0.87	201.1	197.7	208.8	202.3
0.83	1.77	0.91	216.2	213.5	221.1	217.1
1.00	1.83	0.95	230.1	—	—	—
esd in ($\theta_E - \theta_C$)				2.7	6.2	0.85
AgCl _x -AgBr _(1-x) System						
0.00	4.06	0.89	136.7	—	—	—
0.19	4.05	0.86	137.4	138.4	138.7	138.5
0.39	4.04	0.84	138.9	140.2	140.6	140.4
0.56	4.07	0.83	140.2	141.9	142.4	142.1
0.78	4.19	0.81	143.1	144.2	144.5	144.3
1.00	4.4	0.807	146.5	—	—	—
esd in ($\theta_E - \theta_C$)				1.3	1.7	1.5
(Mg _x Fe _{1-x}) O System						
0.000	17.4	5.4	471.3	—	—	—
0.230	17.4	6.3	530.6	507.9	612.7	532.5
0.482	16.9	7.9	630.6	565.1	737.1	620.9
0.744	16.7	10.0	759.1	669.4	847.4	750.5
0.781	17.2	10.5	786.6	691.5	861.8	773.3
0.846	16.8	10.9	819.2	742.0	886.1	822.5
1.000	16.3	13.1	942.7	—	—	—
esd in ($\theta_E - \theta_C$)				74.6	86.7	8.4

Combining this equation with the assumption of additivity, one gets:

$$\theta_c^2 = x \theta_1^2 + (1-x) \theta_2^2 \quad \dots(3)$$

The values calculated from Eq. (3) are also given in Table 1. These values and the esd of $(\theta_E - \theta_c)$ show that Eq. (3) is not better than Eq. (1). In fact, the deviations are more.

It is possible to obtain yet another relation connecting the Debye temperature and the composition of the solid solution from empirical considerations. It is known that the lattice constant a of a solid solution is given in terms of the lattice constants a_1 and a_2 of the end members by Vegard's law:

$$a = x a_1 + (1-x) a_2 \quad \dots(4)$$

It has been observed that a simple relation exists between the lattice constant and the Debye temperature. This is given by

$$\theta = K/a \quad \dots(5)$$

where K is a constant. This relationship has been found to hold in the case of alkali halides and alkaline earth chalcogenides having the NaCl-structure¹⁰ and also in some garnets.¹¹ Assuming that such a relationship holds over a solid solution series, Eqs. (4) and (5) lead to:

$$\theta_c^{-1} = x \theta_1^{-1} + (1-x) \theta_2^{-1} \quad (6)$$

The values calculated from Eq. (6) are also included in Table 1 and it can be seen that they are closer to the θ_E values than the values obtained from Eqs. (1) and (3). The relative performance of Eqs. (1), (3) and (6) can be best seen in the values for the MgO-FeO system where the values of the esd vary from 86 to 8.

Considering the data for these three systems, it is suggested that Debye temperatures of a solid solution series conform to Eq. (6) better than to the Kopp-Neumann relation, i.e. Eq. (1).

References

1. Anderson O L, *Physical acoustics*, Vol. IIIB (Academic Press, New York) 1965.
2. Konti A & Varshni Y P, *Can. J Phys.*, 49 (1971), 3115.
3. Verma J K D & Aggarwal M D, *J. appl. Phys.*, 47 (1976), 2778.
4. Subhadra K G & Sirdeshmukh D B, *Indian J. pure appl. Phys.*, 16 (1978), 693.
5. Slagle O D & McKinstry H A, *J. appl. Phys.*, 38 (1967), 446.
6. Cain L S, *J. Phys. Chem. Solids*, 38 (1977), 73.
7. Jackson I, Libermann R C & Ring Wood A E, *Phys. Chem. Minerals*, 3 (1978), 11.

8. Anderson O L, *J. Phys. Chem. Solids*, 24 (1963), 909.
9. Ghatak A K & Kothari L S, *Lattice Dynamics* (Addison Wesley, London) 1972.
10. Baldwin T O & Tompson C W, *J. chem. Phys.*, 41 (1964), 1420.
11. Nagaiah B, Rambabu M & Sirdeshmukh D B, *Indian J. pure appl. Phys.*, 17 (1979), 838.

A Low Noise High Gain Amplifier for Acoustic Emission

J SAMPATH KUMAR, S P MALLIKARJUN RAO & M SURYANARAYANA

Physics Department, University College of Science
Osmania University, Hyderabad 500 007

Received 2 June 1979; accepted 29 May 1980

A very low noise high gain amplifier has been designed for amplifying low level signals. The amplifier has a gain of 58 dB and a band-width of about 2.5 MHz. The root mean square value of the equivalent input noise is better than $8\mu\text{V}$ and the amplifier has a dynamic range of 54 dB. The circuit can be operated from a $\pm 12\text{ V}$ supply with a nominal consumption of about 40mA while delivering a maximum output of 8 V peak-to-peak in the double ended mode. The circuit is found to be very useful as a pre-amplifier for amplifying the low level signals of the order of few tens of microvolts usually encountered in the acoustic emission work.

Acoustic emission is becoming one of the important tools of non-destructive testing.^{1,2} The heart of the instrumentation is the pre-amplifier which must receive very low level signals from the piezoelectric transducer, of the order of few tens of microvolts. The frequency range of acoustic emission work is usually between 50 kHz and 2 MHz. In the present communication, a low noise amplifier designed by the authors, suitable for the above purpose is detailed.

The low noise amplifier is shown in Fig. 1. The low level signals received from the transducer are amplified by the first low noise amplifier stage consisting of a FET, BFW-10 which is operated in the common source configuration. The output of this is given to a differential amplifier (SG 840). For minimum component count and to reduce the noise from passive devices, a split supply of $\pm 12\text{ V}$ is used for this stage to eliminate the biasing network. The noise from the active devices is kept to a minimum by choosing low values of collector current.³ The differential output from this stage is further amplified successively by two LM 733 integrated circuits operated in the '10' gain mode. The final output can be single ended or double ended. The overall circuit has a bandwidth of about 2.5 MHz and a gain of 58 dB in single ended operation. The root

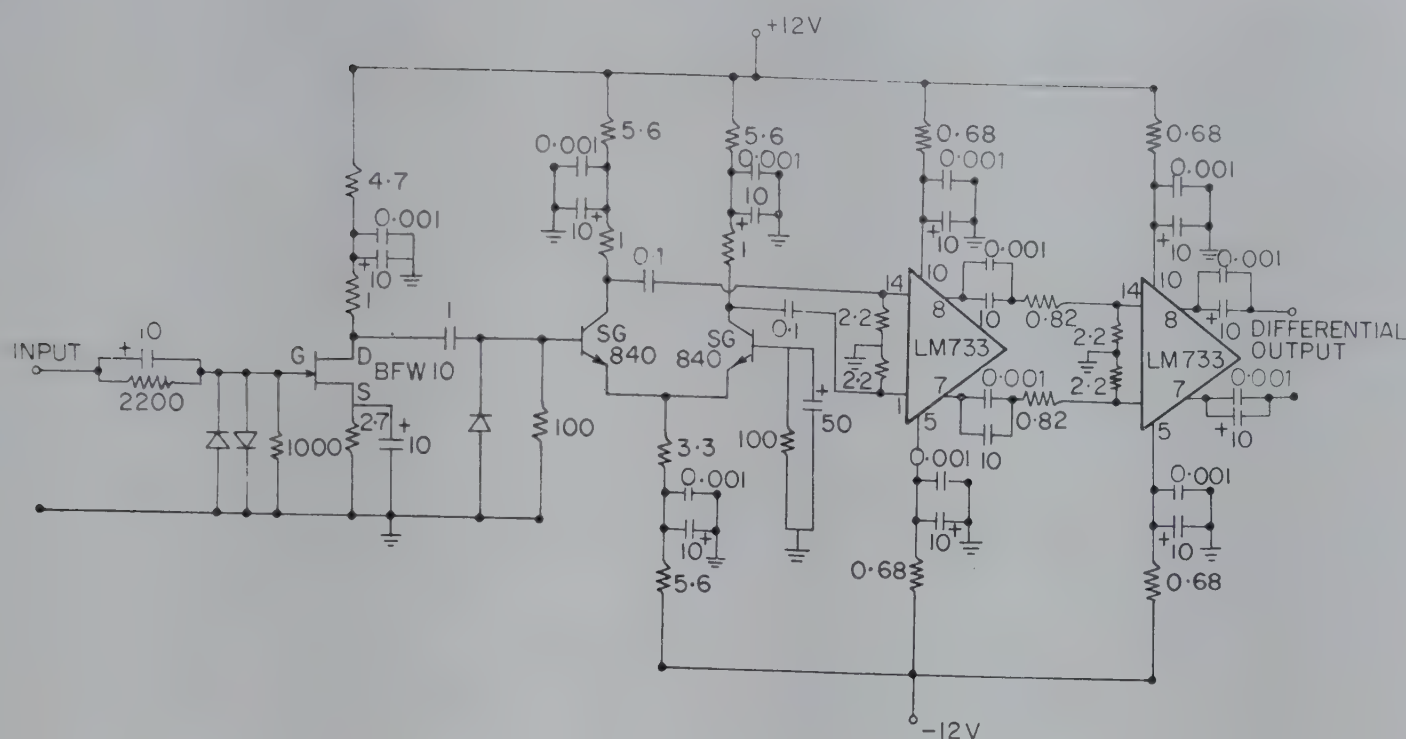


Fig. 1—Circuit diagram of the low noise, high gain amplifier [All the resistance values are in kilo ohms and the capacitor values in microfarads]

mean square value of the equivalent input noise is better than $8 \mu\text{V}$. The amplifier has a dynamic range of about 54 dB and can deliver 4 V (or 8 V) peak-to-peak in single ended (or double ended) operation. The complete circuit is simple to assemble and with a standard printed circuit board layout, gives very satisfactory performance. The circuit can be operated from a $\pm 12 \text{ V}$ supply and consumes a nominal current of 40 mA while delivering the maximum output of 8V(4V) peak-to-peak in double ended (single ended) operation.

Very low noise index metal film resistances have been used in the circuit and also each active device has been specifically picked for its low noise performance from large numbers pertaining to the same family. The standard printed circuit board layout of interweaving the ground plane to avoid oscillations and spurious pick-ups which are very common to high gain amplifiers, has been used.

It may be mentioned that in acoustic emission work, the bandwidth of the amplifier has to be restricted to about 2 MHz (except while performing the spectrum analysis of the received signal, wherein higher bandwidth is very much desirable) to eliminate extraneous electrical noise.

This work is undertaken under a University Grants Commission (UGC), New Delhi, sponsored project. One of the authors (J S) thanks the UGC for the award of a fellowship.

References

1. *Acoustic emission*, ASTM, STP 505 (American Society for Testing and Materials, Philadelphia, USA) 1972.
2. *Monitoring structural integrity by acoustic emission*, ASTM, STP (American Society for Testing and Materials Philadelphia, USA), 1975.
3. Motchenbacher C D & Fitchen F C *Low noise electronic design*, (John Wiley, New York) 1973.

Accurate Measurement of Tangential Vibrations of Quartz Crystals

HARISH BAHADUR & R PARSHAD
National Physical Laboratory, New Delhi 110 012

Received 14 May 1980

Vibrating quartz crystals having polished surfaces are examined in the scanning electron microscope (SEM) at known high magnifications (2000-5000) and at low accelerating voltages (2 kV). The length of the line images in the SEM electron pictures produced by the residual surface point defects yields a precise measurement of the amplitude.

Accurate measurement of the amplitudes of vibration of quartz crystals and other resonators has always been a difficult problem. Earlier, interferometric methods¹ were devised to detect the oscillations but these were not quantitative. In the recent past, Sauerbrey²⁻⁴ has developed an optical method for measuring the amplitude of vibrations and their distribution patterns. The method is, however, complex and tends to disturb the quartz vibrating surface



Fig. 1—SEM micrographs of a quartz crystal [(a) dormant, and (b) vibrating state of the crystal]

due to the need of reflecting and non-reflecting metal strips on the surface.

This communication presents an accurate and easy method of measurement of amplitude of tangential vibrations of quartz and other resonators using scanning electron microscope (SEM). In general, the SEM pattern of the vibrating surface of a piezoelectric material like the quartz crystal would depict both the electric potential distribution on the surface (due to the piezoelectric nature of the crystal) and the topographical features. Fortunately, the two influences on the formation of SEM patterns can be separated out by operating the SEM at two levels of magnification. At the lower magnifications (~ 20), the contrast due to the potential distribution is dominant while at the high magnifications (2-5 k), it is the topographical features which give the dominant contrast, the potential at the small part of the surface being examined determining only the overall hue of the pattern.

It has been found that at high magnifications the SEM pattern in general looks smeared.⁵⁻¹¹ This is due to the different point objects on the surface of the vibrating crystal forming line images due to tangential vibrations, these line images intermixing to produce the smeared pattern. Gerdes and Wagner⁶⁻⁸ using the smeared patterns attempted to measure the amplitudes of vibrations but the error was about as great as the amplitude itself.

In the present work, the precision of measurement has been vastly improved by proceeding as follows. The faces of the crystal were polished enough so as to leave only a few surface marks in the SEM micrographs observed at high magnifications. Due to this, there would be no smearing, instead, lone, topographical point-like features existing on the surface would mark out clear lines caused by tangential vibrations. Fig. 1 represents a set of micrographs of an area for the dormant and oscillating states of the polished crystal. The micrographs clearly indicate the direction of vibrations, their amplitude being given by the relation $(l_2 - l_1) / 2M$ where l_1 is the maximum length of a region on the surface of the dormant crystal, l_2 the corresponding length along the direction of vibration of the resonator, and M is the total SEM magnification employed. In a particular case, an amplitude of $0.85 \mu\text{m}$ was determined with an accuracy of 0.5%.

Different parts of the crystal can of course be easily brought under the scanning beam, by the mechanical arrangement provided in the SEM, to obtain the amplitude map of the crystal.

The authors thank Mr V K Lall of the Indian Institute of Technology, New Delhi, for instrumental help with the SEM.

References

1. Osterberg H, *J. opt. Soc. Am.*, **22** (1932), 19.
2. Sauerbrey G, *Z. Phys.*, **178** (1964), 457.
3. Sauerbrey G, *Proc. Annual. Freq. Contr. Symp.*, **17** (1963), 28.
4. Sauerbrey G, *Proc. Annual Freq. Contr. Symp.*, **21** (1967), 63, 211.
5. Hearn E W, *IBM tech. Rep. TR 22*, 1003 May, (1970).
6. Gerdes R J & Wagner C E, *Proc. Third Annual SEM Symposium*, (IIT Res. Institute, Chicago), 1970, 441.
7. Gerdes R J & Wagner C E, *Proc. Annual Freq. Control Symp.*, **25** (1971), 118.
8. Gerdes R J & Wagner C E, *Appl. Phys. Lett.*, **18** (1971), 39.
9. Bahadur H, Hepworth A, Lall V K & Parshad R, *IEEE Trans.*, **SU-25** (1978), 309.
10. Bahadur H, Hepworth A, Lall V K & Parshad R, *Proc. Annual. Freq. Contr. Symp.*, **32** (1978), 207.
11. Bahadur H, Hepworth A, Lall V K & Parshad R, *Scanning electron microscopy*, /Pt I/AMF O'Hare I L, (1979), 333.

Parallel Plate Electron Multiplier Using $\text{SnO}_2\text{-Al}_2\text{O}_3$

P W MAHAJAN & S V BHORASKAR

Department of Physics, University of Poona, Poona 411 007

Received 19 April 1980; revised received 3 June 1980

The details of the fabrication of a parallel plate electron multiplier (PPEM) using $\text{SnO}_2\text{-Al}_2\text{O}_3$ combination have been described. It is found that this combination is simpler technologically than other conventional combinations of PPEMs such as $\text{Si-Al}_2\text{O}_3$, etc. It is shown that a PPEM using thin films of $\text{SnO}_2\text{-Al}_2\text{O}_3$ offer gains in the range of 10^3 and this low gain is attributed to high resistance of the order of $10^{11} \Omega$ across SnO_2 film.

The channel electron multipliers (channeltron) are available on commercial scale for detection of photons, electrons, neutrons or charged particles, but it seems that it has never been thought to use a parallel plate electron multiplier (PPEM) as a substitute to the channeltron. In fact, owing to its simplicity of construction, it can be fabricated in any well equipped thin film laboratory according to the users requirements.

We have fabricated the parallel plate electron multiplier using tin oxide as semiconducting film and aluminium oxide as secondary emissive film. The combination of materials in parallel plate electron multiplier, so far reported, include $\text{C-Al}_2\text{O}_3$, $\text{Si-Al}_2\text{O}_3$, C and $\text{SnO}_2\text{-Sb}$.¹⁻⁴ Here we have introduced, therefore, for the first time the parallel plate electron multiplier using $\text{SnO}_2\text{-Al}_2\text{O}_3$ combination. Moreover, it is technologically simpler to deposit both SnO_2 and Al_2O_3 .

Microscope slides of size $30 \times 25 \times 1.5 \text{ mm}^3$ were first gold deposited by vacuum evaporation. The size of the gold electrodes was $25 \times 3 \text{ mm}^2$. Tin and aluminium were then vacuum evaporated and oxidized by heating in oxygen atmosphere one after the another. The length-to-diameter (separation in this case) ratio of 75 was obtained by using stainless steel strips of 0.4 mm as spacers between

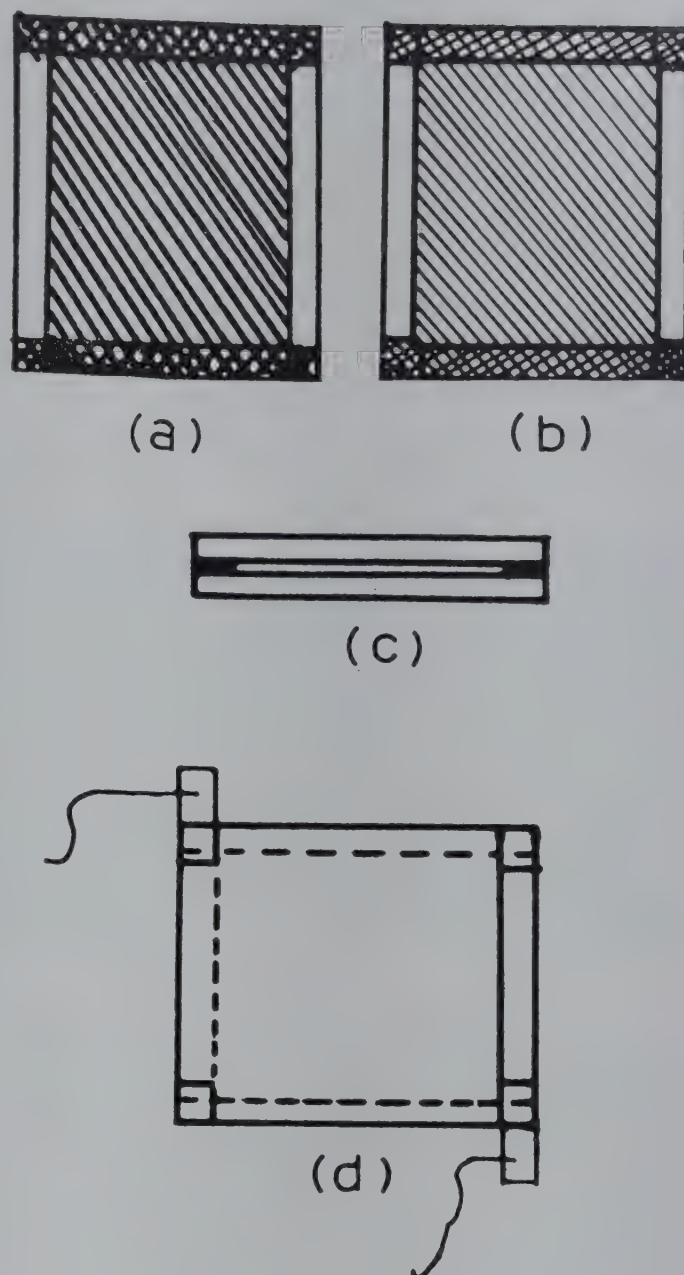


Fig. 1—Parallel plate electron multiplier assembly [(a) and (b), $\text{SnO}_2\text{-Al}_2\text{O}_3$ coated glass platelets along with gold contacts, (c) side view of PPEM; and (d) top view of PPEM]

two glass platelets. The parallel plate assembly is shown in Fig. 1. The detailed specifications of the PPEM are shown in Table 1.

The electron source for testing of electron multiplier consisted of a tungsten filament and an aperture. The system was sealed-off on mercury diffusion pump at a pressure of 10^{-8} torr, along with a getter bulb for frequent vacuum improvements. This sealed-off system was as shown in the Fig. 2. While testing the parallel plate electron multiplier in pulsed electron input detection mode, the pulse shape was found to change as shown in the Fig. 3, with a maximum pulse height at 800 V applied across the multiplier. The pulsed electron input of energy 30 eV was obtained by using a variable duty cycle (msec to μ sec) pulse generator. The gain

Table 1—Specifications of the PPEM

Dimension	$30 \times 25 \times 1.2 \text{ mm}^3$
Spacing	0.4 mm
Dynode composition	Semiconducting SnO_2 Secondary emitter Al_2O_3
Resistance	$10^{11} \Omega$
Capacitance	13 pF
Operating pressure	10^{-5} to 10^{-7} torr
Electrodes	$25 \times 3 \text{ mm}^2$ gold electrodes
Output impedance	$10^{11} \Omega$

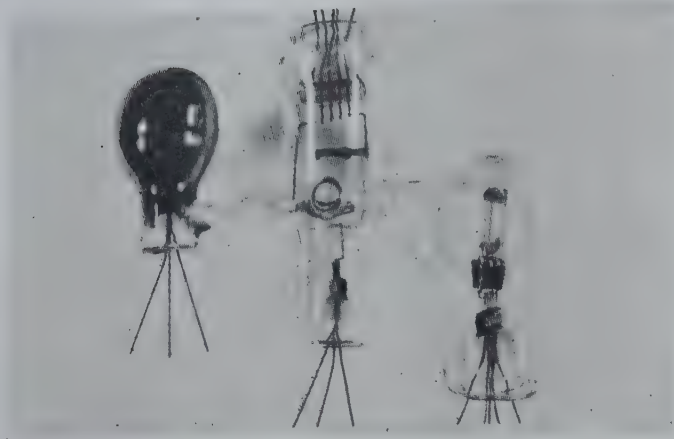


Fig. 2—Sealed electron multipliers

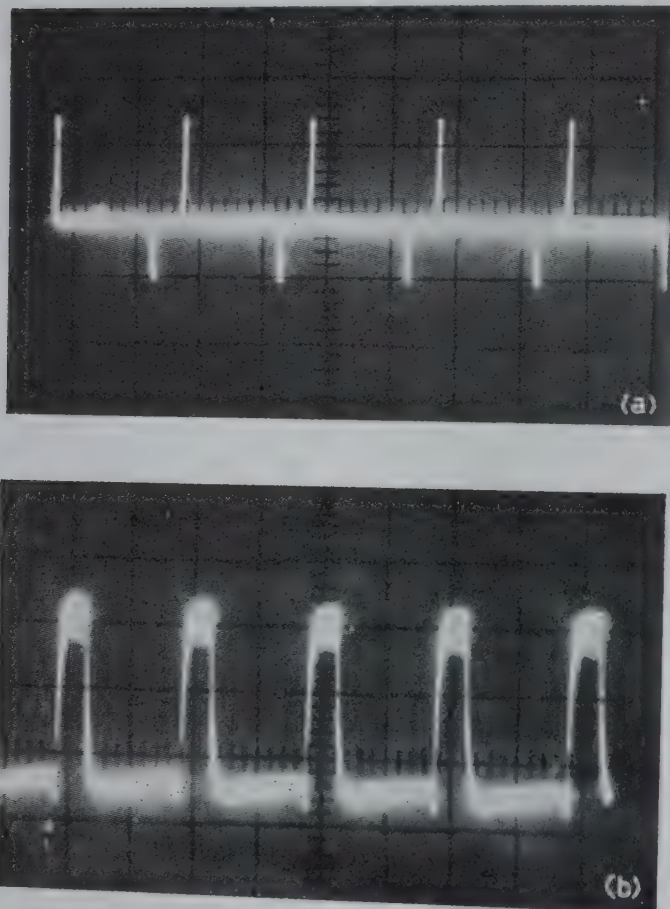


Fig. 3—Oscilloscope pattern of output pulses [(a) without input electrons; (b) with input electrons]

corresponding to the maximum pulse height for an applied voltage of 800 V across the PPEM was calculated to be 10^4 .

The gain was calculated from $Q = CV$ where, Q is charge collected; C capacitance of PPEM; V voltage pulse at the output of PPEM.

The output pulse height was detected to be of the order of 30.1 mV [Fig. 3(b)]. The corresponding input electron pulse was of the order of $3 \mu\text{V}$. The results were consistent and the gain remained at 10^4 even after prolonged operation and exposure of PPEM to atmosphere. Fig. 4 shows the block

diagram of the circuit for detection in the pulse electron input detection mode.

In the continuous electron input detection mode of testing, the current was measured at the front electrode using a dc micro-voltmeter. The nature of the current as observed with respect to time is

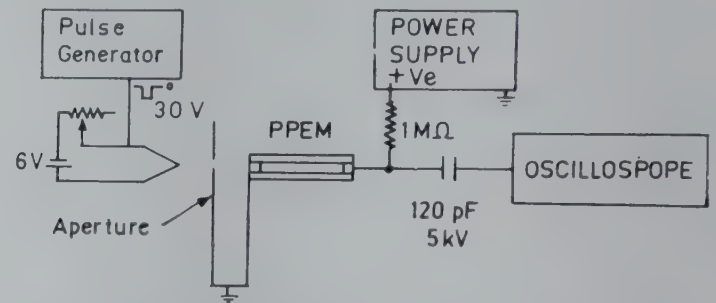


Fig. 4—PPEM in pulsed electron input detection mode

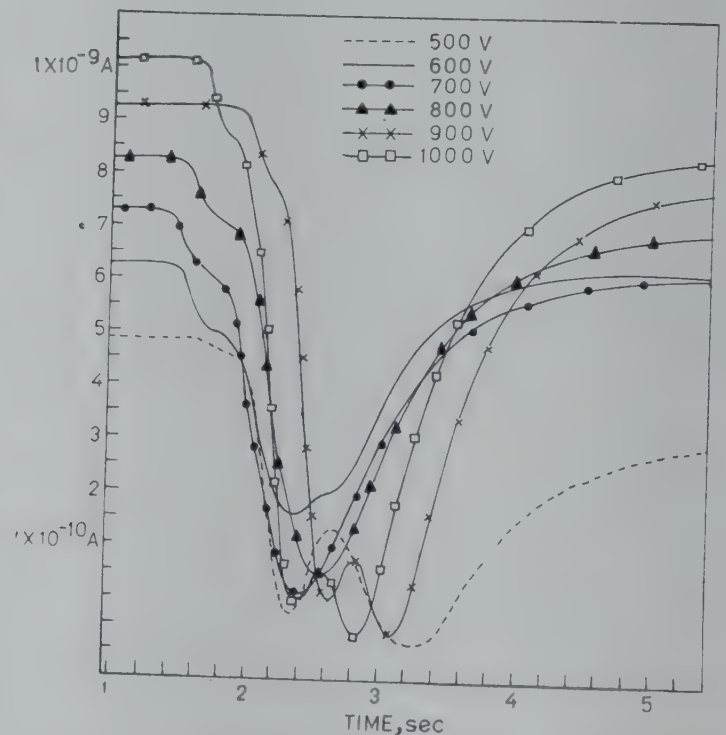


Fig. 5—Variation of output current with time at various applied voltages

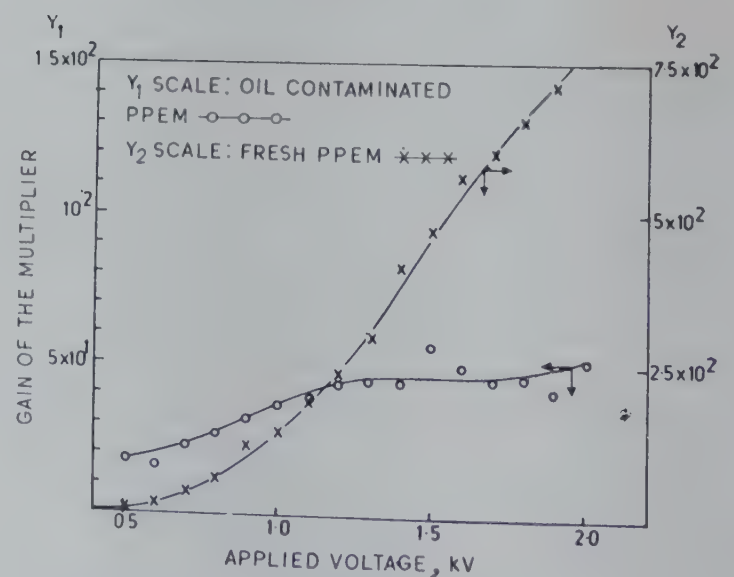


Fig. 6—Gain degradation due to oil cracking

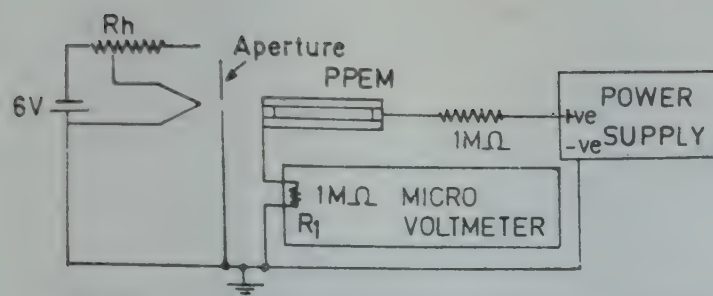


Fig. 7—PPEM in continuous electron input detection mode

shown in Fig. 5 for different voltages (V_A) applied across the multiplier. The saturation in the gain is due to space charge formation between the parallel plates which changes the potential distribution across the multiplier. The variation of gain, in continuous mode of testing, as a function of voltage across the PPEM, is shown in Fig. 6. Fig. 7 shows the circuit diagram in the continuous electron input detection mode of operation.

While testing an identical PPEM on oil diffusion pump system in continuous electron input mode of detection, it was found that the initial gain value of

7×10^2 reduced to 50 in two consecutive (evacuations of the system) cycles of operation. The effect of gain reduction can be attributed to the oil cracking which reduces the secondary yield of Al_2O_3 .

The low gain obtained in our PPEM was most probably due to the high resistance ($10^{11} \Omega$) across the film of SnO_2 . Work for high gain by optimizing the design parameters is in process.

The authors wish to thank Profs. M R Bhiday and A S Nigavekar for their constant encouragement, during the progress of the work. One of the authors (PWM) thanks the University Grants Commission, New Delhi, for providing the financial assistance.

References

1. Kanayama M, Konno T, Kiyono S, *Rev. scient. Instrum.*, 40 (1969), 129.
2. Nilsson ö, Hasselgren L, Sigbann K, Berg S, Anderson L P & Tove P, *Nucl. Instrum. Meth.*, 84 (1970), 301.
3. Feser K, *Rev. scient. Instrum.*, 42 (1971), 888.
4. Heroux L & Hintergger H E, *Rev. scient. Instrum.*, 31 (1960), 280.

Notes

Heat Transmission through Jute-Fibre Packings at Low Temperature

S K DAS & S C CHAKRAVARTY

Solid State Physics Laboratory, Jadavpur University
Calcutta 700 032

Received 16 May 1979; accepted 16 October 1979

A preliminary investigation of thermal insulation property of jute fibre packings in air has been reported between temperatures 100 and 300 K. A small sized guarded hot plate assembly which can be inserted in liquid nitrogen metal cryostat has been fabricated for the purpose. Variations of thermal insulation (λ_a) with packing density and temperature have been studied. Results indicate that such packings have satisfactory thermal insulation property and can be considered for use as thermal insulators in cryogenic industry.

It is well known that heat transmission through a system of fibrous aggregate depends mainly on the packing of fibres, fibre diameters, intervening air pressure inside the system and also on the material of the fibre. The last factor becomes important particularly when the material used is in evacuated and sealed condition, serving as a superinsulator. Suitable fibrous insulators are being increasingly used especially in cryogenic industry as a thermal insulator. We have been exploring the possibility of using an indigenous and cheap insulating system like jute fibre packings. One of the drawbacks, viz. that jute samples are susceptible to fire hazards, has been largely removed by the Indian Jute Industries Research Association (IJIRA), Calcutta, who have produced fibre-retardant jute fibres by treating the raw fibres with appropriate coating of inorganic material.

The method developed for measuring heat conductivity of fibre packings consists of a sample chamber containing guarded hot plate system of small dimensions. The sample chamber is inserted in the innermost cavity of a conventional three-walled metal cryostat, the middle compartment surrounding the innermost one is filled with cryogen (LN_2 or LO_2) and the outermost one is evacuated by a vacuum pump. The ambient temperature inside the sample chamber can be changed by passing current through a heating coil wound externally over the body of the sample chamber. To attain thermostatic control, a relay is included in series with this

heating circuit which can be activated by a photocell. A thermocouple, one junction of which is attached to the body of the sample chamber, governs the deflection of the spot of light of a D'Arsonval galvanometer. According to the desired steady temperature, the window of the photocell is set at a suitable position relative to the deflection of the spot of light, and the heating current is started. With the rise of temperature of the sample chamber, the spot of light advances towards the window of the photocell and as soon as it falls over the opening slit of the window, the relay breaks the heating circuit. As a result, the spot moves back and as it leaves the slit, the heating current automatically resumes. In this way, the spot moves to-and-fro up to the photocell slit and the temperature becomes steady within about 0.1°C . For a different steady temperature, the photocell window needs to be set at a new position corresponding to this new temperature.

The schematic diagram of low temperature guarded hot plate system is illustrated in Fig. 1. In fabricating this assembly, we have followed the ATSM specification.¹ However, to economize the use of cryogens as well as quicker attainment of steady state, we use samples consisting of circular discs of diameter 5 cm and thickness about 0.5 cm so that our sample chamber is small in size and hot plate assembly is situated in the middle (placed vertically). The size of the test heater is 2.4 cm while the gap between the test heater and guard heater is 0.12 cm. Thermocouples made of copper-constantan wires have been calibrated at different temperatures between 77 and 300 K. Thermocouples D are differential thermocouples.

In this experiment, we require two identical discs of fibrous samples so that heat flow is divided equally and symmetrically on the two sides of the hot plate. To ensure this, samples are weighed accurately and taken inside a metal dice and packed by appropriate hydraulic pressure.

Due to smallness in dimension of the hot plate system, the accuracy of our measurement is somewhat low compared to other hot plate methods. The experimental error in the measurement of thermal conductivity has been estimated to be 5-10% depending on low or room temperature range in use. The

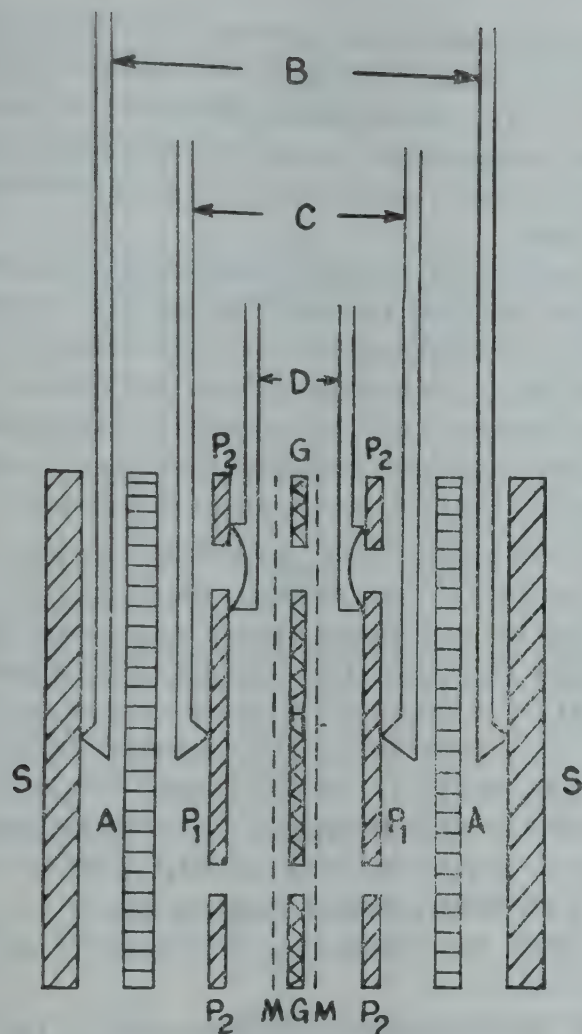


Fig. 1—Schematic diagram of low-temperature hot-plate [Heating unit : H, Central heater; P₁, Central hot plates; G, guard heater; P₂, Guard heater plates; S, sink plates; D, differential thermocouples; C, heating unit surface thermocouple; B, cooling unit surface thermocouple; A, samples; M, mica insulation sheets]

apparatus has been calibrated with a standard sample like cork-board at two different packing densities. The result is found to be very close to the known data of the sample.²

The insulation property of samples, for the present, has been evaluated by measuring a quantity known as apparent thermal conductivity (λ_a) which includes the effect of convection and radiation as well as thermal conduction.

In steady state, λ_a is calculated from the equation:

$$W/2 = \lambda_a A (\theta_1 - \theta_2)/d$$

where $W/2$ is the electrical power in watts transmitted horizontally to either side; W the electrical power imparted to the main heater; A and d being area and thickness of sample disc and θ_1 , θ_2 are the steady state temperatures recorded on hot and cold surface of the sample disc.

Value of λ_a for jute fibre and fire-retardant jute packings has been measured for different packing densities (ρ) at room temperature and the variation

has been presented in Fig. 2. The nature of the curve is similar to the one given by Tye² which has been theoretically interpreted by Fishenden and Saunders.³ The curves (Fig. 2) show that lowest value for (λ_a) of the specimens corresponds to a packing density of 380 kg/m³. A jute fibre sample of this particular packing density has been subjected to temperature variation from 100 to 300 K in a liquid air cryostat and the variation of λ_a with temperature (T) is shown in Fig. 3. In Table 1 are entered some measured values of λ_a including those of calibration specimen, viz. cork-board. The value of λ_a for mineral wool² at room temperature is also given in Table 1 for comparison.

It is seen (Table 1) that fire-retardant sample retains the insulating property better than the raw jute fibre at room as well as low temperatures. It is immediately clear that thermal insulating property of jute fibre packing is similar to other samples like slag wool, mineral wool, glass fibre, cork-board, etc.² The value of λ_a (min) is only slightly higher in the case of jute than those of conventional fibre samples. Another unwelcome feature of jute insulation is that its λ_a (min) corresponds somewhat to

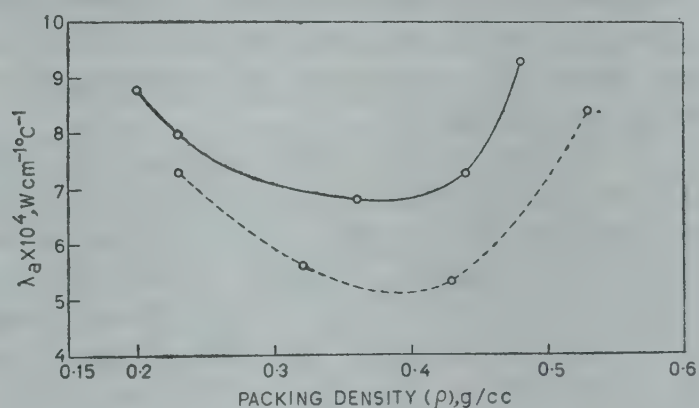


Fig. 2—Variation of apparent thermal conductivity of raw jute fibre (—) and fire-retardant jute fibre (---) with packing density. [The fibre diameter of the samples was taken to be 0.2 mm]

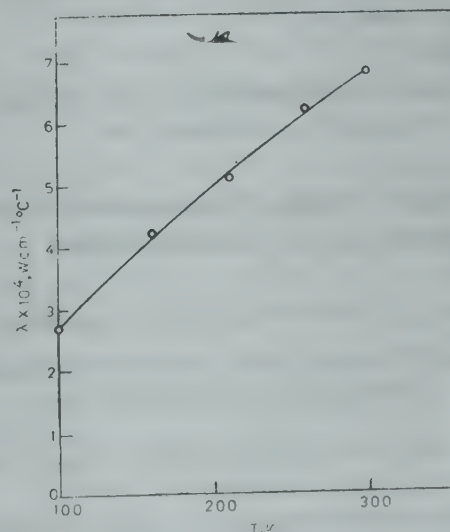


Fig. 3—Variation of apparent thermal conductivity (λ_a) of raw jute fibre with temperature (T)

Table 1—Values of λ_a for Raw and Fire-retardant Jute Samples along with that of Cork-board and Mineral Wool at Different Packings Densities

Sample	Packing density kg/m ³	$\lambda_a \times 10^4$, W cm ⁻¹ °C ⁻¹ at 300 K	at 100 K	Temp. gradient (dθ/dx) at 100 K
Cork-board*	200	4.8	2.6	2.0°C/mm
Cork-board*	340	5.8	2.8	2.3°C/mm
Raw jute packing (Mean fibre diameter 0.2 mm)	380	6.8	2.7	1.8°C/mm
Fire-retardant jute packing (Mean diameter 0.2 mm)	380	5.1	2.2	2.3°C/mm
Mineral wool**	150	3.3		

* used for calibration; ** given here for comparison.

a packing density higher than that for the fibres mentioned above. Nevertheless, the indigenous and cheap jute fibres deserve better attention in respect of cryogenic thermal insulation in our country as the fire retardant samples are available with marginally extra cost.

Studies on thermal insulation property of jute packing in vacuum which will evaluate the utility of such fibres as a component of a superinsulation device, are in progress.

The authors express their gratitude to the Jute Technological Research Laboratory (ICAR) Calcutta, for supplying the requisite jute samples and to the Indian Jute Industries Research Association for kindly making out the jute sample fire-retardant. They also acknowledge the help rendered by Dr P Sengupta of the Indian Cryogenic Council during this investigation.

References

1. Tye R P, *Thermal conductivity*, Vol. 1 (Academic Press, New York), 1969, 342.
2. Ref. 1, p 307.
3. Fishenden M & Saunders O A, *An Introduction to heat transfer* (Clarendon Press, Oxford), 1961.

Centrifugal Distortion Constants of Some Phosphorus (V) Chlorofluorides

R RAMASAMY, K SABAPATHY & K VENKATESWARLU
Department of Physics, P S G College of Arts & Science
(Autonomous), Coimbatore 641 014

Received 16 July 1979; revised received 7 January 1980

The centrifugal distortion constants of four phosphorus (V) chlorofluorides, PCl_4F , PCl_3F_2 , PCl_2F_3 and PClF_4 have been evaluated.

The structure of phosphorus (V) chlorofluorides, $\text{PCl}_n\text{F}_{5-n}$, has been studied by several investigators.¹⁻⁴ These investigations show that the structure of these compounds is a trigonal bipyramid and that the axial sites are occupied by the more electronegative atoms.

A preliminary normal coordinate analysis has been performed by Holmes^{5,6} for all these molecules. Recently, Venkateswarlu and coworkers⁷⁻⁹ have studied these molecules and evaluated some molecular constants. In the present investigation, the centrifugal distortion constants have been evaluated for the first time and are reported in this note.

The molecules PClF_4 and PCl_2F_3 belong to the C_{2v} symmetry. The normal vibrations of these molecules are distributed among various species as $5a_1 + 1a_2 + 3b_1 + 3b_2$. The molecule PCl_3F_2 has D_{3h} symmetry and its normal modes consist of $2a'_1 + 2a'_2 + 3e' + 1e''$ vibrations. The molecule PCl_4F possesses C_{3v} symmetry and its normal vibrations are distributed in $4a_1 + 4e$ species. The centrifugal distortion constants of PClF_4 , PCl_2F_3 , PCl_3F_2 and PCl_4F have been calculated making use of the relations given by Kivelson and Wilson^{10,11} and by Cyvin *et al.*¹²

The thermodynamic functions, namely, the heat content, free-energy, entropy and heat capacity have also been computed from the observed vibrational frequencies over the temperature range 100-1000 K. The calculations have been made for the ideal gaseous state at normal pressure based on a rigid-rotor harmonic-oscillator model. The results are available with the authors for any interested research worker.

The observed frequencies and the structural parameters have been taken from literature.¹⁻⁵ The force constants used in the present investigation have been taken from the work of Venkateswarlu and coworkers.⁷⁻⁹

The centrifugal distortion constants, $\tau_{\alpha\beta\gamma\delta}$ are presented in Table 1. PCl_3F_2 and PCl_4F are symmetric top molecules and hence, with regard to the numerical values of the non-vanishing $\tau_{\alpha\beta\gamma\delta}$ elements, the following relations are found to hold good:

$$\tau_{xxxx} = \tau_{yyyy}; \tau_{yyzz} = \tau_{zzzz}; \tau_{xxzz} = \tau_{yyzz};$$

$$2\tau_{xyxy} = \tau_{xxzz} - \tau_{xyxy}$$

The centrifugal stretching coefficients, D_J , D_K , D_{JK} , R_5 , R_6 and δ_J are listed in Table 2. D_J is positive for all the molecules. This indicates that the centrifugal forces about any given axis will always tend to increase the moment of inertia about that axis which in turn decreases the effective rotational constant. Since PClF_4 and PCl_2F_3 are asymmetric molecules, all the six centrifugal stretching

Table 1— $\tau_{\alpha\beta\gamma\delta}$ Elements of PClF_4 , PCl_2F_3 , PCl_3F_2 and PCl_4F (All values are in kHz)

$\tau_{\alpha\beta\gamma\delta}$	PClF_4	PCl_2F_3	PCl_3F_2	PCl_4F
τ_{zzzz}	-0.8878	-1.2007	-0.3422	-0.1853
τ_{yyyy}	-0.5736	-0.3521	-0.3422	-0.1853
τ_{zzzz}	-1.4948	-0.4399	-0.1722	-0.4929
τ_{xyxy}	-1.8469	-0.2178	-0.1570	-0.0587
τ_{yzyz}	-2.6920	-0.0572	-0.0612	-0.2120
τ_{zzzz}	-0.5429	-0.2609	-0.0612	-0.2120
τ_{xxxy}	-0.5874	-0.2387	-0.0281	-0.0678
τ_{zzzz}	-0.3338	-0.0448	-0.1490	-0.1512
τ_{yyzz}	-0.2295	-0.2809	-0.1490	-0.1512

Table 2—Centrifugal Stretching Coefficients of PClF_4 , PCl_2F_3 , PCl_3F_2 and PCl_4F (All values are in kHz)

Coefficient	PClF_4	PCl_2F_3	PCl_3F_2	PCl_4F
D_J	0.4048	0.0990	0.0856	0.0463
D_K	-0.9798	0.1140	-0.0071	-0.1180
D_{JK}	0.9487	0.0898	-0.0355	0.1950
R_5	0.2719	0.01508	—	—
R_6	0.1110	-0.00002	—	—
δ_J	0.0196	0.0055	—	—

coefficients exist for them. In the case of PCl_3F_2 and PCl_4F which are symmetric top molecules, the coefficients R_5 , R_6 and δ_J vanish.

The centrifugal stretching coefficients D_J , D_K , D_{JK} , R_5 , R_6 and δ_J which are linear combinations of the $\tau_{\alpha\beta\gamma\delta}$ elements can be used for the microwave spectral analysis of these molecules. The experimental values of the centrifugal distortion constants are often used as additional information for accurate determination of the force field of a molecule. Since no experimental values of the centrifugal distortion constants are available for these molecules, no comparison could be made.

References

- Griffiths J E, Carter (Jr) R P & Holmes R R, *J. chem. Phys.*, 41 (1964), 863.
- Holmes R R, Carter (Jr) R P & Petterson, *Inorg. Chem.*, 3 (1964), 1748.
- Holmes R R & Carter (Jr) R P *J. chem. Phys.*, 43 (1965), 1645.
- Holmes R R, *J. chem. Phys.*, 46 (1967), 3718.
- Holmes R R, *J. chem. Phys.*, 46 (1967), 3724.
- Holmes R R, *J. chem. Phys.*, 46 (1967), 3730.
- Venkateswarlu K & Girijavallabhan C P, *Z. Naturf.*, 24B (1969), 1256.
- Venkateswarlu K & Girijavallabhan C P, *Indian J. pure appl. Phys.*, 11 (1973), 393.

- Venkateswarlu K & Joseph P A, *Bull. Roy. Soc., Liege*, 38 (1969), 773.
- Kivelson D & Wilson (Jr) E B, *J. chem. Phys.*, 20 (1952), 1575.
- Kivelson D & Wilson (Jr) E B, *J. chem. Phys.*, 21 (1953), 1220.
- Cyvin S J, Cyvin B N & Hagen G, *Z. Naturf.*, 23a (1968), 1649.

Viscosity Behaviour of Diphenylamine-*p*-Toluidine System

NARSINGH BAHADUR SINGH*

Chemistry Department, T D Postgraduate College
Jaunpur UP

Received 30 December 1978; revised received 19 May 1980

Viscosity of diphenylamine-*p*-toluidine system has been determined at different temperatures above the melting point. The energy of activation for viscous flow is maximum in the case of eutectic mixture. The viscosity measurements suggest the maximum clustering of molecules in eutectic melt. There is no gradual rise or fall of activation energy for viscous flow with composition of the mixture. The values of excess volume also support the concept of maximum clustering between the parent molecules at eutectic composition.

In the past few years, there has been considerable addition¹⁻⁴ to the knowledge of microstructure, solidification behaviour thermochemistry and thermodynamics of eutectics. On the basis of heats of fusion measurements, Rastogi and coworkers⁵ have shown that ordering or clustering takes place during the melting of solid eutectics. Although organic eutectics are more suitable for studies and provide wider choice of materials, very little attention⁶ has been paid to the organic eutectics. Since *p*-toluidine forms simple eutectic with diphenylamine ($C_e = 0.53$ mole fraction of *p*-toluidine) having low melting temperature ($t_e = 18.4^\circ\text{C}$), it was proposed to study the viscosity behaviour and clustering phenomena at various temperatures near the melting point.

Diphenylamine (BDH) and *p*-toluidine (BDH) were purified by repeated crystallization in ethanol. The purity of each sample was checked by determining the melting points. The melting points of purified samples are 52.9 and 45.0°C respectively.

Viscosity measurements were made for pure components and various mixtures at various temperatures by technique similar to that adopted in Ref. 4. Ostwald viscometer washed with distilled water and finally by absolute alcohol was placed in

* Present address: Materials Research Centre, RPI Troy, NY, USA

an oven maintained at a temperature above the melting point of the substance. Molten liquid of the substance to be studied was transferred to the viscometer up to a fixed volume for the parent components and other mixtures. The viscometer was placed in an oil thermostat to record the flow time.

The measured densities of all binary molten mixtures showed a linear temperature dependence (Fig. 1) and fitted the equation;

$$d = A - BT \quad \dots (1)$$

The values of A and B are given in Table 1.

The results of viscosity measurements are plotted in Fig. 2 in the form of $\log \eta$ versus $1/T$. Straight lines are obtained indicating the validity of Arrhenius equation:

$$\log \eta = \log \eta_0 + E_\eta / 2.303 RT \quad \dots (2)$$

The activation energy E_η for the viscous flow is also recorded in Table 1. There is no gradation in increase and decrease of energy of activation for viscous flow and composition of the mixture.

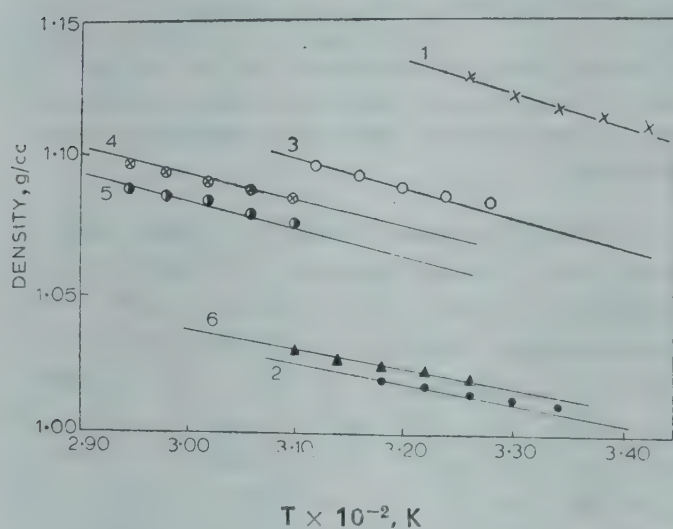


Fig. 1—Variation of density with temperature [Curve : 1, pure diphenylamine; 2, pure *p*-toluidine; mixtures containing different mole fractions *p*-toluidine ; 3, 0.282; 4, 0.495; 5, 0.534 and 6, 0.867]

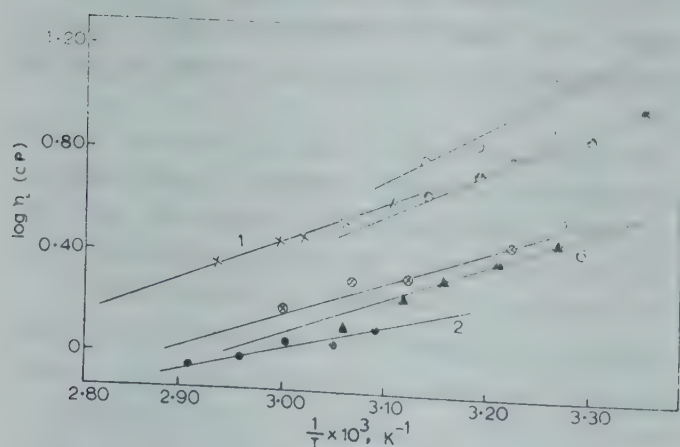


Fig. 2—Variation of viscosity with temperature [1, pure diphenylamine; 2, pure *p*-toluidine; mixtures containing different mole fractions of *p*-toluidine; 3, 0.282; 4, 0.495; 5, 0.534 and 6, 0.867]

Table 1—Computed Parameters for Density Equation, V^E and E_η for the Diphenylamine-*p*-Toluidine System

Mole fraction of <i>p</i> -toluidine	A	$B \times 10^5$	V^E (cc/mole)	E_η (cal/mole) $\times 10^{-3}$
Pure Diphenylamine	1.174	9.692	—	1.518
0.282	1.134	9.524	-1.1744	1.384
0.495	1.116	8.335	-0.6910	1.840
0.534 (eutectic)	1.105	7.691	-0.5853	2.223
0.867	1.052	6.122	-2.2342	1.359
1.000 Pure <i>p</i> -toluidine	1.044	5.557	—	1.021

The values of viscosity and activation energy for eutectic are greater than those for other mixtures and parent components. The higher values of viscosity and activation energy for eutectic at melting point indicate that the molecules arrange their structure with greater tendency of interlocking at eutectic composition. This behaviour has been attributed to the cluster formation in eutectic melt. Structurally the clusters can be regarded as the combined molecules of parent phases whose life is sufficiently long and compel them to move as whole in viscous flow. As the temperature of the liquid is raised, degree of clustering goes on diminishing. The idea of clustering was supported by excess molar volume also. The value of the excess volume for the eutectic is highest among all the mixtures. This indicates maximum attraction between the molecules at this composition. Schneider⁷ has indicated that prefreezing might be regarded in connection with a change in nature of chemical bond in the liquid or solid state. In case of simple binary eutectics, it has been established that molecules in crystals of pure parent components are held together by van der Waal's forces. One would expect that in eutectic mixture, the molecules of components 1 and 2 should be distributed at random and held by van der Waal forces of some definite magnitude. It can be regarded that eutectics are formed by most preferred arrangements of the phases. The gradual change from random distribution of two kinds of molecules at high temperature to close linking of same kind of molecules occurs as the solidification approaches. This is supported by the fact that viscosity decreases with the increase of temperature of mixtures. Viscosity definitely has correlation with linkage property of different molecules in binary melts. In the eutectics, where mutual solid solubility is restricted, the heterogeneity in the liquid state

near solidification temperature can be well explained from the view-point of binding energy between the molecules of first-second, first-first and second-second components. It can be assumed that the linkage between the molecules of first-first and second-second components gradually increases as the solidification temperature approaches. Holding at this temperature merely gives⁸ more opportunity to the alloy to segregate prior to solidification.

The author is indebted to Prof. R P Rastogi, Chairman, Chemistry Department, Gorakhpur University and Prof. M E Glicksman, Chairman, Materials Engineering Department, R P I, Troy, N Y for valuable guidance and encouragement. Thanks are also due to John I Mickalonis for helpful suggestions.

References

1. Jackson K A & Hunt J D, *Trans. Met. Soc. AIME*, **236** (1966), 1129.
2. Chalmers B, *Principle of solidification* (John Wiley, New York), 1964.
3. Bassi P S & Sachdev G P, *Indian J. Chem.*, **12** (1974), 727.
4. Singh Narsingh Bahadur, *J. Crystal Growth*, **43** (1978), 637.
5. Rastogi R P, Singh N B & Singh Narsingh Bahadur, *J. Crystal Growth*, **40** (1977), 234.
6. Singh N B & Singh Narsingh Bahadur, *J. Crystal Growth*, **28** (1975), 267.
7. Schneider A, Heymer G & Hilmer O, *Z. anorg. allgem. Chem.*, **286** (1956), 118.
8. Glicksman M E & Sokolowski Robert W, Unpublished work.

Estimation of Limiting Solid Volume of Polar Substances: An Analytical Method

B K SHARMA

Department of Physics, Physical Sciences Laboratories
Regional College of Education, Bhubaneswar 751 007

Received 25 September 1978

An analytical method has been suggested for the evaluation of triple-point limiting solid volume of polarizable and hydrogen-bonded liquids in terms of the characteristic volume. The calculated values show fair agreement with literature values for 20 substances.

The phase transition from solid to liquid results in a sudden increase in all transport properties and an indefiniteness of positional ordering of atoms. In the theory of melting, solid volume V_s at the triple point (or melting point as the case) has been found to be a very useful tool for studying the thermodynamic properties of liquids,¹⁻⁵ locating solid-liquid phase transition and examining melting behaviour.⁶ No significant effort has so far been

made to estimate such an important parameter on theoretical basis. Hence, its evaluation is very important for a correct understanding of the mechanism of melting process.

Recently, Sharma⁷ has proposed an analytical method of estimating V_s of simple non-polar liquids in terms of characteristic volume V^* . As an extension to this method to include polarizable non-polar, and hydrogen-bonded liquids, we modify the treatment and compute, in this note, the values of V_s in case of the liquids having strong polar interactions.

Thermal motions of molecules in liquids are complex⁸ and the instantaneous liquid structure continuously varies markedly with thermodynamic state. Consequently, unlike crystalline solids, the coordination number Z is not constant but steadily decreases with temperature.⁹ For simple liquids, having fcc structure ($Z=12$), Z decreases from 12 to about 10 at the melting point T_m and further to about 4 at the critical points.^{2,9} Hence, the effective coordination number Z' in expanded liquid region at any temperature T can be written as⁷

$$Z' = Z A (V_s/V) \quad \dots(1)$$

in which

$$A = a (T_B/T_c) \quad \dots(2)$$

where Z is the coordination number at absolute zero temperature, T_B and T_c are respectively Boyle temperature and critical temperature, a is the critical state compressibility ratio and V the molar volume of liquid at reference temperature T .

Holborn and Otto¹⁰ find experimentally the following relation for liquids

$$(T_B/T_c) = 2.75 \quad \dots(3)$$

The present proposal of Eq. (1) is in close qualitative and quantitative agreement with experiment^{2,9} throughout the whole liquid range of temperature from T_m to T_c .

For simple non-polar liquids, the expression for V_s at T_m is given by⁷

$$V_s = 2^{1/2} A V^* \quad \dots(4)$$

Eq. (4) cannot be utilized directly to estimate values of V_s of polar molecules since the nature of intermolecular interactions in polar molecules differs markedly from that in simple spherical (non-polar) molecules.

Following inverse dependence of Z on molar volume V as suggested earlier,⁷ we obtain an alternative expression for Z' for polar liquids by introducing an approximation

$$\frac{\sim}{a} \sigma_0^3 Z' = \sigma^3 Z \quad \dots(5)$$

where $\tilde{a} (= a_0/a)$ is the reduced parameter and a_0 is the critical compressibility factor of argon, σ_0 the equilibrium molecular diameter and σ the nearest neighbour distance of the lattice.

At the melting point, the molar volumes of solid and liquid are related to molecular diameters by an expression given by⁷

$$V_s/V^* = 2^{1/2} (\sigma/\sigma_0)^3 \quad \dots(6)$$

From Eqs. (1), (5) and (6), we obtain final a expression for V_s for the solid phase at the melting point

$$V_s = 2^{1/2} B V^* \quad \dots(7)$$

where

$$B = \tilde{a} A \quad \dots(8)$$

Sharma and Bhatnagar¹¹ have suggested that V^* of any simple liquid has been assumed to bear a certain ratio to its critical volume V_c such that

$$V^* = a V_c \quad \dots(9)$$

An alternative suggestion has been given by Fang and Wiehe¹² that V^* of any molecule may be expressed in terms of V_c of argon. Combining both these proposals, we obtain an expression for V^* of any general molecule including polar molecules as

$$V^* = V_c (V^*/V_c)_{\text{argon}} = \tilde{a} a V_c = a_0 V_c \quad \dots(10)$$

Table 2—Comparison of Calculated and Literature Values of V^* and V_s of Strongly Polar and Hydrogen-Bonded Molecules

Substance	a (Ref. 13,14)	V^* , cc mole ⁻¹		V_s , cc mole ⁻¹	
		[Eq. (10)]	(Ref. 17)	[Eq. (7)]	(Ref. 3, 19)
Water	0.243	17.17	15.07	19.49	19.82
Ammonia	0.244	21.02	18.84	23.86	22.32
Phosphine	0.273	33.11	—	37.58	41.44
Acetone	0.238	62.20	54.45	70.62	—
Methanol	0.220	34.45	31.72	39.12	—
Ethanol	0.249	48.82	45.98	55.43	—

It may be observed that Eqs. (7) and (10) of V^* and V_s respectively, for polar liquids have been obtained from Eqs. (4) and (9) for simple non-polar liquids

only by introducing the parameter \tilde{a} .

Eqs. (4), (7) and (10) are very simple and important since V_s and V^* can be readily calculated from the knowledge of critical constants only. Hence, they are very convenient and involve fewer experiments. In Table 1 the calculated values of V^* using Eq. (10) and V_s using Eq. (4) for several slightly polarizable non-spherical substances have been compared with those reported by other workers. Table 2 reports the calculated values of V^* and V_s using Eqs. (10) and (7) for hydrogen-bonded and strongly polar substances for which experimental data for comparison are available.

It may be observed from Tables 1 and 2 that the agreement between the calculated and literature values of V^* and V_s in most of the substances considered is fair, in view of the simplicity of the model and approximations. However, the calculated values are limited by the accuracy of the experimental values of critical constants utilized in the model calculations. The estimated values of V_s have been utilized for explaining the melting point properties of liquids. Financial assistance from CSIR, New Delhi, is thankfully acknowledged by the author.

References

1. Mansoori G A & Canfield F B, *J. chem. Phys.*, **51** (1969), 4958, 4967.
2. Marchi R P & Eyring H, *J. Chem. Educ.*, **40** (1963), 562.
3. Lu W C, Jhon M S, Ree T & Eyring H, *J. chem. Phys.*, **46** (1967), 1075.
4. Yosim S J & Owens B B, *J. chem. Phys.*, **39** (1963), 2222.
5. Kanno H, *Bull. Chem. Soc., Japan*, **45** (1972), 2687.
6. Hoover W G & Ross M, *Contemp. Phys.*, **12** (1971), 339.
7. Sharma B K, *Phys. Status Solidi (C)*, **99** (1980), K 121.

Table 1—Comparison of Calculated and Literature Values of V^* and V_s of Slightly Polarizable Non-Spherical Molecules

Substance	a (Ref. 13, 14)	V^* , cc mole ⁻¹		V_s , cc mole ⁻¹	
		[Eq. (10)]	(Ref. 15-17)	[Eq. (4)]	(Ref. 3, 18-20)
Ethylene	0.275	36.81	37.11	39.36	39.96
Benzene	0.265	74.66	70.13	77.05	77.00
Carbon tetra-chloride	0.272	80.60	76.00	85.23	87.10
Deuterium	0.310	17.52	—	21.12	20.48
Methyl chloride	0.276	41.77	37.94	44.81	45.54
Carbon monoxide	0.283	26.28	26.30	28.92	29.05
Chlorine	0.275	36.14	—	38.64	39.18
Bromine	0.288	39.55	—	44.28	41.58
Carbon dioxide	0.274	27.51	25.71	29.30	—
Ethane	0.275	41.37	41.05	44.23	—
Propane	0.270	56.94	55.68	59.77	—
Propylene	0.275	52.84	50.92	56.49	—
Cyclohexane	0.271	89.95	85.12	94.77	—
Neopentane	0.269	88.47	85.99	92.53	—

8. Singwi K S & Sjolander A, *Phys. Rev.*, **119** (1960), 863.
9. Mikolaj P G & Pings C J, *J. chem. Phys.*, **46** (1967), 1401, 1412.
10. Holborn L & Otto J, *Phys. Z.*, **33** (1925), 9; 38 (1926), 359.
11. Sharma B K & Bhatnagar H L, *Indian J. pure appl. Phys.*, **13** (1975), 328.
12. Fang H H & Wiehe I A, *Ind. Engng. Chem. Fundam.*, **12** (1973), 173.
13. Lange N A, *Handbook of chemistry*, (McGraw-Hill, New York), 1967, 1669-1674.
14. Kobe K A & Lynn R E, *Chem. Rev.*, **52** (1953), 117.
15. Abe A & Flory P J, *J. Am. Chem. Soc.*, **87** (1965), 1838.
16. Renon H, Eckert C A & Prausnitz J M, *Ind. Engng. Chem. Fundam.*, **6** (1967), 52.
17. Winnick J, *Ind. Engng. Chem. Fundam.*, **11** (1972), 239.
18. Mc Laughlin D R & Eyring H, *Proc. natn. Acad. Sci.*, **55** (1966), 1031.
19. Moelwyn-Hughes E A, *Physical chemistry*, (Pergamon, London), 1965, 748.
20. Ree T S, Ree T & Eyring H, *J. chem. Phys.*, **41** (1964), 524.

Appendix

Derivation of Eq. (4) for simple liquids

$V_s = 2^{1/2} A V^*$ (taken from Ref. 7).

The effective coordination number Z' in expanded liquid region is given by

$$Z' = Z A (V_s/V) \quad \dots(A.1)$$

If σ^* is hard core molecular diameter, σ the nearest neighbour distance of the lattice and σ_0 the equilibrium molecular diameter (distance between two successive equilibrium positions) then we may readily obtain

$$(V_s/V^*) = (\sigma/\sigma^*)^3 \quad \dots(A.2)$$

Since thermal atomic vibrations in liquids are complex, not necessarily confined to their particular equilibrium position, σ is not necessarily equal to σ_0 . However, the ratio (σ/σ_0) may be close to unity for liquids [Eyring *et al.*, 'Theory of rate processes'; (McGraw-Hill, New York), 1941, 481]. Hence, we introduce the approximation

$$\sigma = D \sigma_0 \quad \dots(A.3)$$

where D is a constant close to unity for most substances. It is well known that limiting value of molecular diameter σ_0 for the L-J potential [J E Lennard-Jones and A F Devonshire, *Proc. R. Soc.*, **A163** (1937), 53; **A165** (1938), 1.] is given by

$$\sigma_0 = 2^{1/6} 6^* \quad \dots(A.4)$$

From Eqs. (2) to (4) we obtain

$$(V_s/V^*) = 2^{1/2} D^3 = 2^{1/2} (\sigma/\sigma_0)^3 \quad \dots(A.5)$$

Following inverse dependence of Z on molar volume V , we obtain an alternative expression for Z' by introducing approximation

$$Z' \sigma_0^3 = Z \sigma^3 \quad \dots(A.6)$$

For the solid phase, at the melting point, substitution of Eqs. (1), (4), (5) into Eq. (6) gives the required expression for V_s as

$$V_s = 2^{1/2} V^* A \quad \dots(A.7)$$

and

$$D = (Z'/Z)^{1/3} = A^{1/3} \quad \dots(A.8)$$

with $A = a(T_B/T_c)$ for the solid phase at T_m from Eq. (1).

Green's Function Calculations on the Photoelectron Spectra of Some Small Heteroatomic π -Electron Systems

R GOPAL & P C MISHRA

Spectroscopy Laboratory, Department of Physics
Banaras Hindu University, Varanasi 221 005

Received 4 August 1979; revised received 4 January 1980

The Green's function diagrammatic technique has been applied to calculate the orbital energies and charge distributions for some small heteroatomic π -electron systems. The electron-electron interactions have been treated as perturbation on the remaining part of the Hamiltonian and the Pariser-Parr-Pople approximation has been employed to calculate the integrals. Ionization potentials of the molecules estimated in the Koopmans' approximation are in reasonably good agreement with experimental results.

Molecular orbital (MO) theory with proper configuration interaction (CI) provides accurate description of molecular electronic structure and spectra. The Pariser-Parr-Pople (PPP) theory is very reliable for calculating π -electronic properties of conjugated systems. But the slow convergence of CI expansions seriously limits the usefulness of this approach, showing the need for alternative techniques. Fortunately, quite powerful alternatives are provided by the methods which do not require the calculation of wavefunctions and one of these is the Green's function or propagator method (1). The diagrammatic perturbation formalism of this method is especially simple and elegant since many terms in the perturbation series cancel, and in place of each group of several terms one has to evaluate only one diagram. Obviously, by a proper selection of perturbation and computational procedure, one can evaluate the perturbation series very satisfactorily. The situation gets further simplified if the important diagrams in the series could be selected or if a series of diagrams summed. Thus inclusion of electronic correlations is easier in the Green's function formalism (GFF) than in the molecular orbital approach. Therefore, it is desirable that propagator formalisms of the various MO methods be developed and their predictive power tested and further enhanced beyond the existing limits.

Scope of the study—The Green's function method, in its various forms has been applied to molecular problems by many workers.^{1,2} Probably the most widely investigated approximate form of molecular orbital theory in GFF, is the PPP scheme.³⁻⁶ Tanimoto and coworkers⁴⁻⁶ have shown how, taking the electron-electron (e-e) interaction as a perturbation on the remaining part of the Hamiltonian, the Green's function method can be applied to study the electronic structure and spectra of π -electron systems using the PPP approximations for integrals.^{7,8} They have shown that the method works reasonably well for molecules having carbon atoms as π -electron centres. An aim of the present study was to apply the GFF of the PPP method due to Tanimoto and coworkers^{4,5} to the ground state π -electronic structure of some heteroatomic systems, e.g. ethylene and formaldehyde derivatives. Different types of substituents have been considered in order to examine the quality of results predicted by the method for molecules of varying complexities.

We have selected these molecules for the calculations in order to understand the following additional aspects related to them. The first observed π -ionization potential (π -IP) of formamide is less than that of formaldehyde whereas the first IP of formic acid is about 1.5 eV more. Similarly, it is observed that although the first π -IP of chloro- and fluoro-ethylenes are very close together the second π -IP of the former is appreciably less than that of the latter. In the light of the similarity in behaviour of the F and Cl atoms and the NH_2 and OH groups in substituted π -electron systems, these observations are somewhat surprising. As the systems are small, one may conjecture that these observations may be partly due to the involvement of σ -electrons in the photoelectronic process in some manner. But while studying these problems, firstly it must be accurately investigated as to what differences can arise in the spectra of these molecules due to the differences of their π -electronic structures. Thus the other aim of the present study was to examine if these observations on photoelectron spectra can be explained within the π -electron approximation.

In this work, we have used the Koopmans' theorem according to which first order SCF orbital energies represent IPs. There are a few other methods which may be used reliably to obtain IPs of molecules. In one of these known as the Δ SCF method, separate SCF calculations are performed to obtain total energies for a molecule and its ion and the differences of total energies give the IPs. Since a small difference between two large energies is calculated in this method, the results obtained are

not always quite satisfactory.⁹ In another method, CI is used in the energy calculations for the molecule and its ion.¹⁰ Still another method is based on the ionization operator technique and it leads to a direct evaluation of IPs.²⁻¹¹ The method based on the Koopman's theorem is inferior to the other methods but it is also much simpler than these in actual applications, and by a proper choice of parameters in a semi-empirical theory it may lead to quite reasonable values for IPs. This aspect of the method has been discussed later in this paper. Due to its simplicity, we have used the Koopman's theorem to obtain molecular IPs in this work.

Theory—Let us define the vector operators

$$\vec{a}_\eta^\dagger = (a_{1\eta}^\dagger, a_{2\eta}^\dagger, \dots, a_{n\eta}^\dagger); \vec{a}_\eta = \begin{pmatrix} a_{1\eta} \\ a_{2\eta} \\ \vdots \\ a_{n\eta} \end{pmatrix}$$

where $a_{1\eta}^\dagger$ is an operator that creates an electron in the atomic orbital 1 with spin η and $a_{1\eta}$ is the corresponding destruction operator. Now let us define the one-particle Green's function matrix as follows:

$$\{G_{\eta\eta'}(t, t')\}_{ij} = -i \langle T \{ a_{i\eta}(t) a_{j\eta'}^\dagger(t') \} \rangle$$

where T is the chronological operator. In the zero differential overlap (ZDO) approximation^{7,8} we make the following assumption:

$$\iint d\vec{r}_1 d\vec{r}_2 \phi_{p\eta}(\vec{r}_1) \phi_{r\eta'}(\vec{r}_2) V(|\vec{r}_1 - \vec{r}_2|) \phi_{s\eta'}(\vec{r}_2) \phi_{q\eta}(\vec{r}_1) \\ = \gamma_{pr}(1 - \delta_{\eta\eta'}) \delta_{pq} \delta_{rs}$$

where ϕ is an atomic orbital and γ_{pr} represents repulsion integral. This gives us a PPP Hamiltonian $H = H_0 + H'$ where

$$H_0 = \sum_{r,\eta} (\alpha_{rr} - \mu) a_{r\eta}^\dagger a_{r\eta} + \sum_{r \neq s} \beta_{rs} a_{r\eta}^\dagger a_{s\eta}$$

and

$$H' = \frac{1}{2} \sum_{\substack{p, q, r \\ \eta \neq \eta'}} \gamma_{pq} a_{p\eta}^\dagger a_{q\eta} a_{r\eta}^\dagger a_{r\eta} \\ + \frac{1}{2} \sum_{\substack{p, q, r \\ \eta \neq \eta'}} \gamma'_{pr} a_{p\eta}^\dagger a_{q\eta} a_{r\eta'}^\dagger a_{r\eta'}$$

Here α_{rr} and β_{rs} are the usual core integrals and μ is the chemical potential. The value of μ is set somewhere between the energies of the highest filled and lowest empty π -molecular orbitals. The prime on γ_{pr} implies that $p \neq r$. The calculations are carried out treating H' as a perturbation on H_0 .

Now it can be shown that the unperturbed Green's function matrix $\hat{G}_0(\omega)$ corresponding to H_0 would satisfy the equation

$$\omega \hat{G}^0(\omega) = \hat{I} + (\hat{\epsilon} + \hat{\beta}) \hat{G}^0(\omega)$$

where \hat{I} is the unit matrix and ω represents frequency. The energies of elementary excitation corresponding to $\hat{G}_0(\omega)$ can be obtained by solving the secular equation

$$\det |\hat{I} - (\hat{\epsilon} + \hat{\beta})| = 0$$

If the perturbation be represented in matrix form by the self-energy matrix $\hat{\Sigma}$, the perturbed Green's function can be obtained from the Dyson equation

$$\hat{G}(\omega) = [\hat{G}^0(\omega) - \hat{\Sigma}(\omega)]^{-1}$$

The perturbation can be calculated using the diagrammatic technique and the Feynman-Dyson rules described by Taminoto and Shimada.⁴

The first order diagrams are given in Fig. 1

The total first order (FO) self-energy matrix elements in the PPP approximation are given as follows:

$$\begin{aligned} \sum_{lm}^{(1)} &= i \gamma_{lm} (1 - \delta_{lm}) \int_{-\infty}^{\infty} \frac{d\omega'}{2\pi} e^{-L\omega'(0-)} G_{lm}^0(\omega') \\ &- i \sum_p \gamma_{lp} (2 - \delta_{lp}) \int_{-\infty}^{\infty} \frac{d\omega'}{2\pi} e^{-L\omega'(0-)} G_{pp}^0(\omega') \delta_{lm} \end{aligned}$$

The total e-e interactions have been treated in this approach as a perturbation on the rest of the Hamiltonian. But as the e-e interactions are quite large, this approach may not adequately account for the total perturbed energy. To remedy this shortcoming, the FO perturbation calculation was repeated including the FO perturbation correction (say χ) in the unperturbed Hamiltonian. That is, we redefine the perturbation as follows:

$$\begin{aligned} H &= (H_0 + \chi) + (H' - \chi) \\ &= \tilde{H}_0 + \tilde{H}' \end{aligned}$$

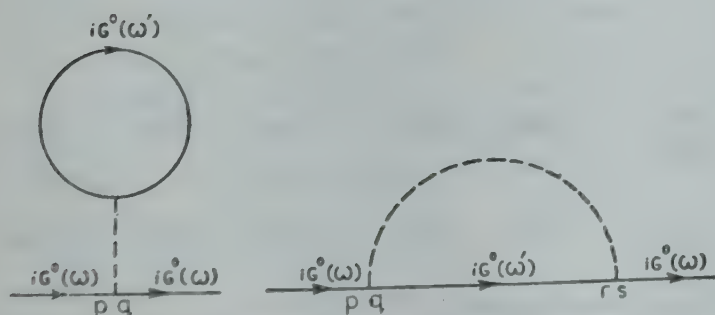


Fig. 1—First order diagrams using the Feynman-Dyson technique for perturbation calculations

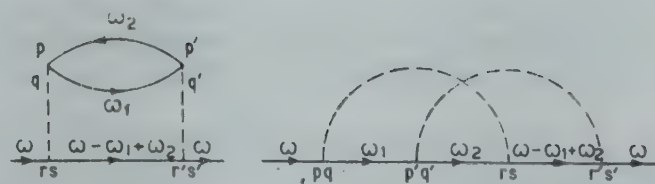


Fig. 2—Irreducible diagrams [p, q, r and s represent atomic orbitals]

Repeating the FO perturbation calculation implies the FO correction due to \tilde{H}' on \tilde{H}_0 . This may be carried out repeatedly till the further FO corrections become negligibly small. At this stage, we have the Hartree-Fock SCF Hamiltonian. Convergence is reached in this calculation in a few (e.g. four) iterations.

Second order (SO) perturbation calculation is performed after the FO SCF level. As the unperturbed Hamiltonian for the SO calculation is the Hartree-Fock Hamiltonian, only two irreducible diagrams which are given in Fig. 2 contribute to the SO perturbation

In the PPP approximation, the matrix elements for the total SO self-energy are given as follows:

$$\begin{aligned} \sum_{lm}^{(2)}(\omega) &= - \sum_{pp'} \gamma'_{lp} \gamma'_{p'm} \int_{-\infty}^{\infty} \int_{-\infty}^{\infty} \frac{d\omega_1}{2\pi} \frac{d\omega_2}{2\pi} \\ &G_{lp}^0(\omega_1) G_{p'p}^0(\omega_2) G_{pm}^0(\omega - \omega_1 + \omega_2) \\ &+ \sum_{pp'} (\gamma_{lp} \gamma_{p'm} + \gamma'_{lp} \gamma'_{p'm}) \int_{-\infty}^{\infty} \int_{-\infty}^{\infty} \frac{d\omega_1}{2\pi} \frac{d\omega_2}{2\pi} \\ &\times G_{pp'}^0(\omega_1) G_{p'p}^0(\omega_2) G_{lm}^0(\omega - \omega_1 + \omega_2) \end{aligned}$$

Calculations and results—While the orbital energies correct up to the SCF level were calculated for all the molecules. SO calculations were performed only for three representative cases, viz. ethylene, chloroethylene and formaldehyde. The β -integrals were evaluated using the Wolfsberg-Helmholtz formula.^{12,13} The one- and two-centre repulsion integrals were calculated respectively using the (IP-EA) approximation and the Nishimoto-Mataga formula.¹⁴ Molecular geometries were taken from the literature.¹⁵ The valence state IPs and the electron affinities of various atoms which occur in the present calculations were taken from the literature¹⁶ and are presented in Table 1. One can easily calculate the values of the β -integrals as well as the one- and two-centre repulsion integrals from a knowledge of these and the appropriate formulae. The calculated π -orbital energies, electronic charge

Table 1—Valence State Ionization Potential and Electron Affinities of Various Atoms

	Atoms					
	C	O(OH)	O(C=O)	N(NH ₂)	F	Cl
Ionization potential	11.190	36.600	14.640	28.780	36.710	24.650
Electron affinity	0.010	14.570	1.980	12.000	18.040	13.070

densities and bond orders for the molecules studied are presented in Table 2. The results due to Tanimoto and Shimada⁴ for ethylene are compared with those of the present calculations. Experimental values of IPs were taken from literature.^{15,17}

Discussion—Some general comments related with the largeness of perturbation and consequent effects on our results seem to be in order. Whenever perturbation is large, in general, a difficulty is expected in convergence in the calculated energy and in such a case second and higher order perturbation terms may be quite important. This difficulty may be overcome to some extent by proper choice of parameters so as to incorporate electron correlations adequately. But generally it leads to predictions of

IPs by the Koopman's theorem higher by 10-20% than the experimental results. Therefore, the choice of parameters to obtain accurate IPs by the Koopman's theorem amounts to neglect of electron correlations and second and higher order terms in the perturbation series. This will affect the total energy also. Fortunately, the choice of parameters works reasonably well even for a series of related molecules since the electron correlation energy coming from second and higher order perturbations is largely cancelled by the electronic reorganizational energy that follows ionization, both these energies being evaluated by the same parameters. This cancellation is in fact the basis of reliability of the Koopman's theorem.¹⁸ The above arguments may be understood by the example of ethylene studied in this paper (Table 2). In going from the first to the second order correction to the occupied orbital energy of ethylene is larger in our case (~ 0.4 eV) than in that of Tanimoto and Shimada (~ 0.1 eV), since our choice of parameters predicts the IP much better than that of the other workers.⁴ For chloroethylene and formaldehyde also, SO corrections are of the same order of magnitude as it is for ethylene in our calculations. But the

Table 2—Orbital Energies, Charges and Bond Orders

Molecule	Order	Orbital energies (eV)	Exptl IP (eV) †	Charges on atoms			Bond orders for	
				1	2	3	1-2 Bond	2-3 Bond
$\begin{array}{c} \text{H} & & \text{H}' \\ & \diagdown & / \\ & \text{C} = \text{C} \\ & / & \diagdown \\ \text{H} & & \text{H} \end{array}$	First (SCF)	-0.447 (1.115)	10.507	1.000	1.000	1.000		
Second	-10.757 (-12.875) -0.089 (1.195) -11.145 (-12.955)	1.000						1.000
$\begin{array}{c} \text{H} & & \text{F} \\ & \diagdown & / \\ & \text{C} = \text{C} \\ & / & \diagdown \\ \text{H} & & \text{H} \end{array}$	First (SCF)	+0.098 -10.005 -19.361	10.31 (17.97)*	1.958	0.974	1.068	0.206 0.978	
$\begin{array}{c} \text{H} & & \text{Cl} \\ & \diagdown & / \\ & \text{C} = \text{C} \\ & / & \diagdown \\ \text{H} & & \text{H} \end{array}$	First (SCF)	-0.078 -9.889 -14.285 +0.037 -9.502 -13.922	10.00 11.79	1.944	0.984	1.072	0.240 0.970	
	Second							
$\begin{array}{c} \text{H} & & \text{O} \\ & \diagdown & / \\ & \text{C} = \text{O} \\ & / & \diagdown \\ \text{H} & & \end{array}$	First (SCF)	-1.525 -12.197	10.88	1.254	0.746		0.968	
	Second	-1.155 -12.459						
$\begin{array}{c} \text{H} & & \text{O} \\ & \diagdown & / \\ & \text{C} = \text{O} \\ & / & \diagdown \\ \text{H}_2\text{N}_3 & & \end{array}$	First (SCF)	-0.207 -10.343 -15.929	10.52 14.62	1.446	0.768	1.786	0.806 0.514	
$\begin{array}{c} \text{H} & & \text{O} \\ & \diagdown & / \\ & \text{C} = \text{O} \\ & / & \diagdown \\ \text{HO}_3 & & \end{array}$	First (SCF)	-0.951 -11.364 -16.937	12.37 15.40	1.346	0.748	1.906	0.905 0.344	

† All experimental values are adiabatic ionization energies, unless otherwise specified

* Highest observed vertical ionization energy

comparatively larger magnitude of the SO correction in our calculation than in that of Tonimoto and Shimada does not indicate serious errors in the prediction of total energy, as these corrections are less than 4% in all the cases studied.

We make the following specific observations for the IPs of the various molecules. For fluoroethylene the first calculated IP is in reasonably good agreement with experiment (error $\sim 3\%$) while the second calculated IP is higher than the experimental value. Similarly for chloroethylene, the first calculated π -IP is in very good agreement with the experimental value while the second calculated π -IP is appreciably higher than the observed one. However, we find that the calculation agrees with the experimental results, in that the first π -IPs of fluoroethylene and chloroethylene are very close together but the second IP of the former is appreciably higher than that of the latter.

For formaldehyde, the calculated IP is a little higher than the experimental value. In the case of formamide the first observed peak in the photo-electron spectrum¹⁷ is quite complex and the first π -, and first n -IPs are very close together. While the n -IP is estimated to be 10.13 eV, the π -IP is uncertain, but its value lies between 10.13 and 10.52 eV. The calculated π -IP is well between these two limits. The second π -IP is higher than the observed value. For formic acid, the first IP is about 8% less than the observed value while the second one is more than the corresponding experimental value by about the same amount. However, the calculation shows that both the π -IPs of formic acid would be more than those of formamide, in agreement with experiment.

Charges and bond orders are also quite easy to understand physically. In going from ethylene to the halogenated ethylenes we find that the halogen atoms direct the electronic charge to accumulate at their *ortho* position in agreement with the usual experience. The bond orders show that the $C\equiv C$ bonds are strongly double in nature while the $C-F$ and $C-Cl$ bond orders have values similar to those found in aromatic molecules.²⁰ In formaldehyde, the electronic charge density is more at the oxygen atom than at the carbon atom and the $C=O$ bond is strongly double in nature. In formic acid and formamide, electronic charges accumulate further at the oxygen atom which lies at the *ortho* position of the OH and NH_2 groups. This is also expected from the nature of the substituents. Electronic charge densities at the carbon atom and $C=O$ π -bond

orders are appreciably less in formic acid and formamide as compared to those of formaldehyde. The $C-O$ (OH) and $C-N$ (NH_2) π -bond orders are appreciable.

This study has thus shown that the GFF of the PPP model makes reliable predictions for various physical quantities of π -electron systems having different types of atoms. Also it has shown that such a calculation can be very helpful in understanding how the π -IPs would vary in going from one molecule to another in a series. In particular, it has shown that many marked differences between the IPs of formamide and formic acid and similarly between those of chloro- and fluoro-ethylenes can be understood at least qualitatively within π -electron approximation without any inclusion of σ -electron effects.

The authors are thankful to Prof. D K Rai for his interest in the work and to CSIR, New Delhi, for financial assistance.

References

1. Öhrn Y, *The new world of quantum chemistry*, edited by B Pullman and R G Parr, (Riedel, Boston), 1976, 57.
2. Cederbaum L S, *J. Phys.*, **B8** (1975), 290.
3. Linderberg J & Öhrn Y, *Proc. R. Soc.*, **A285** (1965), 445.
4. Tonimoto O & Shimada K, *Molec. Phys.*, **23** (1972), 745.
5. Shimada K & Tonimoto O, *Molec. Phys.*, **23** (1972), 765.
6. Tonimoto O & Toyoda K, *Molec. Phys.*, **24** (1972), 1257.
7. Pariser R & Parr R G, *J. chem. Phys.*, **29** (1953), 466, 767.
8. Pople J A, *Trans. Faraday. Soc.*, **49** (1953), 1375.
9. Cade P E, Sales K D & Wahl A C, *J. chem. Phys.*, **44** (1966), 1973.
10. Billingsley F P, *J. chem. Phys.*, **62** (1975), 864; **63** (1975), 2267.
11. Simons J & Smith W D, *J. chem. Phys.*, **58** (1973), 4899.
12. Wolfsberg M & Helmholz L, *J. chem. Phys.*, **20** (1952), 837.
13. Karlsson G & Mårtensson O, *Theoret. Chim. Acta*, **13** (1969), 195.
14. Nishimoto K & Mataga N, *Z. phys. Chem.*, **12** (1957), 335.
15. Herzberg G, *Molecular spectra and molecular structure III. Electronic spectra and electronic structure of polyatomic molecules* (Van Nostrand, Reinhold Co. New York) 1966.
16. Mishra P C & Rai D K, *Int. J. quant. Chem.*, **6** (1972), 47.
17. Robinson J W, *Handbook of spectroscopy* Vol. I, CRC Press 1978.
18. Von Niessen W, Diercksen & Cederbaum L S, *J. chem. Phys.*, **67** (1977), 4124.

Temperature Variation of NQR Frequencies in 2,6-Dichlorobenzamide

D V RAMANAMURTI, P VENKATACHARYULU &
D PREMASWARUP

Department of Physics, Nagarjuna University
Nagarjunanagar 522 510

Received 20 July 1979; revised received 17 December 1979

Temperature variation study of the two NQR lines in 2,6-dichlorobenzamide compound has been carried out from liquid nitrogen to room temperature. As the compound under investigation is a molecular crystal, Brown's theory is used in analyzing the experimental data. The agreement is good and there are no systematic differences between the calculated and observed frequencies, showing the validity of Brown's theory for these observations. The NQR frequencies decrease with increasing temperature. The coefficients of temperature variation of the resonance frequency due to change in amplitude of torsional motions and torsional frequencies are also estimated. They are of the expected order of magnitude. No phase transition is observed in the temperature range investigated.

Nuclear quadrupole resonance (NQR) frequency generally decreases with increasing temperature. This dependence is attributed mainly to the molecular vibrations in solids. In view of the complexity of the problem, successive theories built up by Bayer,¹ Kushida *et al.*,² Brown³ and others had to remain qualitative and semiquantitative. NQR investigations of any sort, are not available for chlorobenzamides and dichlorobenzamides. As such, it is proposed to conduct investigations on these compounds. As a first step, 2,6-dichlorobenzamide was taken. Two resonance lines were first observed at room temperature as well as at liquid nitrogen temperature for this compound and reported⁴ by the authors. The temperature variation study of these two lines has been carried out from liquid nitrogen temperature (LNT) to room temperature (RT) to look for a phase transition in the temperature range under study, and the results are discussed in this note applying Brown's theory.

A self-quenched super-regenerative spectrometer was used to observe the NQR signals. For observing the resonance at LNT, the rf coil with the tube containing the sample is directly immersed in liquid nitrogen contained in a dewar flask. For temperatures between the LNT and RT, petroleum ether is selected as the suitable coolant. The temperatures were measured with a pentane thermometer and the frequencies with type 121 b frequency meter. The estimated error in the measurement of frequency is ± 100 kHz.

As the compound under investigation is a molecular crystal, Brown's theory was used in analyzing the experimental data. Brown's extension of Bayer's ideas has taken into account (1) the axes of torsional motions not being confined to the principal axes of the electric field gradient tensor and (2) the variation of torsional frequencies themselves with temperature as a result of the expansion of the lattice. Including these two effects, Brown obtained for the NQR frequency at a temperature T

$$\nu_T = \nu_0 + b'(T - T_0) + d(T - T_0)^2$$

where ν_0 is the resonance frequency corresponding to a conveniently chosen reference temperature T_0 . The values of ν_0 , b' and d are evaluated from the observed values of ν_T using least squares method. The constants b' and d are given by

$$\frac{b'}{\nu_0} = (1 + 2 T_0 g) b_0$$

and

$$\frac{2d}{\nu_0} = (4g + 6 T_0 g^2) b_0$$

where b_0 is the value of b at T_0 and

$$b_0 = -\frac{3K}{8\pi^2} \sum_i \frac{A_i}{f_i^2}$$

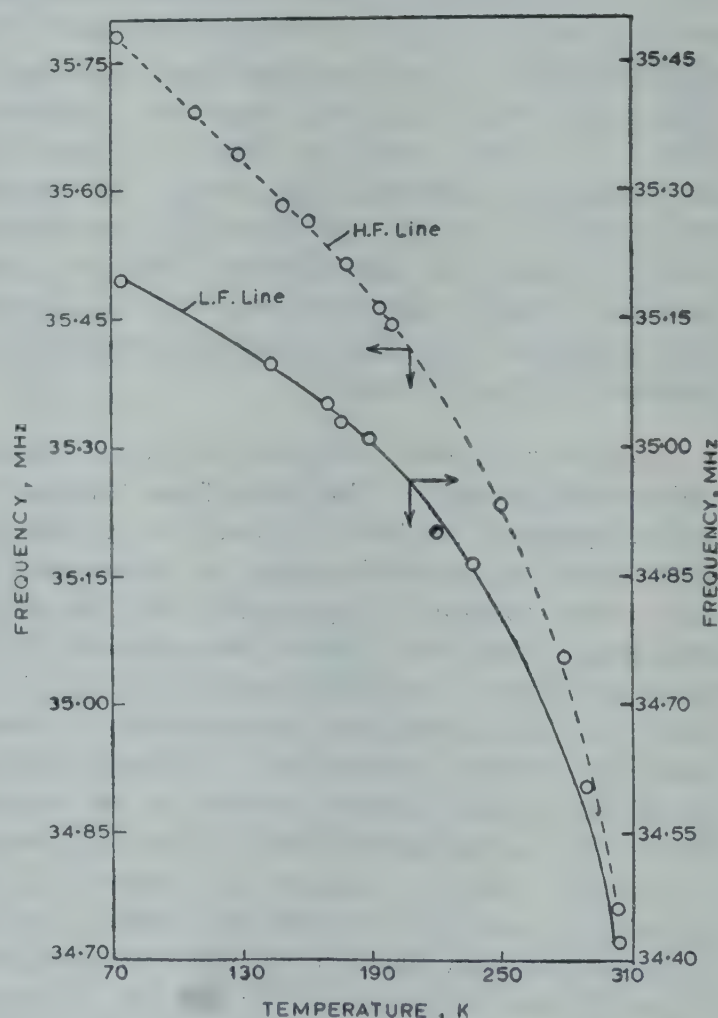


Fig. 1—Temperature variation of NQR lines in 2,6-dichlorobenzamide

Table 1—Observed and Calculated NQR Frequencies in 2,6-Dichlorobenzamide from LNT to RT

Temp. K	$\nu_{\text{obs.}}$, MHz	$\nu_{\text{calc.}}$, MHz
Low frequency line		
77	35.20	35.19
148	35.10	35.12
173	35.05	35.06
180	35.04	35.04
193	35.01	35.01
223	34.90	34.89
238	34.86	34.83
290	34.60	34.55
303	34.42	34.47
High frequency line		
77	35.78	35.74
113	35.69	35.70
133	35.64	35.66
153	35.58	35.61
165	35.56	35.57
183	35.51	35.51
198	35.46	35.45
203	35.44	35.43
252	35.23	35.18
280	35.05	35.00
303	34.76	34.83

Table 2—Values of T_0 , ν_0 , b' , d , b_0 , g , A_X , A_Y and f_t for the Two Observed NQR Lines in 2,6-Dichlorobenzamide

	Low frequency line	High frequency line
T_0 , K	180	183
ν_0 , MHz	35.044	35.513
b' , MHz K	-2.87×10^{-3}	3.81×10^{-3}
d , MHz K ²	-1.45×10^{-5}	-1.56×10^{-5}
b_0 , °C ⁻¹	-0.401×10^{-4}	-0.581×10^{-4}
g , °C ⁻¹	2.89×10^{-3}	2.30×10^{-3}
A_X , g/cm ²	2185×10^{-40}	2185×10^{-40}
A_Y , g/cm ²	1061×10^{-40}	1052×10^{-40}
f_t , cm ⁻¹	45	38

where f_t stands for any torsional frequency with A_i as the corresponding moment of inertia and g is the averaged temperature coefficient of torsional frequencies which are taken as varying linearly with temperature. Although the single b_0 value is insufficient to give values of A_i and f_t , an order of magnitude for f_t can be determined if one assumes that the molecule is executing torsional oscillations

about the X and Y axes with equal frequencies. Any oscillations about Z-axis are not involved in changing NQR frequency. Under these circumstances, the expression for b_0 reduces to

$$b_0 = - \frac{3K}{8\pi^2 f^2} \left(\frac{1}{A_X} + \frac{1}{A_Y} \right)$$

where f is the torsional frequency and A_X and A_Y are the moments of inertia about X and Y axes. The moments of inertia for the molecule are estimated from its structural data.

Graphical representation of the temperature variations for the two observed lines given in Fig. 1 and Table 1 shows the observed and calculated NQR frequencies at various temperatures. The agreement is good and there are no systematic differences between calculated and observed frequencies showing that Brown's theory holds good for these observations. The NQR frequencies decrease with increasing temperature. The values of T_0 , ν_0 , b' , d , b_0 , g , A_X , A_Y and f_t are given in Table 2. The values of b_0 and f_t are of the expected order of magnitude. No phase transition is observed in the temperature range investigated.

One of the authors (DVR) is grateful to the CSIR, New Delhi, for offering the post of a pool-officer.

References

1. Bayer H, *Z. Phys.*, **130** (1951), 227.
2. Kushida T, Benedek G B & Bloembergen N, *Phys. Rev.*, **104** (1956), 1364.
3. Brown R J C, *J. chem. Phys.*, **32** (1960), 116.
4. Ramanamurti D V, Venkatacharyulu P & Premaswarup D, *Pramana*, **13** (1979), 145.

Dielectric Loss Factor in Magnetically Polarized Silicone Rubber Tubular Electrets by TSDC

RUDRAKANT SHRIVASTAVA, M S QURESHI, M L KHARE & C S BHATNAGAR

Department of Physics, M A College of Technology
Bhopal 462 007

Received 17 April 1979; revised received 5 April 1980

Thermally stimulated discharge currents (TSDC) have been obtained from magnetically polarized silicone rubber (silastic) tubular electrets. The typical peak temperatures are 340 ± 2 and 413 K. The results are interpreted in terms of dipole orientation, space charge and electron/ion trapping. The trapping parameters are obtained using Bucci method, which utilizes the whole curve. The results are consistent with two traps in silicone rubber at 0.81 and 1.74 eV. The dielectric loss factor has been evaluated and its variation with the angular frequency and forming magnetic field (H_f) is reported.

Thermally stimulated discharge current (TSDC) technique is an effective tool in the measurement of dielectric properties of electret materials. By this method, dielectric relaxation time and activation energy were determined earlier for magnetically polarized tubular electrets.¹ The present note is an attempt to evaluate the dielectric loss factor in tubular electrets of silicone rubber.

For dipolar relaxation, the maximum dielectric loss occurs at the resonant frequency which is inversely proportional to the relaxation time (τ) of the dipoles at the temperature of measurement (T), and τ is given by

$$\tau = \tau_0 \exp (E_a/kT) \quad \dots(1)$$

where τ_0 is the pre-exponential constant, E_a the activation energy and k the Boltzmann's constant. From Eq. (1) we have

$$\ln \tau = \ln \tau_0 + E_a/kT \quad \dots(2)$$

which ultimately yields²

$$\ln \tau = \ln \left[\int_{t'=t(T)}^{\infty} i(t') dt' \right] - \ln i(T) \quad \dots(3)$$

where $i(t')$ is current at a time t' and corresponding temperature T . From Eq. (2), a plot of $\ln \tau$ versus $1/T$ gives a straight line if a uniform process is operative. The slope and intercept of this line serve to determine the value of E_a and τ_0 . The integration part of Eq. (3) can be estimated graphically, with fairly good accuracy, from the TSDC curve. Once τ_0 and E_a are known τ at any other temperature can be calculated by using Eq. (1).

The area under the TSDC curve gives the charge $Q(T_f, H_f)$ stored in a dielectric after polarization. It can be expressed in terms of steady state dielectric constant (ϵ_s) and high frequency dielectric constant (ϵ_∞) of the material³⁻⁵.

$$Q(T_f, H_f) = (\epsilon_s - \epsilon_\infty) C_0 E_{eq} \quad \dots(4)$$

where C_0 is the air capacitance of the sample assembly and E_{eq} is the equivalent electric field which will give the same charge $Q(T_f, H_f)$. The Debye equation for dielectric loss,

$$\epsilon'' = \frac{(\epsilon_s - \epsilon_\infty) \omega \tau}{1 + \omega^2 \tau^2} \quad \dots(5)$$

can now be rewritten as

$$C_0 E_{eq} \epsilon'' = \frac{Q(T_f, H_f) \omega \tau(T_f)}{1 + \omega^2 \tau^2(T_f)} \quad \dots(6)$$

using the values of Q and $\tau(T_f)$ obtained from the TSDC curve, the factor $C_0 E_{eq} \epsilon''$, which is proportional to the dielectric loss ϵ'' , can be evaluated and represented as a function of ω (Fig. 3).

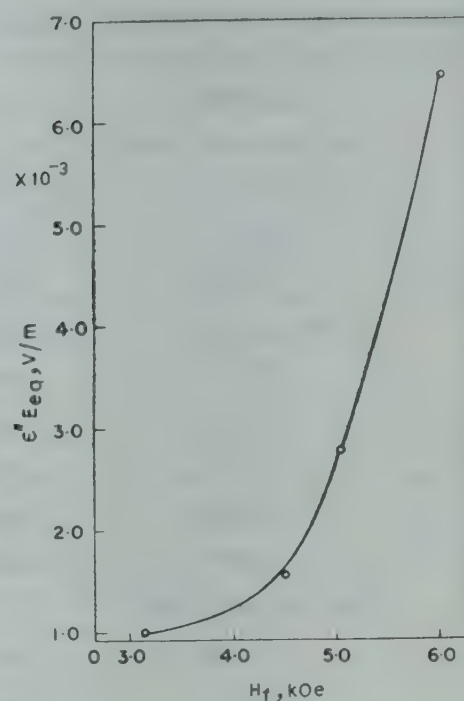


Fig. 1—Variation of $E_{eq} \epsilon''$ with H_f

Silicone rubber (Dow Corning, USA) tubes of length 3.2 cm (diameter 8 mm with wall thickness 2 mm) were used for the experiment. The tubes were cleaned according to the instructions of the manufacturer and then were charged magnetically by the method used earlier.¹ Samples were prepared at the forming temperature $T_f = 95, 120$ and 140°C . Best magneto-electrets were formed at 140°C ; hence only these samples were analyzed. Samples were prepared at magnetic fields of 3.11, 4.45, 5.04 and 5.96 kOe, which were brought to room temperature under the magnetic field. The total poling time was 2 hr 45 min. After polarization, each sample was housed in between two tubular copper electrodes for TSDC measurement. The assembly was then kept in a heating chamber, the temperature of which was controlled at the rate of $1^\circ\text{C}/\text{min}$. The chamber was electrically insulated to avoid stray pick-ups and TSDC measurements were made using Keithley 610 C electrometer. The TSDC spectra show discharge current in both the directions — negative and positive (Fig. 2). The first current peaks are in negative direction and occur at 340 ± 2 K, while the second current peaks occur at 413 K and are positive in nature. TSDC from blank samples show no current peak. Values of E_a , calculated by the method described above, are given in Table 1. The average value of E_a for first and second peaks are 0.811 ± 0.004 and 1.735 ± 0.16 eV respectively. The plots of $\ln \tau$ versus $1/T$ are straight lines. The charge released during TSDC has been calculated by extrapolating the curves to the temperature axis and its values are shown in Table 1. The dielectric loss

factor has been calculated using Eq. (6) by substituting different values of ω .

The variation of dielectric loss with angular frequency is shown in Fig. 3. At lower frequencies, there is considerable increase in the loss factor with magnetic field. Fig. 1 shows variation of E_{eq} against forming magnetic field.

As suggested by Turnhout,⁶ during TSDC we may expect the current peaks for dipole reorientation to occur at a lower temperature than for the excess charge motion. The first process requires only a rotational motion of molecular groups, whereas the latter process involves a motion of molecular groups (ions) over macroscopic distances.

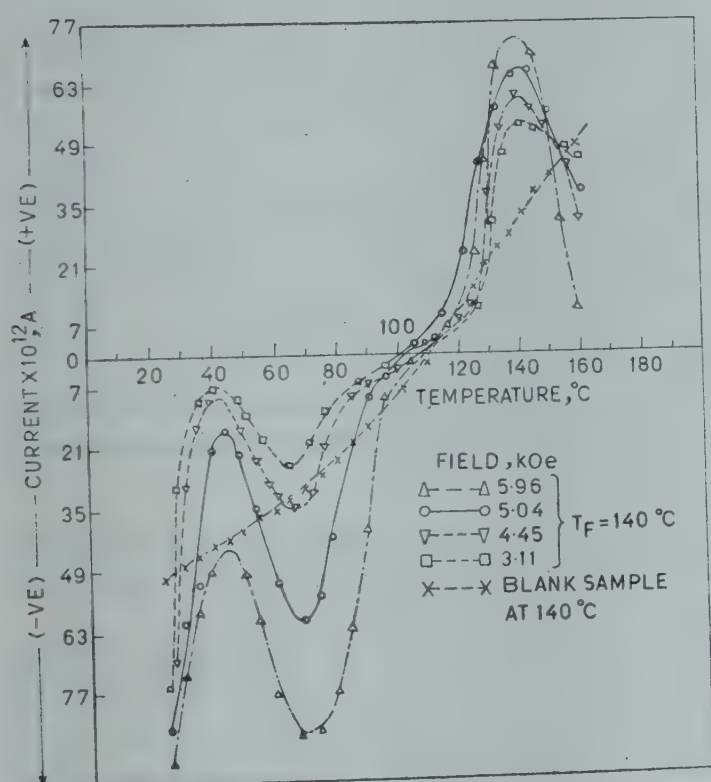


Fig. 2—Effect of different field strengths on the TSDC of magnetically polarized tubular electrets

Hence the first peak in TSDC can be attributed to dipole relaxation while the second peak is due to ionic (space charge) motion. The values of τ_{300} (Table 1) are higher for the second peak than for the first. The decrease of loss factor at higher values of ω shows that the loss factor is due to comparatively larger ions and dipoles which are not free to respond to the higher frequencies.

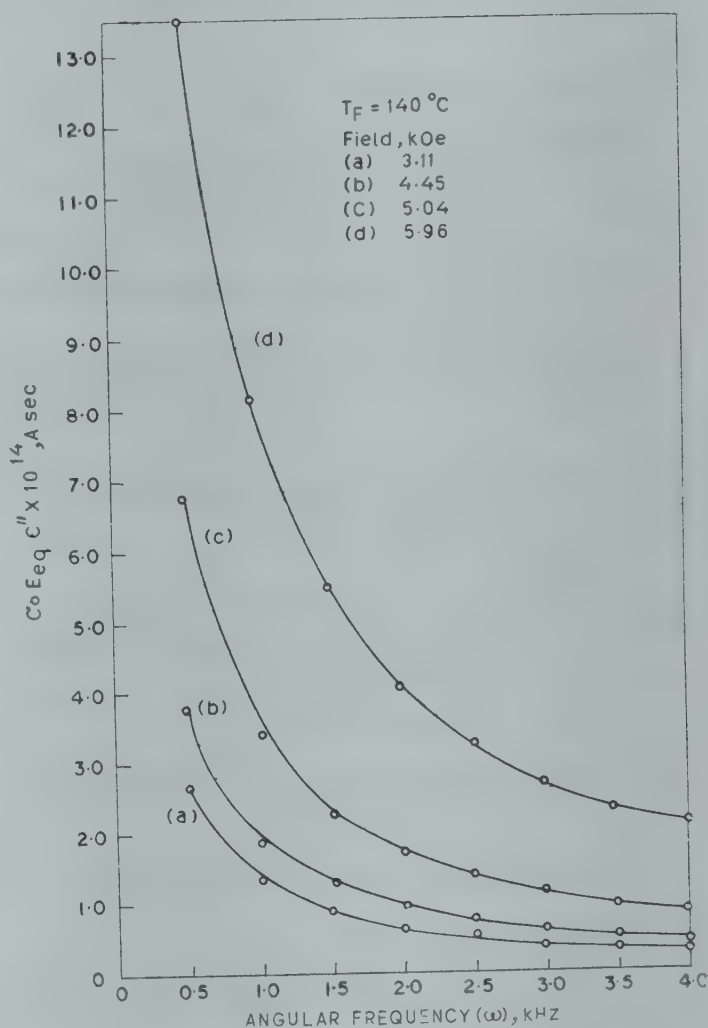


Fig. 3—Variation of dielectric loss factor $C_0 E_{eq} \epsilon''$ with angular frequency for samples prepared at different H_f

Table 1—Values of I_m , Q , E_a , τ_0 , τ_{300} and $\tau(T_f)$ Calculated by BuCCI Plot Method ($T_f = 140^\circ\text{C}$)

H_f kOe	Q 10^{-7} coul	I_m 10^{-11} A	T_m K	E_a eV	τ_0 sec	τ_{300} sec	$\tau(T_f)$ sec
1st Peak							
3.11	1.49	2.6	389	0.758	6.908×10^{-12}	38.87	—
4.45	1.59	3.6	340	0.829	5.169×10^{-13}	44.80	—
5.04	2.36	6.2	341	0.786	1.913×10^{-14}	30.43	—
5.96	3.11	8.8	342	0.872	6.966×10^{-14}	33.76	—
2nd Peak							
3.11	—	5.4	414	1.748	1.451×10^{-18}	3.563×10^{11}	2836.43
4.45	—	6.0	413	1.785	3.349×10^{-19}	3.445×10^{11}	2116.22
5.04	—	6.8	413	1.477	1.579×10^{-15}	1.076×10^{11}	1727.21
5.96	—	7.4	413	1.928	2.687×10^{-21}	7.018×10^{11}	947.12

The authors wish to thank R C Gunter of College of Holy Cross, Worcester, USA for many helpful discussions during his visit to the institutions. The authors wish to express their thanks to Dr J K Quamara for his valuable suggestions. They are also thankful to the National Science Foundation, USA for financial assistance. Thanks are also due to the Principal, Maulana Azad College of Technology, Bhopal, for providing facilities to work.

References

1. Srivastava Rudra Kant *et al.*, *Japan J. appl. Phys.*, **17** (1978), 1537.
2. Bucci C & Fieshi R, *Phys. Rev.*, **148** (1966), 816.
3. Perlman M M, *J. electrochem. Soc.*, **119** (1972), 892.
4. Hino T, Suzuki K & Yamashita K, *Japan J. appl. Phys.*, **12** (1973), 651.
5. Turnhout J V & Ong P H, *Proc. International Elect. Engg. Conf., Cambridge*, 1975.
6. Turnhout J V, *Thermally stimulated discharge of polymer electrets*, PhD thesis, Central Laboratorium, Netherlands, 1972.

Structure & Vibrational Spectra of Ethylthionformate

H S RANDHAWA,* G S GREWAL & C L ARORA

Department of Chemistry, Punjab Agricultural University
Ludhiana 141 004
and
V N SARIN

Department of Physics, Indian Institute of Technology
Kanpur 208 016

Received 12 July 1978; accepted 10 June 1980

The molecular structure of ethylthionformate has been suggested using infrared vapour phase spectral data and Raman spectra with polarization ratios of the pure liquid, and vibrational assignments proposed. The ethyl barrier found by CNDO/2 method has been found to be 0.45 kcal/mole.

The structure of simple alkyl esters has been extensively investigated by various physical methods.¹ Thion esters which have been studied by dipole moment measurements have been an analogous conformation.² Structure analysis of methylthionformate on the basis of an electron diffraction³ and vibrational spectroscopic studies⁴ and of methylthiolformate on the basis of infrared, microwave spectra and electric dipole moment studies⁵ have been recently made. Since the simplest of this series has been investigated, a study of slightly more complex system was deemed worthwhile. Therefore, we have recorded the infrared spectrum in the vapour phase and Raman spectra with the polarization data of the pure liquid

sample of ethylthionformate. The assignments of the vibrational frequencies have been made using our data and earlier data available on similar compounds.^{1,4,5} Hence, a tentative molecular structure of the compound has been suggested.

Experimental procedure—Ethylthionformate used in the present spectral measurements was prepared according to the method described by Holsboer and Kloosterziel⁶ and its purity was checked by GLC method. All infrared measurements were carried out on a Perkin-Elmer 325 spectrophotometer. A 10 cm long gas cell was first flushed with dry nitrogen and then the sample was introduced after pumping out the nitrogen. Adequate amount of the sample was introduced in the cell to get well resolved contours in the vapour phase infrared spectrum in the range 4000–540 cm⁻¹. The spectrum has been shown in Fig. 1 and the band positions with relative intensities and assignments are given in Table 1.

The Raman spectra of the pure liquid with and without polarization attachment were recorded on Carry 82 spectrophotometer. For exciting the Raman spectra, 5145.3 Å line of argon ion laser was used. The depolarization ratios were found by comparing the intensities of the bands in the two spectra. The spectra are shown in Fig. 2 and the band positions with intensities and depolarization data are presented in Table 1.

Results and discussion—Assuming that ethylthionformate also has *cis* configuration, like methylthionformate,^{3,4} its 27 vibrations belong to *A'* and *A''* species of *C_s* point group. All these vibrations should be infrared and Raman active. Out of 27 fundamental vibrations, 22 appear in Raman and infrared spectra (Table 1). Most of the fundamental vibrational modes observed in the infrared and Raman spectra of ethylthionformate have been assigned on the basis of comparison with spectral data of related esters^{1,4,5} (Table 1). Some of the CH vibrations in the two groups (CH₂, CH₃) seem to overlap. In the literature⁷ C=S bond when it is not linked with nitrogen must appear in the range 1025–1225 cm⁻¹ as a strong band.

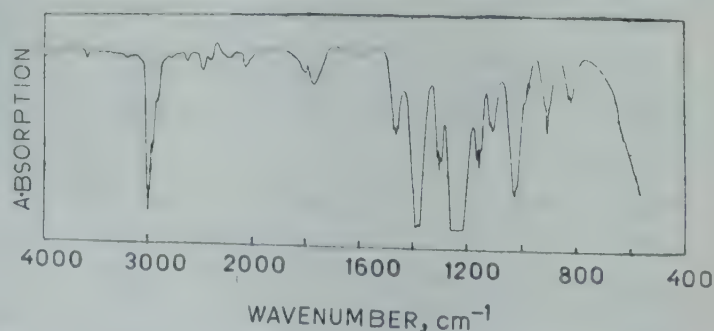


Fig. 1—Infrared spectrum of vapour of ethylthionformate

*To whom all queries should be addressed.

Table 1—Infrared and Raman Band Frequencies of Ethylthionformate

Infrared Spectrum		Raman Spectrum		Assignment species
Vapour		cm ⁻¹	Depolarization ratio	
cm ⁻¹	type			
3580 w	—	—	—	2965 + 602 = 3567
3200 w	—	—	—	2945 + 255 = 3200
2995 st	A	2995 st	0.3	CH ₃ asym/sym str, A''/A'
2960 sh	—	2965 st	p	CH ₃ sym str, A'
2945 sh	—	2945 vst	p?	CH ₂ asym str, A''
2905 sh	—	2900 m	p	CH ₂ sym str, A'
2890 sh	—	2880 m	p	CH str, A'
2775 vw	—	2775 w	p	2 × 1385 = 2770
—	—	2757 w	p	1385 + 1363 = 2748
—	—	2718 w	p	1270 + 1455 = 2725
2696 vvw	—	—	—	1455 + 1230 = 2685
2618 w	—	—	—	2 × 1300 = 2600
2465 m	—	—	—	2 × 1245 = 2490
2400 w	—	—	—	1245 + 1155 = 2400
2220 vw	B	—	—	2 × 1108 = 2216
2060 w	C	—	—	2 × 1025 = 2050
1800 w	B	1820 vvw	?	2 × 912 = 1824
1760 m	—	1745 vvw	—	2 × 815 + 85 = 1715
1595 w	—	—	—	1363 + 212 = 1575
1460 m	C	1455 m	0.75	CH ₃ , asym/sym bend, A''/A'
1380 st	A	1385 m	0.1 (p)	CH bend, A'
—	—	1363 w	dp	CH ₂ asym/sym bend, A''/A'
1300 m	A	1305 vvw	?	CH ₃ sym bend, A'
—	—	1270 vw	dp	CH ₂ wag, A''
1245 bst	—	1230 m	p	C—O str, A'
1155 m	A	1155 w	p?	CH ₂ twist, A''
1112 m	?	1108 m	p	CH ₂ rock, A''
1100 m	?	1098 m	p	CH ₃ rock, A''
1025 st	—	1015 st	0.1 (p)	C=S str, A'
985 sh	—	985 st	0.05 (p)	C—C str, A'
970 sh	—	972 m	p	620 + 360 = 980
900 m	C	912 vw	dp	CH bend, A''
815 m	A	818 st	0.04 (p)	O—C ₂ H ₅ str, A'
—	—	800 hump	p	?
640 sh	—	630 w	0.66	360 + 255 = 615
620 hump	—	602 w	p?	S C O bend, A'
—	—	360 m	p	C O C bend, A'
—	—	330 w	p?	255 + 85 = 340
—	—	300 w	p	212 + 85 = 297
—	—	255 w	0.75	C O torsion, A''
—	—	212 w	0.25	C C torsion, A''
—	—	85*	—	O C ₂ H ₅ torsion, A''

Abbreviations used in the Table have the following meanings: p-polarized, dp-depolarized, w-weak, vw-very weak, vvw-very very weak, bst-broad strong, st-strong sh-shoulder, vst-very strong, m-medium, str-stretch, sym-symmetric, asym-asymmetric, *-estimated from combination tones.

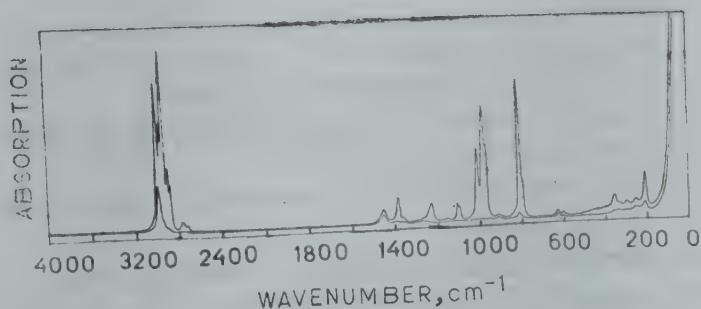


Fig. 2—Raman spectra of liquid ethylthionformate

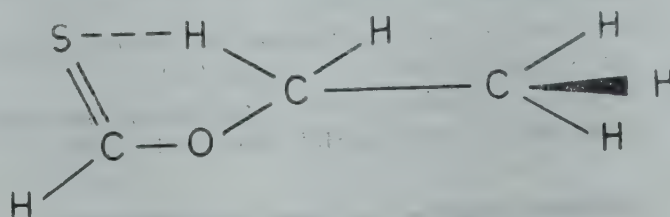


Fig. 3—Molecular model of ethylthionformate

Thus a strong band observed at 1015 and 1025 cm⁻¹ in the Raman and infrared spectra respectively may easily be assigned to the C=S stretching frequency. The position of large number of bands are in conformity with literature.⁷ The vibrations which are weakly depolarized but are supposed to be polarized may be due to environmental effects since the Raman spectra have been recorded for pure liquids.

The absorption seen at 900 cm⁻¹ for the vapour has a type C contour with a strong central Q branch and is almost certainly associated with the C—H (formyl) out-of-plane bend. The presence of such a type C contour is strongly indicative of planar or near planar skeletal molecular structure.^{4,5}

The molecular parameters used in the calculations were taken from the literature³ and the ethyl barrier calculated by CNDO/2 method⁸ has been found to be 0.45 kcal/mole. The origin of ethyl barrier in this molecule can be due to weak hyperconjugation (for conjugation a molecule is supposed to be planar or nearly planar) due to the combination of out-of-plane methylene hydrogen 1s orbitals with π -symmetry which in turn combines with the other π -atomic orbitals. The resulting occupied π -molecular orbitals bear some formal resemblance to those of a five membered ring. This suggests that the configuration is *cis* in nature as shown in Fig. 3.

One of the authors (HSR) is indebted to Alexander Von Humboldt Stiftung, West Germany and CSIR, New Delhi for financial assistance and the Computer Centre authorities of Indian Institute of Technology, Kanpur, for computational work. Thanks are also due to Prof. Dr W Walter of the Institute of Organic and Biochemistry, University of Hamburg (BRD), for hospitality.

References

1. Durig J R & Griffin M G, *J. molec. Spectrosc.*, **64** (1977), 252 and the reference cited therein.
2. Exner O, Jehlicka V & Ohno A, *Collect. Czech. Chem. Commun.*, **36** (1971), 2157.
3. Rooij J De, Mijlhoff F C & Renes G, *J. molec. Struct.*, **25** (1975), 169.
4. Randhawa H S, *Z. phys. Chem.*, (1980), in press.
5. Jones G I L, Lister D G, Owen N L, Gerry M C & Palmieri P, *J. molec. Spectrosc.*, **60** (1976), 348.
6. Holsboer D H & Kloosterziel H, *Rec. Trav. Chem. Phys. Bas.*, **91** (1972), 1371.
7. Rao C N R, *Chemical applications of infrared spectroscopy* (Academic Press, New York), 1961.
8. Pople J A & Beveridge D L, *Approximate molecular orbital theory*, (McGraw Hill, New York), 1970.

Infrared Studies on Some Di-Substituted Pyridines*

R K GOEL, S K GUPTA** & S N SHARMA†

Department of Physics, D N College, Meerut 250 002

Received 23 October 1978; revised received 14 May 1980

The infrared absorption spectra of 2-amino-4-methyl-, 2-amino-5-methyl- and 3-amino-2-chloro-pyridines have been recorded in the region 4000-250 cm^{-1} in KBr pellet, nujol mull and in CS_2/CCl_4 and CHCl_3 solutions. The spectra have been analyzed assuming C_s point group symmetry and the assignments of observed bands to different fundamental modes have been made. Tautomerism caused by NH_2 group is also discussed.

The vibrational and electronic spectra of pyridine and its derivatives have been studied in detail by several workers.¹⁻⁶ So far, no work seems to have been done on the molecules, 2-amino-4-methyl-, 2-amino-5-methyl- and 3-amino-2-chloropyridines which are of the type $\text{C}_5\text{H}_3\text{NXY}$. The present note reports the infrared spectra of these molecules and discusses the tautomerism caused due to NH_2 group.

Pure chemicals, 2-amino-4-methyl-pyridine, 2-amino-5-methyl-pyridine and 3-amino-2-chloropyridine (hereafter referred to as 2,4-AMP; 2,5-AMP and 3,2-ACP respectively), obtained from M/s Fluka AG, Switzerland (2,4-AMP) and Tokyo Kogyo Kasei Co, Tokyo (2,5-AMP & 3,2-ACP), were used as such. The infrared absorption spectra of these molecules have been recorded on Perkin-Elmer spectrophotometer model-521, in KBr pellet, nujol

mull and CS_2/CCl_4 and CHCl_3 solutions in the region 4000-250 cm^{-1} . Some of the fundamental frequencies in KBr pellet and CS_2/CCl_4 solution along with their assignments are given in Table 1 while the remaining frequencies and the infrared data in nujol mull and in CHCl_3 solution are available with the authors. Assuming NH_2 and CH_3 groups as single mass points, the molecules under study would belong to C_s point group symmetry.

The three C—H valence oscillations (aromatic) for 2,4-AMP; 2,5-AMP and 3,2-ACP in the region 3100-3000 cm^{-1} are given in Table 1 which find support from the work of earlier workers.^{4,6,7} The C—H stretching frequencies due to CH_3 group are also shown in Table 1.

In the spectra of pyridine² a pair of bands appearing at 1482, 1439 cm^{-1} and another at 1310 cm^{-1} were assigned to coupled C—C and $\text{C}\equiv\text{N}$ stretching vibrations. In view of this, pairs of strong bands at 1481, 1447 cm^{-1} in 2,4-AMP, at 1487, 1447 cm^{-1} in 2,5-AMP and at 1465, 1435 cm^{-1} in 3,2-ACP and the bands at 1306, 1304 and 1280 cm^{-1} in these 3 molecules respectively have been assigned to coupled C—C and $\text{C}\equiv\text{N}$ stretching vibrations. The bands observed at 787, 817 and 797 cm^{-1} in the 3 molecules respectively have been assigned to C—C—C trigonal bending mode and those at 985, 1017 and 975 cm^{-1} to C—C ring breathing mode, which are in agreement with those given in the literature.^{3,5,6} The ring vibrations corresponding to e_{2g} (1595 cm^{-1}) mode of benzene are shown in Table 1.

The C— CH_3 stretching mode has been identified at 1272 and 1260 cm^{-1} in 2,4-AMP and 2,5-AMP respectively. This finds support from values^{3,7} given in the literature. The absence of a strong band in 3,2-ACP in this region also supports the above assignment. The C— CH_3 out-of-plane bending mode usually lies near 300 cm^{-1} .¹⁸ As presented in Fig. 1(A) bands are observed in KBr and nujol mull near 300 cm^{-1} with considerable intensity in 2,4-AMP and 2,5-AMP and no band in 3,2-ACP in this region. Thus, the bands at 305 cm^{-1} in both 2,4-AMP and 2,5-AMP have been assigned to C— CH_3 out-of-plane bending mode without any ambiguity.

Many workers have assigned the C—Cl stretching mode in the region 550-750 cm^{-1} . Singh and Singh⁹ have reported a Raman frequency around 680 cm^{-1} for the 3 isomeric chlorotoluenes. When the spectra of the molecules presently studied are examined in the region 690-740 cm^{-1} [Fig. 1(B)], it is observed that two very strong bands appear in the spectra of 3,2-ACP, while only one band appears in this region in 2,4-AMP and 2,5-AMP. The additional band

*Part of it was presented at 66th session of the Indian Science Congress Association held at Hyderabad in Jan. 1979.

**Department of Physics, K K Jain College
Khatauli 251 201

†Analytical physics section, Indian Institute of Petroleum
Dehra Dun 248 005

Table 1—Assignments of Fundamental Vibrational Frequencies of Some Di-substituted Pyridines (all values in cm^{-1})
Positions of the bands alongwith their intensities* Assignment

2,4-AMP in		2,5-AMP in		3,2-ACP in		Assignment
KBr	CS_2/CCl_4	KBr	CS_2/CCl_4	KBr	CS_2/CCl_4	
380(m)	375(vsb)	382(m)		383(mw)		β (C—NH ₂)
668(m)	662(ms)	655(s)	665(mw)	630(vw)	—	NH ₂ wagging
—	—	—	—	733(vvs)	730(vvs)	ν (C—Cl)
787(vvs)	795(vvs)	817(vvs)	—	797(vvs)	793(vvs)	(C—C—C) trigonal bend
962(s)	—	957(ms)	—	—	—	CH ₃ rocking
985(vs)	985(s)	1017(vs)	—	975(s)	—	ν (C—C), ring breathing
1037(s)	—	—	—	—	—	CH ₃ rocking
1127(vw)	—	1137(vs)	—	1110(vsb)	—	NH ₂ twisting
1320(s)	1325(s)	1319(sb)	—	1330(vs)	1320(s)	ν (C—NH ₂)
1554(vs)	—	1564(vs)	—	1569(mw)	—	ν (C—C), e_{2g} (1595)
1579(vw)	—	—	1569(mw)	—	—	β (N—H)
1616(vs)	1606(vvs)	—	1589(mw)	1584(m)	—	ν (C—C), e_{2g} (1595)
1644(sb)	—	1609(vvsb)	1609(vs)	1609(m)	—	NH ₂ scissoring
—	—	—	2869(sh)	—	—	ν (C—H), sym. in methyl group.
2904(m)	2929(vw)	—	2929(s)	—	—	ν (C—H), asym. in methyl group.
—	3023(s)	—	3019(vs)	—	3041(mb)	ν (C—H) aromatic
3100(vvw)	3065(ms)	—	—	—	3104(vvw)	ν (C—H) aromatic
3124(vs)	3109(mw)	—	—	—	—	ν (C—H) aromatic
3309(s)	3309(s)	3289(msb)	3319(msb)	—	—	ν (N—H)
—	3411(vs)	—	3409(vs)	—	3404(s)	ν (N—H), sym.
—	3509(vs)	—	3509(vs)	—	3499(s)	ν (N—H), asym.

*Intensities are shown in parentheses against each wavenumber. s, strong; vs, very strong; vvs, very very strong; m, medium; ms, medium strong; mw, medium weak; w, weak; vw, very weak; vvw, very very weak; b, broad; sh, shoulder; ν , stretching; β , in-plane bending.

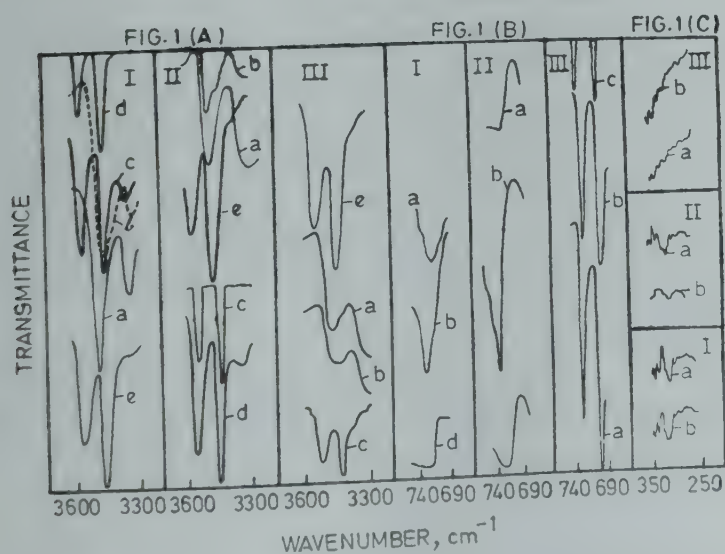


Fig. 1—Infrared absorption frequencies of (I) 2-amino-4-methyl pyridine (II) 2-amino-5-methyl pyridine and (III) 3-amino-2-chloropyridine in (a) KBr, (b) Nujol mull, (c) CS_2 , (d) CCl_4 , (e) CHCl_3

observed in 3,2-ACP at 733 cm^{-1} has thus been clearly assigned to the C—C stretching mode. Here attempts were made to check the assignments of this mode by taking the spectra in different solvents and looking for any frequency shift as has been done by Nabumi Oi and Coetzee,¹⁰ but no frequency shift has been observed in solutions.

The C—NH₂ stretching vibration appears near 1300 cm^{-1} (Ref. 11). This mode has been identified at 1320, 1319 and 1330 cm^{-1} in 2,4-AMP; 2,5-AMP and 3,2-ACP respectively. However, in some spectra it may have some contribution from C—C stretching vibration corresponding to b_{2u} (1310 cm^{-1}) mode of benzene.

It is interesting to note (Table 1) that two bands have been observed in the region $3150\text{--}3600\text{ cm}^{-1}$ in 2,4-AMP and 2,5-AMP with the exception that for

2,4-AMP, three bands appear in CS_2 solution and three for 2,5-AMP in CHCl_3 solution. In the case of 3,2-ACP, the two N—H peaks have not been resolved in KBr and nujol mull but were clearly resolved in CS_2 and CHCl_3 solutions. Bellamy and Williams¹² have shown that symmetric and asymmetric N—H stretching vibrations obey the empirical relation $\nu_{\text{sym}} = 345.53 + 0.876 \nu_{\text{asym}}$. The bands near 3400 and 3500 cm^{-1} (in solutions) in all the molecules under study obey this relation while it has not been followed for the two bands observed in the KBr pellet spectra in 2,4-AMP and 2,5-AMP. The higher frequency band in KBr and nujol mull in all the 3 molecules lies between the respective two bands which obey the empirical relation. This suggests that the asymmetric and symmetric N—H stretching vibrations have not been resolved in KBr or nujol. The second band in KBr and nujol in 2,4-AMP and 2,5-AMP is very well correlated with the third band observed in the solution spectra of these molecules. The occurrence of the third band near 3300 cm^{-1} in 2,4-AMP and 2,5-AMP indicates that tautomerism is taking place in these molecules, i.e. one H-atom of the NH_2 group is loosely bound and has a simultaneous association with the nitrogen of the ring as well as with the NH_2 group, thus giving a third N—H stretching vibration. This is very well exhibited in Fig. 1(C). The absence of a third band in 3,2-ACP (where NH_2 group is away from the nitrogen of the ring) further confirms this effect. The presence of additional N—H planar deformation near 1600 cm^{-1} in 2,4-AMP and 2,5-AMP (Table 1) and its absence in 3,2-ACP also supports this conclusion.

One of the authors (RKG) is thankful to the University Grants Commission, New Delhi, for financial assistance.

References

1. Spomer H & Stucklen H, *J. chem. Phys.*, 14 (1946), 101.
2. Wilmschurst J K & Bernstein H J, *Can. J. Chem.*, 35 (1957), 1183.
3. Medhi K C, *Indian J. Phys.*, 51A (1977), 399.
4. Green J H S, Kynastan W & Paisley H M, *Spectrochim. Acta*, 19 (1963), 549.
5. Tripathi R S, *Indian J. pure appl. Phys.*, 11 (1973), 277.
6. Goel R K, Rohitashava & Sharma S N, *Indian J. pure appl. Phys.*, 17 (1979), 187.
7. Goel R K, Sanyal Nitish K & Srivastava S L, *Indian J. pure appl. Phys.*, 14 (1976), 842.
8. Green J H S, Harrison D J & Kynastan W, *Spectrochim. Acta*, 27A (1971), 793,807.
9. Singh S N & Singh N L, *Indian J. pure appl. Phys.*, 6 (1969), 488.
10. Nabumi O I & Coetzee J F, *J. Am. chem. Soc.*, 91 (1969), 2473.
11. Singh V B, Singh R N & Singh I S, *Spectrochim. Acta*, 22 (1966), 927.
12. Bellamy L J & Williams R L, *Spectrochim. Acta*, 9 (1957), 341.

Infrared Absorption Spectra of 2-Amino-3-Methyl- & 6-Amino-2-Methyl-Pyridine*

R K GOEL, S D SHARMA, K P KANSAL† & S N SHARMA†

Department of Physics, D N College, Meerut 250 002

Received 14 August 1978; accepted 28 November 1979

The infrared absorption spectra of 2-amino-3-methyl- and 6-amino-2-methyl-pyridine have been recorded in thin film on Perkin Elmer spectrophotometer-521 and Grubb Parsons (Mk I) spectrophotometer respectively. The spectra have been analyzed assuming C_s point group and tentative assignment of the observed bands to different fundamental modes has been made. A correlation of the observed fundamental modes has been made. Tautomerism caused by NH_2 group has been discussed.

The vibrational spectra of pyridine and its mono-substituted derivatives have been studied in detail by several workers.¹⁻⁹ The vibrational spectra of di-substituted pyridines also appear in literature.¹⁰⁻¹⁶ The di-substituted pyridines studied so far were mostly of the type $\text{C}_5\text{H}_3\text{NX}_2$ where X is the substituent. With a view to studying the di-substituted pyridines of the form $\text{C}_5\text{H}_3\text{NXY}$ (where X and Y are different substituents), the molecules 2-amino-3-methyl- and 6-amino-2-methyl pyridine have been investigated and their infrared absorption spectra are reported in this note. Since the substituents like OH, SH, NH_2 may exhibit tautomerism in N-heterocyclic molecules, it is also aimed to study the tautomeric behaviour due to NH_2 group as substituent in the molecules under study.

Pure chemicals, 2-amino-3-methyl-pyridine and 6-amino-2-methyl-pyridine (hereafter referred to as 2, 3-AMP and 6, 2-AMP), obtained respectively from M/s Tokyo Kasei Kogyo Co, Tokyo and M/s Fluka AG, Switzerland, in liquid phase, were used as such. The infrared absorption spectra were recorded for 2, 3-AMP on Perkin-Elmer-521 spectrophotometer in the region 250-4000 cm^{-1} and that of 6, 2-AMP on Grubb Parsons (Mk II) spectrophotometer and in the region 400-4000 cm^{-1} respectively. The spectrophotometers were calibrated with the help of the spectrum of thin sheet of polystyrene. The fundamental frequencies along with their assignments are given in Table 1.

Assuming NH_2 and CH_3 groups as single mass points, both the molecules belong to C_s point group symmetry under which the 27 normal vibrations will be distributed as 19a' (planar) and 8a'' (non-planar).

*Part of this note was presented at the National Conference on Molecular Spectroscopy held at the Annamalai University, Annamalai Nagar, Tamil Nadu, in August, 1979

†Department of Physics, S S V College, Hapur

†Analytical Physics Section, Indian Institute of Petroleum Dehra Dun 248 005.

Table 1—Assignments of Fundamental Vibrational Frequencies of Amino-Methyl Pyridines
(All values in cm^{-1})
Band Position and Intensities

2,3-AMP	6,2-AMP	Assignment	2,3-AMP	6,2-AMP	Assignment
3464 (mb)	3335 (mb)	ν (N—H)	1272 (s)	1235 (vvw)	β (C—H)
3339 (vsb)	3242 (m)	ν (N—H)	1297 (vs)	1175 (ms)	ν (C—CH ₃)
3184 (sb)	3175 (mb)	ν (N—H) Add.	1132 (m)	1115 (w)	NH ₂ twisting
3024 (w)	3000 (vvw)	ν (C—H) Aromatic	1077 (vs)	1085 (vw)	CH ₃ rocking
2934 (mb)	—	ν (C—H) asym. in methyl group	1035 (s)	1065 (w)	CH ₃ rocking
2924 (mw)	2905 (vvw)	ν (C—H) asym. in methyl group	992 (s)	992 (s)	β (C—C—C) Trigonal bending
2854 (mw)	2857 (vvw)	ν (C—H) sym. in methyl group	957 (s)	—	γ (C—H)
1606 (sb)	1640 (vs)	ν (C—C), NH ₂ Scissoring	—	886 (vvw)	γ (C—H)
1574 (s)	—	ν (C—C)	—	840 (vw)	γ (C—H)
—	1500 (s)	ν (C—C)	—	823 (vvw)	γ (C—H)
1472 (s)	—	(C—H) Asym. bend in methyl group	772 (vvs)	772 (vvs)	ν (C—C), Ring breathing
1452 (vs)	1440 (ms)	ν (C—C)	742 (m)	724 (vvw)	NH ₂ wagging
1385 (ms)	1385 (vw)	C—H asym. bend in methyl group	667 (m)	675 (m)	ϕ (C—C—C)
—	1345 (vw)	C—H sym. bend in methyl group	—	645 (m)	β (C—C)
1322 (mb)	1315 (vw)	ν (C—C)	525 (ms)	560 (vw)	β (C—C)
1292 (s)	1295 (s)	ν (C—NH ₂)	417 (m)	448 (vw)	ϕ (C—C)
			397 (m)	—	β (C—CH ₃)
			382 (m)	385 (w)†	ϕ (C—C)
			372 (m)	372 (mb)†	β (C—CH ₂)
			322 (w)	322 (m)†	γ (C—CH ₃)
			312 (vw)	—	γ (C—NH ₂)
			297 (w)	—	NH ₂ torsion

*Intensities are shown in parentheses against each wave-number: s, strong; vs, very strong; vvs, very very strong; b, broad; m, medium; ms, medium strong; w, weak; vw, very weak; vvw, very very weak; sh, shoulder; ν , stretching; β , in plane bending, γ or ϕ , out-of-plane bending

†From thin film spectra on Perkin-Elmer-521 spectrophotometer

In addition to these, there will also appear 6 and 9 internal vibrations due to NH₂ and CH₃ groups respectively. All these vibrations are active both in the infrared and Raman spectra. Since neither Raman lines with depolarization data nor the type of contours in the infrared spectra in vapour phase of these molecules are available, the selection rules are not very helpful in the assignment of different types of vibrations. Therefore, vibrational assignments have been made essentially on the basis of magnitudes and relative intensities of the observed infrared bands and the data available for similar molecules. The assignments are briefly discussed in the following.

Skeleton vibrations—In the infrared absorption spectra of these molecules, the bands at 3024 cm^{-1} in 2,3-AMP and 3000 cm^{-1} in 6,2-AMP have been assigned to the C—H stretching mode, which are in agreement with the assignments made by Green *et al.*² The C—C stretching frequencies in pyridine and its related compounds have been observed in the region 1320–1630 cm^{-1} . However, an appreciable mixing of one component of e_{2g} (1595 cm^{-1}) and NH₂

scissoring mode takes place due to near equality of these vibrations. Under such circumstances the normal vibrations of the system cannot be identified with the vibration of a particular bond alone and thus the bands in this region are assigned to the nucleus as a whole. The bands observed at 1606, 1574 and 1452 cm^{-1} , in 2,3-AMP and at 1640, 1500 and 1440 cm^{-1} in 6,2-AMP have been assigned to these modes. The non-degenerate vibration of benzene b_{2u} (1310 cm^{-1}) also corresponds to C—C stretching vibration. The bands observed at 1322 and 1315 cm^{-1} in 2,3-AMP and 6,2-AMP respectively have been assigned to this mode.

As pointed out by several other workers, the C—C ring breathing a_{1g} (995 cm^{-1}) and C—C—C trigonal bending b_{1u} (1010 cm^{-1}) vibrations of benzene give rise to combined modes in molecules belonging to C_s symmetry. Accordingly one of the modified modes reduces to about 800 cm^{-1} while the other keeps itself around 1000 cm^{-1} in trisubstituted benzenes.^{13,16} In the present case, the bands observed at 992 and 992 cm^{-1} in the two molecules have been assigned to C—C—C trigonal bending and bands

at 772 and 772 cm^{-1} respectively to C—C ring breathing vibrations.

The doubly degenerate e_{2g} (608 cm^{-1}) vibration of benzene corresponds to C—C planar bending vibration which under reduced symmetry C_s splits into two components. The corresponding frequencies in pyridine were observed⁹ at 652 and 605 cm^{-1} . In the present study only one band at 525 cm^{-1} in 2,3-AMP and a pair of bands at 645 and 560 cm^{-1} in 6,2-AMP have been assigned to this mode. It is in agreement with the assignments made by Baruah *et al.*¹² in case of 2,6-diaminopyridine.

In pyridine and mono- and di-substituted pyridines, there appear 3 out-of-plane carbon bending vibrations which result from non-degenerate b_{2g} (705 cm^{-1}) and degenerate e_{2u} (404 cm^{-1}) modes of benzene. Under C_s symmetry, the latter vibration splits into two — one remains nearly unchanged at 404 cm^{-1} and the other lying at lower frequency. We have assigned the pair of bending vibrations at 417 and 382 cm^{-1} in 2,3-AMP, and the bending vibrations at 448 and 385 cm^{-1} in 6,2-AMP to correspond to e_{2u} (404 cm^{-1}) mode of benzene.

Group vibrations—In most of the primary aromatic amines, there occur two bands in the region 3350–3550 cm^{-1} which are associated with N—H stretching vibrations. It has been pointed out by Bellamy¹⁷ that in N-octamide in chloroform solution the NH_2 free absorption occurs at 3530 and 3415 cm^{-1} but it also shows additional bands at 3498, 3345, 3300 and 3182 cm^{-1} . This suggests the occurrence of different types of simultaneous association of free and bonded NH bonds. In solid state, the pattern simplifies and gives two broader NH peaks near 3350 and 3164 cm^{-1} . In view of these considerations we have assigned the 3 bands observed at 3464, 3339, and 3184 cm^{-1} in 2,3-AMP and 3335, 3242 and 3175 cm^{-1} in 6,2-AMP to N—H stretching modes.

The bands at 2934, 2924 cm^{-1} in 2,3-AMP and at 2905 cm^{-1} in 6,2-AMP have been assigned to C—H asymmetric mode and those at 2854 and

2857 cm^{-1} in the two molecules respectively to C—H symmetric stretching mode. The bands observed at 1077, 1035 cm^{-1} in 2,3-AMP and at 1085, 1065 cm^{-1} in 6,2-AMP have been assigned to two CH_3 rocking modes. These assignments are in agreement with the assignments proposed by earlier workers.^{18,19}

One of the authors (RKG) is thankful to the University Grants Commission, New Delhi, for financial assistance.

References

1. Sponer H & Stuecklen H, *J. chem. Phys.*, **14** (1946), 101.
2. Green J H S, Kynaston W & Paisley H M, *Spectrochim. Acta*, **19** (1963), 549.
3. Long D A, Murfin F S, Hales J L & Kynaston W, *Trans. Faraday Soc.*, **53** (1957), 1171.
4. Wilmshurst J K & Bernstein H J, *Can. J. Chem.*, **35** (1957), 1183.
5. Stephenson H P & Voetz H F, *J. chem. Phys.*, **22** (1954), 1945.
6. Padhye M R & Bhujle V V, *Indian J. pure appl. Phys.*, **8** (1970), 479.
7. Green J H S & Harrison D J, *Spectrochim. Acta*, **33A** (1977), 75.
8. Pandey B R, *Spectra of some substituted benzenes*, Ph D thesis, Gorakhpur University, Gorakhpur, 1966.
9. Medhi K C, *Indian J. Phys.*, **51A** (1977), 399.
10. Green J H S & Harrison D J, *Spectrochim. Acta*, **29A** (1973), 1177.
11. Green J H S, Harrison D J, Kynaston W & Paisley H M, *Spectrochim. Acta*, **26A** (1970), 2139.
12. Baruah G D, Amma R A, Dube P S & Rai S N, *Indian J. pure appl. Phys.*, **8** (1970), 761.
13. Tripathi R S, *Indian J. pure appl. Phys.*, **11** (1973), 277.
14. Bailey R T & Steele D, *Spectrochim. Acta*, **23A** (1967), 2997.
15. Mochizuki Y, Koyak & Ito M, *J. chem. Phys.*, **65** (1976), 4163.
16. Goel R K, Rohitashava & Sharma S N, *Indian J. pure appl. Phys.*, **17** (1979), 187.
17. Bellamy L J, *The infrared spectra of complex molecules* (Chapman and Hall, London), 1975.
18. Pitzer K S & Scott D W, *J. Am. Chem. Soc.*, **65** (1943), 803.
19. Wilmshurst J K & Bernstein H J, *Can. J. Chem.*, **35** (1957), 911.

